Solar Energy Harvesting In A Photoelectrochemical Cell: Development Of Photoanodes Based On Earth Abundant Materials

Thesis submitted for the degree of

Doctor of Philosophy (Sc.)

in

Physics (Experimental)

By

Dipanjan Maity

Department of Physics

University of Calcutta

December, 2021

Dedicated to my beloved parents...

Acknowledgments

First of all, I would like to express my humble respect, special appreciation, and thanks to my Ph.D. supervisor Professor Kalyan Mandal for allowing me to pursue my research works with complete freedom. His valuable advice, guidance, and discussions always give me a new angle to deal with the research problems. He always encouraged me to think independently. He has had provided tremendous academic support and many excellent opportunities during my days in the laboratory.

I am thankful to S.N. Bose National Centre for Basic Sciences for providing a beautiful campus and good research facilities. I am very much grateful to CSIR for the CSIR JRF/SRF fellowship (Award No. 09/575(0117)/2017-EMR-I).

I want to convey my humble respect and sincere gratitude to Dr. Gobinda Gopal Khan, Assistant Professor at the Department of Materials Science and Engineering, Tripura University (A Central University), for his encouragement, guidance as a collaborator friend, and elder brother. His innovative ideas and valuable discussions have always been motivated me to face the difficulties in my research problems.

I am especially thankful to Dr. Keshab Karmakar for his valuable discussions, support, and encouragement as a responsible senior, collaborator, and friend.

I am thankful to my lab mates Dr. Madhuri Mandal, Dr. Rupali Rakshit, Dr. Souvanik Talukdar, Dr. Keshab Karmakar, Dr. Mahebub Alam, Dr. Indranil Chakraborty, Dr. Subrata Ghosh, Dr. Dipika Mandal, Ms. Piyana Saha, Dr. Deblina Majumder, Mr. Anupam Gorai, Ms. Swarnali Heit, Ms. Saheli Samanta Mr. Soham Saha, Ms. Ishita Jana, and Mr. Sridhar Mahanty. It is my pleasure to have such cooperative lab-mates who provided me excellent research environment.

A special thanks to Dr. Keshab Karmakar, Dr. Mahebub Alam, Dr. Subrata Ghosh, and Dr. Dipika Mandal for being my cooking partners. I have spent some excellent times with them, in the lab, football/cricket ground, various short trips, and supporting our beloved football club Real Madrid.

I am thankful to my seniors Dr. Sayani Chatterjee (Sister from another mother), Dr. Subhasish Chakraborty, Dr. Arghya Das, Dr. Rakesh Das, for their help, support and encouragement throughout my journey at SNB.

I also want to thank all the football players of SNB football group. More than a football team, it was my family.

I am thankful to thank Shakti Nath Das, Samik Roy Moulik, Amit Chanda, Urmi Chakraborty, Joy Bandopadhyay, Debargha Ghosh, and Sourabh Sinha for their technical assistance in the material characterization during research works at S. N. Bose National Centre for Basic Sciences.

I must thank my friends outside my lab, Apurba, Dibyendu, Susmita, Subhanka, Parijat, Sasthi, Pratap, Bijoy, Arkadeep, Ayon, Aditi, Kalyan, Kausik, Asim, Pranab, Sudip, Amir, Ikbal, Subhendu, Gobinda, Dilip and Subhadip.

I am grateful to Mr. Joydeep Nayek for his support and encouragement throughout my journey.

A special thanks to my family. They are the most important people for me in this world. I dedicate this thesis to them. Simply, words can't express their support, sacrifice, love, and affection. I am grateful to my mother Mrs. Putul Maity and father Mr. Binod Maity. I am fortunate to have my younger sister Moumita, elder sister Bitihotri and elder brother Krishnendu.

Dipanjan Maity

List of publications related to thesis work

[1] **D. Maity**, K. Karmakar, K. Mandal, NN type core-shell heterojunction engineering with MoO3 over ZnO nanorod cores for enhanced solar energy harvesting application in a photoelectrochemical cell, Journal of Alloys and Compounds. 791 (2019) 739–746.

[2] **D. Maity**, K. Karmakar, D. Mandal, D. Pal, G.G. Khan, K. Mandal, Earth abundant transition metal ferrite nanoparticles anchored ZnO nanorods as efficient and stable photoanodes for solar water splitting, Nanotechnology. 31 (2020) 475403.

[3] **D. Maity**, K. Karmakar, D. Pal, S. Saha, G.G. Khan, K. Mandal, One-dimensional p-ZnCo2O4/n-ZnO nanoheterojunction photoanode enabling photoelectrochemical water splitting, ACS Applied Energy Materials. 4 (2021) 11599–11608.

[4] **D. Maity**, D. Pal, K. Karmakar, R. Rakshit, G. G. Khan, Kalyan Mandal, Dual co-catalysts activated hematite nanorods with low turn-on potential and enhanced charge collection for efficient solar water oxidation. (Communicated)

List of publications apart from thesis work

[1] K. Karmakar, **D. Maity**, D. Pal, K. Mandal, G.G. Khan, Photo-induced exciton dynamics and broadband light harvesting in ZnO nanorod-templated multilayered two-dimensional MoS_2/MoO_3 photoanodes for solar fuel generation, ACS Applied Nano Materials. 3 (2020) 1223–1231.

[2] **D. Maity**, S. Saha, D. Pal, K. Karmakar, D. Sarkar, G.G. Khan, K. Mandal, CeOx modified $ZnFe_2O_4$ Nanorods as advanced photoanodic material for photoelectrochemical water splitting. (Manuscript under preparation)

[3] **D. Maity**, S. Saha, D. Pal, D. Sarkar, G.G. Khan, K. Mandal, Ternary metal hydroxide decorated $BiVO_4$ photoanode for efficient solar water splitting. (Manuscript under preparation)

CONTENTS

Chapter 1 | Introduction

This chapter describes the basic introduction to the research works addressed in this thesis. The motivation behind selecting the work area of solar energy harvesting in photoelectrochemical cells by using earth abundant metal oxide semiconductor based photoanodes has discussed in details. This chapter also presents the scientific insights and review of the reported literatures in this direction.

1.1 Preamble

The lifestyle of an industrially revolutionized society is dependent on technology and its advancement. The industrial revolution is serving the needs and comforts of everyday life. Energy has become the most basic demand of the global population to maintain the living standard of modern-day life. The world economy and politics are governed mainly by energy resources and associated industries. Since the days of the industrial revolution, the required energy for the economic growth and development of a society has been supplied by fossil fuels such as oil, natural gas, and coal. To date, fossil fuels are the primary energy source in modern society. About 85% of the total energy consumption of the world is supplied from fossil fuels. In the current scenario,7 billion peoples of the world (World population, 2011) consumes 15 TW of energy, which is estimated to be increased to ~9 billion with the consumption of 30 TW of power by the end of 2050 [1]. Fossil fuels, with limited resources, will fail to meet this increasing energy demand. According to the current energy consumption rate, coal reserves will last for 150 to 400 years, natural gas for 60-160 years, and oil for 40-80 years [1].

Apart from the energy crisis, fossil fuels have a significant impact on the environment. The burning of fossil fuels is linked with the emission of greenhouse gases such as CO_2, which have a considerable contribution to global warming and anthropogenic climate change [1]. The atmospheric CO_2 level has increased from 280 to 394 ppm, from the beginning days of the industrial revolution. Currently, it is rising at an alarming rate of 2ppm per year. According to the International Panel on Climate Change (IPCC) report, an atmospheric CO_2 level over 450 ppm can cause global warming of more than 2°C. Human society and the ecosystem will not adapt to such temperature changes and suffer from severe adverse impacts. However, if the change of temperature can be kept below 2°C, there is a high chance that the society and ecosystem will adapt. Several studies indicate that if we cannot reduce CO_2 emissions sharply within the next ten years, achieving a 450 ppm level will be unavoidable.

Therefore, to reduce fossil fuel dependence and CO_2 emission, we must switch towards new and sustainable energy resources. The development of renewable energy technologies in a green and clean way is necessary for the sustainable development of human society. But still, the pathway of using green energy resources on a global scale demand is unclear and uncertain. Therefore enormous and critical research in developing alternative energy technologies is necessary to secure our future.

1.2 Scope of Solar Energy among Sustainable Energy Recourses

German Advisory Council on Global Change (WBGU) has published a report in 2003, which presents the prime concerns regarding energy systems to the policymakers [2]. The report provides several suggestions, which should be fulfilled within 21st century for the reasonable development of sustainable energy systems. This report has presented the global transformation of the energy system, taking into account the atmospheric CO_2 level with its limiting value of 450 ppm, three times increase in energy consumption, and six times increase in the economic development of the society by the end of 2050. The suggestions can be realized by lowering the dependability of fossil fuels by increasing the use, growth, and sustainable development of renewable energy technologies. However, the deficiency of infrastructure and effectively advanced pathway of renewable energy harvesting technologies limits its realization on the global scale and promotes the dominance of fossil fuel dependency. The hope lies in the further development of technology and infrastructure, which could shift the dependence of the energy economy from fossil fuels to renewable energy resources. The future energy experts believe that by 2050, most of the energy demands could be fulfilled by renewable energies. According to their prediction, 50% of the total energy production will be supplied from renewable energy resources by the end of 2050, which will increase to 90% within 2100.

In 1987 United Nations proposed the Brundtland Report [3] on the sustainable development of the society, which speaks about the development of cities, land, communities, business, etc., that "meets the needs of the present without compromising the ability of future generations to meet their own needs." Therefore utilization of energy resources, which has a shallow impact on the environment, is necessary for the planet's future. Solar, water, and wind energy are the three well-known and earth-abundant renewable resources of energy that can be harvested in a clean and green pathway. These energy resources are never-ending, and their power generation capabilities are provided in table 1.1.

Among all renewable energy resources, solar energy is the most abundant energy resource on the earth's crust and is considered the ultimate solution to future energy challenges. $174x10^3$ TW of solar radiation strikes the surface of the planet every 10 minutes, equivalent to the energy demand of a year of current human society [4]. About 816,000 km^2 solar cells with 10% efficiency can generate 20 TW of power by harvesting the incident solar radiation, which is equivalent to an area of about 900x900 km^2 on the earth's surface. This area is equal to the combined surface area of Germany and France [1]. Covering this colossal area with conventional solar cells is a challenging task. Apart

from that, to achieve the production peak of 20TW power, an average of 650 m^2 of solar panels need to be planted per second, 24x7, 365 days in a year, for the next 40 years, which is also a challenging task. The solar cells market is one of the fastest-growing markets, which is growing at a rate of 35-40% every year. However, it will be difficult to predict how the market of solar cells will grow in the next few decades.

Apart from conventional solar cells, dye-sensitized solar cells, solar heaters, and large-scale solar thermal power also have gained sufficient research interest to full fill the need for alternative energy resources in the future.

The major challenge with solar energy harvesting systems is storing the solar energy and delivering it in a global demand when the sun is not present. In the case of a solar cell, the efficient path of storing such substantial electrical energy of TW scale in conventional batteries is still unknown. This problem forces us to find a next-generation fuel that minimally impacts the environment and could replace traditional fossil fuels.

Table 1.1: Power generation capabilities of different renewable energy resources [1].

Energy Resource	Power (TW)	Comments
Hydroelectric	1-2	Remaining untapped potential is 0.5 TW
Wind	4	Have a 10-15% technical potential on a global scale on- and off-shore installations
Geothermal	12	A small part of it can be implemented
Tidal and ocean currents	<2	
Biomass	10	10% of the earth surface need to be covered by switchgrass
Nuclear	10	Uranium supply is finite and nuclear extracts are harmful to the environment
Solar	>20	0.16% of the earth surface needed to be covered with 10% efficient solar cells

1.2.1 Hydrogen as Next Generation Fuel

When solar energy is harvested in a conventional solar cell-based energy harvesting system coupled with a grid system, it makes the work of electricity network operators difficult due to the intermittent nature of the sun. Sun is unenviable during the night cycle and clouds; also, the intensity of solar light varies from time to time during the day cycle. In such a case, large-scale energy storage is required to implement an uninterrupted power supply. However, the suitable pathway for implementing such a large-scale storage system is still unknown. Solar energy can be stored in the form of chemical energy (chemical fuel), an emerging and attractive pathway towards solar energy harvesting based on research and development. Visible-light photons with energy in the range of 1-3 eV, or 100-300 kJ/mol, can initiate the chemical reactions required to produce these chemical fuels. Several kinds of energy-dense chemical fuels are available, such as hydrogen, methanol, methane, etc.

Except for hydrogen, the end product of all the above-mentioned chemical fuels is CO_2. Apart from the energy crisis issue, reducing the atmospheric CO_2 level is also a goal of using renewable energy resources. On the other hand, direct capture and conversion of CO_2 into fuels like methanol or methane is more difficult because the electrochemical half-reactions involved in the conversion need six- and eight-electron transfer steps, respectively. Against this backdrop, hydrogen has emerged as a non-toxic energy carrier with high energy density and zero environmental impact. These criteria make hydrogen the ultimate next-generation fuel suitable for the sustainable development of the pollution-free environment. Hydrogen can be stored in specified containers and transported easily like other conventional fuels like oil and natural gas. Consumption of hydrogen emits water vapour as the end product, which leads us towards achieving zero carbon footprints. Gravimetric and volumetric energy densities of different fuels have been compared with the energy density of hydrogen in Table 1.2.

Table 1.2 Gravimetric and volumetric energy densities of different fuels [1].

Fuel	**Energy density**	
	Gravimetric (MJ/kg) Volumetric (MJ/L)	Gravimetric (MJ/kg) Volumetric (MJ/L)
Coal	24	–
Wood	16	–
Gasoline (petrol)	44	35
Diesel	46	37
Methanol	20	18
Natural gas	54	0.036
Hydrogen	143	0.011

In the future, the focus of the oil-based energy economy will be shifted towards a hydrogen economy, which was pointed out initially during the oil crisis in the 1970s. The term ' hydrogen economy' was first used by John Bockris in a lecture at General Motors (GM) Technical Center in 1970 [5]. The hydrogen-based energy economy involves the technological development of hydrogen production systems, storage systems, transportation, and its proper uses. D. Scholten has discussed these four parameters of hydrogen economy in his book [6]. Nowadays, the production of H_2 involves the consumption of fossil fuels. About 96% of H_2 is produced using natural gas (48%), oil (30%), and coal (18%) [4]. Since carbon-based fuels are used, the H_2 production process involves emitting CO_2, which is undesirable for the sustainable development of the environment. Hence, to fulfill the future energy demand with a sustainable environment, the future energy system must depend only on renewable energy resources. The hydrogen fuels can be produced in several green and clean pathways like Photoelectrochemical water splitting, Photocatalytic water splitting, photovoltaic water electrolysis, Photobiological methods, and Molecular artificial photosynthesis, Plasma-chemical conversion, etc.

In conventional solar cells, electrical energy is harvested from solar energy, which can be used to produce H_2 by water electrolysis. The produced H_2 can be used in fuel cells for further energy demand. However, each step of energy conversion in solar energy-electrical energy-H_2 - electricity involves the loss of energy, which increases the production cost. Bossel's calculation shows that almost 70% of energy is lost during the intermediate steps [7]. If the intermediate steps are somehow reduced, the energy loss and production cost can be minimized. The first step of solar to electric energy conversion can be avoided in photoelectrochemical and photocatalytic water electrolysis systems. They involve the production of H_2 directly using solar energy employing water electrolysis. Different semiconductor materials are the most suitable candidate for these proposals. However, these processes are still confined in the lab-scale production of H_2, and the efficiency of production should be enhanced significantly to produce H_2 in future industrial applications on a large scale.

1.3 Electrolysis of Water

Water electrolysis is the method of dissociating the constituent elements of water i,e, hydrogen, and oxygen, by an externally applied potential. A water electrolysis system involves two electrodes (cathode and anode) and an electrical power supply. Until now, most of the power supply consists of fossil fuels for the production of electricity, which makes the water electrolysis process impactful towards the environment. The

semiconductor materials can serve the role of electrode and power supply by harvesting the solar radiation according to their band-gap. An electrode that employs semiconducting materials to harvest the solar light is called photoelectrode, and hence the water electrolysis process is called photoelectrochemical water electrolysis. However, pure water behaves like a non-conductor. An electrolyte is required to dissolve in the water to make it electrically conductive. Photoelectrochemical water electrolysis is a single-step process to store solar energy as chemical energy. It employs a semiconductor material to generate photovoltage by absorbing the solar radiation, using that voltage to produce hydrogen and oxygen through water electrolysis inside an electrochemical cell.

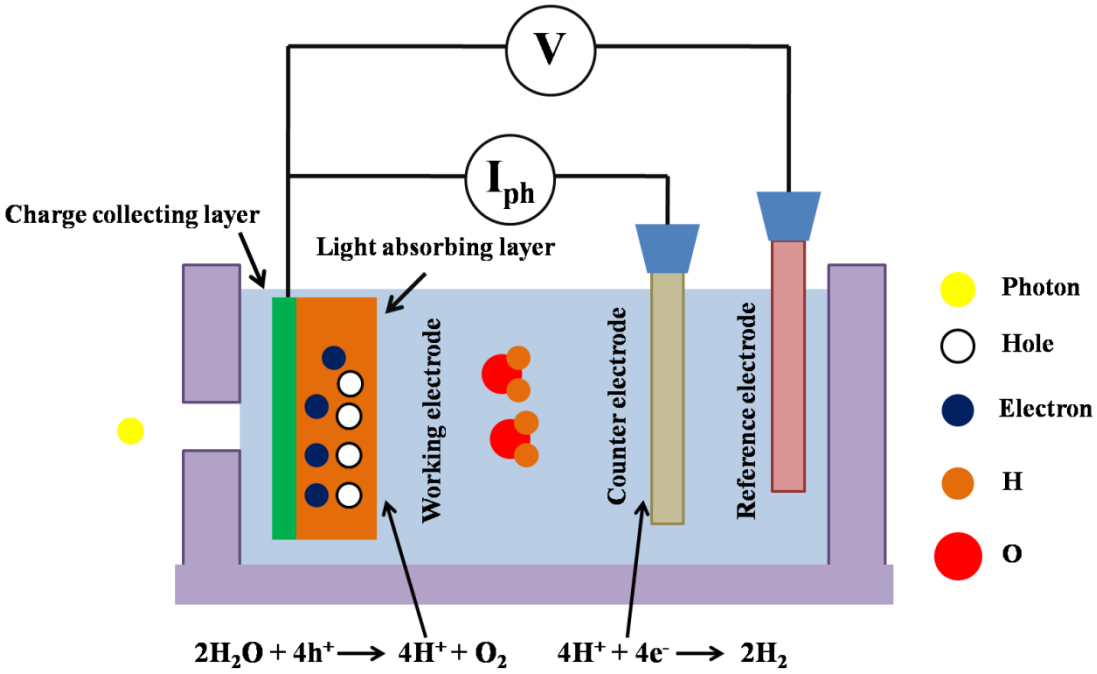

Figure 1.1: Schematic diagram of the photoelectrochemical cell.

1.3.1 Photoelectrochemical Cell

A photoelectrochemical (PEC) cell is a device in which solar energy is converted and stored as chemical energy (chemical fuel, H_2) in an electrochemical route. The PEC cell involves photon-assisted water electrolysis for the generation of hydrogen and oxygen at two macroscopically different places. Figure 1.1 shows the simplified diagram of a PEC cell. A PEC cell consists of a working electrode (WE), a counter electrode (CE), and a reference electrode (RE). The working electrode (Photocathode/photoanode) is the most crucial part of the PEC cell. It consists of a light-absorbing layer and a charge collecting layer. Transparent conducting substrates/conducting substrates serve the

role of the charge collecting layer. The light-absorbing layer consists of one or more semiconductor materials grown/deposited on the charge collecting layer. The counter electrode is a metallic wire of novel metal, preferably platinum electrode, and the reference electrode can be a KCl saturated Ag/AgCl electrode or a Hg/HgO electrode. All the electrodes are immersed in an aqueous electrolyte. The electrolyte can be acidic, base, or nearly neutral, depending on the application and the electrode material.

1.3.2 Water Splitting Half Reactions

The simplified energy diagram of a PEC cell consisting of a photoanode of a single semiconductor and a counter electrode is shown in Fig. 1.2. When a photoanode surface of a PEC cell is illuminated with solar energy photons, having energy greater than the band-gap energy of the photoanode material (semiconductor), it absorbs the incident photons and generates electron-hole pairs. The photo-generated electrons and holes are separated due to the internal electric field generated at the semiconductor electrolyte junction. The origin of the electric field at the semiconductor electrolyte junction will be discussed later in this chapter. The photo-excited holes are transported towards the electrolyte side, and the electron is swept toward the charge collecting layer and transported to the counter electrode through an external wire. The photo-generated holes and electrons oxidize and reduce the water at the photoanode and counter electrode surface to produce O_2 and H_2. The reaction that occurs at the photoanode surface is known as water oxidation half-reaction and is given by

$$2H_2O + 4h^+ \rightleftharpoons 4H^+ + O_2\,; \quad E^0_{ox} = -1.229\,V\ vs.NHE \tag{1.1}$$

Whereas the occurs at the counter electrode is known as water reduction half-reaction and is given by

$$4H^+ + 4e^- \rightleftharpoons 2H_2\,; \quad E^0_{red} = 0.000\,V\ vs.NHE \tag{1.2}$$

Hence the total water-splitting reaction becomes

$$2H_2O + 4h\nu = 2H_2 + O_2 \tag{1.3}$$

$$4h\nu \xrightarrow{semiconductor} 4h^+ + 4e^- \tag{1.4}$$

Since four electrons are involved in a single event of water splitting, the whole process is known as four electronic processes. The change of Gibbs free energy involved in the total water splitting process is given by

$$\Delta G^0 = -nF.\Delta E^0 \tag{1.5}$$

where $\Delta G^0$is the change of Gibbs free energy and ΔE^0 is the standard electric potential of the reaction. At normal temperature (25°C) and concentrations (1 mol/L, 1 bar), a +237 kJ/mol change of Gibbs free energy is required for the total water-splitting reaction to occur, which is equivalent to the electrochemical cell voltage (ΔE^0) -1.229V. The minimum voltage required for the occurrence of a water-splitting event is 1.229V, which is known as the standard thermodynamic water splitting potential.

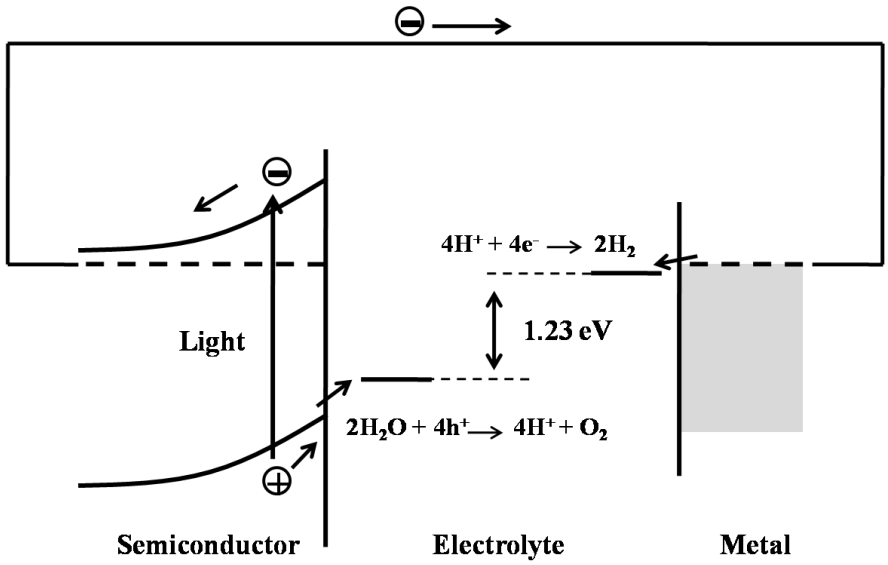

Fig. 1.2: Energy diagram of a simplified PEC cell containing a single semiconductor material as photoanode and a metallic counter electrode.

1.3.3 Energy Conversion Efficiency of the PEC Cell

The energy conversion efficiency is a performance indication parameter of a PEC cell. When all the photo-generated charge carriers (electrons and holes) are involved in the water-splitting half-reactions, the solar to hydrogen (STH) conversion efficiency is governed by the equation

$$\eta_{STH} = \frac{P_{out}^{electrical} - P_{in}^{electrical}}{P_{light}} = \frac{J_{ph}(V_{redox} - V_{bias})}{P_{light}} \quad (1.6)$$

Where, V_{redox} is the room temperature thermodynamic water splitting potential 1.229 V equivalent to the 237 kJ/mol change of Gibbs free energy for water splitting,$J_{ph}$is the photocurrent density and V_{bias} is the applied bias potential. The above expression is known as the applied bias photon-to-current conversion efficiency (ABPE) [8]. At no applied bias condition, assuming the incidence of AM1.5G solar light (P_{light} =1,000 W.m-

^{2}), the efficiency is directly governed by the photocurrent as $\eta_{STH}(\%) = 1.23 \times J_{ph}$, when J_{ph} is in mA.cm^{-2}. This equation indicates that the target efficiency of 10% can be reached by achieving a ~8mA.cm^{-2} current density at no applied bias condition. If the amount of H_2 produced due to the water-splitting reactions can be measured by gas chromatography, η_{STH} can be calculated more directly by using the equation

$$\eta_{STH} = \frac{\Phi_{H_2} G^0_{f,H_2}}{P_{light}} \tag{1.7}$$

Where Φ_{H_2} is the H_2 evolving rate from the illuminated area (mol.s^{-1}.m^{-2}) and G^0_{f,H_2} Gibbs's free energy is required to produce H_2 (237 kJ/mol).

The quantum efficiency of a photoanode can be reported as a function of wavelength. The external quantum efficiency is defined as the fraction of incident monochromatic photon is converted to the electrons and is known as incident photon-to-current conversion efficiency (IPCE) is given by the equation

$$IPCE\ (\lambda) = \frac{hc}{e} \times \frac{j_{ph}(\lambda)}{\lambda P(\lambda)} \tag{1.8}$$

The internal quantum efficiency or absorbed photon-to-current conversion efficiency (APCE) is related to IPCE by the equation

$$APCE\ (\lambda) = \frac{IPCE\ (\lambda)}{A\ (\lambda)} = \frac{IPCE\ (\lambda)}{1 - R - T} \tag{1.9}$$

A is the optical absorbance, R is the reflectance, and T is the transmittance.

1.4 Energy Levels in Semiconductors and Electrolyte

A semiconductor is defined by its electronic energy bands. It consists of a valance band, a conduction band, and a forbidden energy gap between valance and conduction band known as the band-gap. The adjacent molecular orbitals have closely spaced energy levels, making a continuum that originates energy bands in the semiconductors. The highest occupied molecular orbital in a semiconductor is considered the top of the valance band (Ev). The lowest unoccupied molecular orbital is regarded as the bottom of the conduction band (E_c). The electrons of the valance band of a semiconductor can be excited to the conduction band by applying photo-excitation leaving behind holes in the valance band. The photons which produce the photo-excitation must have energy greater than the bandgap energy of the semiconductor (E_g), which defines the cutoff wavelength of the excitation ($\lambda_{cut\ off} = \frac{hc}{E_g}$). The Fermi level ($E_f$) of a semiconductor is

defined as the energy level where the probability of finding an electron per available state is ½. The following equation can determine the position of the Fermi level of a semiconductor

$$E_F = \frac{1}{2}(E_C + E_V) + \frac{1}{2}k_B T ln \frac{N_{VB}^*}{N_{CB}^*} \tag{1.10}$$

whereE_C is the bottom of the conduction band, E_V is the top of the valence band, k_B is the Boltzman constant (1.38×10^{-23} J/K) and T is temperature. N_{CB}^* and N_{VB}^* are the density of states in conduction and valence band respectively are given by

$$N_{VB}^* = 2\left[\frac{2\pi m_h^* kT}{h^2}\right]^{\frac{3}{2}} \tag{1.11}$$

$$N_{CB}^* = 2\left[\frac{2\pi m_e^* kT}{h^2}\right]^{\frac{3}{2}} \tag{1.12}$$

where h is the Plank constant and m_e^* and m_h^* are the effective mass of electron and hole, respectively. In an intrinsic semiconductor, the concentration of electrons and holes in equilibrium is given by equations

$$n_0 = N_{CB}^* e^{\frac{-(E_{CB}-E_F)}{k_B T}} \tag{1.13}$$

$$p_0 = N_{VB}^* e^{\frac{-(E_F-E_{VB})}{k_B T}} \tag{1.14}$$

For an intrinsic semiconductor, the carrier concentration is given by

$$n_i^2 = n_0 p_0 = N_{CB}^* N_{VB}^* e^{\frac{-(E_{CB}-E_{VB})}{k_B T}} \tag{1.15}$$

The carrier concentration of an intrinsic semiconductor exponentially varies with its bandgap.

The position of the Fermi level of a semiconductor defines the nature of conductivity (n-type or p-type) of the semiconductor. For a p-type semiconductor, the Fermi level lies very near the top of the valance band, and for an n-type semiconductor, the Fermi level lies close to the bottom of the conduction band (Fig. 1.3).In an intrinsic semiconductor, the Fermi level is situated at the middle position of the valance and conduction band. The electrolyte has a metal-like behavior. The electrolyte is defined by its three different energy levels, which are $E_{F,red}$, E_{ox}(related to the electron affinity of oxidized species) and E_{red} (related to the ionization energy of the reduced species) are given by

$$E_{ox} = \frac{1}{\sqrt{4\pi kT}} exp\left(\frac{-\left(E - E_{F,red} + \lambda\right)^2}{4kT\lambda}\right) \quad (1.16)$$

$$E_{red} = \frac{1}{\sqrt{4\pi kT}} exp\left(\frac{-\left(E - E_{F,red} - \lambda\right)^2}{4kT\lambda}\right) \quad (1.17)$$

Where λ is the reorganization energy and $E_{F,red}$ is the redox potential.

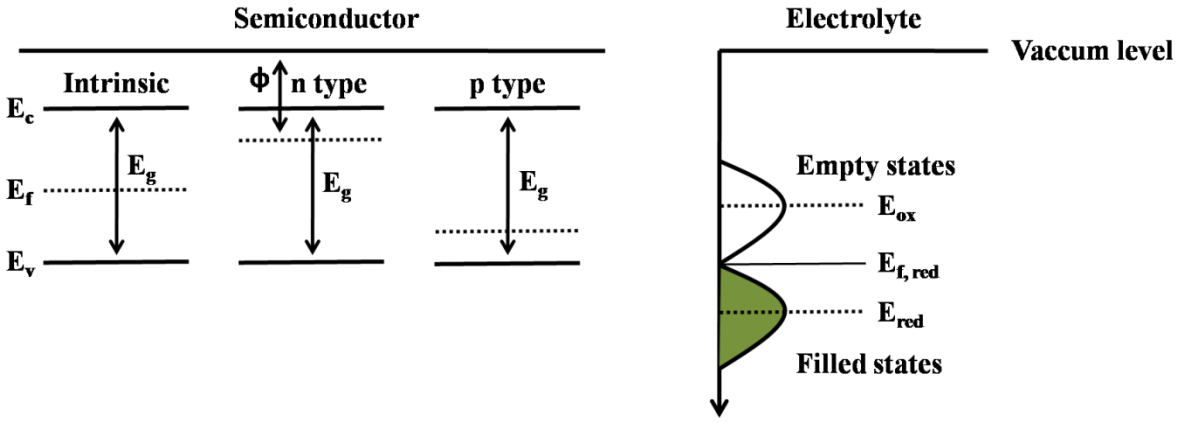

Figure 1.3: Band energy diagram of three different types of semiconductors and energy distribution of an electrolyte.

1.5 Semiconductor Electrolyte Junction

When a semiconductor is in contact with another species (metal, another semiconductor, or electrolyte) having different Fermi levels, charge transfer occurs between them. The charge transfer process continues until equilibrium, and a common Fermi level is established. As a result, a space charge region is developed inside the semiconductor. The space charge region width is dependent on the carrier density of the semiconductor and the nature of the other species. A built-in electric field appears at the space charge region.

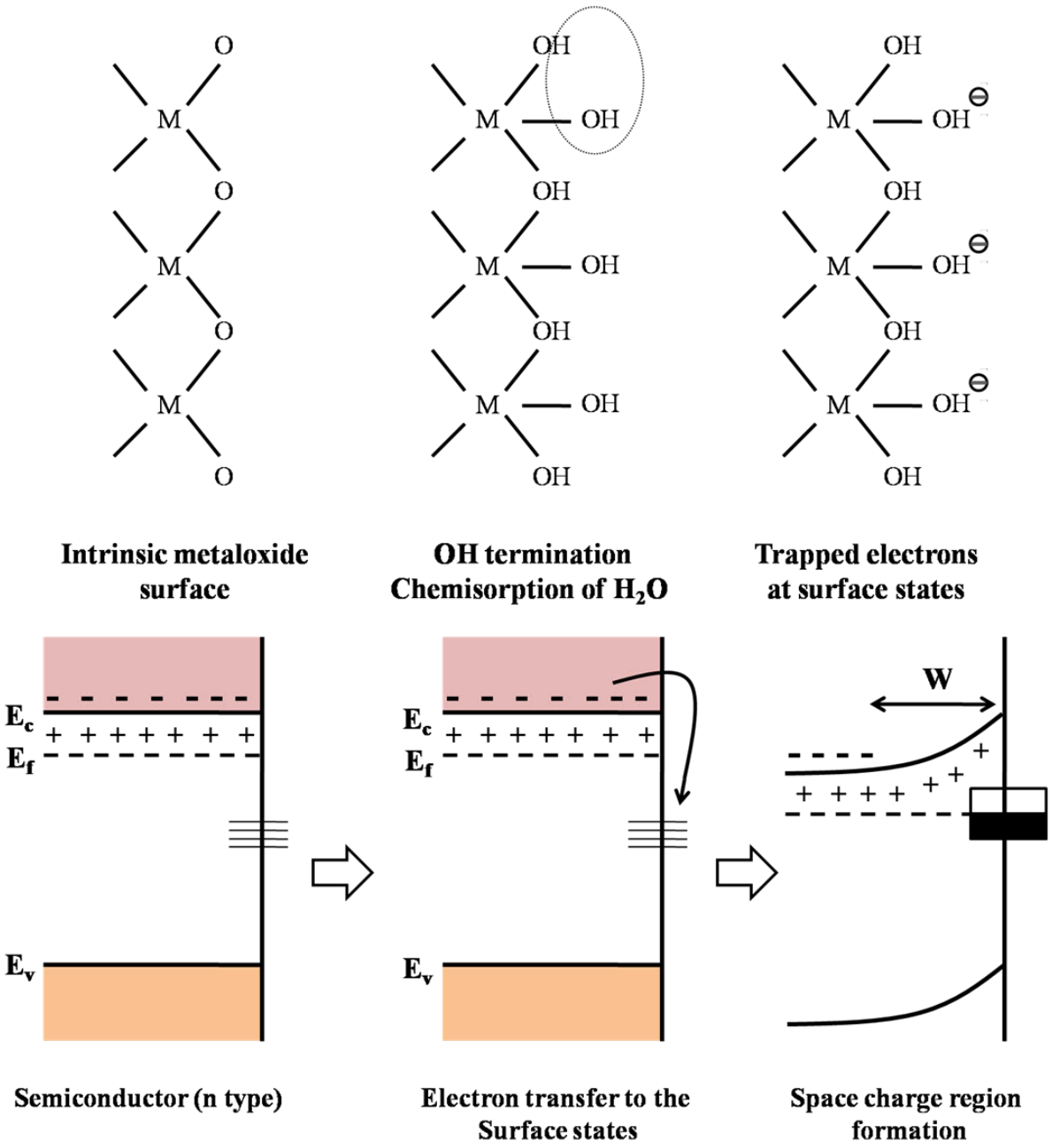

Figure 1.4: Formation of surface states and space charge region in a metal oxide semiconductor absorbing moisture.

Similarly, when a semiconductor is submerged inside an electrolyte, a semiconductor electrolyte junction is formed. A space charge region is developed inside the semiconductor to match the difference between the Fermi level of the semiconductor side and the electrochemical potential of the electrolyte. A built-in electric field is formed at the surface of a metal oxide semiconductor without even making direct contact with another solid/liquid. Metal oxide semiconductors can absorb water

molecules from the air. The surface termination of –OH creates electronic surface states. The energy level of these developed surface states is situated below the conduction band minima of the semiconductor. Since there is a difference between the Fermi level of the semiconductor and the position of the surface states, the electron from the conduction band will jump to the surface state to achieve equilibrium. In equilibrium, the Fermi level of the semiconductor is located at the middle point of the density of states (DOS) of the surface states. The movement of the electrons from the conduction band to the surface states creates a space charge region in the semiconductor as the ionized donors form these electrons stay behind in bulk. Consequently, an electric field is formed, and the situation is illustrated in Fig. 1.4.

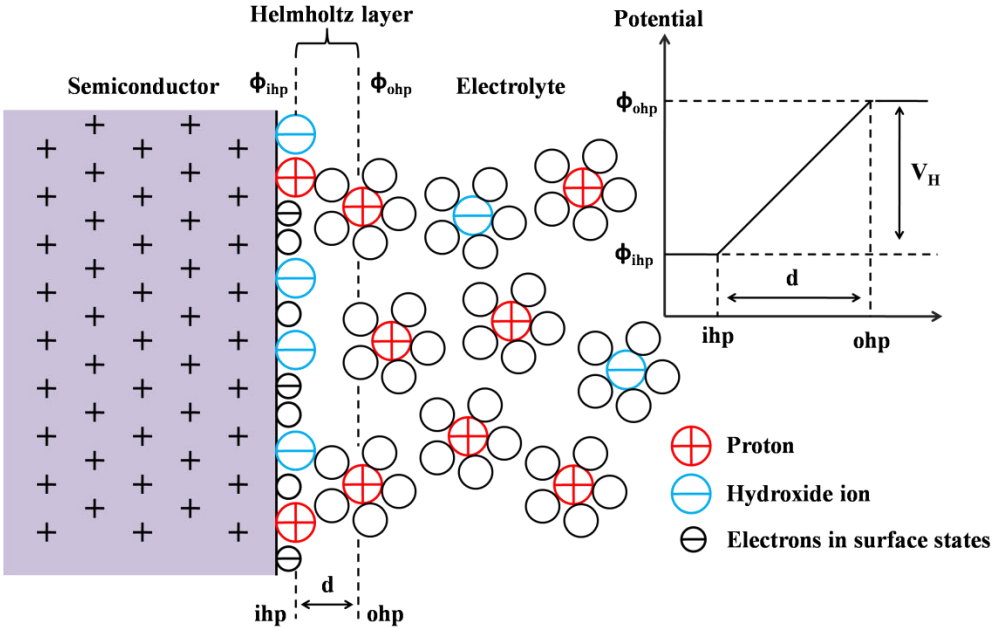

Figure 1.5: Schematic diagrams of the semiconductor electrolyte interface, Helmholtz layer, and potential distribution across the junction.

Similarly, when a semiconductor is submerged inside an electrolyte, a space charge region is also created due to a mismatch between the semiconductor's Fermi level and the electrolyte's electrochemical potential. In PEC cell application, the formation of space charge region and consequent band bending is advantageous. The internal build-in field present at the space charge region promotes the charge separation of photo-generated carriers. However, a semiconductor inside an electrolyte has a slightly more complicated situation than the semiconductor exposed to humid air. Figure 1.5 illustrates the situation when a semiconductor is submerged in an electrolyte. The interfacial properties of the semiconductor can be interoperated by introducing diffused ionic double layer model [9–13]. The Semiconductor electrolyte junction consists of

surface states with trapped electrons or holes and adsorbed ions and other species at the surface of the semiconductor. The ionized donors and acceptors of the semiconductor supply the counter-charges with the accumulation of oppositely charged ions in the solution. Since the water molecules have a significant dipole moment, the ions in the electrolyte are surrounded by a cloud of water molecules, forming a solvation shell. This shell prevents the ions from approaching the surface of the semiconductor closer than a few Å. The region between the ions adsorbed at the semiconductor surface and the nearest ions present in the solution is known as the Helmholtz layer, which has a width of a few Å (2-5 Å). The Helmholtz layer potential is given by

$$V_H = \frac{Q_s d}{\varepsilon_0 \varepsilon_r} \tag{1.18}$$

Where, Q_s is the surface charges, d is the Helmholtz layer width, ε_0 is the permittivity of free space and ε_r is the dielectric constant of water. The charge distribution across the semiconductor electrolyte junction is dependent on the nature of the electrolyte (pH of the solution) and the protons and/or hydroxide species absorbed at the surface of the semiconductor. At 25°C Helmholtz potential changes by 0.059 V (2.3kT/e) per unit change of pH.

1.6 Types of Space Charge Regions

As discussed earlier, when a semiconductor is immersed in an electrolyte, a space charge region is created due to the transfer of electrons. The nature of the space charge region is not always like the depletion layer. Few other types of space charge regions may also originate. In the case of an n-type (p-type) semiconductor, if the number of negative (positive) charges adsorbed at the surface is increased beyond a certain critical number, the Fermi level of the semiconductor crosses the midpoint of the bandgap. In such a situation, the surface region of the n-type (p-type) semiconductor behaves as the p-type (n-type) semiconductor. This type of space charge region is called the inversion layer. If the majority charge carriers in the inversion layer diminished at a higher rate than their generation (thermally), then no free carriers will be available on the surface. Hence the surface of the semiconductor will behave as an insulator. Such kind of space charge region is called the deep depletion layer. When the surface of an n-type (p-type) semiconductor adsorbs an excess amount of positive (negative) charges, free majority carriers of the semiconductor accumulate at the surface to diminish the absorbed surface charges. This accumulating free majority carrier forms the accumulation layer. The formation of different types of space charge layers and corresponding band diagrams are shown in Fig. 1.6.

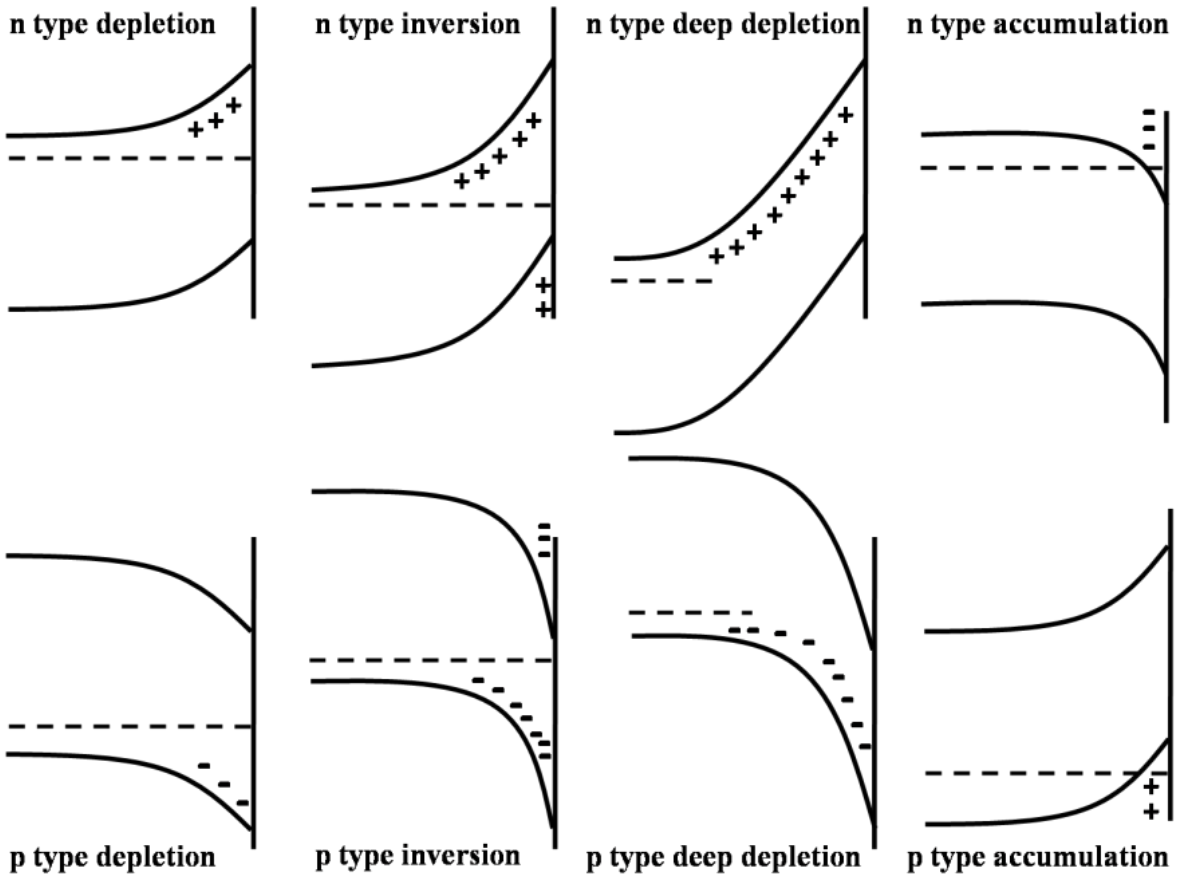

Figure 1.6: Different types of space charge layers and corresponding band bending.

1.6.1 Potential Distribution of the Space Charge Region

When a semiconductor is immersed into an electrolyte, a semiconductor electrolyte junction is formed. At equilibrium, the Fermi level (E_f) of the semiconductor side match up with the electrochemical potential (redox potential, $E_{F,red}$) of the electrolyte side by introducing a space charge region and the consequent band bending. Inside the three-electrode system, a potential difference (ϕ) is set up between the semiconductor working electrode and the reference electrode, which can be expressed as a combination of different potentials as,

$$\phi = \phi_{sc} + \phi_H + \phi_G + C \tag{1.19}$$

Where ϕ_{sc} is the space charge layer potential, ϕ_H is Helmholtz potential and ϕ_G is the diffused double layer potential. However ϕ_G is negligible for an electrolyte with a high ion concentration. The constant part of the potential (C) is determined by the nature of the reference electrode. Here the formation of the space charge region is responsible for constructing the Helmholtz layer and vice versa, and the no of the charge contained in

the respective region must be equal. The capacitance (C_{sc}) of the space charge layer is much smaller compared to the capacitance of the Helmholtz layer. This consideration makes$\phi_H$the constant and applied potential between the working electrode (semiconductor) and reference electrode will dissipate across the space charge region as

$$\phi = \phi_A = \phi_{sc} + \phi_{FB} \tag{1.20}$$

where, ϕ_{FB} is the flat band potential. At this potential concentration of surface, charges are equal to the concentration of charges of the semiconductor bulk. The charge distributions in the space charge layer establish the differential capacitance at the semiconductor electrolyte interface.

The potential distribution of the space charge layer and its width is dependent on two parameters, one is the number of charges transferred to the surface, and the other is the density of donor ions (N_D^+). The variation of potential distribution can be obtained by solving Poisson's equation:

$$\frac{d^2\phi}{dx^2} = -\frac{\rho\,(x)}{\varepsilon_0\varepsilon_r} \tag{1.21}$$

Here the temperature correction term k_BT is negligible compared to the potential drop across the depletion region.

Let us consider an n-type semiconductor with all ionized donors, which give the charge density, $\rho(x) \cong eN_D^+ = eN_D$. Also, considering the situation, the potential drop across the semiconductor bulk is zero ($\phi_{bulk}(x) = 0$) which gives the following equation:

$$\phi_{sc}(x) = -\frac{eN_D}{2\varepsilon_0\varepsilon_r}(x - W_{sc})^2 \tag{1.22}$$

where, ε_0 is the permittivity of free space, and $\varepsilon_r$is dielectric constant, andW_{sc} is the width of the space charge layer. If n be the free electron concentration of the semiconductor, then the total charge concentration across the space charge region is given by:

$$\rho\,(x) = e(N_D^+ - n) \tag{1.23}$$

As described earlier, the free electron concentration in the conduction band of the semiconductor is dependent on the difference between the Fermi level and the conduction band minima, according to equation 1.13. Inside the space charge region, the distance between Fermi level and the bottom of the conduction band is modified by

an amount of $\phi(x)$ due to the formation of band bending. Hence the modified electron concentration is given by

$$n\,(x) = N_{CB}^{*} e^{\frac{-(E_{CB}-E_F-e\phi(x))}{k_B T}} = n_b e^{\frac{e\phi(x)}{k_B T}} \tag{1.24}$$

Where $n_b = N_{CB}^{*} e^{\frac{-(E_{CB}-E_F)}{k_B T}}$ is the bulk electron concentration of the semiconductor, which is equal to $N_D^{+} = N_D$ for an n-type semiconductor with completely ionized donors. Hence, the modified charge density of the space charge region is given by

$$\rho\,(x) = eN_D\left(1 - e^{\frac{e\phi(x)}{k_B T}}\right) \tag{1.25}$$

Combining equations 1.25 and 1.21

$$\frac{d^2\phi}{dx^2} = -\frac{eN_D\left(1 - e^{\frac{e\phi(x)}{k_B T}}\right)}{\varepsilon_0 \varepsilon_r} \tag{1.26}$$

The potential distribution in the space charge region can be obtained by integrating the above equation. Equation 1.26 can be written as

$$\frac{d}{dx}\left(\frac{d\phi}{dx}\right)^2 = 2\frac{d\phi}{dx} * \frac{d^2\phi}{dx^2} = -2\frac{eN_D\left(1 - e^{\frac{e\phi(x)}{k_B T}}\right)}{\varepsilon_0 \varepsilon_r} * \frac{d\phi}{dx} \tag{1.27}$$

The electric field (ξ) is related to the potential as $\xi = -\frac{d\phi}{dx}$, which gives

$$\xi^2 = \left(\frac{d\phi}{dx}\right)^2 = \int_0^{\phi(x)} -2\frac{eN_D(1 - e^{\frac{e\phi(x)}{k_B T}})}{\varepsilon_0 \varepsilon_r} * d\phi \tag{1.28}$$

If Q is the total charge stored in the space charge region and A is the area of the working electrode (semiconductor), then the electric field is given by

$$\xi = \frac{Q}{\varepsilon_0 \varepsilon_r A} \tag{1.29}$$

Hence the total charge in the space charge region is given by

$$Q_{SC} = \sqrt{-2\varepsilon_0 \varepsilon_r A^2 \int_0^{-\phi_{SC}} eN_D\left(1 - e^{\frac{e\phi(x)}{k_B T}}\right) d\phi} \tag{1.30}$$

$$= \sqrt{2\varepsilon_0\varepsilon_r A^2 e N_D \left(\phi_{SC} + \frac{k_B T}{e} e^{-\frac{e\phi_{SC}}{k_B T}} - \frac{k_B T}{e}\right)} \tag{1.31}$$

The potential drop across the space charge region is nearly 0.1 V [1]. The above equation can be simplified as

$$Q_{SC} = \sqrt{2\varepsilon_0\varepsilon_r A^2 e N_D \left(\phi_{SC} - \frac{k_B T}{e}\right)} \tag{1.32}$$

The above equation can be used to calculate the width of the space charge region as

$$Q_{SC} = eN_D * A * W_{sc} \tag{1.33}$$

Combining equations1.33 and 1.32, the width of the space charge region is given by

$$W_{sc} = \sqrt{\frac{2\varepsilon_0\varepsilon_r}{eN_D}\left(\phi_{SC} - \frac{k_B T}{e}\right)} \tag{1.34}$$

This equation can also be used for p-type semiconductors by replacing N_D with N_A, the acceptor ion density.

The following equation can calculate the capacitance developed within the space charge region

$$\frac{1}{C_{sc}^2} = \left(\frac{dQ_{sc}}{d\phi_{sc}}\right)^{-2} = \frac{2}{\varepsilon_0\varepsilon_r e N_D A^2}\left(\phi_{sc} - \frac{kT}{e}\right) \tag{1.35}$$

Flat band potential (ϕ_{FB}) of a semiconductor is an essential parameter for PEC water splitting. It determines the thermodynamic water-splitting ability of the semiconductor. Flat band potential is defined as the potential at which the band is flat, i.e., there is no band bending; also, the space charge region vanishes. The flat band potential of a semiconductor approximately defines the position of the Fermi level of the semiconductor with respect to the reference electrode. The flat band potential of a semiconductor can be measured by Mott-Schottky (MS) measurement, which is governed by the equation 1.35, with a bit of modification by replacing ϕ_{sc} with $(\phi_A - \phi_{\mathrm{FB}})$. The MS plot is the plot of $(\frac{1}{C_{sc}^2})$ against applied potential (ϕ_A) and extrapolation of the linear part of the MS plot to the applied potential axis gives the value of flat band potential. The carrier density of the semiconductor (considering all the carriers originated from the ionized donors) can be calculated from the slope of the MS plot as

$$N_d = \frac{2}{\varepsilon_0 \varepsilon_r e A^2} \frac{1}{\frac{d(\frac{1}{C_{sc}^2})}{d\phi_{sc}}} \tag{1.36}$$

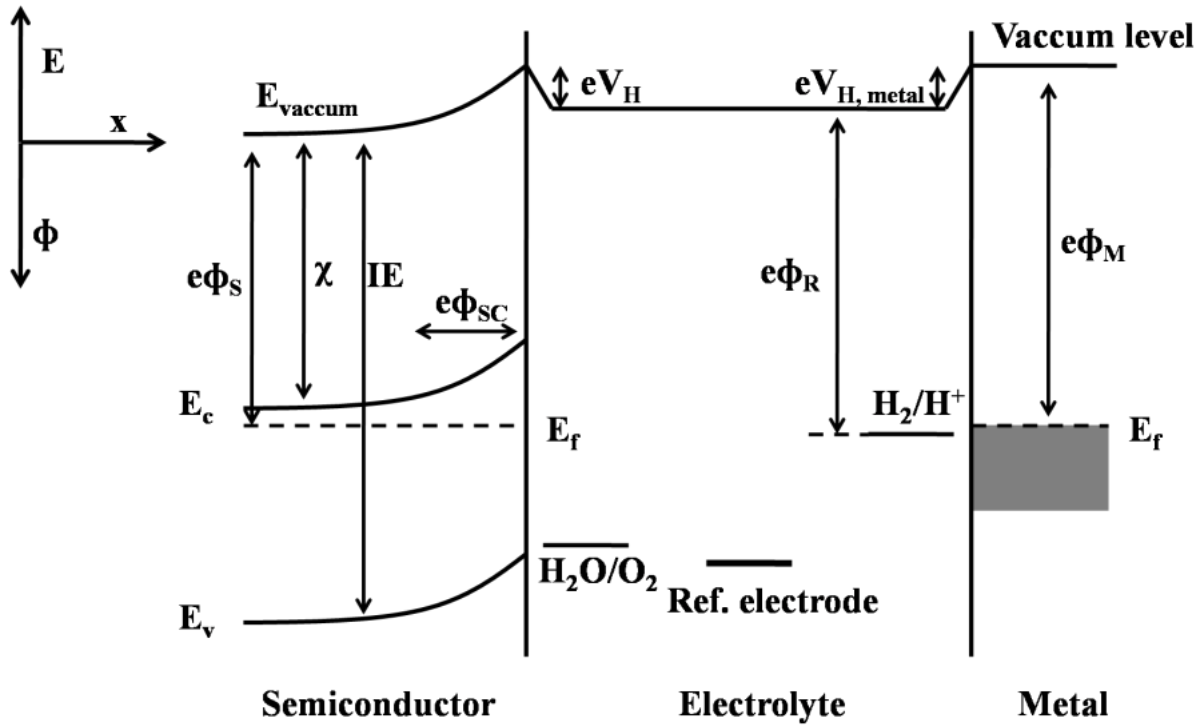

Figure 1.7: Energy band diagram of a PEC cell with an n-type semiconductor, a reference electrode, and a metal counter electrode. In the figure, electron affinity is termed as χ, ionization energy (IE), and semiconductor work function as ϕ_s.

1.6.2 Energy Band Diagram of PEC Cell and the Quasi Fermi Level

Figure 1.7 shows the energy band diagram of a PEC cell with an n-type semiconductor taking vacuum level as reference. In the presence of an electric field, the vacuum level also bends following the potential gradient of the PEC cell. In equilibrium, the Fermi energy of semiconductor and metal and the electrochemical potential of the electrolyte are in the same line. The vacuum level in the electrolyte region is drawn horizontally with the assumption that no electric field exists in the electrolyte at equilibrium. The band positions, the band bending, and the energy gap between E_F and E_C are the critical parameters for a semiconductor to be used as a working electrode material. Inside a PEC cell, the photo-generated electrons and holes oxidize and reduce water into oxygen and hydrogen. The water reduction by the photo-generated electron is

thermodynamically possible only when the electron has higher energy than the water reduction potential.

Similarly, the photo-generated hole should have lower energy than the water oxidation potential. This means a semiconductor will be suitable for water splitting if it has a conduction band positioned over the water reduction potential and a valance band placed below the water reduction potential with respect to the reference electrode. In operating conditions, a reverse bias is applied to the semiconductor, which increases the space charge region width, band bending and also accelerates the charge transfer process. Since the Helmholtz layer capacitance is much higher than the space charge layer capacitance, it can be assumed that the applied potential will affect only the space charge region but not the Helmholtz layer.

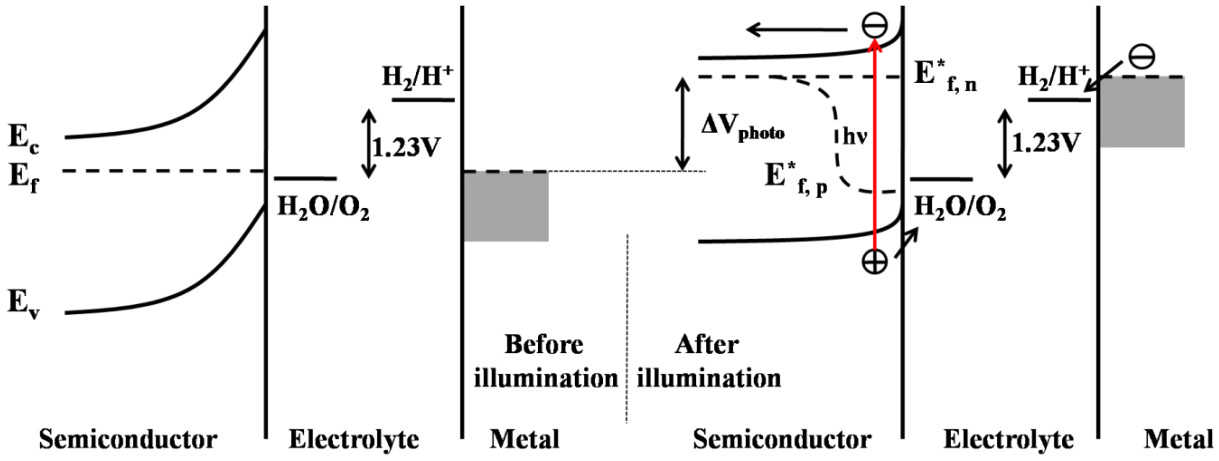

Figure 1.8: Band energy diagram of a PEC cell using an n-type semiconductor as a working electrode and a metal wire as counter electrode in the presence and absence of illumination.

For water splitting reactions inside a PEC cell, it is assumed that the H_2O/O_2 redox couple is the most active species. In the absence of illumination (dark condition), the H_2O/O_2 redox couple dominates the electrochemical potential of the electrolyte. In equilibrium at dark conditions, the Fermi level of the semiconductor and metal and the water oxidation potential adjusted nearly in the same level. When the junction is illuminated, several electron-hole pairs are generated, and a photovoltage (ΔV_{photo}) is developed. The influence of the photovoltage shifts the Fermi level by ΔV_{photo}. Since the election-hole pairs are generated under illumination, instead of a single Fermi level, a quasi-Fermi level appeared at the space charge region of the semiconductor (Fig. 1.8). The quasi-Fermi levels are directly dependent on the modified electrons and holes concentrations, which are defined as

$$n = n_0 + \Delta n = N_c e^{\frac{-(E_c - E_{F,n}^*)}{k_B T}} \quad (1.37)$$

$$p = p_0 + \Delta p = N_v e^{\frac{-(E_{F,p}^* - E_v)}{k_B T}} \quad (1.38)$$

where n_0 and p_0 are the equilibrium electron and hole concentration in dark conditions. For an n-type semiconductor $n_0 >> \Delta n$ and $\Delta p >> p_0$. The electron and hole concentrations of n-type semiconductors under illumination becomes $n = n_0 + \Delta n \approx n_0$ and $p = p_0 + \Delta p \approx \Delta p$. Therefore the quasi-Fermi level $E_{F,n}^*$ remains horizontal and $E_{F,p}^*$ departs from the bulk Fermi level.

1.6.3 Influence of pH on the Band Edges

The Helmholtz potential is dependent on the pH of the solution and not affected by the applied potential. The band edges position of semiconductors changes by -59mV per unit change in pH with respect to the redox potentials of the electrolyte. A semiconductor with a low conduction band position with respect to E_{redox} will not be able to reduce a certain species in the electrolyte. At this point, one can think about increasing the pH of the solution, which will drive the Helmholtz potential to more negative energy (higher energy) and raise the conduction band position with respect to E_{redox}. However, this technique is not applicable for water splitting reactions as the water oxidation and reduction potentials are also dependent on the pH of the solution. The water oxidation and reduction potentials behave in the same way as the conduction and valance band positions of a semiconductor changes with pH change. Therefore, most metal oxide semiconductors have fixed conduction and valance band positions with respect to the water oxidation and reduction potential.

1.6.4 Charge Transfer across the Junction

For a metal electrolyte junction, the charge transfer process occurs at the interface, in an energy range close to the Fermi level, to achieve equilibrium. The electron density of states near the Fermi level is very high for a metal. Therefore for a metal/electrolyte interface, the charge transfer process can be governed by the potential difference applied across the Helmholtz layer. Whereas for a semiconductor electrolyte interface, the applied potential affects the semiconductor only. Hence the potential perturbation technique fails to explain the electron transfer kinetics. According to H. Gerishcher's model for a semiconductor electrolyte junction, the charge transfer occurs via the top of the valance band (or bottom of the conduction band), considering the electrons (or

holes) as individual reactants [14,15]. The equations govern the current through the conduction and valence band:

$$J_{CB} = J_{CB}^{+} - J_{CB}^{-} \tag{1.39}$$

$$J_{VB} = J_{VB}^{+} - J_{VB}^{-} \tag{1.40}$$

Where

$$J_{VB}^{+} = ek_{VB}^{+} p_s c_{red} W_{red}(E_{VB}^{S}) \tag{1.41}$$

$$J_{VB}^{-} = ek_{VB}^{-} N_{VB} c_{ox} W_{ox}(E_{VB}^{S}) \tag{1.42}$$

$$J_{CB}^{+} = ek_{CB}^{+} N_{CB} c_{red} W_{red}(E_{CB}^{S}) \tag{1.43}$$

$$J_{CB}^{-} = ek_{CB}^{-} n_S c_{ox} W_{ox}(E_{CB}^{S}) \tag{1.44}$$

Where the electronic charge is termed as e, rate constant as k and surface charge density of holes and electrons as p_s and n_S respectively.

Whereas $c_{ox}W_{ox}(E_{VB}^{S}) = D_{ox}$ is the density of states of oxidized species and $c_{ox}W_{ox}(E_{CB}^{S}) = D_{red}$ is the density of states of the reduced species.

The overall conduction and valance band current can be written more accurately as a function of the overpotential η as

$$J_{VB} = J_{VB}^{0}\left(exp\left(-\frac{e\eta}{k_{\boldsymbol{B}}T}\right) - 1\right) \tag{1.45}$$

$$J_{CB} = J_{CB}^{0}\left(1 - exp\left(-\frac{e\eta}{k_{\boldsymbol{B}}T}\right)\right) \tag{1.46}$$

It is comparable to the Butler–Volmer equation, which governs the current through the metal electrode.

$$J = J_0\left(exp\left(\frac{(1-\alpha)e\eta}{k_{\boldsymbol{B}}T}\right) - exp\left(-\frac{\alpha e\eta}{k_{\boldsymbol{B}}T}\right)\right) \tag{1.47}$$

where J_0 is the exchange current density and α is the transfer coefficient. A plot of $\log(\frac{J}{J_0})$ against η is known as the Tafel plot. The slope of the Tafel plot (called the TAFEL slope) provides information about the reaction kinetics at the semiconductor/electrolyte interface. Physically the Tafel slope is defined as how much over potential is required to change the reaction rate by a factor of 10. The majority carriers of respective

semiconductors (electrons for n-type and holes for p-type) are responsible for the appearance of dark current. Upon illumination, the electron-hole pairs are generated, and the transfer of minority carriers through the electrode-electrolyte junction gives rise to the photocurrent. In reverse bias condition, the photocurrent is governed by Gartner's [16] equation as

$$J_G = J_0 + e\Phi\left(1 - \frac{exp^{-\alpha W_{sc}}}{1 + \alpha L_P}\right) \tag{1.48}$$

Where saturation current density is termed as J_0, incident light flux as Φ, absorption coefficient as α, depletion layer width as W_{sc} and minority carrier diffusion length as L_P.

1.7 Criteria of an Ideal Photoelectrode Material

The performance of a PEC cell primarily depends on the characteristics of the working electrode material. Therefore choosing a suitable semiconductor as a photoanode/photocathode material is necessary. A semiconductor must have the following properties to be used as active photoelectrode material inside a PEC cell.

a. Suitable optical, electronic, and electrochemical properties
   I. The semiconductor must have a narrow bandgap capable of harvesting the visible part of solar radiation.
   II. It should have a high absorbance.
   III. High photo-generated charge carrier separation efficiency i,e., lower carrier recombination probability.
   IV. High conductivity for better charge carrier transportation.
   V. Suitable band edge positions with respect to the water oxidation and reduction potentials.
   VI. Low overpotential for the water oxidation reaction.

b. Economical
   I. The semiconducting material should e earth-abundant.
   II. It should be low-cost material.
   III. The photoelectrode synthesis route must be easy, cost-effective, and scalable.

c. Durability
   I. The working electrode material must be physically and chemically stable inside the aqueous electrolyte under solar irradiation.

II. It must be stable under the water-splitting reactions.

In a PEC cell, the semiconductor (working electrode material) converts the solar energy into electrical energy by absorbing the incident photons with the generation of photovoltage and electron-hole pairs. The band-gap of the semiconductor determines the absorption threshold. Since the maximum portion of the solar radiation comes under the visible region, the optical band-gap of the semiconductor should be such that it could absorb the UV and visible (Vis) part of solar radiation. For this reason, a narrow band-gap semiconductor is necessary. The photo-generated carriers will contribute to the photocurrent only when they separate and are transported towards the counter electrode and the electrolyte. Therefore high charge separation and transportation efficiency with a lower recombination probability are necessary. Apart from that, the conduction and valance band position of the semiconductor must be situated above and below the water reduction and oxidation potential, respectively. The slandered thermodynamic potential required for water-splitting is 1.229 V. However, the water-splitting reaction is associated with other thermodynamic losses. Therefore a semiconductor with an optical band-gap 1.9-2.2 is ideal for the PEC water splitting applications. However, no single semiconductor has all the criteria mentioned earlier and is associated with different limitations inside the PEC cell.

1.8 Earth Abundant Metal Oxide Semiconductors Based Photoelectrodes

Water splitting was demonstrated by Fujishima and Honda for the first time in 1972, using TiO_2 as a photocatalyst. Since several metal oxide semiconductors have been widely explored as photoelectrode material such as TiO_2, ZnO, Fe_2O_3, WO_3 [17–25]. Metal oxides have gained lots of attention due to their physical and chemical properties, such as chemical stability, preferable band edge positions, natural abundance, low-cost synthesis routes, and tunable bandgaps [26]. Oxide is the most stable form of all metal compounds which can be easily synthesized. As shown in Fig.1.9, oxide semiconductors have a wide range of band gaps and band positions. In the case of metal oxide semiconductors, the O 2p level defines the valance band, whereas the conduction band consists of s, p, or d levels. The semiconductors involve O 2p, and metal s orbital is typically wide band-gap semiconductors such as ZnO (3.4 eV), Al_2O_3 (8.8 eV), and Ga_2O_3 (4.5 eV). In contrast, narrow band-gap semiconductors have O 2p and metal d^n electronic configurations such as Cu_2O (d^{10}, 2.1 eV) and Fe_2O_3 (d^5, 2.2 eV). Also, band edge positions and the band-gap can be customized by coupling two metals to form the ternary oxides. For example, the overlap between Bi 6pempty orbitals and V 3d-O 2p antibonding states results in the conduction band position of $BiVO_4$ close to 0 V vs. RHE

with a bandgap of 2.3 eV [26]. Also, the oxygen vacancies which are spontaneously created in the metal oxide semiconductors act as mid-band-gap defect states and increase the overall light-absorbing ability of the semiconductor [27–32]. Most of the transition metal oxide semiconductors have intrinsic n-type or p-type semiconducting properties depending on the presence of defect states. TiO_2, Fe_2O_3, ZnO, and WO_3 exhibits n-type conductivity and are generally used as photoanodes, whereas NiO, CuO, and Cu_2O have p-type conductivity and are used as photocathodes. The electronic properties of the respective semiconductors (p/n-type) can also be tuned with the p and n-type doping [22,33–38].

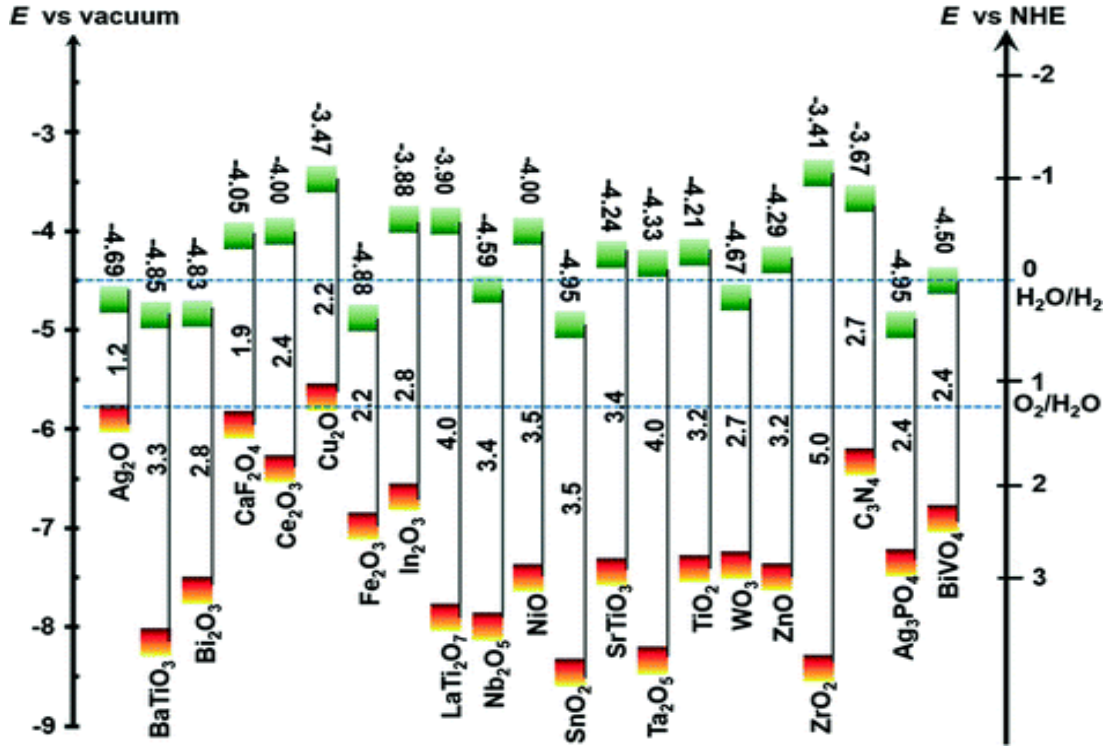

Figure 1.9: The band edge position of different metal oxide semiconductors used in water splitting applications [27].

Moreover, metal oxides like NiO, Co_3O_4, RuO_2, and IrO_x are also used as efficient electrochemical water splitting co-catalysts [39,40]. Thus the rich diversity of multifunctional metal oxide semiconductors provides immense scopes to develop superior photoelectrodes for PEC water splitting cell applications.

1.8.1 Scope of ZnO as an Earth Abundant Photoanode Material

Over the past few years, many earth-abundant metal oxide semiconductors such as TiO_2, ZnO, Fe_2O_3, $BiVO_4$, etc., have emerged as a suitable photoanode material of PEC

water splitting cells [41–51]. Among them, ZnO is the most widely explored photoanode material due to its natural abundance, low cost, facile synthesis, low toxicity to the environment, and suitable band position with respect to water oxidation and reduction potential [52–54]. ZnO is an n-type semiconductor. Fermi level of n-type ZnO is situated above the redox potential of electrolyte. Hence, when a ZnO photoanode is submerged inside the electrolyte, a space charge region, consequent band bending, and an electric field is created at the ZnO electrolyte junction in equilibrium.If the electrode surface is illuminated with solar light, the incident photons will excite the electrons to the conduction band of ZnO, leaving behind holes in the valance band. The system is no longer in equilibrium, and a quasi-Fermi level will appear inside the semiconductor near the junction due to the generation of electron-hole pairs under illumination. The internal built-in electric field will drive the photo-generated electrons away from the ZnO/electrolyte junction and holes towards the junction. The electrons will travel to the counter electrode to reduce water, and the hole will oxidize water at the photoanode surface. The higher electron and hole mobility (~ 205 and 180 $cm^2V^{-1}s^{-1}$) with a longer minority carrier diffusion length makes ZnO one of the most promising photoanode materials for PEC cell designing [55,56]. Poor light absorption due to the wide bandgap, severe charge recombination, and fast degradation under illumination inside an aqueous medium are the critical challenges with ZnO-based nanostructured photoanodes for photoelectrochemical (PEC) water splitting cell applications.

As discussed earlier, the valance band of ZnO is composed of the overlapping O 2p orbitals, and the conduction band is composed of metal (Zn) s orbitals. Such a combination is observed to result in a wide bandgap of the semiconductor. ZnO has an optical band gap of 3.26 eV, which is suitable for the absorption of UV light only (less than 5% of the total solar spectrum) [54,57]. The poor light-harvesting efficiency is the major limitation of ZnO towards the implementation of ZnO-based photoanodes in the PEC cell. Apart from that, ZnO is unstable in an aqueous medium under visible light. The photocorrosion that occurs under UV light significantly decreases the photocatalytic properties of ZnO [58].

To overcome these limitations of ZnO photoanodes, wide ranges of approaches have been made by the researchers, such as nanostructure designing, which facilitate the charge transportation, elemental doping to tune the bandgap and the conductivity, development of hetero-architectures between ZnO and narrow bandgap materials to increase the overall absorbance and charge separation, surface passivation layer

deposition and plasmonic nano-particles anchoring for the optical absorbance improvement [43,53,56,59–61].

PEC water splitting is a surface phenomenon. The PEC activity of a photoanode is dependent on its electrochemically active surface area. The nanostructured photoelectrodes (photoanodes) have a large electrochemically active surface area in contact with the electrolyte. 1 D nanostructures are especially attractive in this direction. That's why different ZnO nanostructures like nanorod, nanotube, nanotree, Caterpillar-like structures have been developed for PEC applications [62–64]. The 1D nanostructures design also facilitates the minority carrier transport reducing the surface recombination.

Elemental doping in ZnO nanostructures-based photoanodes is especially attractive. The optical absorbance, band structure, and PEC performance of ZnO photoanodes can be tuned with external doping. Wang et al. have reported that the gradient N doping to ZnO nanorods shifted the optical absorption edge to the visible wavelength region with a terraced band structure suitable for the charge transport process. N modification improves photocurrent density by about two times higher magnitude than bare ZnO [65]. Salem et al. have synthesized Gd doped ZnO nanorods on FTO coated glass substrates which exhibit a remarkable photoconversion efficiency of 3.6% under AM1.5G illumination [66]. Compared to bare ZnO, a 3-4 fold increase of charge carrier density and a 2-fold increase in the current density with Al-doped ZnO nanowires based photoelectrode was reported by Govatsi et al. [67]. Karmakar et al. have shown that the alkali metal doping in ZnO oxygen vacancies and lattice strain defects play a significant role in enhancing the PEC water splitting activity of ZnO nanorods photoanodes [61]. Na, Li, and K doped ZnO nanorods photoanodes exhibit 0.73%, 0.69%, and 0.70% photoconversion efficiency, respectively, compared to the 0.015% efficiency of pristine ZnO.

The plasmonic nanoparticles anchored ZnO nanostructures also exhibit excellent PEC activities. The plasmonic nanoparticles inject hot carrier to ZnO nanostructures under illumination, which increases charge carrier density which is advantageous for PEC water splitting. Mahala et al. have reported that 35 nm Au nanoparticles decorated ZnO nanosheets display a 0.605%photoconversion efficiency [68]. Khiari et al. have shown that Ag nanoparticles supported ZnO exhibits excellent photocatalytic activity[69].

The unwanted surface state recombination is a PEC performance-limiting parameter of ZnO-based photoanodes. Surface passivating layers can increase the minority carrier lifetime by quenching the surface states mediated recombination. Surface passivation

layers are nearly 2 nm thick. According to Liu et al., ZnO nanowires with ultrathin titian shell layer demonstrate 25% higher PEC water splitting performance than pristine ZnO nanowires [23]. Surface Catalyzing also enhances the water splitting performance and stability ZnO based photoanodes. Li et al. have reported that MOF-based ZIF-8 surface passivating layer along with $Ni(OH)_2$ surface catalyzing layer enhances the photocurrent density of ZnO to 1.95 $mA.cm^{-2}$ (at 1.23 V vs. RHE), which is two times higher than the current density of pristine ZnO [45].

Hetero architecture formation between ZnO and another semiconducting material is an effective route to overcome the limitations of pristine ZnO-based photoanodes for PEC cell applications. The semiconductor overlayer is preferred to have a narrow band-gap with suitable band positions and is chemically stable in nature during water splitting reactions. Yan et al. have synthesized an n/n type heterojunction by depositing n-type $BiVO_4$ over 1D ZnO nanorods through the SAILR method [70]. $BiVO_4$ has a narrow band-gap (2.4 eV). Hence $BiVO_4$ enhanced the overall absorbance of the heterojunction compared to pristine ZnO photoanode and shifted the sharp absorption edge of ZnO from 3.2 eV to 2.5 eV. The deposited $BiVO_4$ overlayer results in a four-fold increase of photocurrent density at 1.23V potential vs. Ag/AgCl electrode compared to pristine ZnO. Apart from that, the $BiVO_4$ layer acts as a surface protective layer for ZnO, which has also increased the photoanodes' stability. Yang et al. have reported that CoPi modified ZnO/$BiVO_4$ heterojunction photoanode exhibits a current density of 3.5 $mA.cm^{-2}$ at 1.23 V vs. RHE [71]. Hsu et al have demonstrated that ZnO/Fe_2O_3 core/shell type heterojunction shows a current density as high as 1.5 $mA.cm^{-2}$ at 0.6 V vs. Ag/AgCl compare to 0.75 $mA.cm^{-2}$ photocurrent density bare ZnO [72]. Chen et al. have designed a dual-heterojunction Cu_2O/CdS/ZnO nanotube array photoanode. The Cu_2O/CdS modification enhances the optical absorption of ZnO and promotes the charge transport process quenching the charge carrier recombination. The dual heterojunction photoanode exhibits 2.8% hydrogen production efficiency with a 7 $mA.cm^{-2}$ current density at 0.4 V vs. Ag/AgCl under AM 1.5G radiation [73]. Karmakar et al. have reported that p/nheterojunction formation between $CuFeO_2$ and ZnO effectively promotes the photoconversion efficiency to a 450% higher value than pristine ZnO [74]. The $CuFeO_2$ deposition enhances the overall absorption with a quenched surface recombination of ZnO. The type-II like band alignment between $CuFeO_2$ and ZnO promotes the charge transfer process and results in excellent PEC water splitting performance.

Among all the techniques mentioned above, heterojunction formation between ZnO and other functional materials is considered the most promising pathway to overcome the limitations of ZnO as a single photoanode material for PEC water splitting cells. In

this projected thesis, we are focused on the fabrication of different types of heterojunctions (p/n, n/n) between ZnO and other earth-abundant metal oxide semiconductors in a cost-effective and scalable route, which will be able to harvest a more significant part of solar energy and convert it into hydrogen energy by reducing all the limitations associated with ZnO based photoanodes.

1.8.2 Scope of Fe_2O_3 as a Photoanode Material

Fe_2O_3 is also a widely explored photoanode material among various metal oxide semiconductors. Fe_2O_3 is especially attractive in the field of photoelectrochemical water oxidation because of its narrow band-gap of ~2.0 eV, suitable for water oxidation under solar light as it absorbs nearly ~15% of the total solar spectrum [75], a very positive valance band position (~2.5 V vs. RHE) which is ideal for water oxidation [75], chemically stable behaviour in broad pH range [76], low toxicity, natural abundance all over the earth crust and low cost and easily scalable synthesis route [76]. Owning to the above-mentioned advantages, theoretically predicted solar-to-hydrogen efficiency (STH) of hematite photoanode is about 12.8–16% with a photocurrent density of 12.6 $mA.cm^{-2}$ under AM 1.5G illumination. Despite intense efforts, the practically achievable STH efficiency of hematite photoanodes is much below the predicted value [76]. The short photo-generated carrier lifetime (<10 ps) and the low minority carrier mobility (0.2 $cm^2\ V^{-1}\ s^{-1}$) are the two main limitations associated with hematite photoanodes [77,78]. Combining these two performance-limiting parameters results in minority carrier (hole) diffusion length as low as 2-4 nm [79]. However, as Fe_2O_3 is an indirect bandgap semiconductor, a thicker film is required to absorb a sufficient amount of incident radiation. Also, the surface states mediated recombination in Fe_2O_3 results in the slow OER kinetics with a large overpotential [80]. The researchers have adopted different strategies to overcome these limitations. Yang et al. have shown that surface oxygen vacancies can reduce the space charge region width, effectively reducing surface recombination and charge carrier transportation [75]. Fe_2O_3/Co_3O_4 nanocomposite photoanode exhibits 0.48 $mA.cm^{-2}$ at 1.23 V vs. RHE. over a 0.28 $mA.cm^{-2}$ current density of pristine Fe_2O_3 photoanode [81]. Bai et al. have reported that NiFe-LDH incorporated $Fe_2O_3/BiVO_4$ photoanodes exhibit about 4.25 times and 2 times higher current density than that of pristine α-Fe_2O_3 and $BiVO_4$ photoanodes [82]. In this projected thesis, we have adopted a co electrocatalyst deposition approach to reduce the turn-on potential of Fe_2O_3 photoanodes.

1.9 The Objective of the Thesis

For the development of a sustainable society, the advancement of energy infrastructure is vital. The future energy economy is greatly dependent on renewable energy resources. Since solar energy is the most abundant renewable energy resource, development of solar energy harvesting technologies is extremely important. PEC water splitting with earth-abundant metal oxide semiconductors is the most attractive route to convert solar energy into hydrogen energy, which can tackle the global future energy demand with the promise of controlling anthropogenic climate change. Therefore, in this projected thesis, we have developed different heterojunction semiconductor photoanodes using ZnO and other earth-abundant metal oxide semiconductors, providing a suitable pathway to achieve an efficient PEC water splitting system towards a carbon-free future. The specific objectives of the thesis are:

1. Synthesis of earth-abundant metal oxide semiconductor-based nanostructures.
    a. 1D ZnO nanorods fabrication by cost-effective wet chemical and chemical bath route.
    b. Synthesis of 1D Fe_2O_3 nanorods on conducting substrates by solvothermal technique.
    c. Fabrications of surface functionalized nanoheterojunction or mesostructured 1D ZnO or Fe_2O_3 photoanodes by low-cost techniques like spin coating, electrodeposition, SAILR methods etc.
2. Characterization of synthesized nanomaterials.
    a. Structure and morphological characterization.
    b. Crystallographic analysis.
    c. Characterization of chemical composition and oxidation states to constituents elements.
    d. Optical characterizations.
        I. UV Vis absorption study.
        II. PL emission study.
3. Photoelectrochemical characterizations of photoelectrodes for solar energy and solar fuel generation.

1.10 Organization of the Thesis

This thesis contains seven chapters. A brief outlook of each chapter is given below:

Chapter 1: Introduction

This chapter describes the future energy challenges and how renewable energy resources promise to fulfil the energy demand. This chapter also includes the

necessity of hydrogen as an alternative fuel that can be generated by photoelectrochemical water splitting using metal oxide semiconductors as photoanode material. The advantages and limitations of using metal oxide semiconductor photoanodes and strategies to overcome those limitations are also discussed in detail.

Chapter 2: Experimental Details

This chapter includes detailed descriptions of the various synthesis techniques of nanostructured materials. It also describes the methods to characterize them.

Chapter 3: Solar Water Splitting With ZnO/MoO_3 Based n/n Type Core-Shell Heterojunction Photoanodes

This chapter describes the synthesis technique of 1D type ZnO/MoO_3 core-shell heterojunction photoanodes and a detailed study on how the UV active material (MoO_3) improved the photoelectrochemical water splitting activity of 1D ZnO nanorods (NRs) based photoanodes.

Chapter 4: $CoFe_2O_4$/ZnO and $NiFe_2O_4$/ZnO, an n/n and p/n Type-II Heterojunction Photoanode for Solar Fuel Generation.

This chapter addresses the study on the effect of anchoring of different visible light active earth-abundant metal ferrite nanostructures ($CoFe_2O_4$/$NiFe_2O_4$ NPs) on the PEC activity of ZnO NRs photoanodes.

Chapter 5: Solar-Driven PEC Activity of ZnO/$ZnCo_2O_4$ Based Nanoheterojunction Photoanodes

This chapter presents the study on the PEC H_2 production performance of a p/n heterojunction photoanodes form between $ZnCo_2O_4$ and ZnO.

Chapter 6: Dual co-catalyst activated Fe_2O_3 photoanodes for solar water oxidation

This chapter demonstrates an effective pathway to reduce the water spitting turn-on potential of Fe_2O_3 photoanodes through suitable surface engineering.

Chapter 7: Conclusion and Future prospects

This chapter presents the overall conclusion of the thesis along with the scope of further advancement of these works.

Bibliography

[1] R. Van de Krol, M. Grätzel, Photoelectrochemical hydrogen production, Springer, 2012.

[2] G.A.C.O.G. Change, World in Transition 3: Towards Sustainable Energy Systems, Routledge, 2014.

[3] U.G. Assembly, Towards Sustainable Development, Annex to Document A/42/427, Environment: Our Common Future in Report of the World Commission on Environment and Development: Our Common Future. Available at Http://Www. Un-Documents. Net/Ocf-02. Htm. (1987).

[4] F. Le Formal, On the Morphology and Interfaces of Nanostructured Hematite Photoanodes for Solar-Driven Water Splitting, EPFL, 2011.

[5] G.W. Crabtree, M.S. Dresselhaus, M.V. Buchanan, The hydrogen economy, Physics Today. 57 (2004) 39–44.

[6] D. Stolten, Hydrogen and fuel cells: fundamentals, technologies and applications, John Wiley & Sons, 2010.

[7] U. Bossel, Does a hydrogen economy make sense?, Proceedings of the IEEE. 94 (2006) 1826–1837.

[8] Z. Chen, T.F. Jaramillo, T.G. Deutsch, A. Kleiman-Shwarsctein, A.J. Forman, N. Gaillard, R. Garland, K. Takanabe, C. Heske, M. Sunkara, Accelerating materials development for photoelectrochemical hydrogen production: Standards for methods, definitions, and reporting protocols, Journal of Materials Research. 25 (2010) 3–16.

[9] H. Gerischer, Solar photoelectrolysis with semiconductor electrodes, in: Solar Energy Conversion, Springer, 1979: pp. 115–172.

[10] A.J. Nozik, Photoelectrochemical cells, Philosophical Transactions of the Royal Society of London. Series A, Mathematical and Physical Sciences. 295 (1980) 453–470.

[11] A. Heller, Conversion of sunlight into electrical power and photoassisted electrolysis of water in photoelectrochemical cells, Accounts of Chemical Research. 14 (1981) 154–162.

[12] R. Memming, Solar energy conversion by photoelectrochemical processes, Electrochimica Acta. 25 (1980) 77–88.

[13] A.J. Nozik, R. Memming, Physical chemistry of semiconductor− liquid interfaces, The Journal of Physical Chemistry. 100 (1996) 13061–13078.

[14] H. Gerischer, Physical Chemistry: An Advanced Treatise, By H. Eyring et al., Academic Press, New York. (1970) 487–489.

[15] H. Gerischer, Charge transfer processes at semiconductor-electrolyte interfaces in connection with problems of catalysis, Surface Science. 18 (1969) 97–122.

[16] J. Reichman, The current-voltage characteristics of semiconductor-electrolyte junction photovoltaic cells, Applied Physics Letters. 36 (1980) 574–577.

[17] K. Sivula, F. Le Formal, M. Grätzel, Solar water splitting: progress using hematite (α-Fe2O3) photoelectrodes, ChemSusChem. 4 (2011) 432–449.

[18] A.A. Ismail, D.W. Bahnemann, Photochemical splitting of water for hydrogen production by photocatalysis: A review, Solar Energy Materials and Solar Cells. 128 (2014) 85–101.

[19] G. Wang, X. Xiao, W. Li, Z. Lin, Z. Zhao, C. Chen, C. Wang, Y. Li, X. Huang, L. Miao, Significantly enhanced visible light photoelectrochemical activity in TiO2 nanowire arrays by nitrogen implantation, Nano Letters. 15 (2015) 4692–4698.

[20] J. Zhang, X. Jin, P.I. Morales-Guzman, X. Yu, H. Liu, H. Zhang, L. Razzari, J.P. Claverie, Engineering the absorption and field enhancement properties of Au–TiO2 nanohybrids via whispering gallery mode resonances for photocatalytic water splitting, ACS Nano. 10 (2016) 4496–4503.

[21] A.P. Bhirud, S.D. Sathaye, R.P. Waichal, L.K. Nikam, B.B. Kale, An eco-friendly, highly stable and efficient nanostructured p-type N-doped ZnO photocatalyst for environmentally benign solar hydrogen production, Green Chemistry. 14 (2012) 2790–2798.

[22] X. Yang, A. Wolcott, G. Wang, A. Sobo, R.C. Fitzmorris, F. Qian, J.Z. Zhang, Y. Li, Nitrogen-doped ZnO nanowire arrays for photoelectrochemical water splitting, Nano Letters. 9 (2009) 2331–2336.

[23] M. Liu, C.-Y. Nam, C.T. Black, J. Kamcev, L. Zhang, Enhancing water splitting activity and chemical stability of zinc oxide nanowire photoanodes with ultrathin titania shells, The Journal of Physical Chemistry C. 117 (2013) 13396–13402.

[24] J. Zhang, I. Salles, S. Pering, P.J. Cameron, D. Mattia, S. Eslava, Nanostructured WO 3 photoanodes for efficient water splitting via anodisation in citric acid, RSC Advances. 7 (2017) 35221–35227.

[25] A. Kafizas, L. Francàs, C. Sotelo-Vazquez, M. Ling, Y. Li, E. Glover, L. McCafferty, C. Blackman, J. Darr, I. Parkin, Optimizing the activity of nanoneedle structured WO3 photoanodes for solar water splitting: direct synthesis via chemical vapor deposition, The Journal of Physical Chemistry C. 121 (2017) 5983–5993.

[26] R. Marschall, L. Wang, Non-metal doping of transition metal oxides for visible-light photocatalysis, Catalysis Today. 225 (2014) 111–135.

[27] Z. Zhao, Z. Wang, J. Bao, Nanomaterials for hydrogen generation from solar water splitting, in: Nanomaterials for Sustainable Energy, Springer, 2016: pp. 445–470.

[28] B.D. Alexander, P.J. Kulesza, I. Rutkowska, R. Solarska, J. Augustynski, Metal oxide photoanodes for solar hydrogen production, Journal of Materials Chemistry. 18 (2008) 2298–2303.

[29] F. Lei, Y. Sun, K. Liu, S. Gao, L. Liang, B. Pan, Y. Xie, Oxygen vacancies confined in ultrathin indium oxide porous sheets for promoted visible-light water splitting, Journal of the American Chemical Society. 136 (2014) 6826–6829.

[30] J. Gan, X. Lu, J. Wu, S. Xie, T. Zhai, M. Yu, Z. Zhang, Y. Mao, S.C.I. Wang, Y. Shen, Oxygen vacancies promoting photoelectrochemical performance of In 2 O 3 nanocubes, Scientific Reports. 3 (2013) 1–7.

[31] C. Zhu, C. Li, M. Zheng, J.-J. Delaunay, Plasma-induced oxygen vacancies in ultrathin hematite nanoflakes promoting photoelectrochemical water oxidation, ACS Applied Materials & Interfaces. 7 (2015) 22355–22363.

[32] G. Wang, Y. Ling, Y. Li, Oxygen-deficient metal oxide nanostructures for photoelectrochemical water oxidation and other applications, Nanoscale. 4 (2012) 6682–6691.

[33] Y. Ling, Y. Li, Review of Sn-doped hematite nanostructures for photoelectrochemical water splitting, Particle & Particle Systems Characterization. 31 (2014) 1113–1121.

[34] A. Kay, I. Cesar, M. Grätzel, New benchmark for water photooxidation by nanostructured α-Fe2O3 films, Journal of the American Chemical Society. 128 (2006) 15714–15721.

[35] I. Cesar, A. Kay, J.A. Gonzalez Martinez, M. Grätzel, Translucent thin film Fe2O3 photoanodes for efficient water splitting by sunlight: nanostructure-directing effect of Si-doping, Journal of the American Chemical Society. 128 (2006) 4582–4583.

[36] Y. Ling, G. Wang, D.A. Wheeler, J.Z. Zhang, Y. Li, Sn-doped hematite nanostructures for photoelectrochemical water splitting, Nano Letters. 11 (2011) 2119–2125.

[37] G. Wang, Y. Ling, D.A. Wheeler, K.E. George, K. Horsley, C. Heske, J.Z. Zhang, Y. Li, Facile synthesis of highly photoactive α-Fe2O3-based films for water oxidation, Nano Letters. 11 (2011) 3503–3509.

[38] G.K. Mor, O.K. Varghese, R.H. Wilke, S. Sharma, K. Shankar, T.J. Latempa, K.-S. Choi, C.A. Grimes, p-Type Cu− Ti− O nanotube arrays and their use in self-biased heterojunction photoelectrochemical diodes for hydrogen generation, Nano Letters. 8 (2008) 1906–1911.

[39] Y. Wang, T. Zhou, K. Jiang, P. Da, Z. Peng, J. Tang, B. Kong, W.-B. Cai, Z. Yang, G. Zheng, Reduced mesoporous Co3O4 nanowires as efficient water oxidation electrocatalysts and supercapacitor electrodes, Advanced Energy Materials. 4 (2014) 1400696.

[40] S.D. Tilley, M. Schreier, J. Azevedo, M. Stefik, M. Graetzel, Ruthenium oxide hydrogen evolution catalysis on composite cuprous oxide water-splitting photocathodes, Advanced Functional Materials. 24 (2014) 303–311.

[41] D. Pal, A. Sarkar, N.G. Ghosh, D.M. Sanke, D. Maity, K. Karmakar, D. Sarkar, S.S. Zade, G.G. Khan, Integration of LaCo (OH) x Photo-Electrocatalyst and Plasmonic Gold Nanoparticles with Sb-Doped TiO2 Nanorods for Photoelectrochemical Water Oxidation, ACS Applied Nano Materials. (2021).

[42] Y. Li, Y.-K. Peng, L. Hu, J. Zheng, D. Prabhakaran, S. Wu, T.J. Puchtler, M. Li, K.-Y. Wong, R.A. Taylor, Photocatalytic water splitting by N-TiO 2 on MgO (111) with exceptional quantum efficiencies at elevated temperatures, Nature Communications. 10 (2019) 1–9.

[43] Z. Kang, H. Si, S. Zhang, J. Wu, Y. Sun, Q. Liao, Z. Zhang, Y. Zhang, Interface engineering for modulation of charge carrier behavior in ZnO photoelectrochemical water splitting, Advanced Functional Materials. 29 (2019) 1808032.

[44] C.X. Guo, Y. Dong, H.B. Yang, C.M. Li, Graphene quantum dots as a green sensitizer to functionalize ZnO nanowire arrays on F-doped SnO2 glass for enhanced photoelectrochemical water splitting, Advanced Energy Materials. 3 (2013) 997–1003.

[45] X. Li, S. Liu, K. Fan, Z. Liu, B. Song, J. Yu, MOF-based transparent passivation layer modified ZnO nanorod arrays for enhanced photo-electrochemical water splitting, Advanced Energy Materials. 8 (2018) 1800101.

[46] P. Sharma, J.-W. Jang, J.S. Lee, Key strategies to advance the photoelectrochemical water splitting performance of α-Fe2O3 photoanode, ChemCatChem. 11 (2019) 157–179.

[47] X. She, J. Wu, H. Xu, J. Zhong, Y. Wang, Y. Song, K. Nie, Y. Liu, Y. Yang, M.-T.F. Rodrigues, High efficiency photocatalytic water splitting using 2D α-Fe2O3/g-C3N4 Z-scheme catalysts, Advanced Energy Materials. 7 (2017) 1700025.

[48] K.-Y. Yoon, J.-S. Lee, K. Kim, C.H. Bak, S.-I. Kim, J.-B. Kim, J.-H. Jang, Hematite-based photoelectrochemical water splitting supported by inverse opal structures of graphene, ACS Applied Materials & Interfaces. 6 (2014) 22634–22639.

[49] M. Zhou, J. Bao, W. Bi, Y. Zeng, R. Zhu, M. Tao, Y. Xie, Efficient Water Splitting via a Heteroepitaxial BiVO4 Photoelectrode Decorated with Co-Pi Catalysts, ChemSusChem. 5 (2012) 1420–1425.

[50] Z. Tian, P. Zhang, P. Qin, D. Sun, S. Zhang, X. Guo, W. Zhao, D. Zhao, F. Huang, Novel black BiVO4/TiO2− x photoanode with enhanced photon absorption and charge separation for efficient and stable solar water splitting, Advanced Energy Materials. 9 (2019) 1901287.

[51] Y. Kuang, Q. Jia, H. Nishiyama, T. Yamada, A. Kudo, K. Domen, A front-illuminated nanostructured transparent BiVO4 photoanode for> 2% efficient water splitting, Advanced Energy Materials. 6 (2016) 1501645.

[52] S. Panigrahi, D. Basak, Core–shell TiO 2@ ZnO nanorods for efficient ultraviolet photodetection, Nanoscale. 3 (2011) 2336–2341.

[53] Y.I. Choi, H.J. Jung, W.G. Shin, Y. Sohn, Band gap-engineered ZnO and Ag/ZnO by ball-milling method and their photocatalytic and Fenton-like photocatalytic activities, Applied Surface Science. 356 (2015) 615–625.

[54] K. Jeong, P.R. Deshmukh, J. Park, Y. Sohn, W.G. Shin, ZnO-TiO2 core–shell nanowires: a sustainable photoanode for enhanced photoelectrochemical water splitting, ACS Sustainable Chemistry & Engineering. 6 (2018) 6518–6526.

[55] A. Janotti, C.G. Van de Walle, Fundamentals of zinc oxide as a semiconductor, Reports on Progress in Physics. 72 (2009) 126501.

[56] D. Commandeur, G. Brown, E. Hills, J. Spencer, Q. Chen, Defect-rich ZnO nanorod arrays for efficient solar water splitting, ACS Applied Nano Materials. 2 (2019) 1570–1578.

[57] C. Mahala, M.D. Sharma, M. Basu, ZnO Nanosheets Decorated with Graphite-Like Carbon Nitride Quantum Dots as Photoanodes in Photoelectrochemical Water Splitting, ACS Applied Nano Materials. (2020).

[58] L. Zhang, H. Cheng, R. Zong, Y. Zhu, Photocorrosion suppression of ZnO nanoparticles via hybridization with graphite-like carbon and enhanced photocatalytic activity, The Journal of Physical Chemistry C. 113 (2009) 2368–2374.

[59] J. Jiang, X. Zhang, P. Sun, L. Zhang, ZnO/BiOI Heterostructures: Photoinduced Charge-Transfer Property and Enhanced Visible-Light Photocatalytic Activity, J. Phys. Chem. C. 115 (2011) 20555–20564. https://doi.org/10.1021/jp205925z.

[60] C. Liu, Y. Qiu, F. Wang, K. Wang, Q. Liang, Z. Chen, Design of Core–Shell-Structured ZnO/ZnS Hybridized with Graphite-Like C3N4 for Highly Efficient Photoelectrochemical Water Splitting, Advanced Materials Interfaces. 4 (2017) 1700681.

[61] K. Karmakar, A. Sarkar, K. Mandal, G.G. Khan, Investigating the role of oxygen vacancies and lattice strain defects on the enhanced photoelectrochemical property of alkali metal (Li, Na, and K) doped ZnO nanorod photoanodes, ChemElectroChem. 5 (2018) 1147–1152.

[62] X. Ren, A. Sangle, S. Zhang, S. Yuan, Y. Zhao, L. Shi, R.L. Hoye, S. Cho, D. Li, J.L. MacManus-Driscoll, Photoelectrochemical water splitting strongly enhanced in fast-grown ZnO nanotree and nanocluster structures, Journal of Materials Chemistry A. 4 (2016) 10203–10211.

[63] Q. Li, X. Sun, K. Lozano, Y. Mao, Facile and scalable synthesis of “caterpillar-like” ZnO nanostructures with enhanced photoelectrochemical water-splitting effect, The Journal of Physical Chemistry C. 118 (2014) 13467–13475.

[64] Y.-K. Hsu, Y.-G. Lin, Y.-C. Chen, Polarity-dependent photoelectrochemical activity in ZnO nanostructures for solar water splitting, Electrochemistry Communications. 13 (2011) 1383–1386.

[65] M. Wang, F. Ren, J. Zhou, G. Cai, L. Cai, Y. Hu, D. Wang, Y. Liu, L. Guo, S. Shen, N doping to ZnO nanorods for photoelectrochemical water splitting under visible light: engineered impurity distribution and terraced band structure, Scientific Reports. 5 (2015) 1–13.

[66] K.E. Salem, A.M. Mokhtar, I. Soliman, M. Ramadan, B.S. Shaheen, N.K. Allam, Ge-doped ZnO nanorods grown on FTO for photoelectrochemical water splitting with exceptional photoconversion efficiency, International Journal of Hydrogen Energy. 46 (2021) 209–220.

[67] K. Govatsi, G. Syrrokostas, S.N. Yannopoulos, S.G. Neophytides, Optimization of aluminum doped ZnO nanowires for photoelectrochemical water splitting, Electrochimica Acta. 392 (2021) 138995.

[68] C. Mahala, M.D. Sharma, M. Basu, Near-field and far-field plasmonic effects of gold nanoparticles decorated on ZnO nanosheets for enhanced solar water splitting, ACS Applied Nano Materials. 3 (2020) 1153–1165.

[69] M. Khiari, M. Gilliot, M. Lejeune, F. Lazar, A. Hadjadj, Effects of Ag Nanoparticles on Zinc Oxide Photocatalytic Performance, Coatings. 11 (2021) 400.

[70] L. Yan, W. Zhao, Z. Liu, 1D ZnO/BiVO 4 heterojunction photoanodes for efficient photoelectrochemical water splitting, Dalton Transactions. 45 (2016) 11346–11352.

[71] J.-S. Yang, J.-J. Wu, Low-potential driven fully-depleted BiVO4/ZnO heterojunction nanodendrite array photoanodes for photoelectrochemical water splitting, Nano Energy. 32 (2017) 232–240.

[72] Y.-K. Hsu, Y.-C. Chen, Y.-G. Lin, Novel ZnO/Fe2O3 core–shell nanowires for photoelectrochemical water splitting, ACS Applied Materials & Interfaces. 7 (2015) 14157–14162.

[73] N. Chen, Y. Hu, X. Liu, J. Yang, W. Li, D. Lu, J. Fu, Y. Liang, W. Wang, A Dual-Heterojunction Cu2O/CdS/ZnO Nanotube Array Photoanode for Highly Efficient Photoelectrochemical Solar-Driven Hydrogen Production with 2.8% Efficiency, The Journal of Physical Chemistry C. 124 (2020) 21968–21977.

[74] K. Karmakar, A. Sarkar, K. Mandal, G.G. Khan, Nano-engineering of p–n CuFeO2-ZnO heterojunction photoanode with improved light absorption and charge collection for photoelectrochemical water oxidation, Nanotechnology. 28 (2017) 325401.

[75] Q. Yang, J. Du, J. Li, Y. Wu, Y. Zhou, Y. Yang, D. Yang, H. He, Thermodynamic and kinetic influence of oxygen vacancies on the solar water oxidation reaction of α-Fe2O3 photoanodes, ACS Applied Materials & Interfaces. 12 (2020) 11625–11634.

[76] L. Jia, K. Harbauer, P. Bogdanoff, I. Herrmann-Geppert, A. Ramírez, R. van de Krol, S. Fiechter, α-Fe 2 O 3 films for photoelectrochemical water oxidation–insights of key performance parameters, Journal of Materials Chemistry A. 2 (2014) 20196–20202.

[77] N.J. Cherepy, D.B. Liston, J.A. Lovejoy, H. Deng, J.Z. Zhang, Ultrafast studies of photoexcited electron dynamics in γ-and α-Fe2O3 semiconductor nanoparticles, The Journal of Physical Chemistry B. 102 (1998) 770–776.

[78] A.J. Bosman, H.J. Van Daal, Small-polaron versus band conduction in some transition-metal oxides, Advances in Physics. 19 (1970) 1–117.

[79] J.H. Kennedy, K.W. Frese Jr, Photooxidation of water at α-Fe2 O 3 electrodes, Journal of the Electrochemical Society. 125 (1978) 709.

[80] G.M. Carroll, D.R. Gamelin, Kinetic analysis of photoelectrochemical water oxidation by mesostructured Co-Pi/α-Fe 2 O 3 photoanodes, Journal of Materials Chemistry A. 4 (2016) 2986–2994.

[81] J. Leduc, Y. Goenuellue, P. Ghamgosar, S. You, J. Mouzon, H. Choi, A. Vomiero, M. Grosch, S. Mathur, Electronically-coupled phase boundaries in α-Fe2O3/Fe3O4 nanocomposite photoanodes for enhanced water oxidation, ACS Applied Nano Materials. 2 (2019) 334–342.

[82] S. Bai, H. Chu, X. Xiang, R. Luo, J. He, A. Chen, Fabricating of Fe2O3/BiVO4 heterojunction based photoanode modified with NiFe-LDH nanosheets for efficient solar water splitting, Chemical Engineering Journal. 350 (2018) 148–156.

Chapter 2 | Experimental Details

This chapter elaborates the details of the various experimental techniques employed for the fabrication of different nanostructures like nanotubes, nanorods, and nano-heterostructures etc., along with the different characterization techniques used to study the nanostructures.

2.1 Preamble

Nanomaterials are essential for converting solar energy in the chemical route due to their unique features. In the electrochemical route, an electrode is submerged into an electrolyte. The performance of the electrode is dependent mainly upon the surface area which is in contact with the electrolyte. A large electrochemically active surface area provides better electrochemical performance. For the fabrication of a PEC cell, a photoanode with a high electrochemically active surface area is necessary. Due to the high aspect ratio, nanostructured photoelectrodes like nanorods (NRs), nanotubes (NTs), nanoparticles (NPs) provide more exposed surfaces inside the electrolyte. This unique feature of nanomaterials triggered us to fabricate such nanostructured photoanodes. In the previous chapter, we already have discussed our motivation behind choosing metal oxide semiconductors as photoanode material in PEC cell applications. This chapter will discuss the in-depth experimental techniques used to fabricate ZnO NRs, Fe_2O_3 NRs, different nanoparticles, and nanoheterostructures. We will also discuss the experimental methods employed to study the structural, morphological, optical, and electrochemical properties of the synthesized photoanode material. We have synthesized ZnO NRs on the conducting fluorine-doped tin oxide (FTO) coated glass substrates by two steps aqueous chemical growth process. In the first step of ZnO NRs synthesis, a thin seed layer of ZnO is deposited over FTO by using spin-coating and a consequent post deposition annealing treatment. ZnO NRs were grown on seed layer coated FTO substrates by chemical bath deposition in the second step. We also designed nano hetero structure photoanodes by spin coating, electrodeposition, and SAILR techniques.

For the characterization purpose, we have employed X-Ray Diffraction (XRD) to investigate the crystal structure, Field Emission Scanning Electron Microscope (FESEM), and Transmission Electron Microscope (TEM) to visualize the morphology, High-Resolution Transmission Electron Microscope (HRTEM), and Selected Area Electron Diffraction (SAED) to understand the crystallinity, Energy Dispersive X-Ray (EDAX) and X-ray photoelectron spectroscopy (XPS) to investigate the constituent elements and their oxidation states of the synthesized photoanode material. The optical properties of the materials are studied with a UV-Vis absorption spectrometer and PL emission spectrofluorometer.

The electrochemical properties of the photoanode materials are investigated using techniques like linear sweep voltammetry (LSV), Chronoamperometry (I-t profile), Mott-Schottky (MS), and electrochemical impedance spectroscopy (EIS) inside a

software-controlled three-electrode electrochemical workstation (potentiostat AutoLab-30 and CHI 660E).

2.2 Synthesis of Nanostructured Materials

There are two different approaches of nanomaterials synthesis with different nanostructures: top-down and bottom-up approaches. In the top-down approach, the bulk material is sliced, cut, or broken down into its nano-sized structures or particles through external control. Mechanical cutting, etching, grinding, ball milling, photolithography, electron beam lithography are the standard techniques of nanoparticle synthesis through a top-down approach. These approaches are advantageous due to their large-scale production possibility and noninvolvement of chemical purification. However, the most significant disadvantage associated with the top-down method is the imperfection of the surface structure of synthesized nanomaterials. Impurities like stress and defects are introduced, which may have a large impact on the chemical and physical properties of the nanomaterials. Apart from that, the crystallographic damage that occurs during the fabrication of nanomaterials leads to extra challenges in device fabrication. These techniques are generally expensive, and deposition parameters are difficult to control.

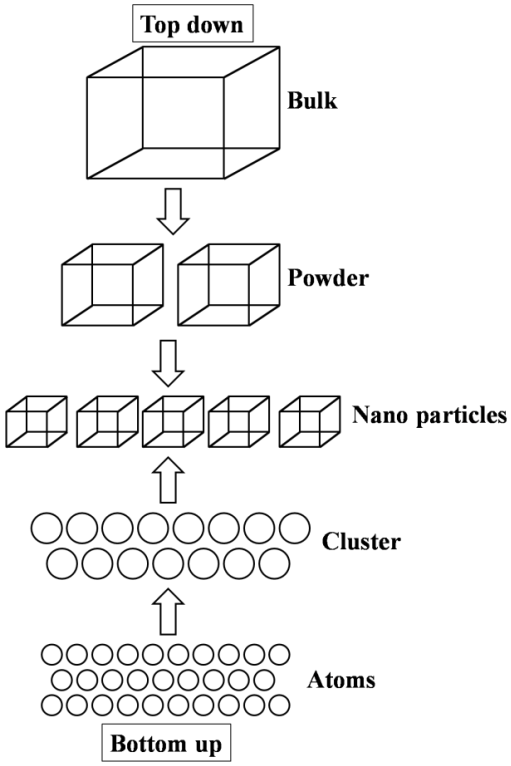

Figure 2.1: Top-down and bottom-up approaches for nanomaterial synthesis.

Bottom-up approaches are the alternative techniques in which a nanomaterial is built up from the bottom by assembling atom-by-atom, cluster-by-cluster, or molecule-by-molecule. Thermal and electron beam evaporation, laser ablation, sputtering, chemical vapor deposition, electrodeposition, photo electrodeposition, sol-gel, chemical bath deposition, solvothermal, hydrothermal synthesis, etc. are standard techniques to fabricate nanomaterials in bottom-up approaches. These techniques can generate less waste and are proven economical or cheaper. Since, in these techniques, the deposition parameters can be controlled in a better way, ultra-fine nanostructures such as nanorods, nanoparticles, and nanotubes can be synthesized with narrow size distribution and better perfection. However, most of these techniques are under lab-scale development and far away from large-scale or industrial production. Only the production of salt and nitrates in chemical industries uses such methods.

Synthesis of nanostructures of uniform size in a controlled and economical way is still a challenging task to researchers [1,2]. We will describe the commonly used synthesis techniques (spin coating, chemical bath deposition, solvothermal technique, electrodeposition) that have been used to prepare different nanostructures like nanorods, nanoparticles, etc., in the next portion of this chapter.

2.3 Synthesis Techniques

2.3.1 Spin Coating

The spin-coating technique is employed to synthesize uniform thin films of thickness ranging from micrometer to nanometer. Over a decade's spin coating techniques are used in industries to manufacture integrated circuits, data storage magnetic disc, optical mirrors, solar cells, different sensors and detectors, CD and DVD ROM, insulating layer deposition in microcircuit fabrication, anti-reflection coatings, etc. In the spin coating technique, a few drops of coating precursor are dropcast at the middle of a substrate. The substrate is rotated at a uniform rotation speed inside the spin coater. The centrifugal acceleration generated from uniform rotation cause the precursor to spread over the substrate and eventually off the substrate edge. The thickness and uniformity of the film depend on the deposition parameters like viscosity and surface tension of the solvents, nature of solids present in the processor, uniform rotation speed, rotation time, and acceleration.

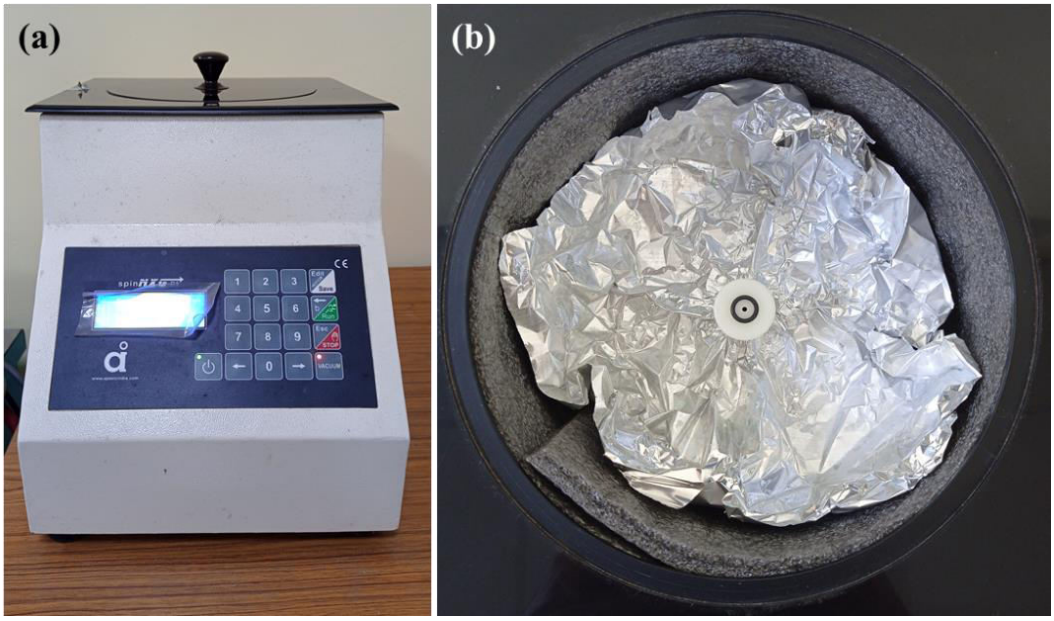

Figure 2.2: (a) front and (b) top view of a spin coater.

The first step of a typical spin coating process is the dispensing step, in which the coating precursor is deposited over the substrate. There are two types of dispense, static dispense and dynamic dispense. In the static dispense, a small amount of precursor (1-10cc) is simply deposited near the center of the substrate. The amount of precursor generally depends upon the size of the substrate and the viscosity of the solvent. A larger substrate and highly viscous solvent require a larger amount of precursor to cover the substrate with a uniform film. The other dispense step is dynamic dispense, where the substrate rotates at a low rotation speed (nearly 500 rpm). Since the rotation causes the precursor to spread over the substrate, a less amount of precursor is required to wet the surface of the substrate, and hence less waste is generated. Dynamic dispense is particularly advantageous if the substrate or the solvent of the precursor has a poor wetting ability. The next step is the spin-up state, where the substrate is accelerated to a much higher rotation speed, typically between 1500-6000 rpm. This step may last from 10 Sec to several minutes. The high rotation speed makes the precursor thin near its desired final thickness. The rotation time and speed are the thickness determining parameters of a spin coating event. Occasionally a separate drying step is required to eliminate the solvents. The required time and temperature to dry the film depends on its thickness and nature of the solvent. For thick films, this step is necessary to achieve its physical stability. Sometimes, further annealing is required to grow a proper crystal phase of the deposited material. The front and top view of a spin coater is presented in Fig. 2.2 a&b.

In our case, during the first step of ZnO NRs synthesis, we have deposited the ZnO seed layer on the conducting surface of FTO coated glass substrates through spin coating. In a typical process, a 0.5M ethanolic precursor of zinc acetate was taken as the casting fluid and drop casted on the substrate through static dispense. The spin coating process was conducted at 2000 rpm for 1 min. The spin coating event was repeated 5 times to achieve the desired thickness of the film. After each subsequent spin coating event, the film was dried under an IR lamp. Furthermore, the film was passed through a post deposition heat treatment at 350°C for 1.5 hr in a tubular furnace to get a stable oxide layer of ZnO.

2.3.2 Chemical Bath Deposition

Chemical bath deposition (CBD) is a cost-effective and straightforward technique to deposit thin films with great scope for industrial and technological purposes. CBD is relatively simple and economical than other chemical routes of thin-film fabrication like evaporation, chemical vapor deposition, molecular beam epitaxy, spray pyrolysis, etc. In a typical process, a substrate is submerged into a dilute solution of metal ions which also contains a source of hydroxide, selenite, or sulfide ions. The whole process of CBD requires only a casting precursor, a magnetic stirrer with a hot plate to get a well crystalline thin film with reasonable control over growth parameters. This process is reproducible and has an excellent scope for large-scale production. Temperature and time are the two main controlling parameters for the crystalline growth and desired size of a nanostructured film. Detailed thin film synthesis techniques through CBD are well reported in the literature [3–5].

The solid phase formation inside a precursor involves two steps, nucleation and particle growth. The solid phase particle size did not depend on the rate of these two processes. The minimum number of molecules or ions required to form a stable phase inside a solution is known as the nucleus. Nucleation formation is necessary for precipitation. In the nucleation step, clusters of molecules inside the solution undergo rapid decomposition to form particles. These particles combined to create a film of a certain thickness.

We have synthesized ZnO NRs on seed layer coated FTO substrates by the chemical bath deposition process. The detailed synthesis procedures will be discussed in the later chapter. Figure 2.3a&b shows the chemical bath deposition process conducted on a hot plate. A FESEM image of ZnO NRs deposited by chemical bath deposition is shown in Fig. 2.3c.

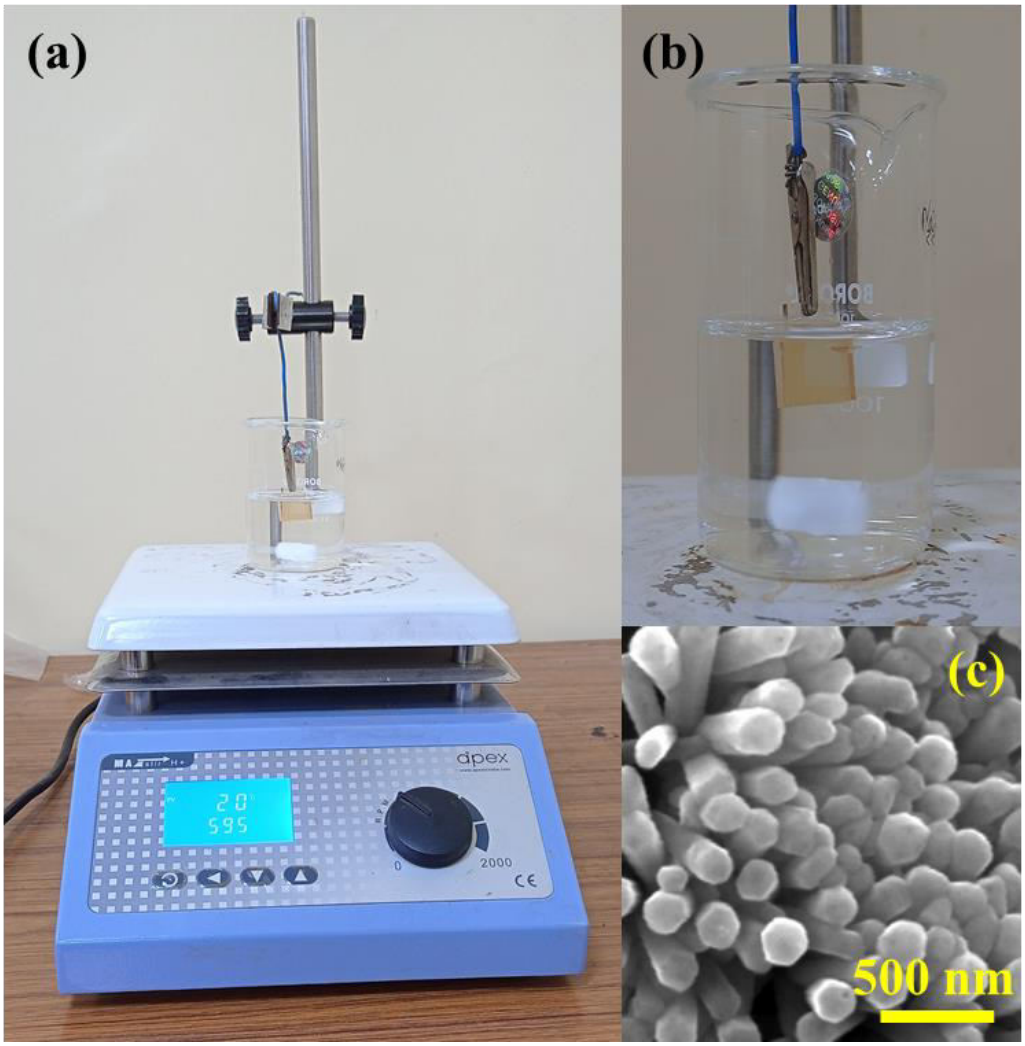

Figure 2.3: (a) Chemical bath deposition (CBD) on a hot plate, (b) CBD unit, and (c) SEM image of a ZnO NRs photoanode synthesized by CBD.

2.3.3 Electrodeposition Technique

Electrodeposition is a widely used, low-cost, and easily scalable technique for semiconductor and catalyst electrode fabrication. Apart from the two-dimensional thin films, various nanostructures like nanoparticles, nanorods, nanotubes, etc., can be grown by template-assisted or template-free electrodeposition technique. This technique is relatively economical and more straightforward than other lithography or epitaxial techniques to fabricate thin films. The whole electrodeposition process is conducted inside a software-controlled three-electrode electrochemical workstation in the presence of an electrolyte. The three-electrode unit consists of a working electrode, a reference electrode, and a counter electrode. The working electrode is the electrode on

which the thin film is deposited. The working electrode must be chemically inert so that it did not react with electrolytes during the deposition process. The working electrode should be inert under annealing conditions because sometimes post-deposition annealing step is required to ensure proper crystalline phase of the material. Different transparent conducting oxide-coated glass-like FTO, ITO is ideal for WE as it allows front and back illumination during its application. Noble metals like Au and Pt are also used as working electrodes. The counter electrode material should be inert in a wide range of applied potential. Generally, Pt and carbon-based electrodes are used as the counter electrode. Ag/AgCl and Hg/HgO are commonly used reference electrodes.

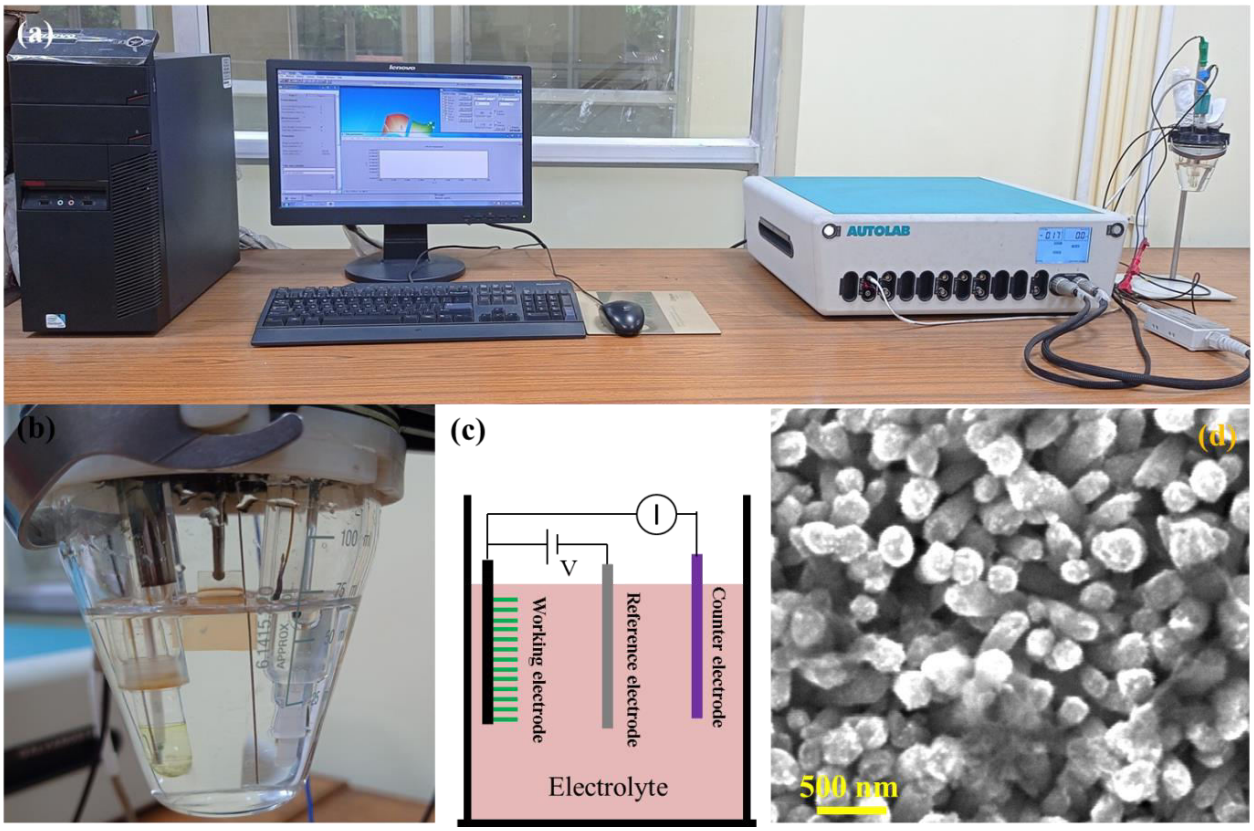

Figure 2.4: (a) Electrochemical workstation, (b) three-electrode electrochemical unit, (c) block diagram of the three-electrode electrochemical unit, and (d) FESEM image of electrodeposited $ZnCo_2O_4$ over ZnO NRs.

The plating solution is prepared using purified water because impurities can affect the nucleation and the growth of the film. Before preparing the planting solution, purified water should be purged with inert gasses like Ar or N_2 to remove the dissolved O_2 which is very active and may oxidize the metal ions and produce unwanted bulk precipitation. The planting solution is an ionic precursor that serves as a source of metal

ions. The desired concentration of metal ions is prepared by liquidized chemical species in water. Now a day's different organic compounds are used in particular electroplating processes. The WE, CE, and RE are submerged into the electrolyte to begin the deposition process. A negative potential is applied at the working electrode to pass an electric current through the circuit. The positively charged metal ions present in the precursor are reduced to metal atoms at the WE surface and deposited over the surface of the substrate to build up a film. The thickness of the film depends on the deposition voltage, current, and time of deposition. After the deposition of the film, a separate annealing process may require to get a well crystalline phase of the film.

Figure 2.4a-c shows the different parts of the electrochemical workstation. In our case, we have modified the surface of ZnO by electrodeposition of $ZnCo_2O_4$ layer with thermal annealing technique (FESEM image is shown Fig. 2.4d). The details of the deposition steps will be discussed further in a later chapter.

2.3.4 Solvothermal/Hydrothermal Synthesis

The solvothermal or hydrothermal process is defined as performing particular chemical reactions in a solvent enclosed inside sealed vessels when the temperature of the vessel is maintained near the critical point of the solvent via heating simultaneously with autogenous pressures. When water is used as a solvent, the whole process is termed the hydrothermal process. The precursor of the solvothermal reaction is taken as a homogeneous solution, suspension, or gel which contains reactants, mineralizers to control the pH, and organic and inorganic additives to facilitate control crystal morphology. Most of the solvothermal/hydrothermal reactions occur inside a sealed reactor called autoclave made of stainless steel with Teflon linings maintained at a high temperature and pressure. The morphology and size of the final product can be controlled by the reaction temperature, concentration of the solution, synthesis time, and additives. The crystallization process inside the solvent requires two steps crystal nucleation and subsequent growth. When the solubility of the solute exceeds the limit in the solution, the solution becomes supersaturated, and nucleation occurs. Then the solutes precipitate and form clusters of crystals that can grow further to form a nano-sized particle. We have synthesized metal oxide nanoparticles in the solvothermal route. The details of the synthesis procedures and synthesis parameters will be discussed further in a later chapter.

2.4 Material Characterization Techniques

2.4.1 X-ray Diffraction

X-ray diffraction is a non-destructive technique for the characterization of crystalline nanomaterials. Information like crystal structure, crystallographic orientation, phase, and other structural parameters like grain size, lattice strain, defects can be obtained from X-ray diffraction. When the surface of a crystal is illuminated with a monochromatic X-ray, atomic planes of the crystal diffract the X-ray in different directions according to their orientation. The intensity of the diffracted beam as a function of diffraction angle gives a three-dimensional idea of electron density in the crystal, from which the mean position of the atoms inside the crystal can be determined.

A typical X-ray diffractometer consists of three basic elements, an X-ray tube, a sample holder, and an X-ray detector. Inside the X-ray tube, X-rays are generated. A filament is electrically heated to produce electrons. These electrons are accelerated towards a target by applying an electric field, and the bombardment of electrons in the target material gives the X-ray. Characteristics X-rays are emitted when the bombarding electrons have sufficient energy to knock out an inner cell electron of the target material. Characteristics X-rays are used in the X-ray diffraction technique. In a practical situation, as shown in the block diagram of the X-ray diffractometer, a beam of monochromatic X-ray from the X-ray tube is allowed to fall on the surface of crystalline material. The electrons present at the different crystal planes of the material elastically diffract the incident beam, forming diffracted spherical waves. In a few specific angular directions, these diffracted waves interfere constructively following Bragg's law given by

$$2d \sin\theta = n\lambda \tag{2.1}$$

Where d is the distance between successive atomic planes, θ is the angle of diffraction, λ is the wavelength of the incident beam, and n is an integer. The diffracted intensity of X-rays is detected at the detector in different directions. The detector scans the diffracted beam through a range of 2θ angles to obtain all the constructive interference that occurs due to all possible planes of the crystalline material. Each crystal has a particular set of crystallographic planes and d-spacing. The X-ray diffraction peaks of a crystalline material allowed calculating the d spacing through Bragg's law. An unknown element or compound is identified by X-ray diffraction by comparing its diffraction pattern with standard reference patterns of the Joint Committee on Powder Diffraction Standards (JCPDS).

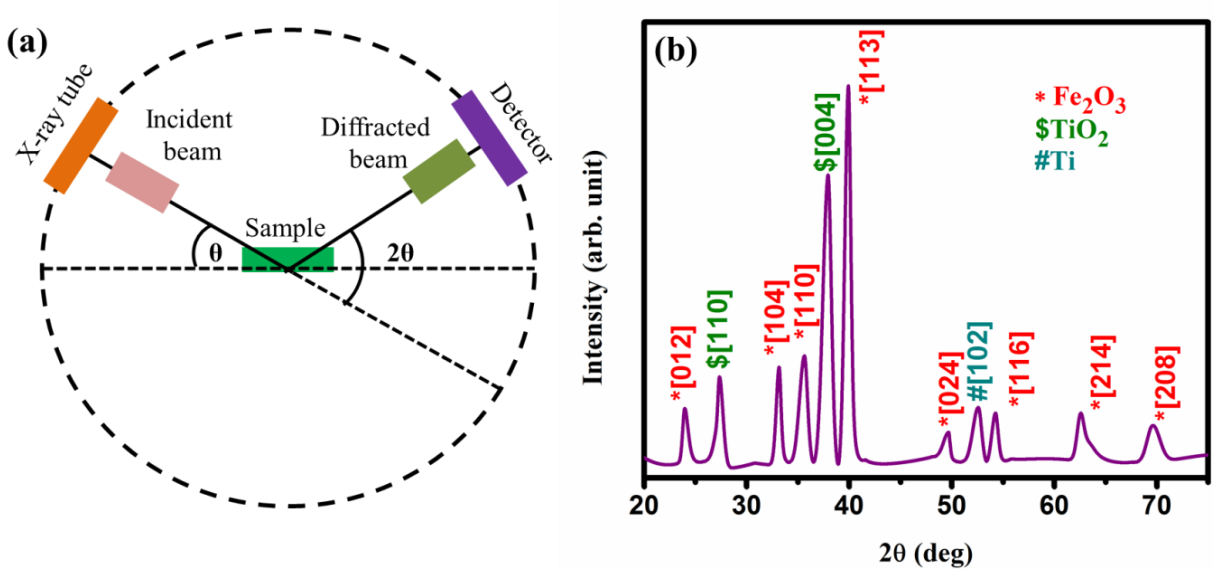

Figure 2.5: (a) Block diagram aX-ray diffractometer in θ-2θ mode and (b) XRD pattern of Fe_2O_3 synthesized over Ti substrate.

There are two basic systems of powder diffractometer, θ-θ system and θ-2θ system. In the θ-θ system, both the X-ray tube and the detector move simultaneously, but the sample holder is fixed, whereas, in the θ-2θ system, the detector moves at speed twice the rotation speed of the sample holder. In this thesis, we have used a θ-2θ system of Panalytical X-ray diffractometer. Fig. 2.5(b) shows the X-ray diffraction (XRD) pattern of Fe_2O_3.

2.4.2 Electron Microscope

A microscope that uses a highly energetic electron beam to investigate a specimen of submicron size is known as an electron microscope. Electron microscopes can provide the topographical information of the specimen, morphological information i.e., shape and size of the constituent particles of the sample, information about the constituent elements and their relative amounts in the specimen, crystallographic information, etc. The main advantage of an electron microscope over an optical microscope is its magnification power. Since the energy of an accelerated electron can be 100,000 times higher than the energy of a visible light photon, the magnification power of an electron microscope is much higher than an optical microscope. Two types of electron microscopes are well known, Transmission Electron Microscope (TEM) and Scanning Electron Microscope (SEM). The first developed microscope was a Transmission Electron Microscope (TEM) in 1931, which was used to see through the specimen [6].

Scanning Electron Microscope (SEM) was developed in 1935 and commercialized in 1965 [7].

The principles of operation of an electron microscope are such that a beam of electrons is generated from the electron gun under a high vacuum, which is accelerated towards the sample using a high electric field. The beam of an electron is collimated to a fine monochromatic beam using electric and magnetic lenses. Then the beam is allowed to interact with the sample, and after an interaction, the interacting electrons are collected and detected at the detector and converted into an image.

2.4.2.1 Scanning Electron Microscope (SEM)

In the SEM instrument, an electron beam is generated from an electron gun either by thermionic emission or cold field emission. In the case of thermionic emission, a fine tip of a tungsten filament or LaB6 crystal or a ZrO/W (Schottky emitter) is electrically heated to generate electrons. These emitted electrons are low energy electrons needed to be accelerated to a specific desired energy before entering the electron column. The electrons are accelerated and guided by an electrostatic field maintained by applying a very high voltage between the source of the electron (cathode) and the anode plate. In cold field emission, electrons are emitted from the tungsten tip at room temperature. Cold field emission is advantageous because the source emits a very high electron yield with very low chromatic aberration suitable for imaging in atomic resolution. A high vacuum ($10^{-7}$to 10^{-10} mbar) is maintained inside the SEM to avoid the burning or oxidation of the filament. Then the accelerated beam of an electron is made to pass through electromagnetic lenses, which consist of insulated copper wire windings, a soft iron cast, and a pole piece. An induced magnetic field is produced by passing an electrical current through the copper winding, and the field is guided by the pole pieces of the lens. The accelerated electrons are deflected by the magnetic field and take a circular path while passing through the lenses. The beam of electron is deflected horizontally and vertically by the search coil and magnetic lenses to scan the whole surface of a specimen. The focal width of the beam can be changed by changing the magnetic field strength inside the lens. SEM works in a voltage range of 2 to 50KV with a beam diameter ranging between 5nm to a few micrometers. Finally, the beam of an electron is allowed to interact with the sample surface. Energy dissipation of the primary electrons at the sample surface produces different signals like secondary electrons, auger electrons, characteristic X-rays, backscattered electrons, cathodoluminescence. The secondary and backscattered electrons are collected and distinguished by the detectors according to their energy and construct the SEM images

using these two signals through the imaging system. Since the probing electron beam has a narrow beam diameter, SEM micrographs provide in-depth, three-dimensional information of the sample surface with a large-scale

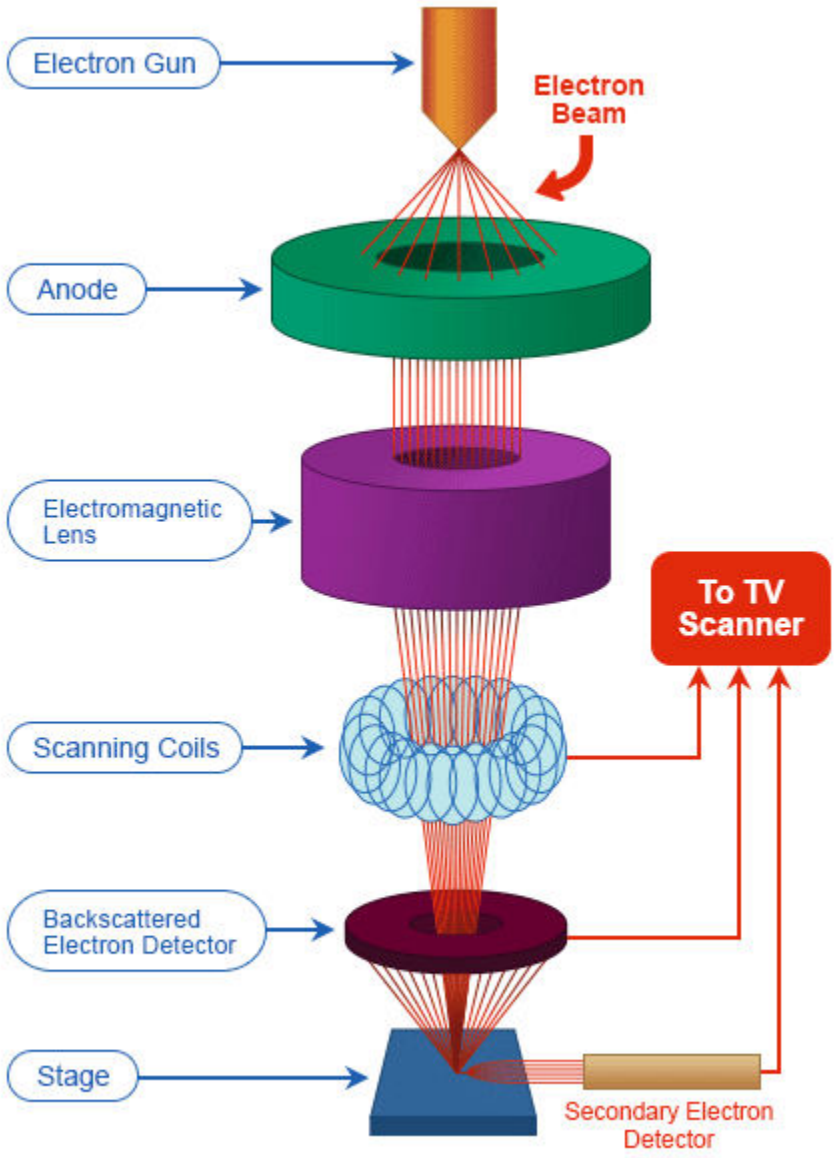

Figure 2.6: Block diagram of an SEM unit.

resolution. The elemental analysis of the specimen is done by distinguishing the energy of the characteristics X-ray signal. When the primary electron beam collides with the orbital electrons of the atoms of specimen characteristics, an X-ray is emitted. Each element has different characteristics of X-ray energy. The constituent elements of the

specimen are identified by identifying the energy of the characteristics X-ray coming out of it during the SEM process. The process is known as energy dispersive analysis of X-ray (EDAX). Figure 2.7 shows the FESEM image of $ZnFe_2O_4$ NRs deposited on an FTO substrate.

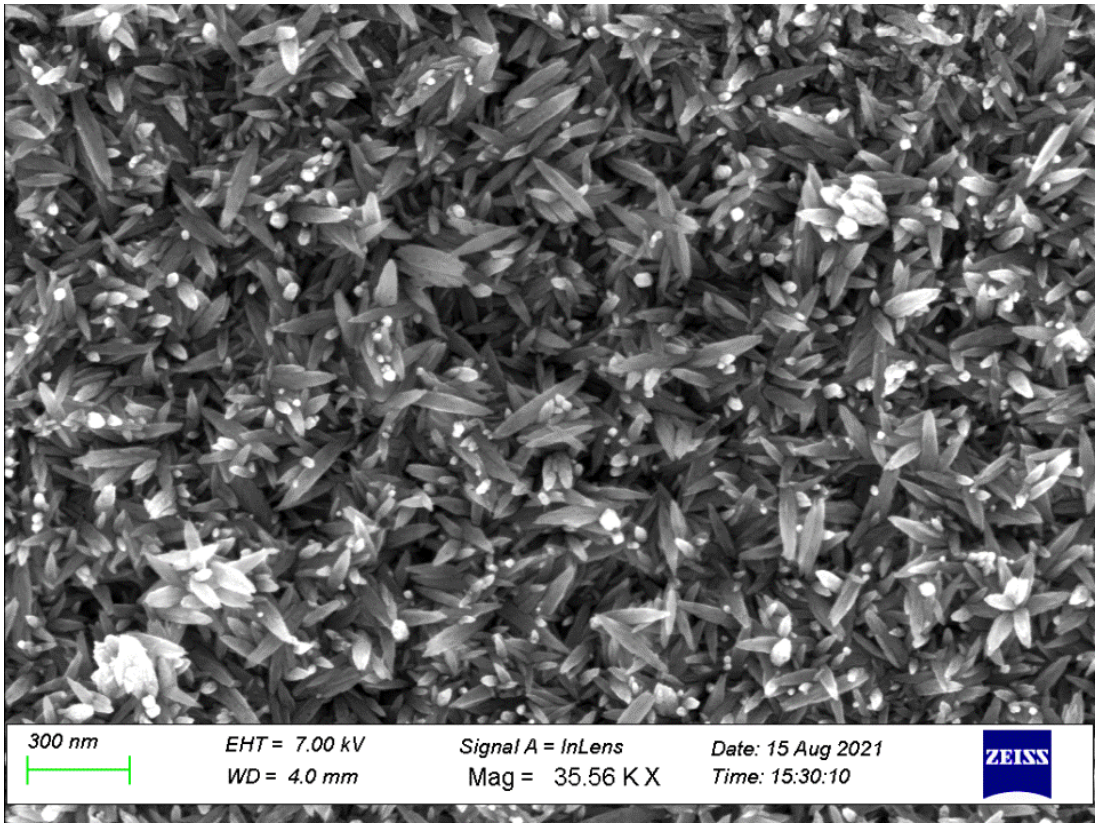

Figure 2.7: FESEM image of $ZnFe_2O_4$ NRs deposited on an FTO substrate.

2.4.2.2 Transmission Electron Microscope (TEM)

In transmission electron microscopy, the beam of the transmitted electron after interacting with an ultra-thin specimen is used in the imaging technique. In comparison to SEM, the beam of electrons is accelerated to a relatively higher voltage range (80-300 kV). Such high voltage is required to make the beam pass through a specimen of ~1µm thickness. In normal operating conditions, electrons of 200-300 kV energy are typically used in the imaging process of a sample. However, for light elements, relatively low energy (less than 100kV) electron beam is required in the imaging process to avoid sample damage. As discussed in the previous section, when the high-energy electron beam interacts with the specimen, several different kinds of signals are emitted from the sample. Among those, two different types of signals are elastically scattered electrons (diffracted beam) and unscattered electrons (transmitted beam), are used in the imaging

process. The intensity of the transmitted electron beam is inversely proportional to the thickness of the sample. A specimen of higher thickness will be able to transmit fewer transmitted electrons (unscattered electrons) and will appear darker in the image, whereas a thinner specimen will be allow a more significant number of unscattered electrons to pass through it, will appear lighter in the image. In this technique, the dark and light contrast of the image of a sample is obtained. This operational mode of TEM is known as bright fringe imaging.

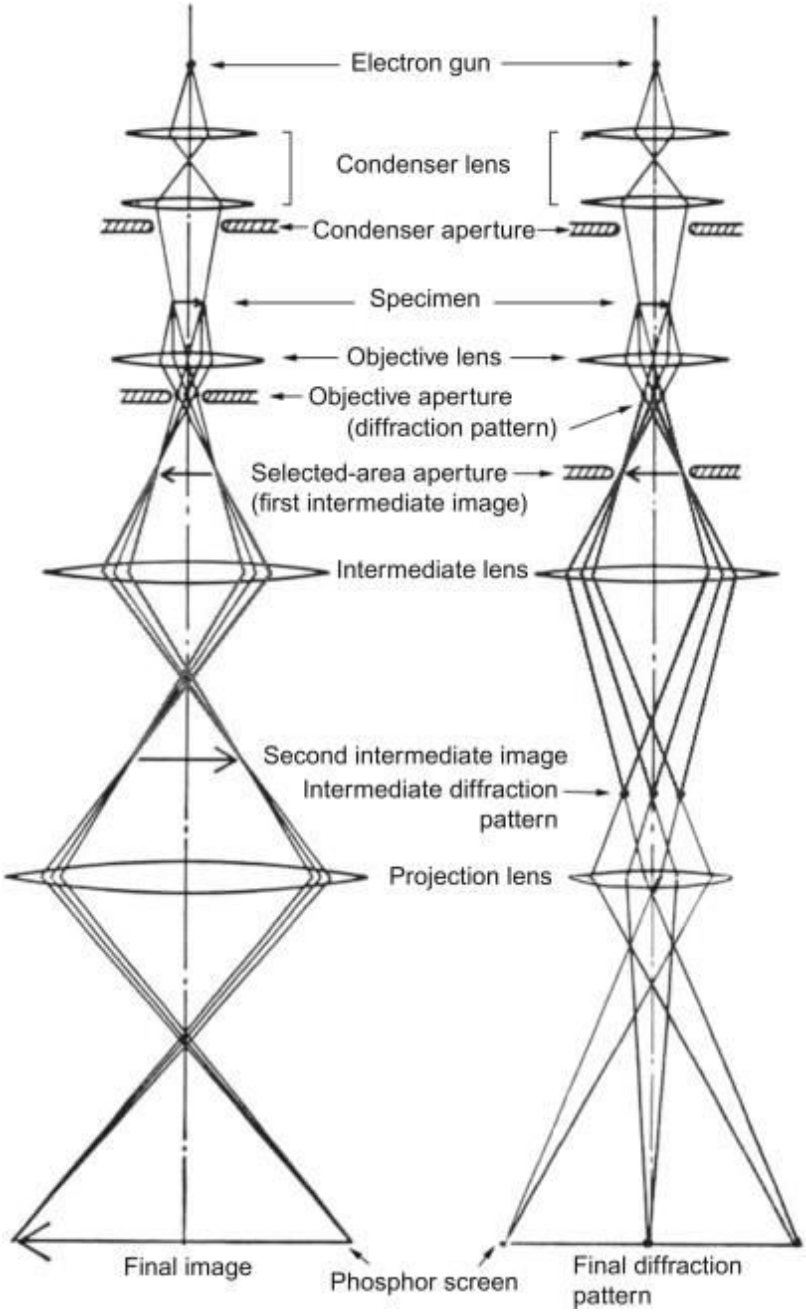

Figure 2.8: Block diagram of a TEM unit. [8].

The other mode is the electron diffraction mode. When the electron beam interacts with a crystalline sample, many electrons suffer Bragg's scattering at the different parallel atomic planes of the crystal. These scattered electrons are collected using magnetic lenses to form a spot pattern or fringe pattern according to the atomic spacing of the crystalline sample. This pattern provides information about the crystallinity, phase, crystal plan orientation, atomic arrangements of the sample. High-resolution transmission electron microscopy (HRTEM) is a class of electron diffraction imaging where a resolution up to 0.2nm can be achieved, which is very efficient for observing lattice fringes of the crystalline specimen. In the energy filtrated transmission electron microscopy (EFTEM) mode, electrons having particular energies are used for imaging and provides information about the constituent elements of the material under investigation. Another mode of imaging is electron energy loss spectroscopy (EELS). In this technique, a specimen is illuminated by electrons with a known narrow range of kinetic energy, which suffers inelastic scattering at the sample with some energy loss. An electron spectrometer measures the loss of energy and represents in terms of what caused the energy loss. Figure 2.9a-c shows a typical TEM, HRTEM, and SAED micrograph of $ZnFe_2O_4/CeO_x$ heterojunction.

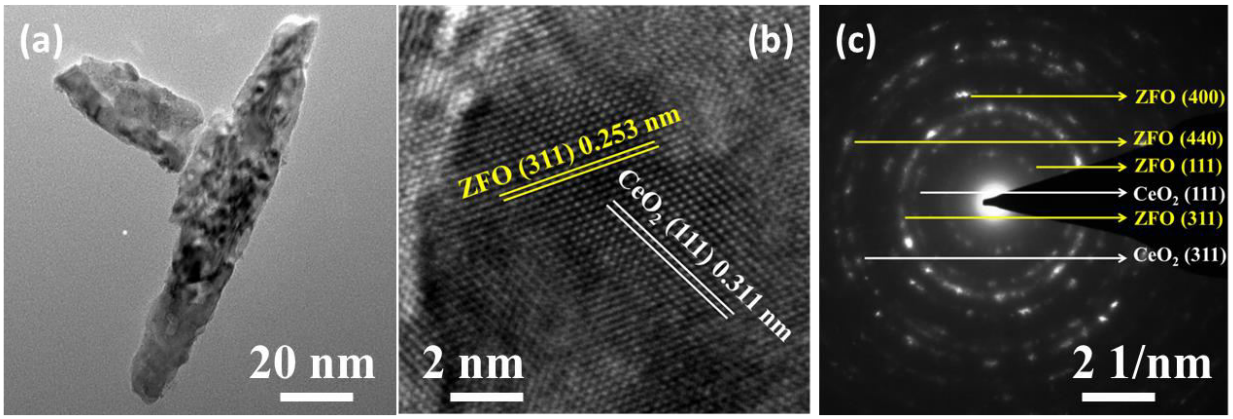

Figure 2.9: (a) TEM, (b) HRTEM and (c) SAED image of $ZnFe_2O_4/CeO_x$ heterojunction.

2.4.3 X-Ray Photoelectron Spectroscopy (XPS)

X-ray photoelectron spectroscopy is a quantitative spectroscopic technique to investigate the elemental composition, chemical state, chemical formula, and electronic state of the constituent elements of the material under observation. In the XPS technique, a sample is illuminated with a beam of energetic X-rays, and then the number of expelled electrons and their kinetic energy are measured. If the energy of the incident X-ray photon is hv then, the binding energy of the emitted electron is given by the Ernest Rutherford equation as given below,

$$BE = h\nu - KE - \phi_{spec} \quad (2.2)$$

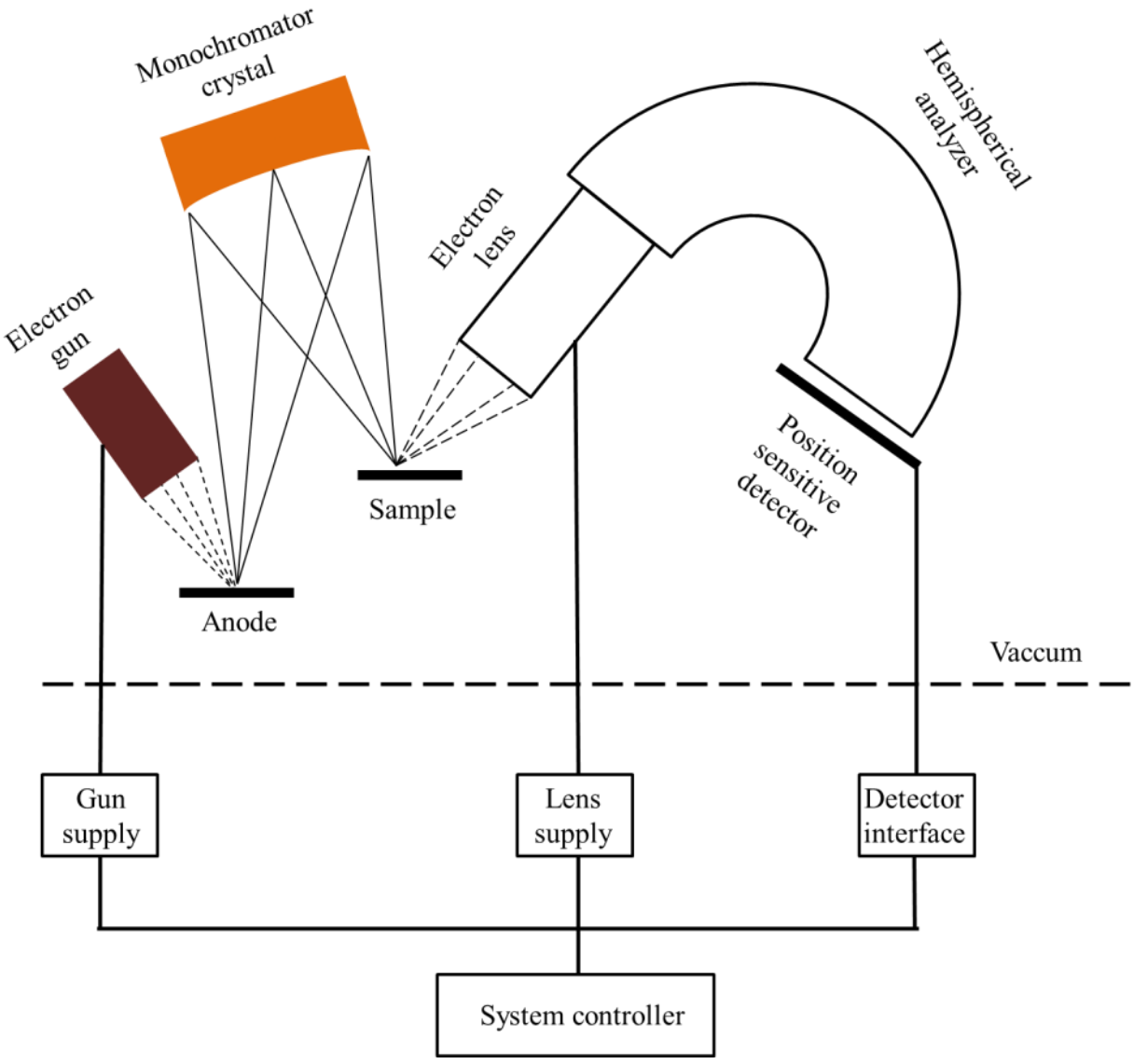

Figure 2.10: Block diagram of different parts of an XPS unit.

Where KE is the kinetic energy of the emitted photon and ϕ_{spec} is the spectroscopic workfunction of the spectrometer. The kinetic energy of the emitted electrons provides information about the constituent elements of the sample. The intensity of the expelled electron gives an idea about the quantity of the elements present in the material. Each element has a unique characteristic peak of atomic orbital in the XPS spectrum. Inside an XPS instrument, the electron detector is placed 1m away from the illuminated sample. XPS is performed under ultra-high vacuum (UHV) conditions.

2.4.4 Ultra Violate (UV) and Visible (Vis) Spectroscopy

Spectroscopy is a technique that deals with the interaction of the electromagnetic wave with the material. Ultra violate and visible lights are associated with the transitions between electronic energy levels of ions, atoms, or molecules. In our projected thesis, we have worked with different types of photoanodes to capture solar radiation and use it to split water by generating solar photovoltage. In the case of solar energy conversion with a semiconductor material, the primary requirement is that the semiconductor should have high absorbance in the solar broadband spectrum region. We have investigated the absorption behavior of our synthesized photoanode materials with UV-Vis spectroscopy. The basic instrumentation of a UV Vis spectrometer (Fig. 2.11) is a light source, a monochromator (prism or grating), a sample holder, and a detector. When a beam of monochromatic light from the source after passing through the monochromator falls on the sample, a fraction of it is transmitted through the sample. The intensity of the transmitted beam is predicted by Beer-Lambert law

$$I = I_0 e^{-\sigma(N_1 - N_2)l} \tag{2.3}$$

Where I_0 is the incident beam intensity, σ is the absorption cross-section, l is the optical path length through the sample, and N_1 and N_2 are the population densities at the initial and final energy state, respectively. The Beer-Lambert equation can be written in the form of Beer's law as

$$A = \varepsilon cl = -log_{10}\left(\frac{I}{I_0}\right) \tag{2.4}$$

Here, A is the absorption, ε is the molar absorptivity coefficient, and l is the material concentration. The absorption coefficient of a material is determined as the normalization of absorbance with respect to the optical path length following the equation

$$\alpha\ (cm^{-1}) = \frac{\ln(10)XA}{l\ (cm)} \tag{2.5}$$

In a practical UV-Vis experiment of material, we get a plot of absorbance of the material against the wavelength of light. Tauc plot and Kubelka-Munk plot are used to determine the optical band-gap of the material under investigation. In the Tauc method, the extrapolated baseline of $(\alpha h\nu)^n$ vs. hν plot gives the optical band-gap of the material. The value of n is taken ½ for indirect band-gap material, and 2 for direct band-gap material, and hν is the energy of light. The Kubelka-Munk model is suitable for diffuse reflectance measurements and is associated with the calculation of Kubelka-Munk function (f(R)) as,

$$f(R) = \frac{(1-R)^2}{2R} = \frac{\alpha}{s} \quad (2.6)$$

Where R = e^{-A}, s is the scattering coefficient. Generally, s is wavelength-independent which makes *f*(r) directly proportional to α.

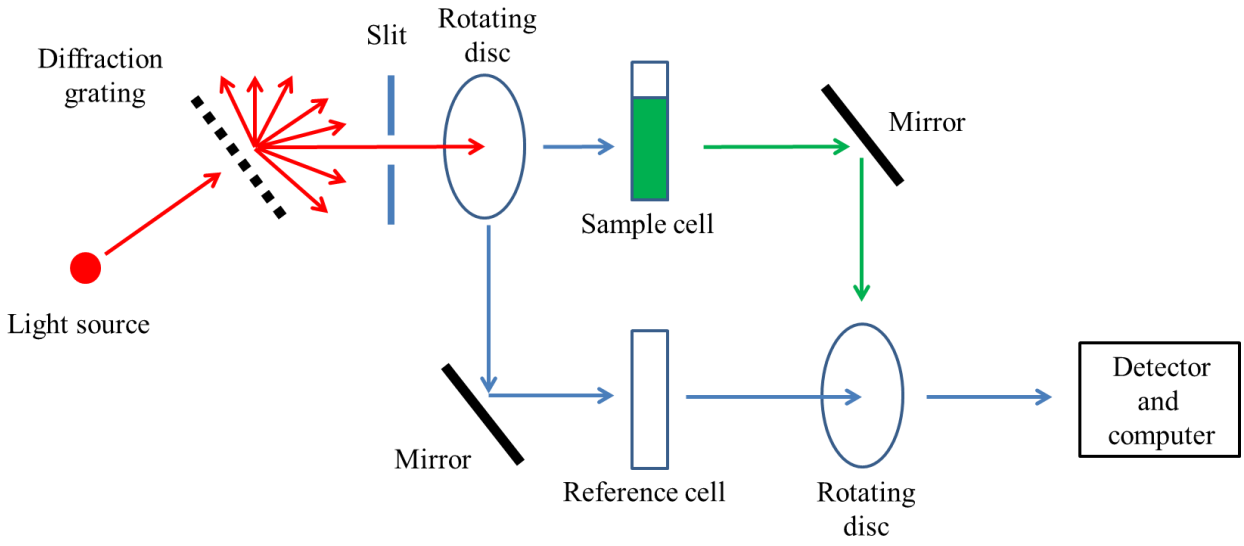

Figure 2.11: Block diagram of UV Vis spectrophotometer.

2.5.2 Photoluminescence (PL) Spectroscopy

Photoluminescence (PL) spectroscopy is a technique to probe the electronic structure of a material in a contactless and non-destructive path. The PL spectroscopy is conducted with an instrument known as a spectrofluorometer. A typical spectrofluorometer consists of a source of illumination, an excitation monochromator, a sample cell, slits, an emission monochromator, a detector, an amplifier, and a recorder, as shown in Fig. 2.12. A 150W Xenon arc lamp (Ozone free) is used as the source of illumination. A diamond-turned elliptical mirror is used to accumulate the rays of light from the lamp and focus it on the entrance slit of the excitation monochromator. In both the monochromators i,e., excitation and emission monochromator, the reflective optics technique is used to avoid spherical aberrations and optical rediffraction as well as to have a great spectrum resolution. Reflection Gratings are used in the monochromators. Two slits are used at the entrance and exit point of the sample cell. The slit width can control the resolution and the intensity of the emission spectrum. When the slit width is high more light is falling on the sample as well as the detector; there will be highly intense emission spectra, but the resolution of the spectrum will be low, and when the slit width is low, we will have a high resolution at the cost of the intensity of the emission spectrum. The

sample compartment provides several options for the attachment of solid and liquid samples. Two types of detectors are used in a spectrofluorometer which is signal and reference detector. The signal detector counts the photon coming from the emission monochromator. An R928P photomultiplier tube is used for this proposal.

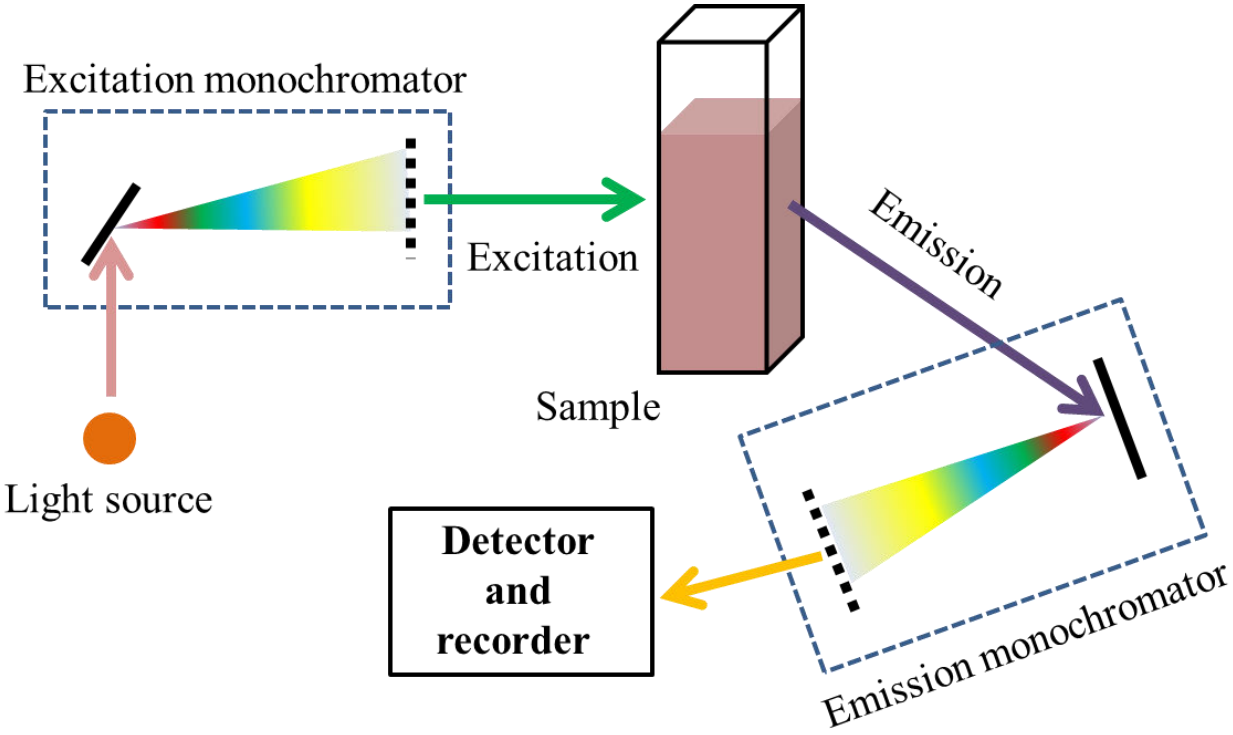

Figure 2.12: Block diagram of PL spectrophotometer.

The reference detector monitors the source of illumination for wavelength correction. Silicon photodiodes are used as reference detector. When the sample under investigation is illuminated with monochromatic light from the excitation monochromator known as excitation, the electrons in the material are allowed to occupy higher energy levels (excited state) by absorbing the energy of incident photons. These excited electrons can return to the ground state in two ways, one is by releasing extra energy in the form of light known as radiative transition, and the other is by releasing heat known as nonradiative transitions. In the case of radiative transition, the energy of an emitted photon is the same as the energy difference between the two electronic states involved in the transition. This radiative transition is called photoluminescent. PL spectroscopy can be used to determine the bandgap of a material, identify defects and impurities, and recombination process.

2.6 Electrochemical Characterization Techniques

In this proposed thesis, we are interested in analyzing the electrochemical behaviors of different kinds of photoanodes inside an electrolyte in the presence and absence of illumination. Our samples are electrochemically characterized in a software-controlled three-electrode electrochemical workstation using a potentiostat (CHI 660E). Inside the electrochemical cell, the as-synthesized photoanodes are used as working electrodes, an Ag/AgCl electrode as a reference electrode, a platinum wire as the counter electrode, and a 0.5M Na_2SO_4 solution as an electrolyte. Different electrochemical techniques like linear sweep voltammetry (LSV), chronoamperometry (i-T), electrochemical impedance spectroscopy (EIS), and Mott-Schottky (MS) measurements were employed for the characterization of photoanodes. A solar simulator (AM 1.5G, LCS-100, Newport, Model 94011A) is used as a source of illumination.

2.6.1 Electrochemical Impedance Spectroscopy (EIS)

Electrochemical impedance spectroscopy is a highly sensitive, complex, and non-destructive technique to characterize the frequency-dependent electrical response of a chemical system. Initially, this technique was widely used to measure the double-layer capacitance. Modern-day research is employing EIS to investigate different electrode processes and complex interfaces. A practical EIS experiment is conducted at open circuit conditions by applying an alternative potential of small amplitude (5 ~ 10 mV) in a wide range of frequencies (generally 0.01 to 100 kHz).

The impedance behavior of a real photoelectrode system can be connected to different idealized equivalent circuits through EIS analysis. The equivalent circuits consist of elements like resistors, capacitors, constant phase elements, etc., with their series and parallel combinations. The equivalent circuit provides information like charge transfer resistance, equivalent source resistance, trap capacitance, and other important parameters of the electrode-electrolyte system. The impedance behavior of an ideal and real electrode is shown in the form of a Nyquist plot (Fig. 2.13). The Nyquist plot of a real system consists of a semicircular part and a real part at high frequency and low-frequency regions, respectively. A semicircle with a larger arc indicates higher charge transfer resistance at the electrode-electrolyte interface due to the poor electrical conductivity of the material. The total impedance (Z) has a real part (Z′) and an imaginary part (Z′′) as $Z = Z' + j\,Z''$. The imaginary part of impedance data is used to calculate the surface capacitance of an electrode as

$$C = -\frac{1}{\omega Z''} \tag{2.7}$$

Where ω is the angular frequency.

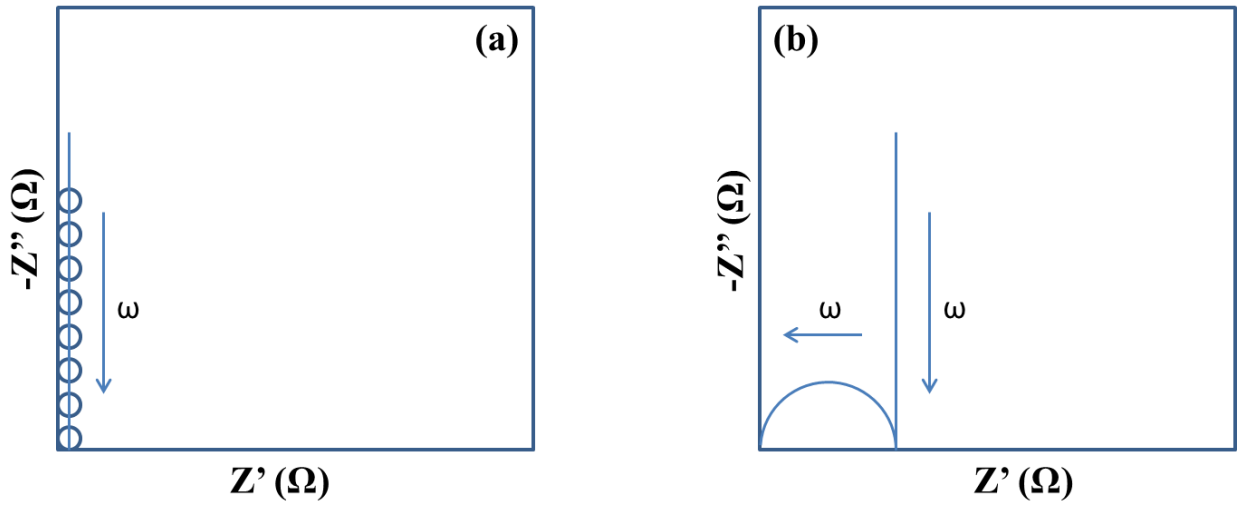

Figure 2.13: Nyquist plot: Impedance spectra of an ideal and a real capacitor electrode.

Bibliography

[1] H. Hahn, Gas phase synthesis of nanocrystalline materials, Nanostructured Materials. 9 (1997) 3–12.

[2] H. Hahn, Unique features and properties of nanostructured materials, Advanced Engineering Materials. 5 (2003) 277–284.

[3] R.S. Mane, C.D. Lokhande, Chemical deposition method for metal chalcogenide thin films, Materials Chemistry and Physics. 65 (2000) 1–31.

[4] S.M. Pawar, B.S. Pawar, J.H. Kim, O.-S. Joo, C.D. Lokhande, Recent status of chemical bath deposited metal chalcogenide and metal oxide thin films, Current Applied Physics. 11 (2011) 117–161.

[5] B.A. Ezekoye, P.O. Offor, V.A. Ezekoye, F.I. Ezema, Chemical bath deposition technique of thin films: a review, International Journal of Scientific Research. 2 (2013) 452–456.

[6] E. Ruska, Ernst ruska autobiography, Nobel Foundation. (1986).

[7] M. Knoll, Aufladepotentiel und sekundäremission elektronenbestrahlter körper, Zeitschrift Für Technische Physik. 16 (1935) 467–475.

[8] F. Bergaya, G. Lagaly, Handbook of clay science, Newnes, 2013.

Chapter 3

Solar Water Splitting with ZnO/MoO_3 Based n/n Type Core Shell Heterojunction Photoanodes

Photoelectrochemical (PEC) properties of ZnO and ZnO/MoO_3 photoanodes have been presented in this chapter. The underlying role of a UV active MoO_3 overlayer in enhancing the PEC water splitting activity of ZnO nanorods (NRs) based photoanodes has been discussed in this chapter.

A part of the content of this chapter has been published in the journal of Journal of Alloys and Compounds [1] and is reproduced herein with permission from Elsevier.

3.1Preamble

The capture of enormous solar energy in the form of the chemical bond, i.e., the next-generation energy carrier hydrogen, is accelerating because of the growing demand for renewable and sustainable energy [2,3]. Since its first invention by Fujishima and Honda in 1972 [4], hydrogen generation technology, based on water splitting in a photoelectrochemical (PEC) cell with significantly engineered solar energy harvesting materials, has gained tremendous importance as it reduces the enormous use of fossil fuels [2–5]. However, there are several challenges to fabricate ideal semiconducting material with certain crucial characteristics such as low cost, suitable band gap, effective separation of charge carrier with reduced electron-hole pair recombination, higher charge carrier mobility, and fast surface reaction kinetics [2,5,6]. Otherwise, these will limit the large-scale application of the materials in the PEC technology [2]. A single semiconductor material cannot harvest a pronounced portion of solar light with reduced charge carrier recombination and transportation to a greater extent [2]. In this backdrop, enormous utilization of metal oxide semiconductors are in the forefront of research to alleviate all the limitations [6–8].

Moreover, the transition metal oxides have a positive role in water-splitting activity due to spontaneously created oxygen vacancies, which develop mid-band-gap defect states, acting as light-absorbing donor sites also the multiple oxidation states leading to excellent photocatalytic properties [6,8–10]. Significant reports are available on water splitting based on earth-abundant transition metal oxide semiconductors such as TiO_2, ZnO, Fe_2O_3, WO_3 where the authors claimed the improvement in photocatalytic activity of nanostructures by minimizing all the limitations mentioned above [11–19]. Still extensive research is needed to employ the materials on an industrial scale.

Among all transition metal oxides semiconductors, ZnO is extensively investigated because of its favorable band edge position for water oxidation and reduction, remarkable electrochemical activity, and low-cost earth-abundant material [20]. However, the band-gap (3.26 eV) positioned in the UV region (only 4% of solar spectrum) limits its light-harvesting operation. Though oxygen vacancies [6,7,21] in ZnO are very effective in harvesting visible part of the solar spectrum, high carrier recombination due to poor charge separation efficiency always inhibit a large amount of photoconversion [22,23]. Therefore, the strategy to fabricate additional oxide semiconductor material over ZnO i.e.; the semiconductor junction architecture, can mitigate those limitations up to a large extent with improved photocarrier generation and electron-hole separation by suppressing carrier recombination, which leads to higher photoconversion efficiency and improved surface reaction kinetics. Therefore, research related to the semiconductor junction photocatalysts materials has also been

proliferating rapidly to pledge a suitable platform for water splitting, reported in a few reviews [24–26] where authors explored the strategies employed in the junction architecture.

On the other hand, MoO_3, with an orthorhombic crystal structure and optical band gap ~ 3.1 eV, has been extensively studied because of its layered structure, high electrochemical and catalytic properties [27,28]. It exhibits strong intralayer covalent bonding but displays weak Vander Waals interlayer coupling. The best part of MoO_3 is that water molecules have an affinity to intercalate in between MoO_3 layers, which results in the expansion of interlayer distances weakening the bond and enhancing the catalytically active sites [27]. Apart from that, MoO_3 also acts as a hole transporting material and is highly stable in aqueous environment [29].

Following the above advantages, we have deposited MoO_3 nanolayer over ZnO nanorods core by a simple and scalable spin coating method, and the resultant heterostructure acts as n-n type junction. Although several reports on several kinds of heterojunction [30–34] and their photon harvesting properties, there are still no reports on the n-n heterojunction of ZnO/MoO_3 for water reduction. Herein, we have investigated the photoelectrochemical behavior of ZnO/MoO_3 core-shell n-n heterojunction. We also optimized the thickness of the MoO_3 overlayer by maximizing the photon harvesting efficiency with low carrier recombination and good transportation through the ZnO core materials.

3.2 Experimental Section

3.2.1 Synthesis of ZnO Nanorods (NRs)

ZnO nanorods (NRs) on fluorine-doped tin oxide (FTO) substrate were grown in two steps aqueous chemical growth process. In the first step, a seed layer of ZnO was deposited over FTO substrate by spin coating method with a speed of 2000 rpm for 1 minute, which was repeated 5 times with 0.1M ethanolic solution of zinc acetate. Each successive spin-coated layer was dried under an IR lamp for 1 minute, and finally, it was annealed at 350°C for 2 hours. After that, the seed layer was further cleaned in ethanol for a few minutes. In the second step, ZnO NRs were grown over the seed layer by dipping the seed layer coated substrate in an aqueous solution of zinc acetate and hexamethylenetetramine (1: 1) for 2 hours. After ZnO NRs deposition, residuals are washed out by distilled water and ethanol.

3.2.2 Fabrication of n-n Core-Shell Heterojunction

The oxide layer of molybdenum (MoO_3) was deposited over the ZnO NRs array with different thicknesses by repeated spin coating method with 2000 rpm for 1 minute each time, taking a precursor solution of ammonium tetrathiomolybdate (0.1M) dissolved in N,N-dimethyl formamide. The spin coating event was repeated 2, 5, 7, 9, and 11 times and the respective samples were marked as 2T, 5T, 7T, 9T, and 11T, respectively. Finally the samples were annealed at 400°C for one hour in O_2 atmosphere to get the stable oxide layer of MoO_3 over ZnO NRs, resulting in a core-shell n/n type heterojunction. The sample preparation steps are shown in Fig.3.1.

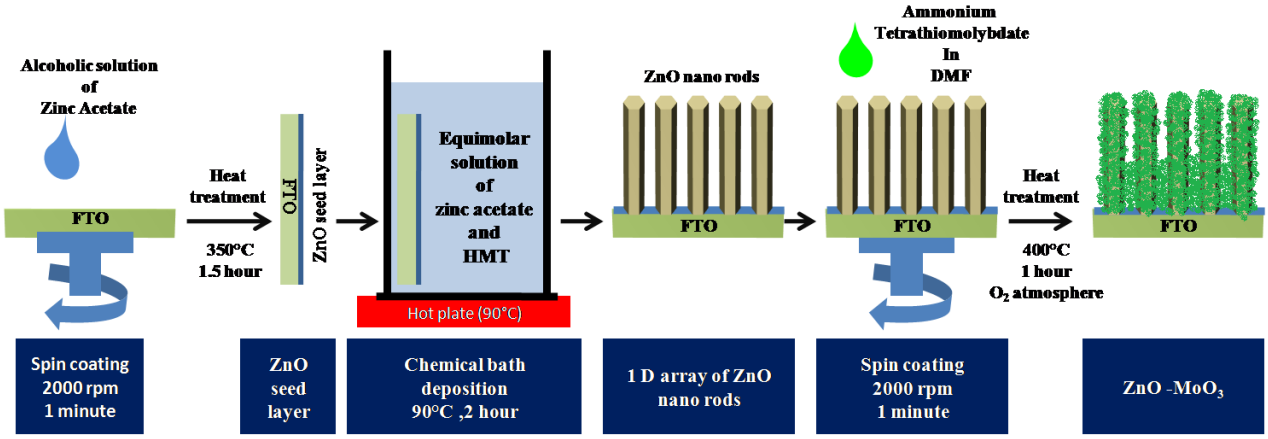

Figure 3.1: The steps involved during synthesis of ZnO/MoO_3 core-shell heterostructure.

3.2.3 Material Characterization

The surface morphology and structure of ZnO NRs and ZnO/MoO_3 based photoanodes were characterized by field emission scanning electron microscope (FEI Quanta-200 Mark-2) and transmission electron microscopy (JEOL JEM 2100). The elemental composition was confirmed with energy-dispersive X-ray spectroscopy (EDS, Oxford Instruments, and EDAX) equipped with the FESEM. The crystal structure of the materials was investigated with grazing incidence X-ray diffraction pattern (GIXRD, Panalytical X'Pert Pro diffractometer) using the Cu K_α line (λ= 1.54 Å) with a step size of 0.15°. The ionic state of the materials and also the elemental compositions of the materials have been confirmed with X-ray photoelectron spectroscopy analysis. The optical properties of the materials were determined with the UV−Vis−NIR absorption spectroscopy (PerkinElmerLambda 1050 UV/Vis spectrometer) and photoluminescence spectroscopy (PL, Horiba, FluoroLog-3).

3.2.4 Photoelectrochemical (PEC) Studies

The PEC properties of ZnO NRs and ZnO/MoO_3 based photoanodes were investigated in detail. For this proposal, a visible light source (Visible light, 10 mW cm^{-2}) was used to perform the linear sweep voltammetry (LSV), i−t amperometry, Mott−Schottky (MS), and electrochemical impedance spectroscopy (EIS) studies. Electrochemical properties were investigated with the help of a software-controlled three-electrode electrochemical workstation (CHI660E, CH Instruments) where ZnO and ZnO/MoO_3 over FTO based photoanodes were used as the working electrode, a platinum wire as the counter electrode, and Ag/AgCl as the reference electrode. A 0.5M aqueous solution of Na_2SO_4 (pH 6.4) was used as electrolyte to investigate the electrochemical characteristics of different photoanodes. LSV was performed in a potential (vs. Ag/AgCl) window of 1.5V to 0V both in dark and light and also in continuous light on/off conditions. I-t amperometry was performed at a 0.6 V potential against Ag/AgCl. To get an idea about the band position of the semiconductor heterostructure, Mott−Schottky measurement was conducted at a frequency of 1 KHz. To investigate the charge transfer process (from semiconductor surface to electrolyte as well as FTO surface), electrochemical impedance spectroscopy (EIS) within a frequency range 1 MHz to 0.1 Hz was performed in the frequency response analyzer mode with an AC perturbation of 5 mV.

3.3 Result and Discussions

3.3.1 Morphological and Structural Analysis

Figure 3.2a-g shows the field emission scanning electron microscopy (FESEM) top view images of the as-designed 1D ZnO NRs and different ZnO/MoO_3, respectively. Hexagonal morphology of the as-prepared ZnO nanostructure is visible (Fig. 3.2a) with a diameter ~70-80 nm. ZnO NRs are coated with MoO_3 which made the NRs heads a little deformed (Fig. 3.2b-g). The cross-sectional view (Fig.3.2h) shows the length of ZnO NRs to be ~ 450 nm over a ~50 nm seed layer. The nine times spin-coated ZnO/MoO_3 had an overlayer thickness of ~ 120 nm (average ~100 nm). EDAX spectrum (Fig. 3.3a) shows the presence of zinc, oxygen, and molybdenum in the nanostructure. The crystal structure of the materials was investigated by GIXRD, which is shown in Fig. 3.3b. The XRD pattern indicates that pristine ZnO NRs exhibit polycrystalline behavior with a preferential growth direction along (002) which confirms the hexagonal wurtzite structure having $P6_3mc$ space group (JCPDS #89-1397).

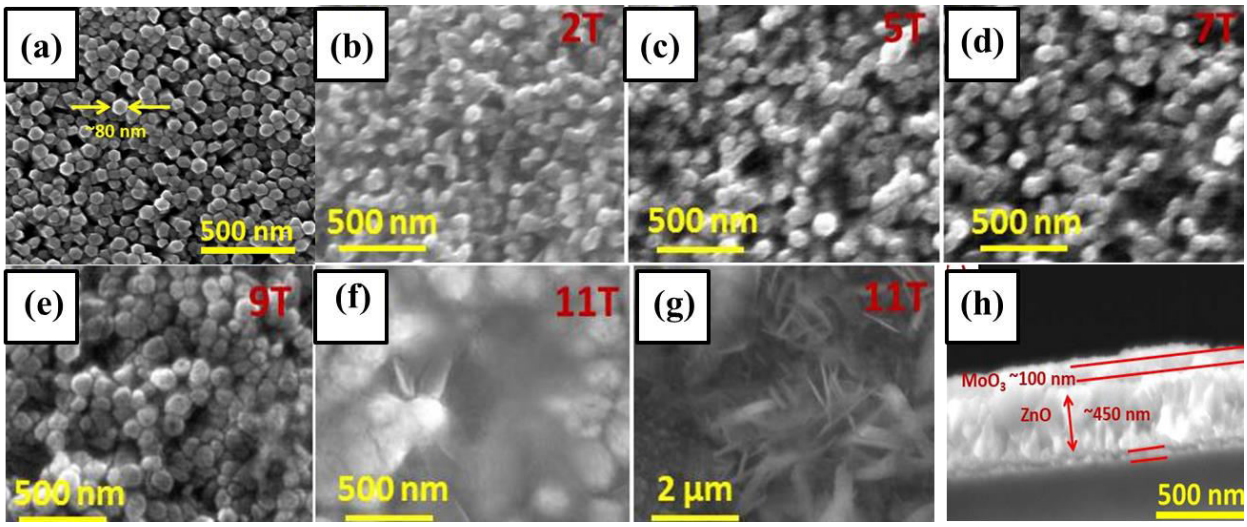

Figure 3.2: FESEM image of (a) ZnO, (b) 2T, (c) 5T, (d) 7T, (e) 9T and (f)-(g) 11T ZnO/MoO_3 samples. (h) cross sectional FESEM image of ZnO/MoO_3 9T sample.

It also confirms the crystalline behavior of the MoO_3 spin-coated layer, which has a preferential growth direction along (111) with space group Pnma (reference code 00-001-0706, X'PertHighScore Plus).

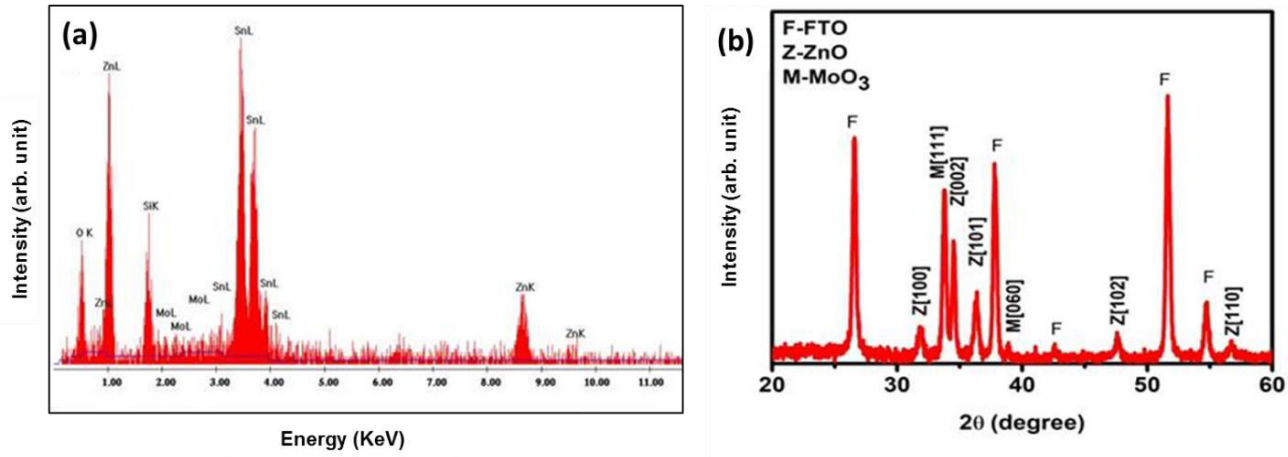

Figure 3.3: (a) EDAX spectrum of ZnO/MoO_3 and (b) GIXRD pattern of ZnO/MoO_3 nanoheterostructure.

Figure 3.4a shows the transmission electron microscopy (TEM) image of a mechanically broken part of ZnO/MoO_3, which confirms the rod-like behavior of ZnO along with MoO_3 layer over it. From high-resolution transmission electron microscopy (HRTEM) image (Fig. 3.4b), the interplanar spacing ~0.26 and ~0.266 nm are corresponding to the ZnO (002) and MoO_3 (111) lattice planes. The selected area electron diffraction (SAED) pattern (Fig. 3.4c) depicts the polycrystalline behavior of the sample with an interplanar

spacing of ~ 0.24 and ~0.266 nm corresponding to ZnO (101) and MoO_3 (111), respectively. Scanning transmission electron microscopy (STEM) image (Fig. 3.4d) also confirms the rod-like behavior of the sample. Figure 3.4e-g is the elemental mapping of Zn, O, and Mo elements, whereas Fig. 3.4h shows uniform distribution of all elements along the rod.

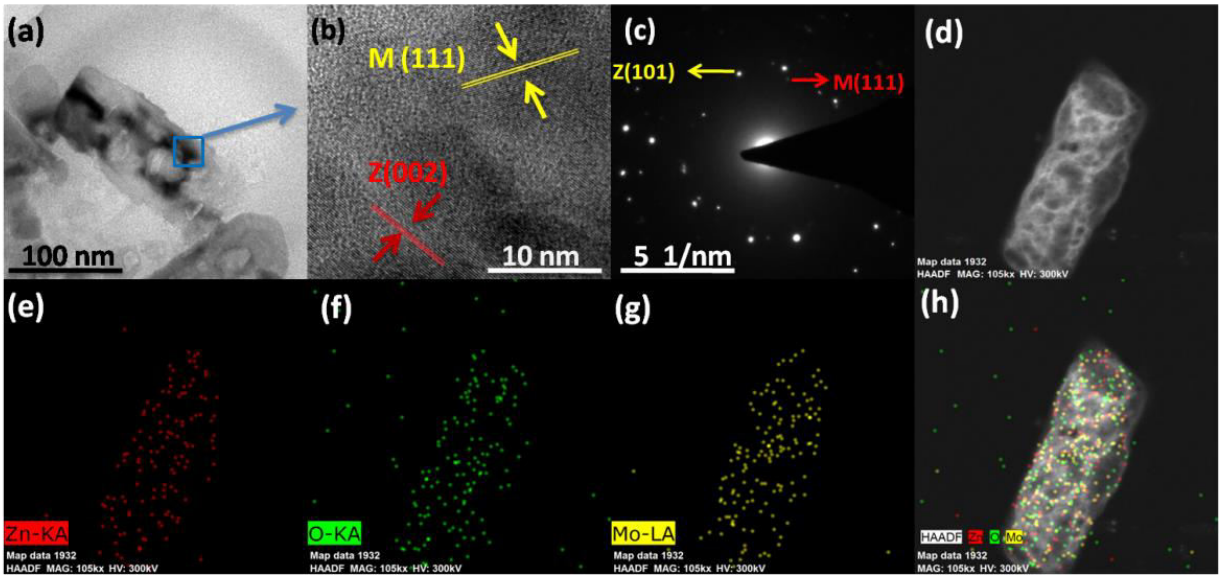

Figure 3.4: (a) TEM micrograph, (b) HRTEM micrograph, (c) SAED pattern, (d) STEM image, (e)-(g) elemental mapping of individual elements, and (h) elemental mapping of all the constituent elements of the ZnO/MoO_3 heterojunction.

3.3.2 Chemical State Analysis

Elemental analysis by X-ray photoelectron spectroscopy (XPS) (Fig.3.5) confirms the presence of Zn, O & Mo in the sample, and it also gives valuable information about the oxidation state of the constituent elements. For ZnO/MoO_3 sample, the doublet peaks at 1044.8 and 1021.7 eV (Fig.3.5a) are attributed to the Zn $2p_{1/2}$ and Zn $2p_{3/2}$ of Zn 2p core-level spectra. The spin-orbit splitting energy of Zn 2p core-level spectra is 23.1 eV which indicates the +2 oxidation state of Zn [20]. Whereas for bare ZnO NRs, the corresponding peaks are obtained at 1044.57 and 1021.47 eV, respectively. Therefore a Small shift of 0.23eV [35,36] in Zn 2p core-level spectra (Fig. 3.5a) is observed which might be due to the modulation of the interfacial electronic structure due to the formation of n-n ZnO/MoO_3 heterojunction. XPS core-level spectra of O 1s (Fig. 3.5b) show a peak at 531.4 eV, which corresponds to the -2 oxidation state of oxygen associated with Zn-O and Mo-O bond formation [20,37,38]. The doublet peaks, positioned at 235.6 and 232.5 eV (Fig. 3.5c), are attributed to Mo $3d_{3/2}$ and Mo $3d_{5/2}$ of

Mo 3d core level spectra with a spin orbit energy splitting of 3.1 eV, which indicates the +6 oxidation states of Mo [39].

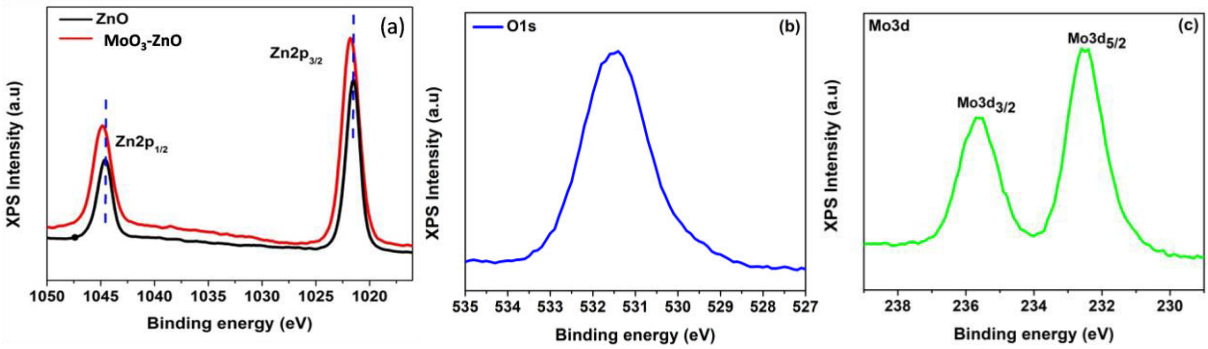

Figure 3.5: X-ray photoelectron spectroscopy of (a) Zn 2p core level spectra, (b) O 1s core level spectra, (c) Mo 3d core level spectra.

3.3.3 PEC Characterizations

Photoelectrochemical (PEC) properties of the as-prepared and MoO_3 layer coated ZnO NRs were thoroughly investigated by linear sweep voltammetry (LSV) measurement i.e., by Current density (*J*) vs. Voltage (V) plot in dark condition (D) and illuminated condition (L) within an applied potential range 1.5 to 0.5V with respect to the reversible hydrogen electrode (RHE) at a scan rate of 100 mVS^{-1} (Fig. 3.6a). To show the change of photocurrent with respect to its dark counterpart, LSV was also conducted in the presence of chopped light illumination (Fig. 3.6b). Pristine ZnO NRs photoanode exhibits poor photocurrent enhancement with respect to its dark current counterpart.

Photocurrent density of ZnO NRs photoanodes was found to increase after the deposition of MoO_3 overlayer, which is also increasing with the repetation of spin coating up to 9 times (Fig. 3.6a). However, beyond 9-time spin-coating, the photocurrent density was significantly decreased. To show the change of photocurrent with respect to its dark counterpart, LSV curves of all the photoanodes were recorded under chopped light illumination (Fig. 3.6b). Figure 3.6c shows the applied bias photon current conversion efficiency (ABPE, η %) of the all investigated samples where ABPE (η %) is calculated using the following equation [40–42]

$$\eta\% = \frac{J_{ph} \times (1.229 - V)}{P_{in}} \times 100\% \qquad (3.1)$$

Here, J_{ph} is the photocurrent density measured from the linear sweep voltammetry curve, 1.229 V is the standard thermodynamic water splitting potential, V is the applied

bias potential, and P_{in} is the intensity of the illuminated light source (Visible light, 10 $mW.cm^{-2}$). The maximum η% value is observed for ZnO/MoO_3 heterostructure with a value of 0.062% at ~ 0.9 V applied bias voltage with respect to RHE (E_{RHE}= $E_{Ag/AgCl}$ + $E^0_{Ag/AgCl}$ + 0.059*pH) [2] which is 4.76 fold higher than the bare ZnO NRs photoanodes (0.013%). Moreover, η% value for 7T, 5T, and 2T ZnO/MoO_3 samples is 0.054%, 0.044%, 0.039%, respectively, which are 4.15, 3.38, 3 times higher than that of bare ZnO NRs. However, η% reduces to <0.01% for 11 times spin-coated MoO_3 over ZnO NRs. Figure 3.6d represents the photoresponse of ZnO and different ZnO/MoO_3 samples under chopped light illumination at an applied potential 0.6 vs. Ag/AgCl.

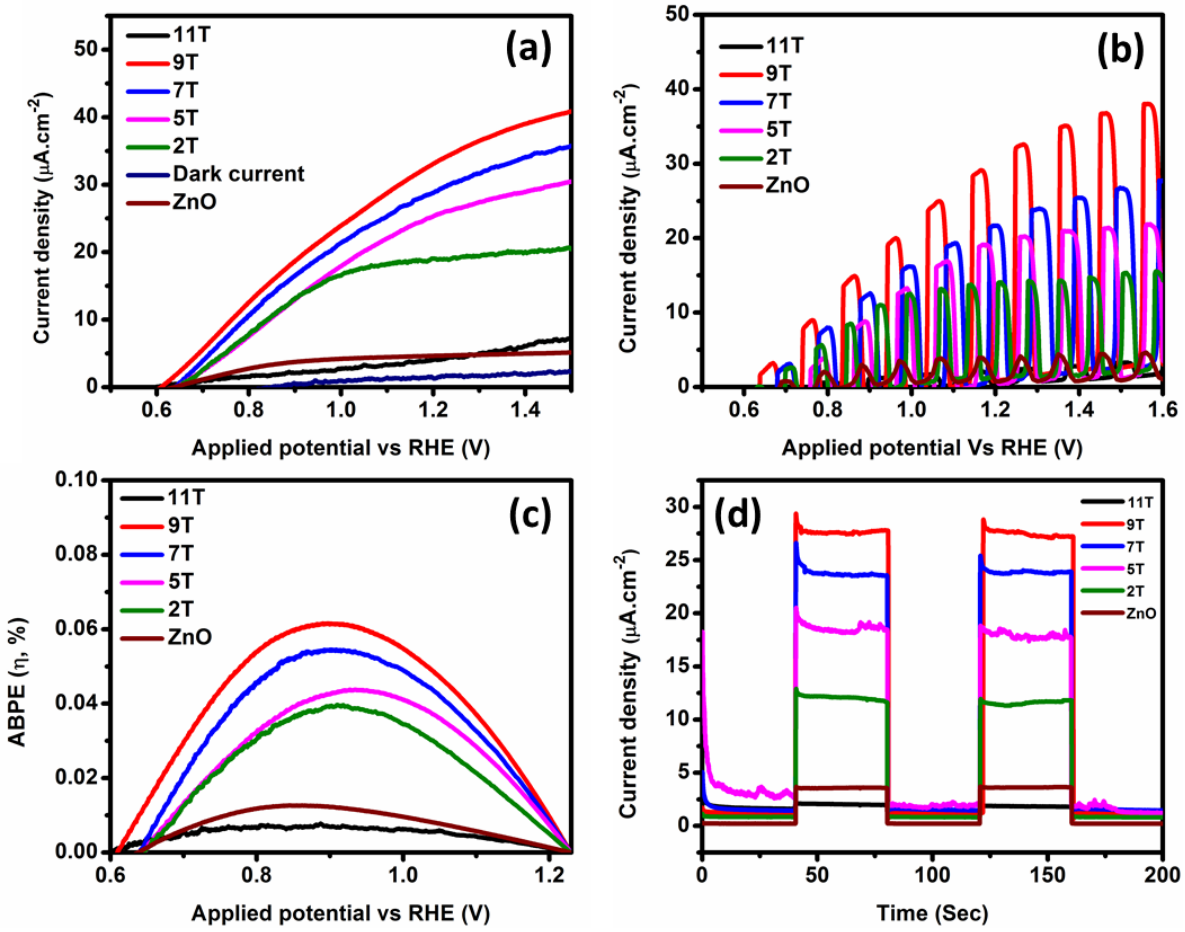

Figure 3.6: (a) Linear sweep voltammetry (LSV) curves, (b) LSV under chopped light illumination, (c) Applied bias photon to current conversion efficiency (ABPE, η %) plots, and (d) I-t (current density vs. time) amperometric curves at 0.6V potential vs. Ag/AgCl of all the ZnO/MoO_3 photoanodes.

Pristine ZnO NRs photoanode exhibits a current density of 3.3 μAcm^{-2}, whereas J_{ph} increases on increasing MoO_3 layers and achieved a maximum value of 27.6 μAcm^{-2} for

nine times spin coating repetition, i,e. for ZnO/MoO_3 (9T) sample, which is comparable to the already reported literature [43–45]. However, J_{ph} reduces to 2.04 μAcm^{-2} for 11 times spin-coated MoO_3 over ZnO. The photocatalytic H_2 evolution performance of ZnO and ZnO/MoO_3 photoanodes were investigated with a gas chromatograph (GC), in the presence of 25% (Vol) methanol as hole scavenger, under visible light (Fig. 3.7a). The H_2 evolution rate of pristine was 2 $\mu mol.cm^{-2}.h^{-1}$ which was increased to 5.6 $\mu mol.cm^{-2}.h^{-1}$ after the deposition of MoO_3 (9T).

Figure 3.7b shows the UV-Vis absorption profile of all the samples, indicating an increase in absorption of visible light on increasing MoO_3 layer thickness. ZnO shows a sharp absorption edge near 380 nm, which was shifted towards the higher wavelength region on adding MoO_3. The band-gap of the MoO_3 sample is found to be 3.12 eV (Fig. 3.7c) which closely matches with the theoretical investigation by *Guo et al.* [46]. Absorbance in the higher wavelength range was increased due to the addition of MoO_3, which was increasing with spin coating repetition. However, for 11T ZnO/MoO_3 sample band edge has shifted toward a smaller wavelength because of the bulk behavior of the sample [47]. The bulk ZnO/MoO_3 11T sample may contain fewer defects than other samples, which may be a reason behind the increased band-gap. The effective band gaps of all the samples are provided in table 3.1.

Table 3.1: Effective band-gap of different ZnO/MoO_3 samples obtained from UV-Vis absorbance spectra.

ZnO/MoO_3 Samples	Effective band gap (eV)
2T	3.24
5T	3.21
7T	3.17
9T	3.13
11T	3.31
MoO_3	3.12
ZnO	3.26

Furthermore, We have recorded the photoluminese (PL) spectra in Fig. 3.7d, with an excitation wavelength of 380 nm. The high intensity of the PL spectrum indicates the population of near band edge defect states, which are ascribed due to emission from the oxygen vacancy states in MoO_3[46]. On the other hand, the mid band-gap defect states are ascribed mainly due to the controversial deep level emission of oxygen vacancy (around 490 nm) states in ZnO NRs [21]. The intensity of PL emission peak increases due to additional MoO_3 layers, but for 11T spin-coated MoO_3 layer, somehow the visible

region defect states are reduced, which might be ascribed due to bulk behavior of the sample. The reduced number of defect states might also be the cause of shifting the absorption edge of 11 times spin-coated ZnO/ MoO_3 sample.

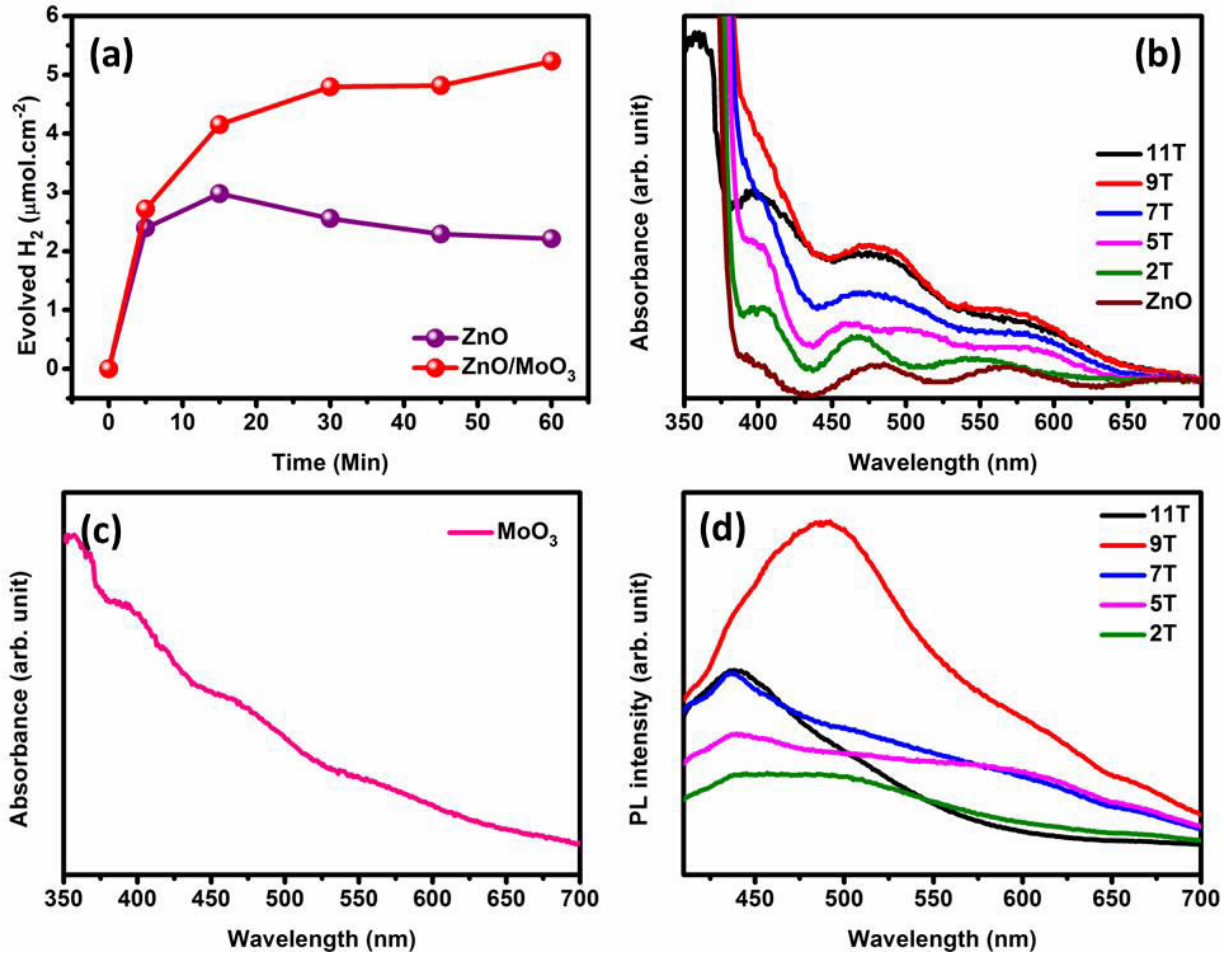

Figure 3.7: (a) Photocatalytic hydrogen evolution performance of ZnO and ZnO/MoO_3 (9T). UV-Visible absorbance spectra of (b) different ZnO/MoO_3 samples, and (c) MoO_3.(d) Photoluminescence (PL) spectra of different ZnO/MoO_3 photoanodes with the excitation of 380 nm.

Figure 3.8a shows the electrochemical impedance behavior of ZnO and ZnO/MoO_3 photoanodes under investigation with ac perturbation of 5 mV, and the inset of the Fig. 3.8apresents the corresponding equivalent circuit model. The equivalent circuit elements for different photoanodes are summarized in table 3.2. Here, R_s denotes resistance appeared in between FTO and ZnO interface, R_{trap} is the charge trapping resistance, and R_{ct} is the charge transfer resistance appeared across the MoO_3-electrolyte interface. R_{ct} for each sample is plotted in Fig. 3.8b shows that on increasing thickness by repeating the spin coating event from 2 to 9 times, R_{ct} decreases, resulting in

enhanced charge carrier mobility and hence photocurrent and photoconversion efficiency[48].

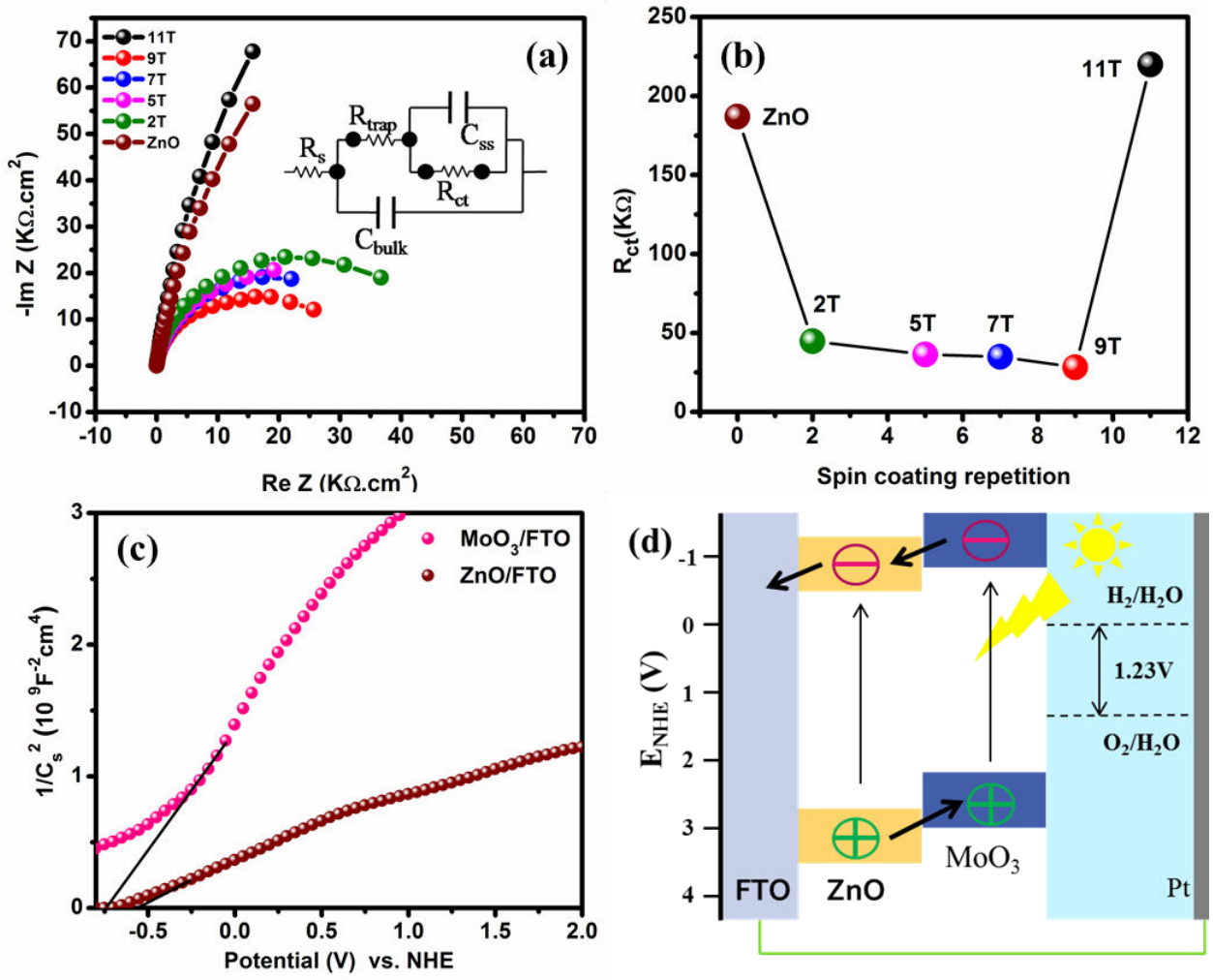

Figure 3.8: (a) Electrochemical impedance spectroscopy plot (inset: equivalent circuit), (b) variation of charge transfer resistance (R_{ct}) of different ZnO/MoO_3 samples, (c) Mott-Schottky plot, (d) band straddling of ZnO and MoO_3 with respect to water oxidation and reduction potential.

Again, R_{ct} is much higher for 11 times spin-coated sample, which represents the bulk behavior of the sample. Charge transfer resistance largely depends on electrochemically active surface area i,e., the contact area between electrode and electrolyte. It is evident from FESEM images that the space between the consecutive ZnO NRs and heads of the ZnO NRs are entirely blocked by MoO_3 for 11 times spin coating. Therefore, the electrochemically active surface area has been reduced than the other samples. Therefore the water oxidation rate at the anode interface has slow down due to the poor

charge transportation at the electrode electrolyte interface. Apart from that, the intensity of incident light decreases exponentially as it traversed through a material. It will be able to penetrate a certain thickness of a material only by generating electron-hole pair. After that, the addition of extra thickness will serve as a resistive element in the circuit since light will not generate electron-hole pair in that extra thickness, which may be a reason behind the increased R_{ct} value in 11T sample. Also, the R_{ct} vale for 11T sample may have increased due to the presence of less defect states than other samples. Charge carrier mobility again depends on the interfacial electronic structure of MoO_3 and ZnO. Therefore, higher photoconversion efficiency is due to effective modulation of interfacial electronic structure, which has enhanced the mobility of the charge carrier.

Table: 3.2 Electrochemical impedence spectroscopy, fitted data in circuit.

ZOMO Samples	R_s $\Omega.cm^{-2}$	R_{trap} $\Omega.cm^{-2}$	R_{ct} $\Omega.cm^{-2}$	C_{bulk} Farad	C_{ss} Farad	Error
2T	7.576	5.974	$4.479x10^4$	$1.756x10^{-5}$	$7.231x10^{-8}$	0.07
5T	7.552	11.98	$3.630x10^4$	$3.54x10^{-5}$	$3.018x10^{-8}$	0.09
7T	7.705	8.195	$3.500x10^4$	$3.078x10^{-5}$	$4.272x10^{-8}$	0.09
9T	7.709	9.392	$2.832x10^4$	$2.257x10^{-5}$	$3.673x10^{-8}$	0.08
11T	8.834	14.770	$2.206x10^5$	$1.694x10^{-5}$	$2.246x10^{-8}$	0.14
ZnO	8.156	13.653	$1.870x10^5$	$1.703x10^{-5}$	$2.135x10^{-8}$	0.11

The space charge behavior of the samples in the electrolyte solution was investigated by Mott-shottky measurement governed by the following equation[2,49–52]

$$\frac{1}{C_s^2} = \frac{2}{e\epsilon\epsilon_0 A^2 N_d}\left(V - V_{fb} - \frac{kT}{e}\right) \quad (3.2)$$

Where C_s is the space charge capacitance, e, the electronic charge, V, the applied bias voltage, V_{fb}, the flat band potential and, $\frac{kT}{e}$, the temperature correction term,ϵ and$\epsilon_0$are the permittivity of semiconductor and free space, respectively. The slope of this equation determines the behavior of the working electrode as either p type or n-type and also the condition when no space charge is formed, which provides the value of flat band potential and hence the position of Fermi level, which is very close to the conduction band for n-type photoanode. From the positive slope of the Mott-Shottky curve in Fig. 3.8c, it is confirmed that individual ZnO and MoO_3 samples behave as n-type semiconductors and the flat band potential of ZnO and MoO_3 is -0.54 and -0.74 V, respectively vs. NHE. Therefore, due to the difference in conduction band position, electron can migrate easily from MoO_3 to core ZnO NRs and charge separation is

accelerated. Figure 3.8d shows the band edges straddling of the samples, which indeed confirm that upon irradiation of visible light, the generated electron-hole pair have sufficient energy to oxidize and reduce water to give oxygen and hydrogen.

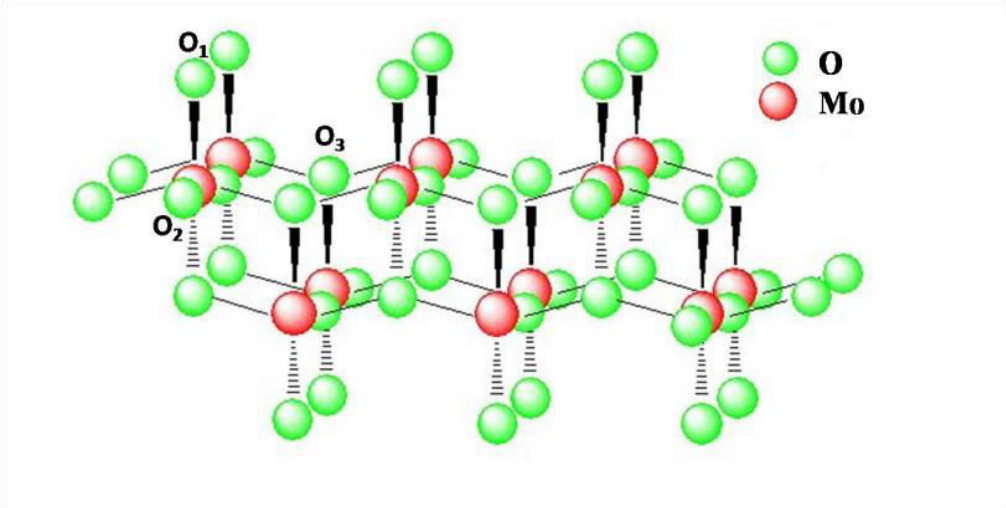

Figure 3.9: Chemical structure of MoO_3.

The structure of MoO_3 provides certain advantages in water splitting. There are three unique oxygen atoms in MoO_3constitute distorted edge shared octahedra [53]. As shown in Fig. 3.9, the Mo-O layers in MoO_3 are terminated by a non-bridging O_1 site, which lays on the outer side of the layer, which is exposed to the electrolyte. The external Mo-O arrangement creates an additional dipole layer which reduces the internal electrostatic force and accelerates the charge transfer rate. Moreover, the external oxygen anion traps electrons and prevents electron-hole recombination. Also, due to large work function (6.6 eV) and dipole present in the external Mo-O layer, it easily transfer hole for water oxidation [46,53]. Additionally, oxygen vacancy at twofold O_2 site is more stable, and it acts as a shallow donor, which indeed enhances the conductivity of the sample[46]. Another aspect of the addition MoO_3 layer is that the absorption of visible light increases. However, there exists a critical thickness of MoO_3 for which a balance is achieved between higher carrier generation and more recombination in the trap states in the thicker MoO_3 layer. Therefore, no further increase in photocurrent is possible after a certain thickness, and in fact, it decreases. The photoelectrochemical eater splitting performance of ZnO/MoO_3 photoanodes has compared with the literature in table 3.3.

Table 3.3: Photoelectrochemical performance of ZnO-based heterojunction.

Heterojunction	Incident light	Aqueous reaction solution	Photocurrent density (mA/Cm^2)	Applied potential (V)
ZnO/TiO_2 nano particle [43]	Wave length 365nm, 1.2 mW/Cm^2	1 mM $NaNO_3$	0.006	0.4 (Vs Ag/AgCl)
ZnO@TiO_2 Core–Shell Nanostructures [54]	AM 1.5G light illumination, $100mW/Cm^2$	0.1 M NaOH	0.4	1.23(Vs RHE)
ZnO/ Bi_2S_3 [44]	Wave length>395nm	0.1 M KOH	0.25	0.8 (Vs Ag/AgCl)
C-ZnO [20]	Wave length> 420nm, 10 mW/Cm^2	0.5M Na_2SO_4	0.0148	0.3(Vs Ag/AgCl)
ZnO/ $CuFeO_2$ [55]	Wave length> 420nm, 10 mW/Cm^2	0.5M Na_2SO_4	0.054	1.2(Vs Ag/AgCl)
ZnO/ $BiVO_4$ [56]	AM 1.5G light illumination, $100mW/Cm^2$	0.3M Na_2SO_4	2.60	1.5(Vs RHE)
ZnO/ In_2O_3 [57]	Wave length> 420nm, 200 mW/Cm^2	0.5M Na_2SO_4	0.75	0.5(Vs Ag/AgCl)
ZnO/ MoO_3 (Present work)	Visible light, 10 mW/Cm^2	0.5M Na_2SO_4	0.026	0.6(Vs Ag/AgCl)

3.4 Conlcusions

In summary, we employ a low-cost, easy, and scalable spin-coating strategy to fabricate ZnO/MoO_3 nano heterostructure on the FTO substrate, which is indeed the first time demonstration of making this particular N-N heterostructure for hydrogen generation to the best of our knowledge. After thorough investigation, it is evident that the introduction of MoO_3 shell layer over ZnO NR cores remarkably improves the visible-light-driven PEC activity. We find that the thickness of the outer MoO_3 shell layer has a crucial role in tailoring the PEC properties. The critical thickness for maximum photocurrent generation (27.6 μAcm^{-2}) is about 100 nm, for 9T ZnO/MoO_3 NHs with a visible light source having an intensity of 10 $mWcm^{-2}$ which is 8.3 times higher than

bare ZnO NRs. Photoluminescence study suggests the population of near band defect states, shallow donor as well as deep level oxygen vacancy states which are the reason of enhanced photocurrent. Smaller photocurrent transient decay parameter of 9T ZnO/MoO_3 than the 2T, 5T, 7T ZnO/MoO_3 leads to higher conductivity and faster charge transportation. Furthermore, EIS data suggests the reduced charge transfer resistance of the NHs. In addition to the band bending in the interfacial region as elucidated from MS plot, Mo-O dipole layer also helps the electron-hole pair for easy separation and migration from the space charge region. Finally, we find 4.76 fold enhancement of ABPE efficiency for 9T spin-coated sample with efficiency value 0.062% at 0.9V vs. RHE. Moreover, 5.6μmolcm^{-2}of hydrogen is produced only by visible light illumination with enhanced stability. Therefore, N-N heterojunction engineering with ZnO/MoO_3 might be a potential strategy to mitigate the limitations involved in solar energy conversion in PEC cells.

Bibliography

[1] D. Maity, K. Karmakar, K. Mandal, NN type core-shell heterojunction engineering with MoO3 over ZnO nanorod cores for enhanced solar energy harvesting application in a photoelectrochemical cell, Journal of Alloys and Compounds. 791 (2019) 739–746.

[2] R. Van de Krol, M. Grätzel, Photoelectrochemical hydrogen production, Springer, 2012.

[3] M. Grätzel, Photoelectrochemical cells, in: Materials For Sustainable Energy: A Collection of Peer-Reviewed Research and Review Articles from Nature Publishing Group, World Scientific, 2011: pp. 26–32.

[4] A. Fujishima, K. Honda, Electrochemical photolysis of water at a semiconductor electrode, Nature. 238 (1972) 37–38.

[5] M. Pagliaro, A.G. Konstandopoulos, R. Ciriminna, G. Palmisano, Solar hydrogen: fuel of the near future, Energy & Environmental Science. 3 (2010) 279–287.

[6] B.D. Alexander, P.J. Kulesza, I. Rutkowska, R. Solarska, J. Augustynski, Metal oxide photoanodes for solar hydrogen production, Journal of Materials Chemistry. 18 (2008) 2298–2303.

[7] F. Lei, Y. Sun, K. Liu, S. Gao, L. Liang, B. Pan, Y. Xie, Oxygen vacancies confined in ultrathin indium oxide porous sheets for promoted visible-light water splitting, Journal of the American Chemical Society. 136 (2014) 6826–6829.

[8] J. Gan, X. Lu, J. Wu, S. Xie, T. Zhai, M. Yu, Z. Zhang, Y. Mao, S.C.I. Wang, Y. Shen, Oxygen vacancies promoting photoelectrochemical performance of In 2 O 3 nanocubes, Scientific Reports. 3 (2013) 1–7.

[9] C. Zhu, C. Li, M. Zheng, J.-J. Delaunay, Plasma-induced oxygen vacancies in ultrathin hematite nanoflakes promoting photoelectrochemical water oxidation, ACS Applied Materials & Interfaces. 7 (2015) 22355–22363.

[10] G. Wang, Y. Ling, Y. Li, Oxygen-deficient metal oxide nanostructures for photoelectrochemical water oxidation and other applications, Nanoscale. 4 (2012) 6682–6691.

[11] K. Sivula, F. Le Formal, M. Grätzel, Solar water splitting: progress using hematite (α-Fe2O3) photoelectrodes, ChemSusChem. 4 (2011) 432–449.

[12] A.A. Ismail, D.W. Bahnemann, Photochemical splitting of water for hydrogen production by photocatalysis: A review, Solar Energy Materials and Solar Cells. 128 (2014) 85–101.

[13] G. Wang, X. Xiao, W. Li, Z. Lin, Z. Zhao, C. Chen, C. Wang, Y. Li, X. Huang, L. Miao, Significantly enhanced visible light photoelectrochemical activity in TiO2 nanowire arrays by nitrogen implantation, Nano Letters. 15 (2015) 4692–4698.

[14] J. Zhang, X. Jin, P.I. Morales-Guzman, X. Yu, H. Liu, H. Zhang, L. Razzari, J.P. Claverie, Engineering the absorption and field enhancement properties of Au–TiO2 nanohybrids via whispering gallery mode resonances for photocatalytic water splitting, ACS Nano. 10 (2016) 4496–4503.

[15] A.P. Bhirud, S.D. Sathaye, R.P. Waichal, L.K. Nikam, B.B. Kale, An eco-friendly, highly stable and efficient nanostructured p-type N-doped ZnO photocatalyst for environmentally benign solar hydrogen production, Green Chemistry. 14 (2012) 2790–2798.

[16] X. Yang, A. Wolcott, G. Wang, A. Sobo, R.C. Fitzmorris, F. Qian, J.Z. Zhang, Y. Li, Nitrogen-doped ZnO nanowire arrays for photoelectrochemical water splitting, Nano Letters. 9 (2009) 2331–2336.

[17] M. Liu, C.-Y. Nam, C.T. Black, J. Kamcev, L. Zhang, Enhancing water splitting activity and chemical stability of zinc oxide nanowire photoanodes with ultrathin titania shells, The Journal of Physical Chemistry C. 117 (2013) 13396–13402.

[18] J. Zhang, I. Salles, S. Pering, P.J. Cameron, D. Mattia, S. Eslava, Nanostructured WO 3 photoanodes for efficient water splitting via anodisation in citric acid, RSC Advances. 7 (2017) 35221–35227.

[19] A. Kafizas, L. Francàs, C. Sotelo-Vazquez, M. Ling, Y. Li, E. Glover, L. McCafferty, C. Blackman, J. Darr, I. Parkin, Optimizing the activity of nanoneedle structured WO3 photoanodes for solar water splitting: direct synthesis via chemical vapor deposition, The Journal of Physical Chemistry C. 121 (2017) 5983–5993.

[20] K. Karmakar, A. Sarkar, K. Mandal, G.G. Khan, Stable and enhanced visible-light water electrolysis using C, N, and S surface functionalized ZnO nanorod photoanodes: engineering the absorption and electronic structure, ACS Sustainable Chemistry & Engineering. 4 (2016) 5693–5702.

[21] K. Karmakar, A. Sarkar, K. Mandal, G.G. Khan, Investigating the role of oxygen vacancies and lattice strain defects on the enhanced photoelectrochemical property of alkali metal (Li, Na, and K) doped ZnO nanorod photoanodes, ChemElectroChem. 5 (2018) 1147–1152.

[22] G. Wang, X. Yang, F. Qian, J.Z. Zhang, Y. Li, Double-sided CdS and CdSe quantum dot co-sensitized ZnO nanowire arrays for photoelectrochemical hydrogen generation, Nano Letters. 10 (2010) 1088–1092.

[23] Y. Wei, L. Ke, J. Kong, H. Liu, Z. Jiao, X. Lu, H. Du, X.W. Sun, Enhanced photoelectrochemical water-splitting effect with a bent ZnO nanorod photoanode decorated with Ag nanoparticles, Nanotechnology. 23 (2012) 235401.

[24] A. Kudo, Y. Miseki, Heterogeneous photocatalyst materials for water splitting, Chemical Society Reviews. 38 (2009) 253–278.

[25] L.I. Kimfung, D. Martin, T. Junwang, Conversion of solar energy to fuels by inorganic heterogeneous systems, Chinese Journal of Catalysis. 32 (2011) 879–890.

[26] R. Marschall, Semiconductor composites: strategies for enhancing charge carrier separation to improve photocatalytic activity, Advanced Functional Materials. 24 (2014) 2421–2440.

[27] A.S. Etman, H.N. Abdelhamid, Y. Yuan, L. Wang, X. Zou, J. Sun, Facile water-based strategy for synthesizing MoO3–x nanosheets: efficient visible light photocatalysts for dye degradation, ACS Omega. 3 (2018) 2193–2201.

[28] K. Inzani, M. Nematollahi, F. Vullum-Bruer, T. Grande, T.W. Reenaas, S.M. Selbach, Electronic properties of reduced molybdenum oxides, Physical Chemistry Chemical Physics. 19 (2017) 9232–9245.

[29] A. Ashok, S.N. Vijayaraghavan, S.V. Nair, M. Shanmugam, Molybdenum trioxide thin film recombination barrier layers for dye sensitized solar cells, RSC Advances. 7 (2017) 48853–48860.

[30] Y. Wang, W. Tian, L. Chen, F. Cao, J. Guo, L. Li, Three-dimensional WO3 nanoplate/Bi2S3 nanorod heterojunction as a highly efficient photoanode for improved photoelectrochemical water splitting, ACS Applied Materials & Interfaces. 9 (2017) 40235–40243.

[31] S.Y. Chae, C.S. Lee, H. Jung, O.-S. Joo, B.K. Min, J.H. Kim, Y.J. Hwang, Insight into charge separation in WO3/BiVO4 heterojunction for solar water splitting, ACS Applied Materials & Interfaces. 9 (2017) 19780–19790.

[32] M.M. Islam, R.D. Tentu, S. Basu, Synthesis of g-C3N4/ZnGa1. 9Al0. 1O4 Heterojunction Using Narrow and Wide Band Gap Material for Enhanced Photoelectrochemical Water Splitting, ChemistrySelect. 3 (2018) 486–494.

[33] A. Belhadi, I. Nadjem, S. Zaidat, A. Boudjemaa, M. Trari, Hydrogen evolution under visible light over the heterojunction p-CuO/n-ZnO prepared by impregnation method, International Journal of Energy Research. 39 (2015) 1909–1916.

[34] W. Feng, L. Lin, H. Li, B. Chi, J. Pu, J. Li, Hydrogenated TiO2/ZnO heterojunction nanorod arrays with enhanced performance for photoelectrochemical water splitting, International Journal of Hydrogen Energy. 42 (2017) 3938–3946.

[35] L. Zhu, H. Li, Z. Liu, P. Xia, Y. Xie, D. Xiong, Synthesis of the 0D/3D CuO/ZnO heterojunction with enhanced photocatalytic activity, The Journal of Physical Chemistry C. 122 (2018) 9531–9539.

[36] L. Xu, B. Wei, W. Liu, H. Zhang, C. Su, J. Che, Flower-like ZnO-Ag 2 O composites: precipitation synthesis and photocatalytic activity, Nanoscale Research Letters. 8 (2013) 1–7.

[37] J. Huang, X. Wang, S. Li, Y. Wang, ZnO/MoO3 mixed oxide nanotube: A highly efficient and stable catalyst for degradation of dye by air under room conditions, Applied Surface Science. 257 (2010) 116–121.

[38] B.R. Lee, H. Choi, J. SunPark, H.J. Lee, S.O. Kim, J.Y. Kim, M.H. Song, Surface modification of metal oxide using ionic liquid molecules in hybrid organic–inorganic optoelectronic devices, Journal of Materials Chemistry. 21 (2011) 2051–2053.

[39] S. Bai, C. Chen, Y. Tian, S. Chen, R. Luo, D. Li, A. Chen, C.C. Liu, Facile synthesis of α-MoO3 nanorods with high sensitivity to CO and intrinsic sensing performance, Materials Research Bulletin. 64 (2015) 252–256.

[40] M.G. Walter, E.L. Warren, J.R. McKone, S.W. Boettcher, Q. Mi, E.A. Santori, N.S. Lewis, Solar water splitting cells, Chemical Reviews. 110 (2010) 6446–6473.

[41] M. Qureshi, K. Takanabe, Insights on measuring and reporting heterogeneous photocatalysis: efficiency definitions and setup examples, Chemistry of Materials. 29 (2017) 158–167.

[42] B. Lamm, B.J. Trześniewski, H. Döscher, W.A. Smith, M. Stefik, Emerging postsynthetic improvements of BiVO4 photoanodes for solar water splitting, ACS Energy Letters. 3 (2017) 112–124.

[43] S. Yuan, J. Mu, R. Mao, Y. Li, Q. Zhang, H. Wang, All-nanoparticle self-assembly ZnO/TiO2 heterojunction thin films with remarkably enhanced photoelectrochemical activity, ACS Applied Materials & Interfaces. 6 (2014) 5719–5725.

[44] S. Bera, S. Ghosh, R.N. Basu, Fabrication of Bi 2 S 3/ZnO heterostructures: an excellent photocatalyst for visible-light-driven hydrogen generation and photoelectrochemical properties, New Journal of Chemistry. 42 (2018) 541–554.

[45] A. Brayek, S. Chaguetmi, M. Ghoul, I.B. Assaker, R. Chtourou, P. Decorse, P. Beaunier, S. Nowak, F. Mammeri, S. Ammar, The structural and the photoelectrochemical properties of ZnO–ZnS/ITO 1D hetero-junctions prepared by tandem electrodeposition and surface sulfidation: on the material processing limits, RSC Advances. 8 (2018) 11785–11798.

[46] Y. Guo, J. Robertson, Origin of the high work function and high conductivity of MoO3, Applied Physics Letters. 105 (2014) 222110.

[47] S. Balendhran, S. Walia, M. Alsaif, E.P. Nguyen, J.Z. Ou, S. Zhuiykov, S. Sriram, M. Bhaskaran, K. Kalantar-Zadeh, Field effect biosensing platform based on 2D α-MoO3, ACS Nano. 7 (2013) 9753–9760.

[48] Z. Wang, G. Liu, C. Ding, Z. Chen, F. Zhang, J. Shi, C. Li, Synergetic effect of conjugated Ni (OH) 2/IrO2 cocatalyst on titanium-doped hematite photoanode for solar water splitting, The Journal of Physical Chemistry C. 119 (2015) 19607–19612.

[49] T. Kirchartz, W. Gong, S.A. Hawks, T. Agostinelli, R.C. MacKenzie, Y. Yang, J. Nelson, Sensitivity of the Mott–Schottky analysis in organic solar cells, The Journal of Physical Chemistry C. 116 (2012) 7672–7680.

[50] W.J. Albery, G.J. O'Shea, A.L. Smith, Interpretation and use of Mott–Schottky plots at the semiconductor/electrolyte interface, Journal of the Chemical Society, Faraday Transactions. 92 (1996) 4083–4085.

[51] P. Xu, T.J. Milstein, T.E. Mallouk, Flat-band potentials of molecularly thin metal oxide nanosheets, ACS Applied Materials & Interfaces. 8 (2016) 11539–11547.

[52] N.P. Herring, L.S. Panchakarla, M.S. El-Shall, P-type nitrogen-doped ZnO nanostructures with controlled shape and doping level by facile microwave synthesis, Langmuir. 30 (2014) 2230–2240.

[53] Q. Qu, W.-B. Zhang, K. Huang, H.-M. Chen, Electronic structure, optical properties and band edges of layered MoO3: A first-principles investigation, Computational Materials Science. 130 (2017) 242–248.

[54] S. Hernández, V. Cauda, A. Chiodoni, S. Dallorto, A. Sacco, D. Hidalgo, E. Celasco, C.F. Pirri, Optimization of 1D ZnO@ TiO2 core–shell nanostructures for enhanced photoelectrochemical water splitting under solar light illumination, ACS Applied Materials & Interfaces. 6 (2014) 12153–12167.

[55] K. Karmakar, A. Sarkar, K. Mandal, G.G. Khan, Nano-engineering of p–n CuFeO2-ZnO heterojunction photoanode with improved light absorption and charge collection for photoelectrochemical water oxidation, Nanotechnology. 28 (2017) 325401.

[56] J.-S. Yang, J.-J. Wu, Low-potential driven fully-depleted BiVO4/ZnO heterojunction nanodendrite array photoanodes for photoelectrochemical water splitting, Nano Energy. 32 (2017) 232–240.

[57] Y. Zhang, J. Zhang, M. Nie, K. Sun, C. Li, J. Yu, Photoelectrochemical water splitting under visible light over anti-photocorrosive In 2 O 3-coupling ZnO nanorod arrays photoanode, Journal of Nanoparticle Research. 17 (2015) 1–11.

Chapter 4

$CoFe_2O_4$/ZnO and $NiFe_2O_4$/ZnO, an n/n and p/n type-II Heterojunction Photoanode for Solar Fuel Generation

Poor light absorption, severe surface charge recombination and fast degradation are the key challenges with ZnO nanostructures based electrodes for photoelectrochemical (PEC) water splitting. This chapter demonstrates the designing of an efficient nano-heterojunction photoelectrode by integrating earth abundant, chemically stable, narrow band-gap transition metal spinel ferrites MFe_2O_4 (M = Co and Ni) nano-particles on ZnO nanorod arrays, which offers excellent PEC activity.

A part of the content of this chapter has been published in the journal of Nanotechnology [1] and is reproduced herein with permission from IOP science.

4.1 Preamble

In the era of energy demand and environmental crisis, solar energy technologies are at the frontline of renewable energy research [2–4]. Solar energy is the most abundant form of renewable energy resource and is considered the ultimate solution to the global energy crisis [4]. Energy-dense hydrogen fuel is the next generation energy carrier. It has tremendous potential to be used for the replacement of fossil fuels due to its minimal impact on the environment. However, the green and eco-friendly production of hydrogen fuel through water splitting by using solar power remain challenging. Photoelectrochemical (PEC) water splitting is a cost-effective and scalable approach to convert and store solar energy in the chemical bond of hydrogen, which can be used on a global scale energy demand [5]. H2 and O2 are produced during PEC water splitting at two macroscopically different places, cathode, and anode, respectively, submerged in an aqueous electrolyte [6,7]. In semiconductor electrodes, the photo-excited holes convert the hydroxyl (OH^-) to O_2 at the photoanode surface through oxygen evolution reaction (OER), whereas the electrons reduce the hydronium molecules (H_3O^+) to H_2 gas at the photocathode through hydrogen evolution reaction (HER) [8]. However, the slow OER rate and large overpotential of semiconductor photoanodes limit their application at PEC cells towards large-scale hydrogen fuel production [9,10]. To reduce the overpotential and boost the OER rate by enhancing charge carrier generation, separation, and transportation, it is necessary to design photoanodes with electrochemically stable and earth abundant materials in a cost effective way.

Over the past few years, numbers of photoactive semiconductors such as TiO_2, GaN, $BiVO_4$, InGaN, WO_3, g-C_3N_4, and ZnO were reported as photoanode materials for PEC cells [11–16]. Among those materials, ZnO is extensively explored as a photoanode due to its natural abundance, facile synthesis, low cost, low toxicity to the environment, and proper band position with respect to water oxidation and reduction potential [17–19]. The higher electron mobility of ~ 205 $cm^2V^{-1}s^{-1}$ and longer minority carrier diffusion length makes ZnO one of the most promising photoanode material [20,21]. However, the wide band gap, suitable to absorb only the UV radiation of solar spectrum (less than 5% of total solar spectrum), and the poor photo-stability of ZnO limits its efficiency and utilization as a photoanode material [12,19,22]. To overcome these limitations and enhance its photoactivity, different strategies are employed, such as designing of ZnO nanostructure based photoanode to facilitate the charge transportation, elemental doping, which tune the band gap and enhance the conductivity, hetero-architecture development between ZnO and a visible light active narrow band gap material which efficiently increase the overall absorbance and charge separation and plasmonic nano-particles deposition to improve the optical absorbance [18,21,23–26]. Light absorbance

in semiconductor-based nano-heterojunction photoanodes (between a wide and narrow band gap material) has improved due to the presence of a narrow band gap semiconductor. Moreover, suitable band alignment at heterojunction increase the charge separation and photocarrier lifetime.

In this backdrop, the earth-abundant transition metal ferrite semiconductors with the empirical formula of MFe_2O_4 (M=Ni, Cu, Co, Zn etc.) have gained sufficient attention as narrow band gap electrode materials because of their visible-light-driven photoactivity, high chemical and structural stability, low cost, low toxicity and easy recycling for their magnetic behavior [27–31]. Magnetic ferrites (MFe_2O_4) have a spinel crystal structure. Inside the spinel structure, metal cations M and Fe arrange themselves in the octahedral and tetrahedral sides, and oxide anions occupy the cubic closed-packed lattice sites [29]. The random hopping process among the different oxidation states of transition metal ions is helpful in charge transport and is a reason behind the good electrical conductivity of the ferrites [30]. Moreover, the metal ions in the octahedral side of the spinel provide the electrochemically active sites for OER [32,33]. Considering this, different magnetic ferrite-based nano-heterostructures are synthesized with enhanced PEC properties. In the family of metal ferrites, $CoFe_2O_4$ and $NiFe_2O_4$ are the two extensively studied attractive materials with the optical band-gap of ~1.6 and 2.19 eV, respectively [30,34,35]. The *n*-type $CoFe_2O_4$ based nano-heterostructures have been used for waste water treatment, catalysis, water splitting, and organic/inorganic pollutant removal [36,37]. $CoFe_2O_4$ nanoparticles anchored 3D carbon fiber papers were used as OER electrocatalyst leading to a small overpotential of 378 mV to achieve a current density of 10 $mAcm^{-2}$ [38]. Chang *et al.* have reported the H_2 production rate of 1650 $\mu molg^{-1}h^{-1}$ by using $CoFe_2O_4/ZnS$ heterostructure electrode [39]. Hafeez *et al*. also have reported an H_2 production rate of 76559 $\mu molg^{-1}h^{-1}$ using reduced graphene oxide (rGO)-supported $CoFe_2O_4/TiO_2$ photocatalyst [35]. Similarly, the *p*-type semiconductor $NiFe_2O_4$ has shown excellent performance for water splitting, degradation of organic pollutants, and other photocatalytic applications. Enhanced photocatalytic activity and an H_2 generation rate of 904 $\mu mol\ h^{-1}$ under visible-light were reported for $NiFe_2O_4$/P-doped g-C_3N_4 nano-composite electrode [30]. Liang *et al.* synthesized reduced graphene oxide (RGO) coupled $NiFe_2O_4$ NPs electrode having excellent photodegradation performance of organic pollutants and superior recycling stability [40]. An applied bias photon-to-current efficiency (ABPE) of 0.206% was reported for *p*-$NiFe_2O_4$/*n*-Fe_2O_3 composite, which is 4.7 times higher than that of pure hematite [31]. Core-shell type $NiFe_2O_4/TiO_2$ was reported to have enhanced photocatalytic water splitting activity [41]. $NiFe_2O_4$ and $CoFe_2O_4$ modified TiO_2 nanorods arrays were also reported to exhibit enhanced photoelectrochemical and photocatalytic properties [42].

In this work, we have assembled solvothermally synthesized $CoFe_2O_4$ and $NiFe_2O_4$ NPs and ZnO NRs, grown on fluorine-doped tin oxide (FTO) glass resulting the formation of type-II *n-n* and *p-n* heterojunction photoelectrodes, respectively. The three-dimensional (3D) morphology of the photoelectrode obtained by anchoring $CoFe_2O_4$/$NiFe_2O_4$ NPs on one dimensional (1D) ZnO NRs provides a large electrochemically active surface area, where the narrow band gap ferrites help to harvest the solar UV-visible light effectively. The type-II band alignment at the heterojunction improves rapid photocarrier separation and reduced electron-hole pair recombination leading to enhanced photocurrent density and applied bias photon-to-current efficiency as high as 1.23 $mA.cm^{-2}$ at 1.23 V vs. RHE and 0.32% for the ZnO/$NiFe_2O_4$ photoanode. Here, photocatalytic water splitting performance of the ZnO/$CoFe_2O_4$ and ZnO/$NiFe_2O_4$ nanoheterojunction photoanodes has been studied, exploring the basic science involved in the photocarrier dynamics.

4.2 Experimental Methods

4.2.1 Synthesis of ZnO Nanorods (NRs)

Vertically aligned arrays of ZnO NRs were grown on the conducting surface of fluorine-doped tin oxide coated glass substrates (FTO, Sigma Aldrich, surface resistivity ~7 Ω/cm^2) as reported previously [43]. At first, a thin seed layer of ZnO was deposited on the FTO through spin coating using appropriate precursor followed by annealing. Later on, the seed layer coated FTO substrates were inserted into an equimolar aqueous solution of Zinc Acetate, and Hexamethylenetetramine maintained at 90°C and for 2 hours under continuous stirring to fabricate arrays of ZnO NRs.

4.2.2 Synthesis of MFe_2O_4 (M= Co and Ni) Nano-Particles (NPs)

MFe_2O_4 (M= Co and Ni) NPs were synthesized by a facile solvothermal method using oleylamine as a capping agent. Precursors MCl_2 (M = Co or Ni), $6H_2O$ (~ 0.36 gm) and $FeCl_3$, $6H_2O$ (~ 0.82 gm) are taken in 1:2 molar weight ratios with Urea (~ 0.53 gm) as reducing agent dissolved in 30 ml 2:1 mixture of Ethylene Glycol (EG) and Ethyl Alcohol. Afterward, Oleylamine (1ml) was added to the precursor solution, and a clear homogeneous solution was obtained through stirring for 30 min. Finally, this solution was transformed into a 50 ml sealed Teflon-lined stainless steel autoclave and heated at 200°C for 15 h in an oven. The as-prepared MFe_2O_4 NPs were washed extensively by ethanol and distilled water and collected through magnetic separation, and dried by heating at 60°C for 30 min.

4.2.3 Fabrication of $ZnO/CoFe_2O_4$ and $ZnO/NiFe_2O_4$ Hetero-Junction Photoanode

To prepare the ZnO/MFe_2O_4 (M= Co or Ni) heterojunction photoanodes, first MFe_2O_4 NPs were dispersed in EG at a 1mg/ml concentration through ultra-sonication for 2 hr and spin-coated on the ZnO NRs encrusted FTO substrates at 2000 rpm for 1 min. The spin coating of MFe_2O_4 NPs was repeated for 5 times, and after each coating, ZnO NRs/FTO substrates were dried under an IR lamp for 10 min and finally, the $ZnO/CoFe_2O_4$ and $ZnO/NiFe_2O_4$ heterojunction electrodes were prepared through heat treatment at 500 °C for 2 hr in a tube furnace in air.

4.2.4 Material Characterization

The crystal structures of MFe_2O_4 NPs and ZnO/MFe_2O_4 heterojunctions were characterized using the X-ray diffraction (XRD, Panalytical X'Pert Pro diffractometer) technique, using the Cu K_α radiation ($\lambda = 1.54$ Å). Morphology of as-synthesized different nanostructures was inspected by field emission scanning electron microscope (FESEM, FEI Quanta-200 Mark-2) and transmission electron microscopy (TEM, JEOL JEM 2100). Elemental compositions of as-synthesized heterojunction photoanodes were investigated with energy-dispersive X-ray spectroscopy (EDS, Oxford Instruments) equipped with the FESEM. Optical characteristics of different nanomaterials were examined with UV–Vis absorption spectroscopy (Perkin Elmer Lambda 105 0UV-Vis spectrometer) and photoluminescence spectroscopy(PL, Horiba, FluoroLog-3).

4.2.5 Photoelectrochemical (PEC) Study

PEC properties of as-synthesized ZnO NRs, $ZnO/CoFe_2O_4$, and $ZnO/NiFe_2O_4$ heterojunction electrodes were investigated using a software-controlled three-electrode electrochemical workstation (CHI660E), where ZnO NRs, $ZnO/CoFe_2O_4$, and $ZnO/NiFe_2O_4$ heterojunctions were used as working electrodes. A platinum wire and Ag/AgCl electrode were employed as counter and reference electrodes, respectively, in the PEC cell containing 0.5M Na_2SO_4 aqueous electrolyte (pH 6.4) under the simulated solar illumination of intensity 100 $mW.cm^{-2}$ (AM 1.5G, LCS-100, Newport, Model 94011A). Electrochemical and photoelectrochemical properties of the as-prepared electrodes were studied by performing Linear sweep voltammetry (LSV), Chrono-amperometry (i-T), Open circuit potential vs. time plot (OCPT), Mott-Schottkyplot (MS), and Electrochemical impedance spectroscopy (EIS) under dark and illumination conditions. The applied bias potential (vs. Ag/AgCl) was converted to Reversible Hydrogen Electrode (RHE) scale using the equation

$$E_{RHE} = E_{Ag/AgCl} + 0.059\times pH + E^{0}_{Ag/AgCl} \quad (4.1)$$

where, $E^{o}_{Ag/AgCl}$= 0.1976 at 25°C and $E_{Ag/AgCl}$isthe experimentally recorded potential against Ag/AgCl reference electrode.

4.3 Result and Discussions

4.3.1 Morphological and Structural, and Chemical Analysis

Figure 4.1a, b, and c are the FESEM images of as-synthesized ZnO NRs, $CoFe_2O_4$ NPs, and $NiFe_2O_4$ NPs, respectively. Hexagonal morphology of vertically oriented one dimensional (1D) ZnO NRs of ~90 nm diameter is evident from Figure 4.1a.

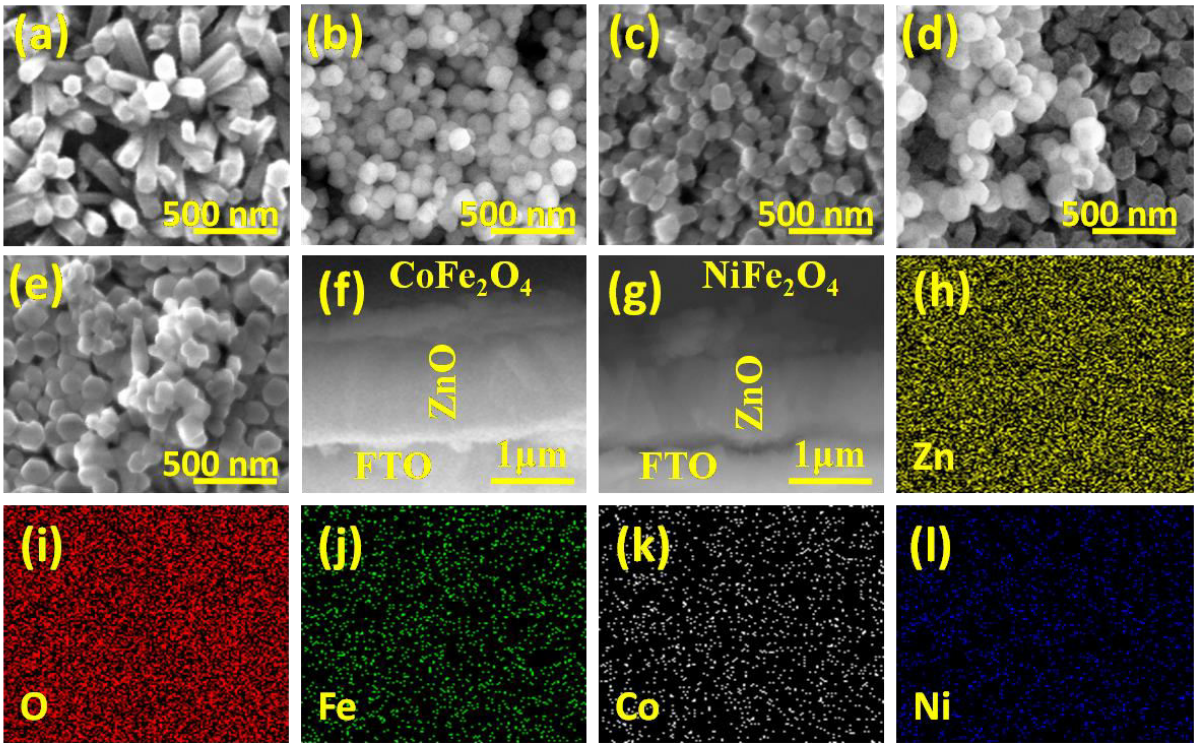

Figure 4.1: FESEM images of (a) pristine ZnO NRs, (b) $CoFe_2O_4$ NPs, (c) $NiFe_2O_4$ NPs, (d) ZnO/$CoFe_2O_4$ and (e) ZnO/$NiFe_2O_4$ heterostructures. Cross-sectional view of (f) ZnO/$CoFe_2O_4$ and (g) ZnO/$NiFe_2O_4$ heterostructure. Elemental mapping of the nano-heterostructures obtained from EDAX: (h) Zn, (i) O, (j) Fe, (k) Co, and (l) Ni.

The nearly spherical morphology of the as-prepared $NiFe_2O_4$ and $CoFe_2O_4$ NPs of average dimension~70 to 80 nm is confirmed from the FESEM micrographs. Figure 4.1d & e are the top view FESEM images of the ZnO/$CoFe_2O_4$ and ZnO/$NiFe_2O_4$ nano-heterojunction electrodes. It is clear from FESEM images that the anchoring of

$CoFe_2O_4/NiFe_2O_4$ NPs covers the heads and the sidewalls near the heads of the ZnO NRs uniformly for the nano-heterostructures (Fig. 4.1f & g).

However, the $CoFe_2O_4/NiFe_2O_4$ NPs cannot uniformly cover the whole ZnO NRs to form a core-shell type structure because of their large dimension, which is bigger than the space between the successive ZnO NRs. Elemental composition and the distribution of $CoFe_2O_4/NiFe_2O_4$ NPs over ZnO NRs were studied by EDAX element mapping (Fig.4.1 h-l). Figure 4.2 shows the XRD pattern of all the different as-prepared nanostructures. Synthesis of polycrystalline $NiFe_2O_4$ (JCPDS#10-0325) and $CoFe_2O_4$ (JCPDS#22-1086) NPs with a preferential growth direction along [311] was confirmed with XRD [44,45].

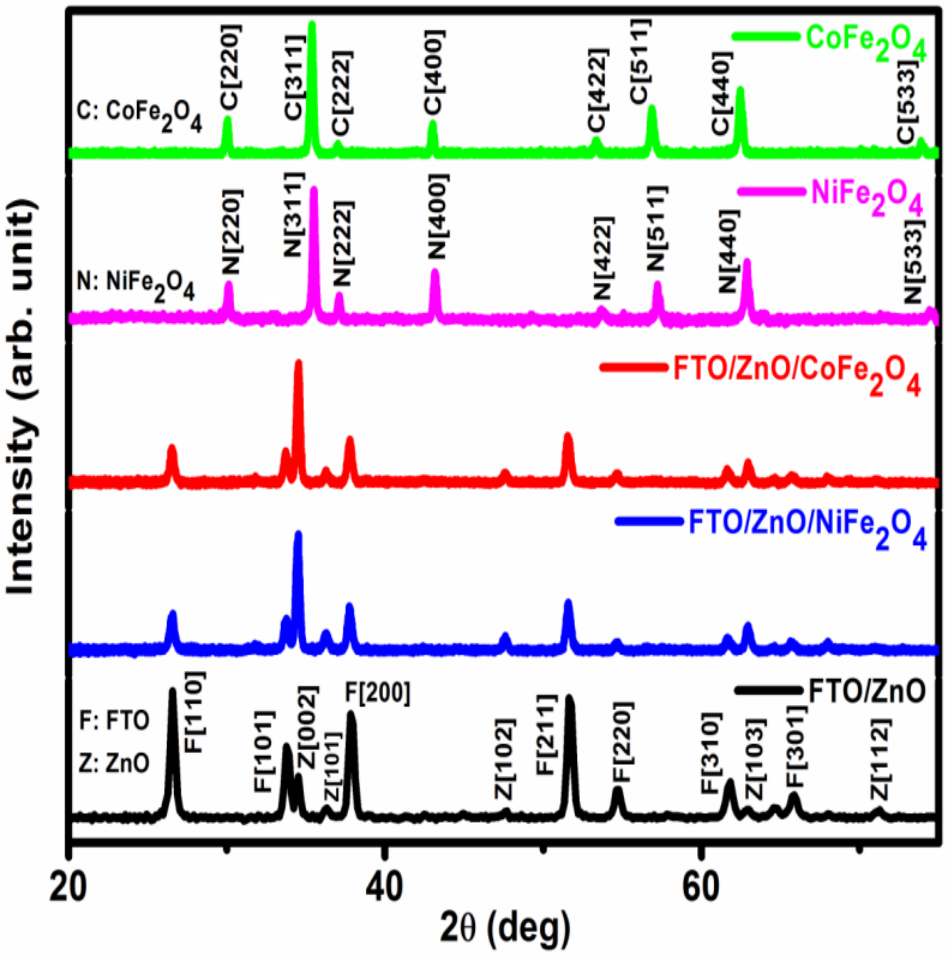

Figure 4.2: XRD pattern of the as-prepared nanostructures.

The XRD patterns of pristine ZnO NRs, $ZnO/CoFe_2O_4$, and $ZnO/NiFe_2O_4$ heterostructures confirm the polycrystalline hexagonal wurtzite structure of the ZnO NRs (JCPDS#89-1397) with P63mc space group symmetry, with a preferential growth

direction along [002] [43]. However, the absence of diffraction peaks for $CoFe_2O_4$ and $NiFe_2O_4$ in the heterostructures is because of the presence of a very small quantity of the NPs in the nano-heterostructures[7].

Figure 4.3a, b, e, and f display the TEM micrographs of as prepared $CoFe_2O_4$ NPs, $NiFe_2O_4$ NPs, ZnO/$CoFe_2O_4$, and ZnO/$NiFe_2O_4$ heterojunction electrodes, respectively. TEM images confirm the formation of $CoFe_2O_4$ and $NiFe_2O_4$ NPs as well as the 1D ZnO NRs and $CoFe_2O_4$/$NiFe_2O_4$ NPs nano-heterojunction. Figures 4.3b and f confirm the anchoring of $CoFe_2O_4$ and $NiFe_2O_4$ NPs over the head and adjacent side walls to the head of ZnO NRs. The image of the lattice fringes of the ZnO NRs/MFe_2O_4 (M= Co, Ni) NPs heterojunctions obtained from the high-resolution TEM (HRTEM), with *d*-spacing of ~0.24 and ~0.2 nm (Fig.4.3c) corresponds to the ZnO (101) and $CoFe_2O_4$ (400) planes, respectively. In Fig. 4.3g, the *d*-spacing of ~0.24 and ~0.2 nm represents the ZnO(101) and $NiFe_2O_4$ (400) planes, respectively. The Selected area electron diffraction (SAED) pattern of ZnO/$CoFe_2O_4$ and ZnO/$NiFe_2O_4$ heterojunctions shown in Figure 4.3d and h, respectively, displays the polycrystalline behavior of the samples and also confirms the formation of heterojunction between ZnO NRs and MFe_2O_4 (M = Co, Ni) NPs.

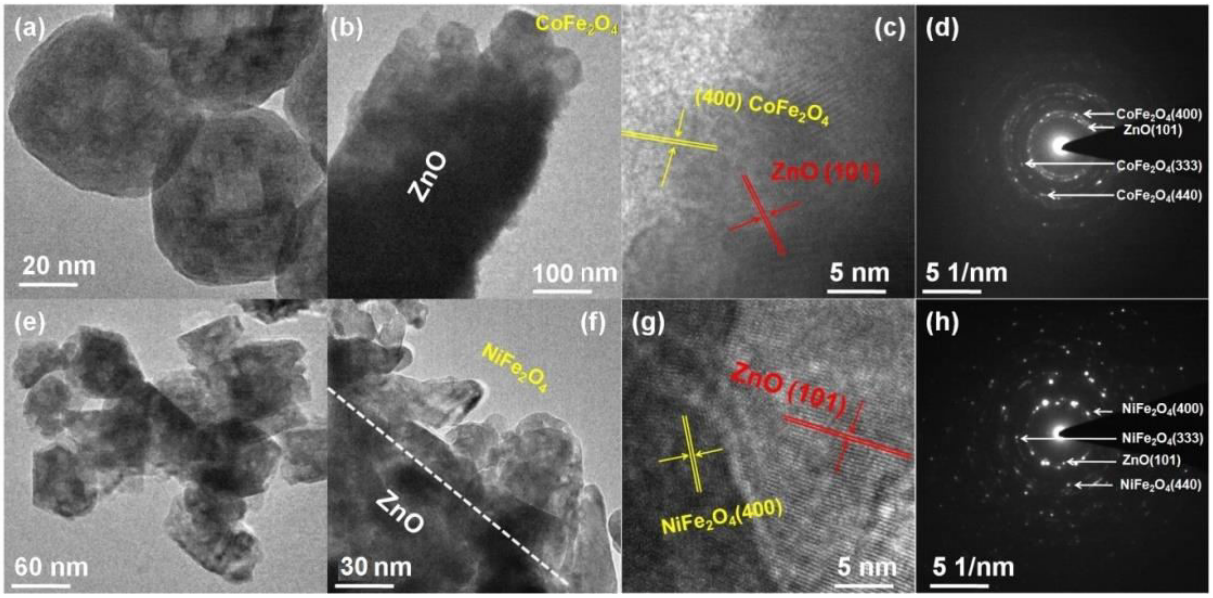

Figure 4.3: TEM micrograph of (a) $CoFe_2O_4$ NPs and (b) ZnO/$CoFe_2O_4$ heterostructure. HRTEM image of (c) ZnO/$CoFe_2O_4$heterojunction. (d) SEAD pattern of ZnO/$CoFe_2O_4$ heterostructure. TEM micrograph of (e) $NiFe_2O_4$ NPs and (e) ZnO/$NiFe_2O_4$ heterostructure. HRTEM image of (g) ZnO/$NiFe_2O_4$ heterojunction. (h) SAED pattern of ZnO/$CoFe_2O_4$ heterostructure.

4.3.2 PEC and Optical Characterizations

Figure 4.4a presents the linear sweep voltammetry (LSV) curve i,e. the plot of current density vs. applied potential (in RHE) for the ZnO NRs, ZnO/$CoFe_2O_4$, and ZnO/$NiFe_2O_4$ heterojunction photoelectrodes under dark and illumination. The dark current density of all the photoelectrodes was found the same and close to 0.15 mA.cm^{-2}. Under illumination, the as-prepared ZnO NRs photoanode exhibits a photocurrent density of 0.6 mA.cm^{-2} at 1.23 V with an onset potential of ~0.54V vs. RHE. Photocurrent density of pristine ZnO NRs photoanode was found to improve significantly after the decoration of $CoFe_2O_4$/$NiFe_2O_4$ NPs over the NRs. The ZnO/$CoFe_2O_4$ heterojunction photoanode shows a photocurrent density of 1.13 mA.cm^{-2} at 1.23 V with an onset potential of ~0.48V vs. RHE, whereas a photocurrent density of 1.23 mA.cm^{-2} at 1.23 V with an onset potential of 0.44 V vs. RHE was achieved from the ZnO/$NiFe_2O_4$ heterojunction photoanode. More than two times increase of the photocurrent density was recorded for the $CoFe_2O_4$, or $NiFe_2O_4$ NPs anchored ZnO NRs compared to pure ZnO NRs. In comparison to the as-prepared ZnO NRs, a cathodic shift of 60 and 100 mV was observed for ZnO/$CoFe_2O_4$ and ZnO/$NiFe_2O_4$ photoanodes, respectively, which indicates their enhanced charge separation efficiency in the low applied potential range. The current density vs. applied potential plots of the photoelectrodes under chopped illumination (Fig.4.4b) clearly suggests that the incorporation of $CoFe_2O_4$/$NiFe_2O_4$ NPs significantly enhances the photo-response of pristine ZnO NRs.

The applied bias photon-to-current efficiency (ABPE, $\eta\%$) of the photoanodes was calculated (Fig. 4.4c) from LSV plots using the following equation; [46–48]

$$\eta\% = \frac{J_{ph} \times (1.229 - V)}{P_{in}} \times 100\% \qquad (4.2)$$

where J_{ph} is the photocurrent density measured from LSV, 1.229 V is the standard thermodynamic water splitting potential, V is the applied potential in RHE, and P_{in} is the power of the illumination (100 mW.cm^{-2}).

As shown in Fig. 4.4c, pristine ZnO NRs photoanode exhibits only 0.11% ABPE at 0.8 V vs. RHE, whereas the maximum value of ABPE reaches 0.26% at 0.79V and 0.32% at 0.78V vs. RHE for ZnO/$CoFe_2O_4$ and ZnO/$NiFe_2O_4$ photoanodes, respectively. Compared to bare ZnO NRs, 136 and 190% increment in ABPE was recorded after incorporating $CoFe_2O_4$ and $NiFe_2O_4$ NPs over ZnO NRs.

Figure 4.4d shows the chrono-amperometry (i.e., current density vs. time) plots of all the photoanodes recorded at a potential of 0.4V vs. Ag/AgCl electrode, under 40 sec light on/off cycle.

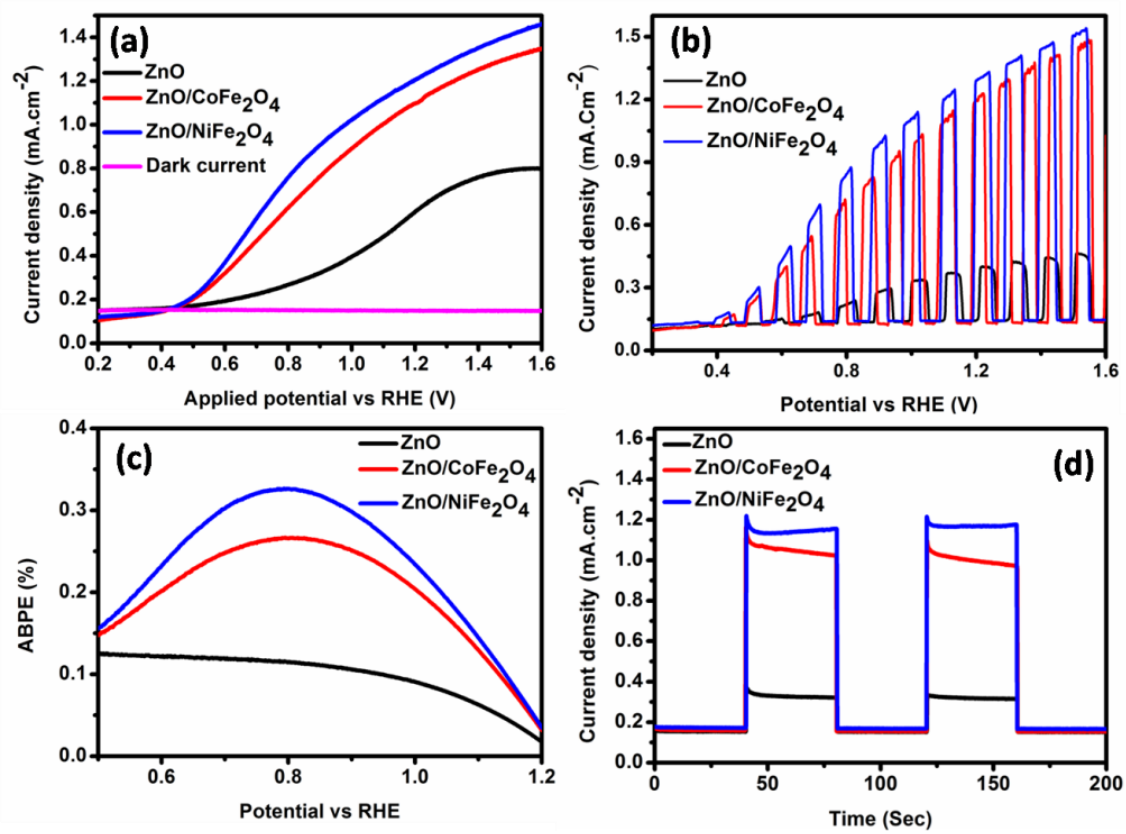

Figure 4.4: (a) Dark and under illumination LSV plots, (b) LSV profile under chopped light illumination, (c) applied bias photon-to-current conversion efficiency (ABPE, %) plots, (d) chrono-amparemmetry plots recorded at 0.4V vs. Ag/AgCl under 40 sec light on/off cycle.

All the as-prepared photoanodes were found to show nearly similar dark current behaviour with a typical current density of 0.15-0.17 mA.cm^{-2} at 0.4 V vs. Ag/AgCl. It is evident from Fig.4.4d that both the ZnO/$CoFe_2O_4$ and ZnO/$NiFe_2O_4$ photoanodes offer remarkably enhanced photo-switching compared with the bare ZnO NRs. The ZnO/$NiFe_2O_4$ heterojunction photoanode shows the best photo-response with a photocurrent density of 1.17 mA.cm^{-2}, whereas the ZnO/$CoFe_2O_4$ and bare ZnO NRs have shown the photocurrent density of 1.05 and 0.3 mA.cm^{-2}, respectively. A transient decay of photocurrent density was observed in the chrono-amperometric profile (Fig. 4.4d) of the photoanodes immediately upon illumination. The generation of large number of electron-hole pairs upon illumination results in the sharp spike in photocurrent followed by transient decay of photocurrent due to carrier recombination. Photocurrent reaches a steady state when the photo-carrier generation and carrier recombination reaches equilibrium. The transient decay time can be estimated from the

logarithmic plot of the parameter D, [49,50] by using $D = (J_t - J_s)/(J_m - J_s)$, where, J_t is the photocurrent density at time t, J_m is the photocurrent density spike, and J_s is the steady-state photocurrent density (inset of Fig. 4.5). The time at which ln(D) reaches -1 defines the transient decay time of the electrode [49]. The calculated transient decay time (from Fig. 4.5) for ZnO NRs, ZnO/$CoFe_2O_4$, and ZnO/$NiFe_2O_4$ nano-heterostructures are 0.6, 1, and 1.75 sec, respectively. As the low recombination rate results in prolonged transient decay time, the increase in transient decay time of the $CoFe_2O_4$ and $NiFe_2O_4$ NPs anchored ZnO NRs photoanodes over pristine ZnO NRs indicates the reduced photocarrier recombination of the nano-heterostructures. The formation of heterojunction between ZnO and $CoFe_2O_4$/$NiFe_2O_4$ has significantly quenched the carrier recombination probability and results in better carrier separation and transportation.

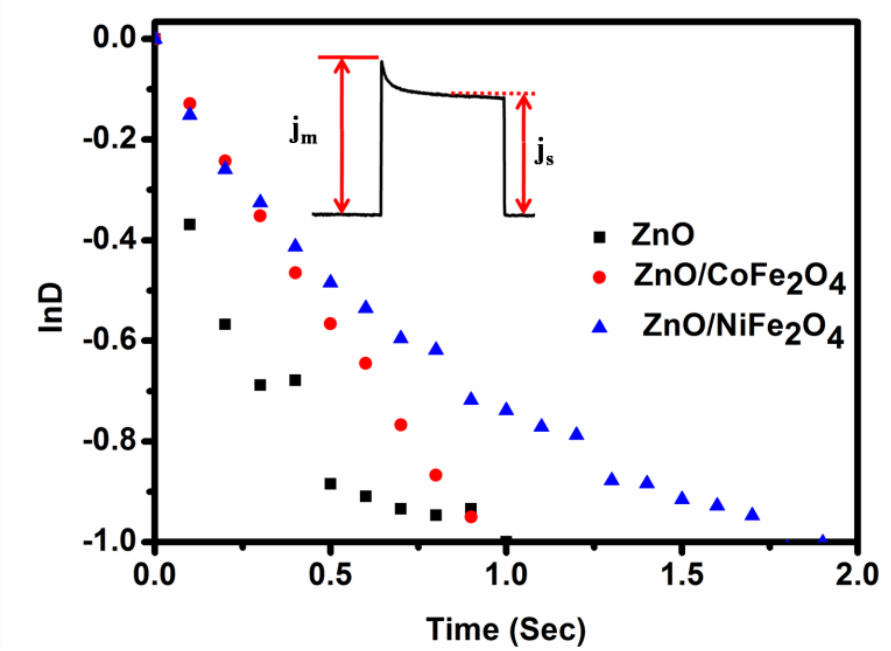

Figure 4.5: ln D vs. Time plot of all the as-prepared photoanodes.

The enhanced light absorption of the photoelectrodes to efficiently generate electron-hole pairs to produce a reasonable amount of photocurrent is the first step in PEC water splitting. The light absorption property of as-prepared electrodes was investigated with UV-Vis spectroscopy. Figure 4.6a shows the UV-Vis absorption spectra of the pristine ZnO NRs, ZnO/$CoFe_2O_4$, and ZnO/$NiFe_2O_4$ heterojunction electrodes.

Band-gap of the as-prepared ZnO NRs, $CoFe_2O_4$, and $NiFe_2O_4$ NPs were calculated from the individual UV–Vis absorption spectrum (Fig.4.6a &b) by Kubelka Munk plots (Fig.4.6c-e). ZnO NRs exhibit a sharp absorption edge at the wavelength of 378 nm

(band-gap energy of 3.26 eV), which can only absorb the UV light of the solar spectrum. The band-gap of $CoFe_2O_4$ and $NiFe_2O_4$ NPs was estimated to be 1.6 and 2.18 eV, respectively. Because of the narrow band-gap, both the $CoFe_2O_4$ and $NiFe_2O_4$ NPs can absorb visible light. In comparison to pristine ZnO NRs, absorbance in the visible light region was significantly improved, and a remarkable red shift in the absorption edge was observed after the formation of $ZnO/CoFe_2O_4$ or $ZnO/NiFe_2O_4$ nano-heterojunction (Fig. 4.6a), which may be due to the formation of near band edge defect levels/interfacial states as a result of heterojunction formation [51,52].

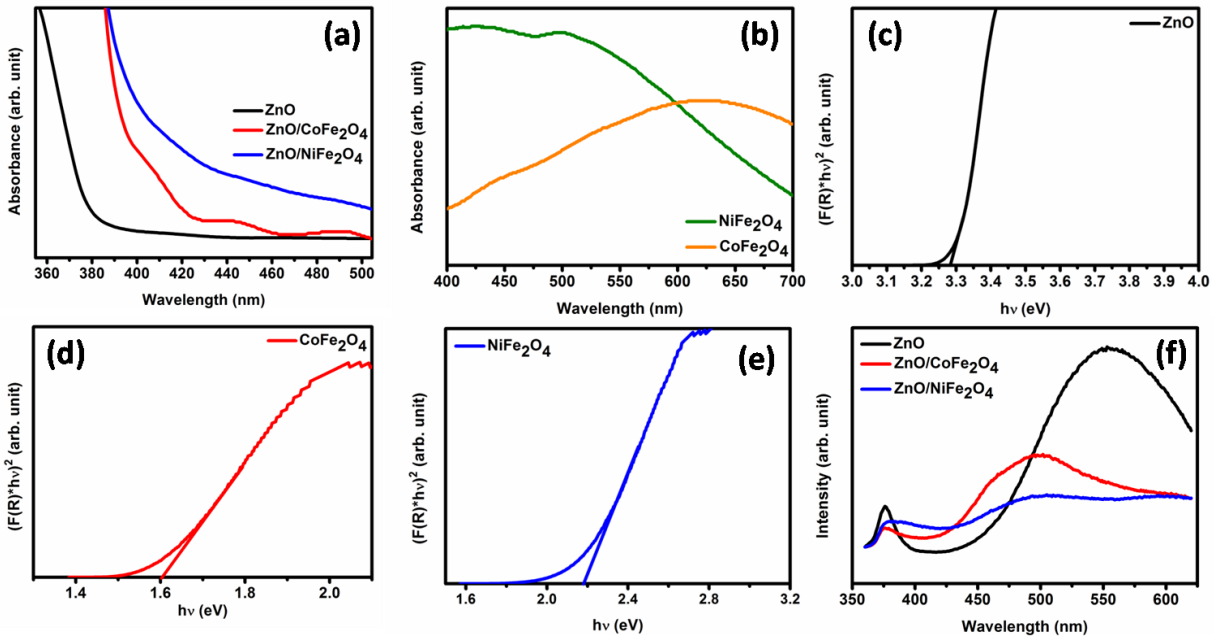

Figure 4.6: UV-Vis spectra of (a) different as prepared photoanodes and (b) $CoFe_2O_4$ & $NiFe_2O_4$ NPs. Kubelka Munk plot of (c) ZnO, (d) $CoFe_2O_4$ and (e) $NiFe_2O_4$. (f) PL emission spectra of the different as prepared photoanodes.

UV-Vis spectra indicate that light absorbance of bare ZnO NRs was notably improved due to the anchoring of low band gap $CoFe_2O_4$ and $NiFe_2O_4$ NPs on ZnO NRs. Enhanced light absorption in the visible wavelength regime leads to the generation of a larger number of photocarriers in $ZnO/CoFe_2O_4$ and $ZnO/NiFe_2O_4$ photoanodes compared to pristine ZnO resulting in higher photocurrent density. The $ZnO/NiFe_2O_4$ heterojunction exhibits a maximum red shift in the absorption edge and hence maximum absorbance in the visible wavelength region, which are the reasons behind maximum photocurrent density and superior PEC property of the same.

In order to understand the charge separation mechanism in the nano-heterojunction and its role behind their excellent PEC performance, the PL emission spectra of the photoanodes were recorded at an excitation of 330 nm and shown in Fig.4.6f. Bare ZnO

NRs exhibit a sharp emission peak at 376 nm corresponding to its band gap energy (3.26 eV) arising due to the radiative-recombination of electrons in the conduction band and holes in the valance band, i.e., the band-edge emission [53,54]. The broad emission peak observed in the visible wavelength region around 550 nm may be related to the defect emission or oxygen vacancies in ZnO NRs [55,56]. Such green emission in ZnO NRs arises when the electrons trapped at a shallow defect level below the conduction band recombines with a photo-generated hole trapped in the valence band or at a deep defect level above the valence band [53,57]. The as-prepared ZnO/$CoFe_2O_4$ and ZnO/$NiFe_2O_4$ nano-heterojunction also exhibit PL patterns similar to ZnO NRs, where the broad defect peak is found to be blue shifted (~500 nm) compared with pristine ZnO NRs. The board peak is expected to be originated from the defects and surface oxygen vacancies present in the $CoFe_2O_4$ or $NiFe_2O_4$ NPs [58,59]. Moreover, the interfacial trap states appear because the formation of heterojunction can also lead to defect-related PL emission. The PL peak intensity was found to suppress remarkably after forming heterojunction between ZnO NRs and $CoFe_2O_4$ or $NiFe_2O_4$ NPs. The quenching of the intensity of PL emission peak in ZnO/$CoFe_2O_4$ or $NiFe_2O_4$ nano-heterojunction compare to pristine ZnO NRs indicates significant reduction of electron-hole pair recombination or rapid separation of photocarriers in the heterojunction electrodes [22]. The quenching of the broad defect PL emission peak of heterojunction compared with ZnO NRs reflects that the electron-hole pair recombination at the surface defects of ZnO NRs was quenched due to anchoring of $CoFe_2O_4$ or $NiFe_2O_4$ NPs over layer [60]. Therefore, for ZnO/$CoFe_2O_4$ or ZnO/$NiFe_2O_4$ nano-heterojunction electrodes it is found that the photocarrier generation process dominates the photocarrier recombination resulting enhanced photocurrent density leading to excellent PEC performance of the nano-heterojunction electrodes.

The behavior of individual semiconductors-electrolyte junction was investigated by performing Mott–Schottky (MS) experiment, which is based on the following equation [61,62].

$$\frac{1}{C_s^2} = \frac{2}{e\epsilon\epsilon_0 A^2 N_d}\left(V - V_{fb} - \frac{kT}{e}\right) \tag{4.3}$$

where C_s is the space charge capacitance, e is the electronic charge, V is the applied bias, V_{fb} is the flat band potential, $\frac{kT}{e}$ is the temperature correction term, and ϵ and ϵ_0 are the permittivity of semiconductor electrodes and free space, respectively. Figure 4.7a, b and c are the MS plots of ZnO NRs, $CoFe_2O_4$ NPs, and $NiFe_2O_4$ NPs grown on FTO, respectively. The positive slope of the MS plot for ZnO NRs and $CoFe_2O_4$ NPs denotes the *n*-type behaviour of the as-prepared semiconductors [34,43,63,64].

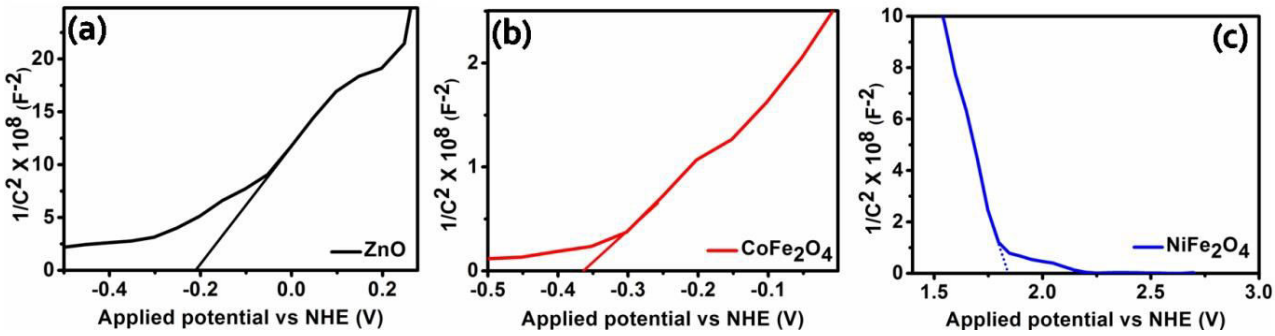

Figure 4.7: Mott-Schottky plot of (a) ZnO NRs, (b) $CoFe_2O_4$ NPs and (c) $NiFe_2O_4$ NPs photoelectrodes.

On the other hand, the negative slope of the MS plot in Fig.4.7c indicates the *p*-type conductivity of $NiFe_2O_4$ NPs [29,65]. However, the positive slope of the MS plots for the ZnO/$CoFe_2O_4$ and ZnO/$NiFe_2O_4$ nano-heterostructure photoelectrodes (Fig.4.8a & b) demonstrates the overall *n*-type semiconductor property of the nano-heterostructure photoelectrodes, as observed from the LSV study.

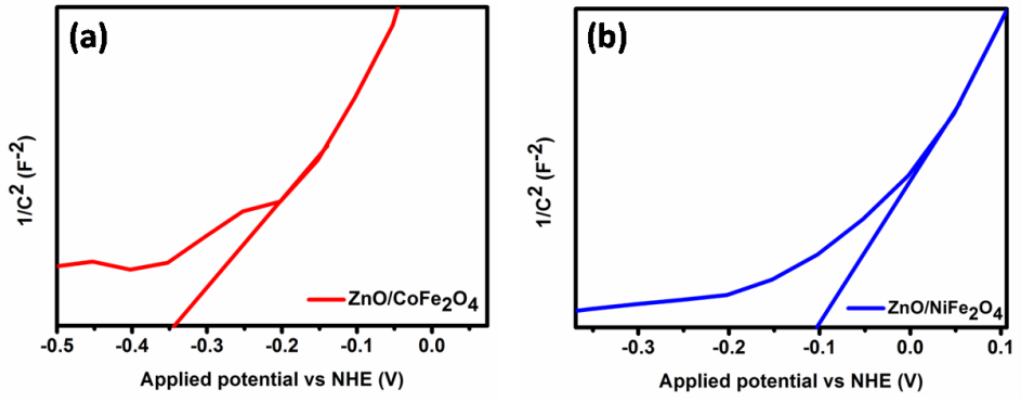

Figure 4.8: Mott-Schottky plot of (a) ZnO/$CoFe_2O_4$ and (b) ZnO/$NiFe_2O_4$ photoelectrodes.

The thermodynamic ability of a semiconductor electrode for water splitting is measured by the position of its flat band potential (V_{fb}). The flat band potential indicates the position of the Fermi level of the semiconductors. Generally, the conduction/valance band of an *n*-type/*p*-type semiconductor material is found to be nearly 0.2 eV more negative/positive than the flat band potential. [7,66]. The position of V_{fb} of ZnO NRs, $CoFe_2O_4$ and $NiFe_2O_4$ NPs are found to be –0.2, –0.36 and 1.84 V respectively with respect to NHE, where $E_{NHE} = E_{RHE} - 0.059*pH$ (at 25° C) or $E_{NHE} = E_{Ag/AgCl} + E^{o}_{Ag/AgCl}$ [67,68]. It is evident that the conduction band minimum (CBM) for *n*-type $CoFe_2O_4$ is more negative than of *n*-type pristine ZnO NRs (Fig. 4.9a). Hence, $CoFe_2O_4$ NPs have

better thermodynamic ability for water splitting than ZnO. After the formation of ZnO/$CoFe_2O_4$ *n-n* heterojunction, the favorable band alignment (Fig. 4.9b) will result in enhanced photocarrier separation. Although the position of the CBM of *p*-type $NiFe_2O_4$ NPs is positive with respect to *n*-type ZnO NRs (Fig. 4.9a), due to shift of Fermi level during *p-n* heterojunction formation, the CBM of $NiFe_2O_4$ NPs appears well above the conduction band of ZnO facilitating photocarrier separation (Fig. 4.9c). As a result the photo-generated electrons in the conduction band of $CoFe_2O_4$ or $NiFe_2O_4$ NPs can easily transfer to current collector FTO through the conduction band of ZnO NRs. Similarly the photo-generated holes in the valance band of ZnO NRs can easily migrate into valance band $CoFe_2O_4$ or $NiFe_2O_4$ NPs and finally get transferred into the electrolyte. Hence, formation of the ZnO/$CoFe_2O_4$ or $NiFe_2O_4$ NPs heterojunction electrodes improves the charge separation efficiency increasing the life time of the photocarriers in the photoelectrodes boosting their PEC activity.

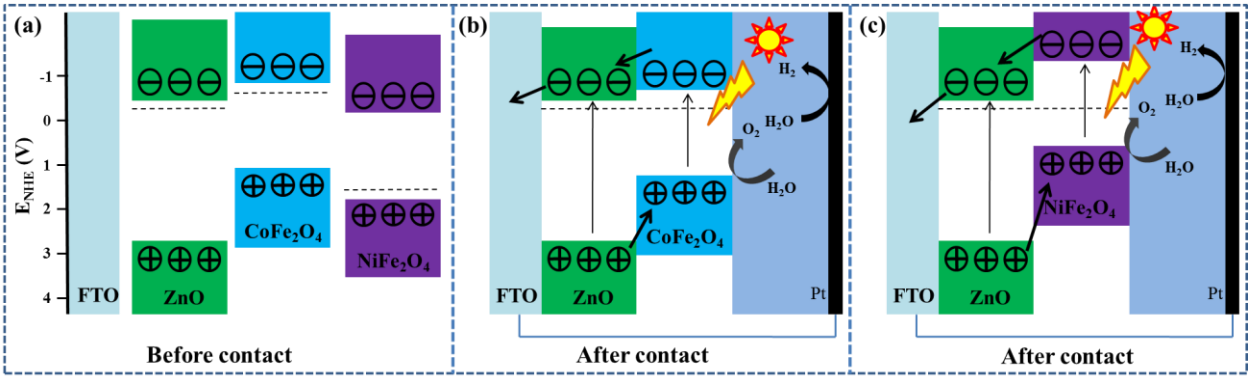

Figure 4.9: Energy band diagrams of (a) ZnO, $CoFe_2O_4$, and $NiFe_2O_4$ before contact, (b) ZnO/$CoFe_2O_4$, and (c) ZnO/$NiFe_2O_4$ heterojunction.

The change in the open circuit potential (V_{OC}) of the electrodes under chopped illumination provides an idea about the charge transport properties of the photoelectrodes. At open circuit conditions, the flow of charge carriers and the corresponding current becomes zero, and the Fermi level in the semiconductor electrode matches precisely with the electrochemical potential of the electrolyte. The V_{OC} vs. time plot (Fig. 4.10a) of the photoanodes under chopped illumination indicates that for the ZnO/$NiFe_2O_4$ heterojunction photoanode, the V_{OC} decreases significantly compared with others when illumination is on. When a semiconductor electrode is illuminated, photon energy excites the electrons to the conduction band leaving behind the holes in the valance band. As a result, carrier concentrations at the valance and conduction band increase. In the case of heterojunction electrodes, electrons from the

conduction band of $NiFe_2O_4$ or $CoFe_2O_4$ transfer to the conduction band of ZnO NRs. The holes from the valance band of ZnO migrate to the valance band of $NiFe_2O_4$ or $CoFe_2O_4$ and flow towards the electrolyte resulting in an increment in photocurrent. Now, to inhibit the flow of holes towards electrolyte and to make the net current flow zero, the V_{OC} decreases under illumination [69]. Therefore, the significant decrease in V_{OC} under illumination indicates the better hole-transport property of heterojunction electrodes over pristine ZnO NRs.

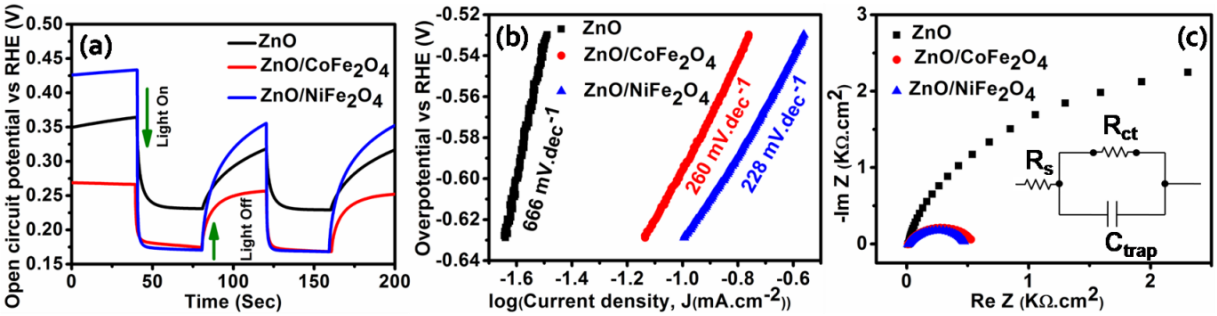

Figure 4.10: (a) Open circuit potential vs. time plot, (b) Tafel plot, and (c) EIS curves of the as-prepared electrodes. Inset in (c): The equivalent circuit model of the photoanodes.

Figure 4.10b shows the Tafel plot (overpotential vs. log (current density)) of the photoanodes. The oxygen evaluation reaction (OER) mechanism of the photoanodes is used to probe with Tafel slope, as it is subjected to mass and electron transport [70–72]. Tafel slope of ZnO NRs, $ZnO/CoFe_2O_4$, and $ZnO/NiFe_2O_4$ heterojunctions are calculated as 666, 260 and 228 $mV.dec^{-1}$, respectively. The slow electron transport in the photoelectrodes gives rise to large Tafel slopes [72,73]. The sluggish electron transport through the surface of ZnO NRs results in higher Tafel slopes. Remarkable decrease of Tafel slope after the incorporation of $CoFe_2O_4$ and $NiFe_2O_4$ NPs over ZnO NRs indicates rapid electron migration through the hetero-interface because of favorable band alignment. The lowest value of Tafel slope in $ZnO/NiFe_2O_4$ electrode signifies the excellent photocarrier transportation across hetero-interface leading to enhanced PEC activity.

For further understanding of interfacial charge transfer process, electrochemical impedance spectroscopy (EIS) was carried out at 0V vs. Ag/AgCl with 5 mV ac perturbation under the illumination. Figure 10c shows the EIS curves of the photoanodes. The EIS curve of the photoanodes consists of a semicircle, from where the equivalent series resistance (R_s) and the charge transfer resistance (R_{ct}) at the

photoelectrode/electrolyte interface was obtained (Table 1) using the equivalent circuit diagram shown in the inset of Fig. 4.10c.

Table 4.1: Summary of the values of equivalent circuit components of the photoelectrodes.

Photoanodes	R_s**(Ω)**	R_{ct}**(KΩ)**	C_{trap}**(x10^{-5} F)**
ZnO NRs	15.11	3.57	2.59
ZnO/$CoFe_2O_4$heterojunction	15.17	0.44	1.92
ZnO/$NiFe_2O_4$heterojunction	14.45	0.37	1.14

The diameter of the EIS curve measures the charge transfer resistance arising because of the charge transfer kinetics at the photoelectrode-electrolyte interface.

Table 4.2: Summary of PEC performance of different transition metal ferrites based heterostructure electrodes.

Photoelectrode materials	**Incident illumination**	**Electrolyte**	**Photocurrent density**	**Applied potential**
$NiFe_2O_4/Fe_2O_3$ [31]	100 mW.cm^{-2}AM 1.5G	1 M NaOH	2.1 mA.cm^{-2}	1.23 V vs. RHE
$NiFe_2O_4$@P-doped g-C_3N_4 [30]	300 W Xe lamp with UV cutoff filter	1.0 M Na_2SO_4	0.53 mA.cm^{-2}	2 V vs. RHE
$ZnFe_2O_4/NiFeO_x$ [74]	100 mW.cm^{-2}AM 1.5 G	1M NaOH	0.35 mA.cm^{-2}	1.23 V vs.RHE
$TiO_2/ZnFe_2O_4/NiFeO_x$ [75]	100 mW.cm^{-2}AM 1.5 G	1M NaOH	0.92 mA.cm^{-2}	1.23 V vs. RHE
$ZnFe_2O_4/NiFeO_x$ [76]	100 mW.cm^{-2}AM 1.5 G	1M NaOH	1.00 mA.cm^{-2}	1.23 V vs. RHE
$NiFe_2O_4/TiO_2$ [42]	100 mW.cm^{-2}AM 1.5 G	0.5 M Na_2SO4	0.41 mA.cm^{-2}	0 V vs.Ag/AgCl
$CoFe_2O_4$/ TiO_2 [42]	100 mW.cm^{-2}AM 1.5 G	0.5 M $Na2SO_4$	0.10 mA.cm^{-2}	0 V vs. Ag/AgCl
ZnO/ $CoFe_2O_4$ present work	100 mW.cm^{-2}AM 1.5 G	0.5 M Na_2SO_4	1.19 mA.cm^{-2}	1.23 V vs. RHE
ZnO/$NiFe_2O_4$ present work	100 mW.cm^{-2}AM 1.5 G	0.5 M Na_2SO_4	1.20 mA.cm^{-2}	1.23 V vs. RHE

Hence, the much lower value of R_{ct} for the $CoFe_2O_4$ and $NiFe_2O_4$ NPs anchored ZnO NRs compared to pristine ZnO NRs indicates the fast charge transfer kinetics at the ZnO/$CoFe_2O_4$ and ZnO/$NiFe_2O_4$ heterojunction photoanode/electrolyte interface compared with pristine ZnO NRs. The lowest value of R_{ct} for ZnO/$NiFe_2O_4$ heterojunction indicates that the resistance at the ZnO/$NiFe_2O_4$ heterojunction/electrolyte interface is lowest among the electrodes, which is the reason behind the enhanced PEC activity of the electrode. The performance of the ZnO/$CoFe_2O_4$ and ZnO/$NiFe_2O_4$ heterojunction photoanodes has been compared with the literature in table 4.2.

4.4 Conclusions

Three dimensional (3D) ZnO/$CoFe_2O_4$ and ZnO/$NiFe_2O_4$ type-II heterojunction photoanodes have been successfully fabricated by assembling $CoFe_2O_4$ and $NiFe_2O_4$ spinel ferrite nano-particles on the one dimensional pristine ZnO NRs by easy and cost-effective wet chemical routes. The narrow band gap of $CoFe_2O_4$ and $NiFe_2O_4$ NPs boost the effective UV-visible light absorption ability of the resultant heterojunction photoelectrodes. Compared to pristine ZnO photoanode, the photocurrent density (0.60 $mA.cm^{-2}$ at 1.23V vs. RHE) was found to increase to 1.13 and 1.23 $mA.cm^{-2}$ with a significant cathodic shift in the onset potential for the ZnO/$CoFe_2O_4$ and ZnO/$NiFe_2O_4$ photoanodes, respectively. The favorable type–II band alignment at heterojunction endows the easy and rapid photocarrier separation and suppresses the electron-hole pair recombination resulting in excellent photocurrent density. The incorporation of earth-abundant transition metal ferrites nanoparticles delivers excellent solar fuel generation performance. The design of these nano-heterostructures provides an effective strategy to develop economic, earth-abundant materials-based stable electrodes with enhanced PEC performance.

Bibliography

[1] D. Maity, K. Karmakar, D. Mandal, D. Pal, G.G. Khan, K. Mandal, Earth abundant transition metal ferrite nanoparticles anchored ZnO nanorods as efficient and stable photoanodes for solar water splitting, Nanotechnology. 31 (2020) 475403.

[2] A. Kudo, Y. Miseki, Heterogeneous photocatalyst materials for water splitting, Chem. Soc. Rev. 38 (2009) 253–278.

[3] F.E. Osterloh, Inorganic nanostructures for photoelectrochemical and photocatalytic water splitting, Chem. Soc. Rev. 42 (2013) 2294–2320.

[4] S. Chu, W. Li, Y. Yan, T. Hamann, I. Shih, D. Wang, Z. Mi, Roadmap on solar water splitting: current status and future prospects, Nano Futur. 1 (2017) 022001.

[5] M.G. Walter, E.L. Warren, J.R. McKone, S.W. Boettcher, Q. Mi, E.A. Santori, N.S. Lewis, Solar water splitting cells, Chem. Rev. 110 (2010) 6446–6473.

[6] S.P. Berglund, F.F. Abdi, P. Bogdanoff, A. Chemseddine, D. Friedrich, R. van de Krol, Comprehensive evaluation of CuBi2O4 as a photocathode material for photoelectrochemical water splitting, Chem. Mater. 28 (2016) 4231–4242.

[7] S. Wang, T. He, J.-H. Yun, Y. Hu, M. Xiao, A. Du, L. Wang, New Iron-Cobalt Oxide Catalysts Promoting BiVO4 Films for Photoelectrochemical Water Splitting, Adv. Funct. Mater. 28 (2018) 1802685.

[8] H. Li, Y. Yu, M.B. Starr, Z. Li, X. Wang, Piezotronic-enhanced photoelectrochemical reactions in Ni (OH) 2-decorated ZnO photoanodes, J. Phys. Chem. Lett. 6 (2015) 3410–3416.

[9] T. Zhang, M.R. Nellist, L.J. Enman, J. Xiang, S.W. Boettcher, Modes of Fe Incorporation in Co–Fe (Oxy) hydroxide Oxygen Evolution Electrocatalysts, ChemSusChem. 12 (2019) 2015–2021.

[10] L.J. Enman, A.E. Vise, M. Burke Stevens, S.W. Boettcher, Effects of Metal Electrode Support on the Catalytic Activity of Fe (oxy) hydroxide for the Oxygen Evolution Reaction in Alkaline Media, ChemPhysChem. 20 (2019) 3089–3095.

[11] P.R. Mishra, P.K. Shukla, O.N. Srivastava, Study of modular PEC solar cells for photoelectrochemical splitting of water employing nanostructured TiO2 photoelectrodes, Int. J. Hydrog. Energy. 32 (2007) 1680–1685.

[12] A. Wolcott, W.A. Smith, T.R. Kuykendall, Y. Zhao, J.Z. Zhang, Photoelectrochemical study of nanostructured ZnO thin films for hydrogen generation from water splitting, Adv. Funct. Mater. 19 (2009) 1849–1856.

[13] B. AlOtaibi, H.P.T. Nguyen, S. Zhao, M.G. Kibria, S. Fan, Z. Mi, Highly stable photoelectrochemical water splitting and hydrogen generation using a double-band InGaN/GaN core/shell nanowire photoanode, Nano Lett. 13 (2013) 4356–4361.

[14] Y.J. Hwang, C.H. Wu, C. Hahn, H.E. Jeong, P. Yang, Si/InGaN core/shell hierarchical nanowire arrays and their photoelectrochemical properties, Nano Lett. 12 (2012) 1678–1682.

[15] H. Yoon, M.G. Mali, J.Y. Choi, M. Kim, S.K. Choi, H. Park, S.S. Al-Deyab, M.T. Swihart, A.L. Yarin, S.S. Yoon, Nanotextured pillars of electrosprayed bismuth vanadate for efficient photoelectrochemical water splitting, Langmuir. 31 (2015) 3727–3737.

[16] A.K. Nayak, Y. Sohn, D. Pradhan, Facile green synthesis of WO3 · H2O nanoplates and WO3 nanowires with enhanced photoelectrochemical performance, Cryst. Growth Des. 17 (2017) 4949–4957.

[17] S. Panigrahi, D. Basak, Core–shell TiO 2@ ZnO nanorods for efficient ultraviolet photodetection, Nanoscale. 3 (2011) 2336–2341.

[18] Y.I. Choi, H.J. Jung, W.G. Shin, Y. Sohn, Band gap-engineered ZnO and Ag/ZnO by ball-milling method and their photocatalytic and Fenton-like photocatalytic activities, Appl. Surf. Sci. 356 (2015) 615–625.

[19] K. Jeong, P.R. Deshmukh, J. Park, Y. Sohn, W.G. Shin, ZnO-TiO2 core–shell nanowires: a sustainable photoanode for enhanced photoelectrochemical water splitting, ACS Sustain. Chem. Eng. 6 (2018) 6518–6526.

[20] A. Janotti, C.G. Van de Walle, Fundamentals of zinc oxide as a semiconductor, Rep. Prog. Phys. 72 (2009) 126501.

[21] D. Commandeur, G. Brown, E. Hills, J. Spencer, Q. Chen, Defect-rich ZnO nanorod arrays for efficient solar water splitting, ACS Appl. Nano Mater. 2 (2019) 1570–1578.

[22] C. Mahala, M.D. Sharma, M. Basu, ZnO Nanosheets Decorated with Graphite-Like Carbon Nitride Quantum Dots as Photoanodes in Photoelectrochemical Water Splitting, ACS Appl. Nano Mater. (2020).

[23] J. Jiang, X. Zhang, P. Sun, L. Zhang, ZnO/BiOI Heterostructures: Photoinduced Charge-Transfer Property and Enhanced Visible-Light Photocatalytic Activity, J. Phys. Chem. C. 115 (2011) 20555–20564. https://doi.org/10.1021/jp205925z.

[24] C. Liu, Y. Qiu, F. Wang, K. Wang, Q. Liang, Z. Chen, Design of Core–Shell-Structured ZnO/ZnS Hybridized with Graphite-Like C3N4 for Highly Efficient Photoelectrochemical Water Splitting, Adv. Mater. Interfaces. 4 (2017) 1700681.

[25] Z. Kang, H. Si, S. Zhang, J. Wu, Y. Sun, Q. Liao, Z. Zhang, Y. Zhang, Interface engineering for modulation of charge carrier behavior in ZnO photoelectrochemical water splitting, Adv. Funct. Mater. 29 (2019) 1808032.

[26] K. Karmakar, A. Sarkar, K. Mandal, G.G. Khan, Investigating the role of oxygen vacancies and lattice strain defects on the enhanced photoelectrochemical property of alkali metal (Li, Na, and K) doped ZnO nanorod photoanodes, ChemElectroChem. 5 (2018) 1147–1152.

[27] R. Marschall, Semiconductor composites: strategies for enhancing charge carrier separation to improve photocatalytic activity, Adv. Funct. Mater. 24 (2014) 2421–2440.

[28] S.J. Moniz, S.A. Shevlin, D.J. Martin, Z.-X. Guo, J. Tang, Visible-light driven heterojunction photocatalysts for water splitting–a critical review, Energy Environ. Sci. 8 (2015) 731–759.

[29] R. Dillert, D.H. Taffa, M. Wark, T. Bredow, D.W. Bahnemann, Research Update: Photoelectrochemical water splitting and photocatalytic hydrogen production using ferrites (MFe2O4) under visible light irradiation, APL Mater. 3 (2015) 104001.

[30] P. Mishra, A. Behera, D. Kandi, K. Parida, Facile construction of a novel NiFe 2 O 4@ P-doped gC 3 N 4 nanocomposite with enhanced visible-light-driven photocatalytic activity, Nanoscale Adv. 1 (2019) 1864–1879.

[31] S. Hussain, M.M. Tavakoli, A. Waleed, U.S. Virk, S. Yang, A. Waseem, Z. Fan, M.A. Nadeem, Nanotextured Spikes of α-Fe2O3/NiFe2O4 Composite for Efficient Photoelectrochemical Oxidation of Water, Langmuir. 34 (2018) 3555–3564.

[32] C. Wei, Z. Feng, G.G. Scherer, J. Barber, Y. Shao-Horn, Z.J. Xu, Cations in octahedral sites: a descriptor for oxygen electrocatalysis on transition-metal spinels, Adv. Mater. 29 (2017) 1606800.

[33] Y. Niu, X. Huang, L. Zhao, W. Hu, C.M. Li, One-pot synthesis of Co/CoFe2O4 nanoparticles supported on N-doped graphene for efficient bifunctional oxygen electrocatalysis, ACS Sustain. Chem. Eng. 6 (2018) 3556–3564.

[34] S. Singh, N. Khare, Low field magneto-tunable photocurrent in CoFe 2 O 4 nanostructure films for enhanced photoelectrochemical properties, Sci. Rep. 8 (2018) 1–8.

[35] H.Y. Hafeez, S.K. Lakhera, N. Narayanan, S. Harish, Y. Hayakawa, B.-K. Lee, B. Neppolian, Environmentally sustainable synthesis of a CoFe2O4–TiO2/rGO ternary photocatalyst: a highly efficient and stable photocatalyst for high production of hydrogen (solar fuel), ACS Omega. 4 (2019) 880–891.

[36] C. Santhosh, E. Daneshvar, P. Kollu, S. Peräniemi, A.N. Grace, A. Bhatnagar, Magnetic SiO2@ CoFe2O4 nanoparticles decorated on graphene oxide as efficient adsorbents for the removal of anionic pollutants from water, Chem. Eng. J. 322 (2017) 472–487.

[37] V. Dutta, S. Sharma, P. Raizada, A. Hosseini-Bandegharaei, V.K. Gupta, P. Singh, Review on augmentation in photocatalytic activity of CoFe2O4 via heterojunction formation for photocatalysis of organic pollutants in water, J. Saudi Chem. Soc. (2019).

[38] A. Kargar, S. Yavuz, T.K. Kim, C.-H. Liu, C. Kuru, C.S. Rustomji, S. Jin, P.R. Bandaru, Solution-processed CoFe2O4 nanoparticles on 3D carbon fiber papers for durable oxygen evolution reaction, ACS Appl. Mater. Interfaces. 7 (2015) 17851–17856.

[39] C.-J. Chang, Z. Lee, K.-W. Chu, Y.-H. Wei, CoFe2O4@ ZnS core–shell spheres as magnetically recyclable photocatalysts for hydrogen production, J. Taiwan Inst. Chem. Eng. 66 (2016) 386–393.

[40] J. Liang, Y. Wei, J. Zhang, Y. Yao, G. He, B. Tang, H. Chen, Scalable green method to fabricate magnetically separable NiFe2O4-reduced graphene oxide nanocomposites with enhanced photocatalytic performance driven by visible light, Ind. Eng. Chem. Res. 57 (2018) 4311–4319.

[41] H.S. Kim, D. Kim, B.S. Kwak, G.B. Han, M.-H. Um, M. Kang, Synthesis of magnetically separable core@ shell structured NiFe2O4@ TiO2 nanomaterial and its use for photocatalytic hydrogen production by methanol/water splitting, Chem. Eng. J. 243 (2014) 272–279.

[42] X. Gao, X. Liu, Z. Zhu, X. Wang, Z. Xie, Enhanced photoelectrochemical and photocatalytic behaviors of MFe 2 O 4 (M= Ni, Co, Zn and Sr) modified TiO 2 nanorod arrays, Sci. Rep. 6 (2016) 30543.

[43] D. Maity, K. Karmakar, K. Mandal, NN type core-shell heterojunction engineering with MoO3 over ZnO nanorod cores for enhanced solar energy harvesting application in a photoelectrochemical cell, J. Alloys Compd. 791 (2019) 739–746.

[44] V. Šepelák, I. Bergmann, A. Feldhoff, P. Heitjans, F. Krumeich, D. Menzel, F.J. Litterst, S.J. Campbell, K.D. Becker, Nanocrystalline nickel ferrite, NiFe2O4: mechanosynthesis, nonequilibrium cation distribution, canted spin arrangement, and magnetic behavior, J. Phys. Chem. C. 111 (2007) 5026–5033.

[45] S. Mitra, P.S. Veluri, A. Chakraborthy, R.K. Petla, Electrochemical properties of spinel cobalt ferrite nanoparticles with sodium alginate as interactive binder, ChemElectroChem. 1 (2014) 1068–1074.

[46] K.-H. Ye, H. Li, D. Huang, S. Xiao, W. Qiu, M. Li, Y. Hu, W. Mai, H. Ji, S. Yang, Enhancing photoelectrochemical water splitting by combining work function tuning and heterojunction engineering, Nat. Commun. 10 (2019) 1–9.

[47] K. Karmakar, D. Maity, D. Pal, K. Mandal, G.G. Khan, Photo-Induced Exciton Dynamics and Broadband Light Harvesting in ZnO Nanorod-Templated Multilayered Two-Dimensional MoS2/MoO3 Photoanodes for Solar Fuel Generation, ACS Appl. Nano Mater. 3 (2020) 1223–1231.

[48] D. Ghosh, P. Devi, P. Kumar, Modified p-GaN Micro-wells with Vertically Aligned 2D-MoS2 for Enhanced Photoelectrochemical Water-Splitting, ACS Appl. Mater. Interfaces. (2020).

[49] L. Zhang, E. Reisner, J.J. Baumberg, Al-doped ZnO inverse opal networks as efficient electron collectors in BiVO 4 photoanodes for solar water oxidation, Energy Environ. Sci. 7 (2014) 1402–1408.

[50] N.J. Bell, Y.H. Ng, A. Du, H. Coster, S.C. Smith, R. Amal, Understanding the enhancement in photoelectrochemical properties of photocatalytically prepared TiO2-reduced graphene oxide composite, J. Phys. Chem. C. 115 (2011) 6004–6009.

[51] S.J. Moniz, J. Zhu, J. Tang, 1D Co-Pi modified BiVO4/ZnO junction cascade for efficient photoelectrochemical water cleavage, Adv. Energy Mater. 4 (2014) 1301590.

[52] A. Sarkar, A.K. Singh, G.G. Khan, D. Sarkar, K. Mandal, TiO 2/ZnO core/shell nano-heterostructure arrays as photo-electrodes with enhanced visible light photoelectrochemical performance, RSC Adv. 4 (2014) 55629–55634.

[53] M.L. Singla, M. Kumar, Optical characterization of ZnO nanoparticles capped with various surfactants, J. Lumin. 129 (2009) 434–438.

[54] H. Hu, X. Huang, C. Deng, X. Chen, Y. Qian, Hydrothermal synthesis of ZnO nanowires and nanobelts on a large scale, Mater. Chem. Phys. 106 (2007) 58–62.

[55] W.I. Park, D.H. Kim, S.-W. Jung, G.-C. Yi, Metalorganic vapor-phase epitaxial growth of vertically well-aligned ZnO nanorods, Appl. Phys. Lett. 80 (2002) 4232–4234.

[56] K. Karmakar, A. Sarkar, K. Mandal, G.G. Khan, Stable and enhanced visible-light water electrolysis using C, N, and S surface functionalized ZnO nanorod photoanodes: engineering the absorption and electronic structure, ACS Sustain. Chem. Eng. 4 (2016) 5693–5702.

[57] M.L. Kahn, T. Cardinal, B. Bousquet, M. Monge, V. Jubera, B. Chaudret, Optical properties of zinc oxide nanoparticles and nanorods synthesized using an organometallic method, ChemPhysChem. 7 (2006) 2392–2397.

[58] S. Joshi, M. Kumar, Effect of Ni2+ substitution on structural, magnetic, dielectric and optical properties of mixed spinel CoFe2O4 nanoparticles, Ceram. Int. 42 (2016) 18154–18165.

[59] J. Zeng, T. Song, M. Lv, T. Wang, J. Qin, H. Zeng, Plasmonic photocatalyst Au/gC 3 N 4/NiFe 2 O 4 nanocomposites for enhanced visible-light-driven photocatalytic hydrogen evolution, RSC Adv. 6 (2016) 54964–54975.

[60] H.O. Seo, S.-Y. Park, W.H. Shim, K.-D. Kim, K.H. Lee, M.Y. Jo, J.H. Kim, E. Lee, D.-W. Kim, Y.D. Kim, Ultrathin TiO2 films on ZnO electron-collecting layers of inverted organic solar cell, J. Phys. Chem. C. 115 (2011) 21517–21520.

[61] K. Gelderman, L. Lee, S.W. Donne, Flat-band potential of a semiconductor: using the Mott–Schottky equation, J. Chem. Educ. 84 (2007) 685.

[62] P. Xu, T.J. Milstein, T.E. Mallouk, Flat-band potentials of molecularly thin metal oxide nanosheets, ACS Appl. Mater. Interfaces. 8 (2016) 11539–11547.

[63] N. Labchir, E. Amaterz, A. Hannour, A. Ait hssi, D. Vincent, A. Ihlal, M. Sajieddine, Highly efficient nanostructured CoFe2O4 thin film electrodes for electrochemical degradation of rhodamine B, Water Environ. Res. (2019).

[64] A. Kalam, A.G. Al-Sehemi, M. Assiri, G. Du, T. Ahmad, I. Ahmad, M. Pannipara, Modified solvothermal synthesis of cobalt ferrite (CoFe2O4) magnetic nanoparticles photocatalysts for degradation of methylene blue with H2O2/visible light, Results Phys. 8 (2018) 1046–1053.

[65] P. Mishra, A. Behera, D. Kandi, S. Ratha, K. Parida, Novel Magnetic Retrievable Visible-Light-Driven Ternary Fe3O4@ NiFe2O4/Phosphorus-Doped g-C3N4 Nanocomposite Photocatalyst with Significantly Enhanced Activity through a Double-Z-Scheme System, Inorg. Chem. (2020).

[66] R. Van de Krol, M. Grätzel, Photoelectrochemical hydrogen production, Springer, 2012.

[67] N. Poldme, L. O'Reilly, I. Fletcher, J. Portoles, I.V. Sazanovich, M. Towrie, C. Long, J.G. Vos, M.T. Pryce, E.A. Gibson, Photoelectrocatalytic H 2 evolution from integrated photocatalysts adsorbed on NiO, Chem. Sci. 10 (2019) 99–112.

[68] J. Rodríguez-López, A. Minguzzi, A.J. Bard, Reaction of various reductants with oxide films on Pt electrodes as studied by the surface interrogation mode of scanning electrochemical microscopy (SI-SECM): Possible validity of a Marcus relationship, J. Phys. Chem. C. 114 (2010) 18645–18655.

[69] A. Sarkar, K. Karmakar, G.G. Khan, Designing Co-Pi Modified One-Dimensional n–p TiO2/ZnCo2O4 Nanoheterostructure Photoanode with Reduced Electron–Hole Pair Recombination and Excellent Photoconversion Efficiency (> 3%), J. Phys. Chem. C. 121 (2017) 25705–25717.

[70] K. Fan, H. Chen, Y. Ji, H. Huang, P.M. Claesson, Q. Daniel, B. Philippe, H. Rensmo, F. Li, Y. Luo, Nickel–vanadium monolayer double hydroxide for efficient electrochemical water oxidation, Nat. Commun. 7 (2016) 1–9.

[71] T.Y. Ma, S. Dai, M. Jaroniec, S.Z. Qiao, Graphitic carbon nitride nanosheet–carbon nanotube three-dimensional porous composites as high-performance oxygen evolution electrocatalysts, Angew. Chem. Int. Ed. 53 (2014) 7281–7285.

[72] F. Song, X. Hu, Ultrathin cobalt–manganese layered double hydroxide is an efficient oxygen evolution catalyst, J. Am. Chem. Soc. 136 (2014) 16481–16484.

[73] G. Ou, F. Wu, K. Huang, N. Hussain, D. Zu, H. Wei, B. Ge, H. Yao, L. Liu, H. Li, Boosting the Electrocatalytic Water Oxidation Performance of CoFe2O4 Nanoparticles by Surface Defect Engineering, ACS Appl. Mater. Interfaces. 11 (2019) 3978–3983.

[74] N. Guijarro, P. Bornoz, M. Prévot, X. Yu, X. Zhu, M. Johnson, X. Jeanbourquin, F. Le Formal, K. Sivula, Evaluating spinel ferrites MFe 2 O 4 (M= Cu, Mg, Zn) as photoanodes for solar water oxidation: prospects and limitations, Sustain. Energy Fuels. 2 (2018) 103–117.

[75] J.H. Kim, Y.J. Jang, S.H. Choi, B.J. Lee, J.H. Kim, Y.B. Park, C.-M. Nam, H.G. Kim, J.S. Lee, A multitude of modifications strategy of ZnFe 2 O 4 nanorod photoanodes for enhanced photoelectrochemical water splitting activity, J. Mater. Chem. A. 6 (2018) 12693–12700.

[76] X. Zhu, N. Guijarro, Y. Liu, P. Schouwink, R.A. Wells, F. Le Formal, S. Sun, C. Gao, K. Sivula, Spinel structural disorder influences solar-water-splitting performance of ZnFe2O4 nanorod photoanodes, Adv. Mater. 30 (2018) 1801612.

Chapter 5

Solar -Driven PEC Activity of $ZnO/ZnCo_2O_4$ Based Nanoheterojunction Photoanodes

In this chapter we have discussed the photoelectrochemical (PEC) water splitting activity of one-dimensional (1D) *n*-ZnO/*p*-$ZnCo_2O_4$ nano-heterojunction photoanode synthesized *by* using the chemical bath deposition and electrodeposition methods. The type-II analogous band alignment occurs because of *p–n* junction formation between *p*-$ZnCo_2O_4$ and *n*-ZnO nanorods (NRs), accelerates the charge separation and transfer, significantly reducing the photogenerated electron-hole pair recombination. The dual functional $ZnCo_2O_4$ overlayer acts as narrow band-gap light harvesting material and also as an oxygen evolution reaction catalysts to influence the PEC reactions at the electrode/electrolyte interface.

A part of the content of this chapter has been published in the journal of ACS Applied Energy Materials [1] and is reproduced herein with permission from ACS Publications .

5.1 Preamble

Fossil fuels are the primary energy source to society, which is the major cause of global warming, knocking potential threat to the sustainable environment. Therefore, switching to alternative renewable energy resources is the prime avenue to meet current global energy demand in a green and sustainable way [2]. For this purpose, hydrogen could be the most suitable candidate for replacing fossil fuels due to its high energy density and minimal impact on the environment. Hydrogen production through photocatalytic and photoelectrochemical (PEC) water splitting using abundant solar energy has drawn intense research focus since the first discovery of TiO_2 photocatalyst in 1972 [3]. Since then, a wide variety of metal oxide semiconductors such as ZnO, $BiVO_4$, Fe_2O_3, WO_3, MoO_3, etc., have been engaged as photoelectrode (photoanode) material in PEC cells due to their natural abundance, chemical stability, low toxicity, and inexpensive synthesis route [4–12]. Among them, ZnO is employed as one of the most commonly used *n*-type semiconductor photoanode because of its suitable band position, high electron mobility, and longer minority carrier diffusion length [13]. However, being a wide band-gap semiconductor, ZnO is only suitable to absorb UV radiation (3–5% of the total solar spectrum). As a result, ZnO fails to harvest a more significant part of the solar energy spectrum, limiting its application as a single photoanode material in PEC cells [14]. Therefore, to improve its spectral response in the visible wavelength range, several strategies have been employed, such as elemental doping, metal nanoparticle deposition with the plasmonic response, and narrow band-gap semiconductor sensitization or heterojunction formation (*p-n*/*n-n*), etc., [15–23]. Among all of the above-mentioned techniques, fabrication of *p-n* heterojunction through deposition of a *p*-type narrow band-gap material on the surface of ZnO is one of the most effective and inexpensive methods to improve the PEC activity of ZnO. The type-II heterojunction is especially attractive, as it develops a built-in electric field at the interface between two semiconductors, which boosts the photocarrier separation and transportation, beneficial for energy harvesting applications [24,25]. Different type-II heterojunction photoanodes like ZnO/$BiVO_4$, ZnO/Fe_2O_3, WO_3/$BiVO_4$, $CaFe_2O_4$/TaON, TiO_2/ZnO have been reported with remarkable solar-driven water-splitting activity [13,19,26–30]. However, the construction of type-II heterojunction by coupling two semiconductors with the adequately aligned band position for overall water splitting is still challenging.

Mixed metal oxides, with the general formula AB_2O_4, for example, $CuFe_2O_4$, $ZnFe_2O_4$, $NiCo_2O_4$, $MnCo_2O_4$, $ZnCo_2O_4$, etc., have been studied widely in recent times because of their attractive PEC property [31–37]. Among them, *p*-type $ZnCo_2O_4$ is especially attractive due to its potential wide range of applications in various fields, such as

supercapacitor, gas sensing, photocatalytic CO_2 reduction, lithium-ion batteries, photocatalysis, biosensing, and electrochemical water oxidation [36,38–41]. Most interestingly, the broad-band light absorption ability of spinel-type $ZnCo_2O_4$ (band-gap~ 2.1 eV) makes it a suitable candidate for energy harvesting applications [42]. As a metal oxide semiconductor, it exhibits good chemical stability and low overpotential during oxygen evolution reaction (OER) as an electrocatalyst [43]. However, poor conductivity and low exposed catalytically active sites are two major limitations associated with $ZnCo_2O_4$ [43].

This study fabricated a type-II analogous *p-n* heterojunction photoanode by electrochemically depositing the *p*-$ZnCo_2O_4$ layer over the one-dimensional (1D) arrays of n-ZnO nanorods (NRs) for photoelectrochemical water splitting. The 1D structure of ZnO NRs provides a large electrochemically active surface area. Whereas the low energy band-gap $ZnCo_2O_4$ layer boost solar light-harvesting ability. Moreover, the formation of the type-II like *n-p* heterojunction between *n*-ZnO and *p*-$ZnCo_2O_4$ leads to a favorable band arrangement providing ample scope for rapid separation and transportation of photocarriers. The synergistic interaction of ZnO and $ZnCo_2O_4$ drives enhanced PEC activity of the nano-heterostructure photoanode resulting in large photocurrent density and applied bias photon-to-current efficiency of 1.58 mA cm^{-2} at 1.23 V vs. RHE and 0.37%, respectively. The n-ZnO/p-$ZnCo_2O_4$ nano-heterojunction photoanode is found to overcome all the limitations associated with individual material to a great extent considering their PEC water splitting performance.

5.2 Experimental Methods

5.2.1 Synthesis of ZnO NRs Arrays

Highly dense 1D ZnO NRs arrays were grown on the conducting surface of fluorine-doped tin oxide glass (FTO) substrate by two steps aqueous chemical bath growth processes, as described in our previous work [11,44]. In brief, cleaned FTO substrates were spin-coated with an ethanolic precursor of Zn and were annealed at 350°C to form a stable seed layer of ZnO on FTO. Afterward, the ZnO NRs were grown on the ZnO seed layer coated FTO by dipping the substrate in an equimolar aqueous solution of zinc acetate and hexamine at 90°C for 2 hours. Finally, the as-prepared ZnO NRs were thoroughly cleaned with DI water and ethanol to get the final product.

5.2.2 Synthesis of $ZnO/ZnCo_2O_4$ Nano-Heterojunction

The $ZnO/ZnCo_2O_4$ heterojunction photoanode was fabricated through electrochemical deposition of the $ZnCo_2O_4$ shell layer on the vertically aligned arrays of ZnO NRs. The co-electrodeposition of Zn-Co in the surface of ZnO NRs was carried out in a three-electrode electrochemical workstation using the as-prepared ZnO NRs as working electrode, Ag/AgCl electrode as a reference electrode, and a platinum wire as the counter electrode, respectively. An aqueous electrolyte containing 0.3M $ZnNO_3$, 0.3M $CoCl_2$, and 0.3M boric acid used as buffer solution was used for co-electrodeposition of Zn-Co under the applied dc potential of –1 V vs. Ag/AgCl for 1,2, 3, and 4 minutes, respectively, at room temperature. Finally, the $ZnCo_2O_4/ZnO$ heterojunction electrodes were prepared through annealing of the as-prepared materials at 600°C for 2 hr. The 1, 2, 3, and 4 minutes electrodeposited $ZnO/ZnCo_2O_4$ samples were marked as ZnO/ZCO 1, 2,3, and 4, respectively. The different synthesis stages of the $ZnO/ZnCo_2O_4$ core/shell heterojunction photoanodes are shown schematically in Fig. 5.1.

5.2.3 Material Characterization

The morphology and microstructure of the as-prepared photoanodes were characterized by field emission scanning electron microscopy (FESEM, FEI Quanta-200 Mark-2) and transmission electron microscopy (TEM, JEOL JEM 2100), respectively. The chemical compositions were investigated with dispersive x-ray spectroscopy (EDX) equipped with TEM. The crystal structure was identified with grazing incidence X-ray diffraction (GIXRD, Panalytical X'Pert Pro diffractometer) using Cu K_α radiation (λ = 1.54 Å) with a step size of 0.15°. The chemical composition and ionic states of the constituent elements were investigated with the X-ray photoelectron spectroscopy (XPS, Omicron Multiprobe Electron Spectroscopy System XM 500, X-ray source: monochromatic Al K_α line and vacuum level 2.5×10^{-10} mbar). The light absorption property and photocarrier recombination of the as-prepared samples were studied by UV–Vis absorption spectroscopy (Perkin Elmer Lambda 1050 UV/Vis spectrometer) and photoluminescence spectroscopy (PL, Horiba, FluoroLog-3), respectively.

5.2.4 Photoelectrochemical Studies

Different PEC properties of the as-prepared photoelectrodes were investigated by a software-controlled three-electrode electrochemical workstation (CHI660E, CH Instruments) using different as-synthesized photoanodes with 1 cm^2 active areas, as the working electrode, a platinum wire as the counter electrode, and an Ag/AgCl electrode as the reference electrode, respectively. An aqueous solution of Na_2SO_4 (0.5M, pH 6.4) at

room temperature was used as the electrolyte. Photoresponse of all the samples was investigated in the presence of AM 1.5 simulated solar irradiation (LCS-100, Newport, Model 94011A) of the intensity of 100 $mWcm^{-2}$. Linear sweep voltammetry (LSV), chrono-amperometry (j-t), and Mott-Schottky (MS) were carried out in the same electrode configuration. The charge transfer process at the electrode-electrolyte interface was investigated by electrochemical impedance spectroscopy (EIS) measurements, performed in the frequency range of 1 MHz to 0.1 Hz with an AC perturbation of 5mV. The photocatalytic water splitting performance of the photoanode was studied in the presence of 25% (Vol) methanol as a sacrificial agent in water without any applied bias. The hydrogen produced at the counter electrode (Pt) was measured by a gas chromatograph under illumination.

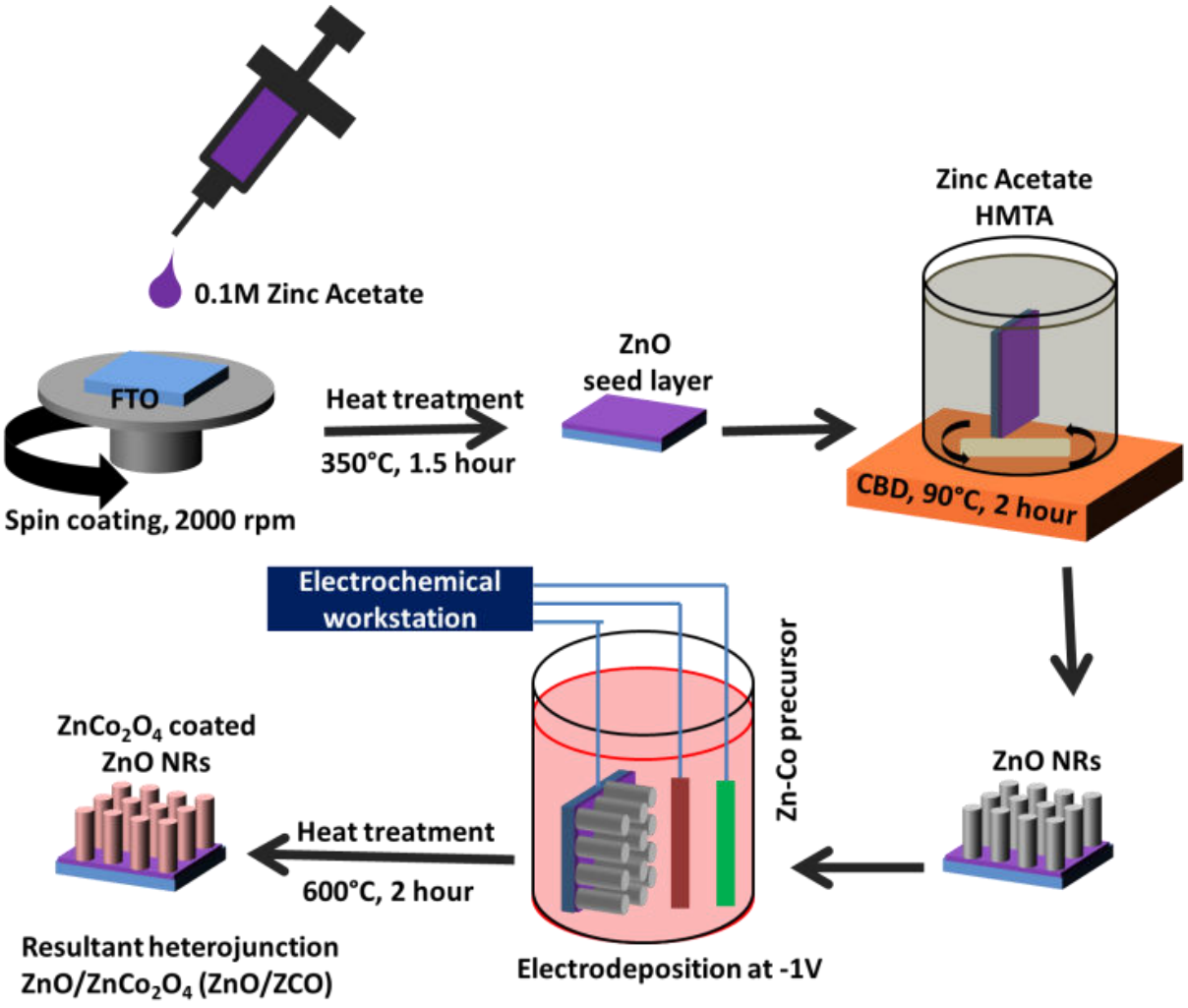

Figure 5.1: Schematic diagram of the synthesis of $ZnO/ZnCo_2O_4$ nano-heterojunction photoanode.

5.3 Results and Discussion

5.3.1 Morphological, Structural, and Chemical Analysis

Figures 5.2a and b show the FESEM images of the ZnO NRs and ZnO/ZCO heterojunction, respectively. Highly dense ZnO NRs arrays were grown vertically on the surface of FTO (Fig. 5.2a). Hexagonal morphology of ZnO NRs with an average dimension of ~80 nm was evident from Fig. 5.2a. The hexagonal morphology of ZnO NRs was found to be a little deformed due to the deposition of $ZnCo_2O_4$ (Fig. 5.2b). It is evident from the inset of Fig. 5.2b that the $ZnCo_2O_4$ layer has grown uniformly over ZnO NRs. Figure 5.2c shows the TEM image of a broken part of ZnO/ZCO core/shell photoelectrode, which confirms the 1D rod-like morphology of the heterostructure. The high-resolution TEM (HRTEM) image (Fig. 5.2d) of the ZnO/ZCO heterojunction confirms the formation of heterojunction with good crystallinity of both ZnO and $ZnCo_2O_4$.

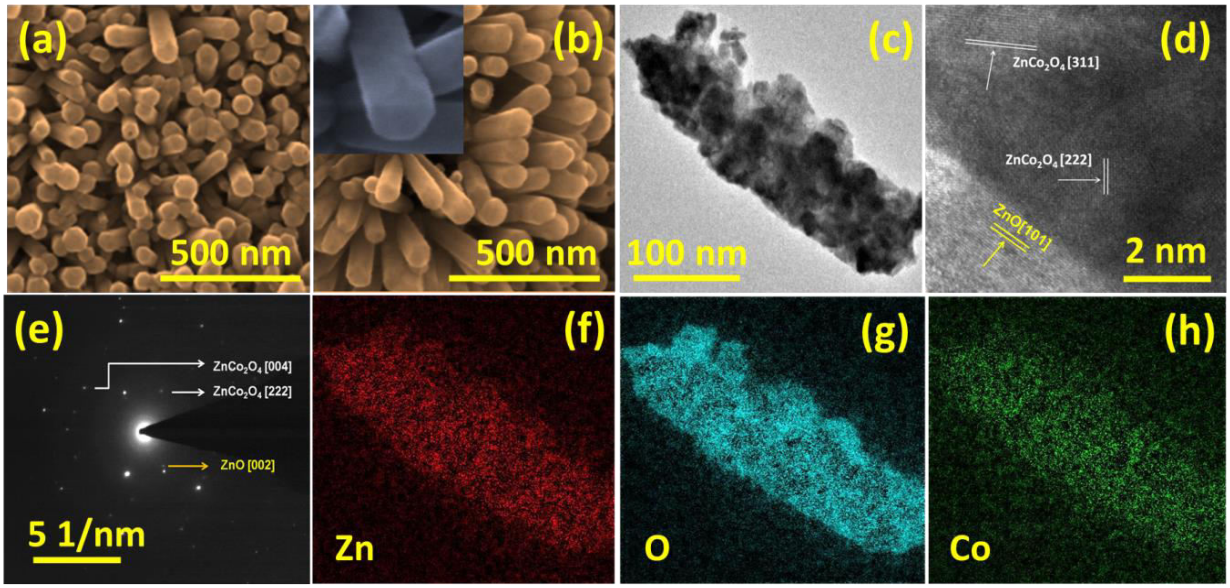

Figure 5.2: FESEM image of (a) pristine ZnO and (b) ZnO/ZCO nano-heterostructure. (c) TEM micrograph, (d) HRTEM image, and (e) SAED pattern of ZnO/ZCO nano-heterostructure. (f), (g) and (h) show the EFTEM mapping for Zn, O, and Co elements, respectively, for ZnO/ZCO nano-heterostructure.

In Fig. 5.2d, the lattice spacing of ~0.246 nm corresponds to the lattice spacing of ZnO (101). On the other hand, the lattice spacing of ~ 0.232 and 0.243 nm corresponds to the $ZnCo_2O_4$ (222) and (311) peaks, respectively. The SAED pattern (Fig. 5.2e) also confirms the presence of ZnO (101) and $ZnCo_2O_4$ (222) and (444) lattice planes, respectively. The

energy filtrated TEM (EFTEM) images (Fig. 5.2f-h) were recorded for a single 1D ZnO/ZCO heterostructure to demonstrate the uniform distribution of constituent elements (Zn, O, and Co) throughout the structure of the ZnO/ZCO nano-heterostructure.

Figure 5.3a demonstrates the XRD pattern of ZnO/ZCO nano-heterostructure, which shows the formation of polycrystalline ZnO and $ZnCo_2O_4$, respectively. It is evident that the ZnO has a preferential growth direction along (002), which confirms its hexagonal wurtzite structure with P63mc space group symmetry (JCPDS#89-1397). The XRD pattern for $ZnCo_2O_4$ indicates spinel structure with $Fd\bar{3}m$ space group (JCPDS#23-1390).

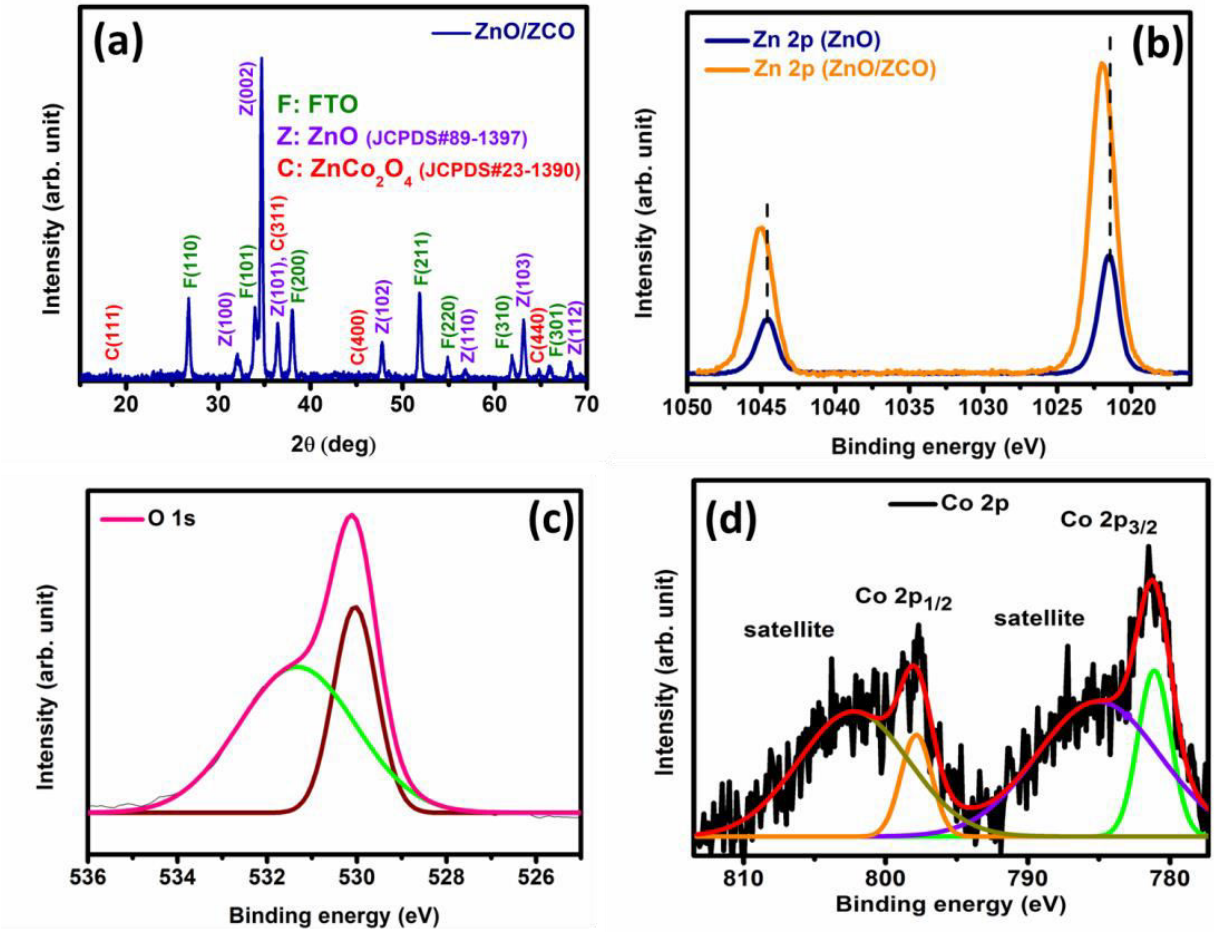

Figure 5.3: (a) XRD pattern of ZnO/ZCO heterojunction photoanode. High-resolution XPS spectrum of (b) Zn 2p for ZnO NRs and ZnO/ZCO nano-heterostructure, (c) O 1s for ZnO/ZCO nano-heterostructure, and (d) Co 2p for ZnO/ZCO nano-heterostructure.

Figure 5.3b shows the high-resolution XPS spectrum of Zn 2p core level for the pristine ZnO NRs and ZnO/ZCO nano-heterostructure. The Zn $2p_{3/2}$ and $2p_{1/2}$ doublet situated

at 1020.9 and 1044.0 eV, respectively, with an energy splitting of ~23.1 eV in between, indicates the +2 oxidation state of Zn in the pristine ZnO NRs [11,42]. The Zn $2p_{3/2}$ and $2p_{1/2}$ doublet is found to shift by ~0.4 eV towards the higher binding energy for the ZnO/ZCO nano-heterostructure, which is due to the lattice strain developed at the interface between ZnO and ZCO because of heterojunction formation [45]. The deconvoluted O 1s spectrum (Fig. 5.3c) shows two major peaks, around 529.8 and 531.3eV, corresponding to the metal-oxygen bonds of ZnO and ZCO and the –OH group present in the materials, respectively [46,47]. The high-resolution XPS spectrum of the Co 2p (Fig. 5.3d) consisting of a doublet centered at 781.1 and 798.2 correspond to Co $2p_{3/2}$ and Co $2p_{1/2}$, respectively, with a couple of shakeup satellite peaks, indicates the presence of Co (Fig. 5.3d) [48]. The spin-orbit splitting between two Co 2p core-level spectra is about ~17.1 eV (>15 eV), which indicates the co-existence of both Co^{2+} and Co^{3+} states in $ZnCo_2O_4$ [49].

5.3.2 PEC and Optical Characterizations

The relative photoresponse of the pristine ZnO and ZnO/ZCO photoelectrodes were determined by comparing the current-voltage plots (Fig. 5.4a) obtained under dark and illumination conditions. The increase of photocurrent with applied positive bias confirms that the electrodes are performing as photoanodes. As shown in Fig. 5.4a, all the photoanodes exhibit the same dark current density (~0.12 $mA.cm^{-2}$), which remains constant over the applied potential range. Under illumination, the anodic photocurrent arises from water oxidation and reduction by the photogenerated holes and electrons, respectively. Pristine ZnO NRs display low photocurrent density, which reaches around 0.35 $mA.cm^{-2}$ at 1.23V vs. RHE with a water splitting onset potential of 481 mV. The photocurrent density is found to increase remarkably after anchoring the $ZnCo_2O_4$ layer over ZnO NRs. The ZnO/ZCO 3 photoanode exhibits the optimized photocurrent density value (1.58 $mA.cm^{-2}$ at 1.23V vs. RHE) with a significant cathodic shift (71 mV) of water splitting onset potential compared to pristine ZnO NRs (Fig. S1). The ZnO/ZCO 1 and ZnO/ZCO 2 photoanodes also show the improved photocurrent density of 1.14 and 1.38 $mA.cm^{-2}$ at 1.23V vs. RHE, with water splitting onset potential of about 475 mV and 429 mV, respectively. However, the photocurrent density for the ZnO/ZCO 4 photoanode was found to decrease, which may be ascribed to the thick deposition of ZCO overlayer (Fig. 5.4a). Hence, it is evident that the formation of nano-heterojunction photoanode initiates water splitting half reactions at a low applied bias potential and delivers enhanced photocurrent. As the ZnO/ZCO 3 photoanode exhibits the optimized PEC performance hence, this work only includes the detailed PEC studies on ZnO, ZnO/ZCO 1, ZnO/ZCO 2, and ZnO/ZCO 3 photoanodes. The LSV

profile under chopped light illumination (Fig. 5.4b) shows the photoresponse of the photoanodes.

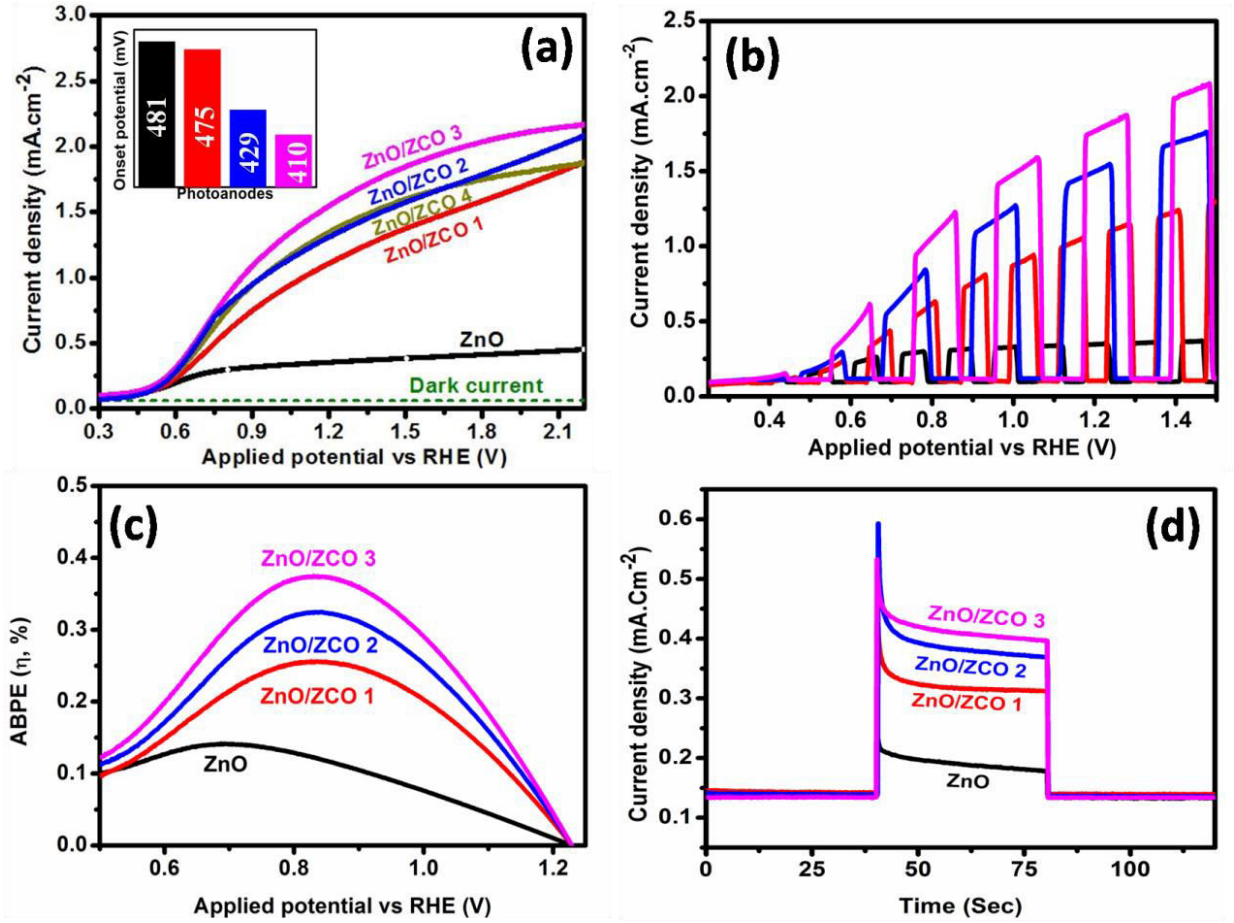

Figure 5.4: (a) The current-voltage plots (inset: onset potential plot), (b) LSV plots under chopped illumination, (c) applied bias photon-to-current conversion efficiency (ABPE, η%) plots, and (d) chrono-amparemmetry (*j*-*t*) plots at 0 V vs. Ag/AgCl.

The photo-conversion proficiency of different photoanodes was evaluated by calculating applied bias photon-to-current efficiency (ABPE, η%). The ABPE was calculated using the following formula [50].

$$\eta\% = \frac{J_{ph} \times (1.229 - V)}{P_{in}} \times 100\% \quad (5.1)$$

Where J_{ph} is the photocurrent density measured from LSV plots, 1.229 V is the thermodynamic water splitting potential, V is the applied potential in RHE between the electrodes, and P_{in} is the power of the illumination (100 mW.cm^{-2}). Figure 5.4c shows the ABPE vs. applied potential plot of all the as-synthesized photoanodes. The ZnO NRs photoanode exhibits only 0.14% ABPE at 0.7 V vs. RHE. The formation of nano-

heterojunction significantly improves the photo-conversion efficiency of the photoanodes. The ABPE for the ZnO/ZCO 3, ZnO/ZCO 2, and ZnO/ZCO 1 photoanodes has been calculated as 0.25, 0.32, and 0.37%, respectively, at 0.83 V vs. RHE. The ZnO/ZCO 3 photoanode shows a ~164% increase in ABPE compared to as-synthesized ZnO.

The photoresponse property of the individual photoelectrodes has been further studied by recording their photoswitching activity obtained from the current-time (*j-t*) plots at the applied potential of 0V vs. Ag/AgCl (Fig. 5.4d). The photoresponse of the photoelectrodes has been found to improve notably after the formation of the $ZnCo_2O_4$ shell layer over ZnO NRs. The self-biased ZnO/ZCO 3 photoanode exhibits the stable and largest saturation photocurrent density of ~ 0.4 $mA.cm^{-2}$.

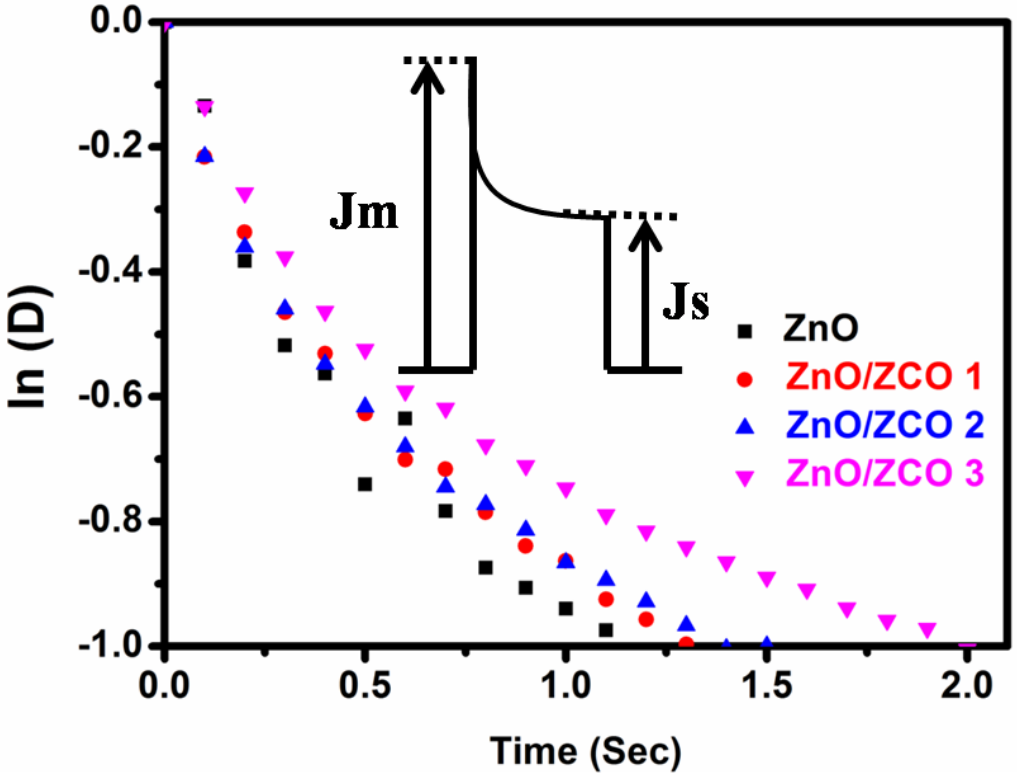

Figure 5.5: Semi logarithmic plots of decay parameter *D* with respect to time for different photoanodes.

In Fig. 5.4d, immediately after solar illumination, a photocurrent spike was observed in the chrono-amperometry profile of all the photoanodes showing the instantaneous generation and separation of electron-hole pairs, offering a high density of photogenerated carriers to the nano-heterostructure photoanodes. A transient decay due to the recombination of photocarriers was also evident before the current density

reached a steady-state saturation value. The transient decay time is a measure of the photocarrier recombination kinetics of individual photoanodes, which can be calculated from a logarithmic plot of decay parameter D, defined as $D = (J_t - J_s)/(J_m - J_s)$, where J_t is the current density at any time t, J_s is the saturation photocurrent, and J_m is the current density of the spike respectively [51,52]. The transient decay time is defined as the time at which ln (D) reaches the value of −1. The calculated decay time (Fig. 5.5) was 1.1, 1.3, 1.4, and 1.9 sec for pristine ZnO, ZnO/ZCO 1, ZnO/ZCO 2, and ZnO/ZCO 3 photoanodes, respectively. Generally, sluggish photocarrier recombination kinetics results in a prolonged decay time. Hence, it is evident that the formation of heterostructure photoanodes significantly reduces photocarrier recombination. Moreover, a prolonged decay time designates that the ZCO shell layer is crucial for quenching or passivating the existing surface defects in ZnO NRs, resulting in photocarrier separation and transportation through the heterojunction interface to higher water splitting efficiency for the nano-heterostructure photoanodes.

In order to deliver a reasonable photocurrent, a photoelectrode should exhibit enhanced solar light absorption efficiency. Here, the light-harvesting performance of pristine ZnO NRs and ZnO/ZCO nano-heterostructure photoanodes were studied using UV-Vis-NIR spectroscopy (Fig. 5.6a). The light absorption threshold for pristine ZnO NRs starts near 378 nm, corresponding to its band-gap 3.26 eV, calculated from the Kubelka Munk plot (Fig. 5.6b).

The ZnO NRs exhibits low absorption of the visible wavelength radiation. The pristine $ZnCo_2O_4$ thin film has been found to have narrow band-gap energy of 2.1 eV (inset of Fig. 5.6b). It is evident from Fig. 5.6a that the deposition of the $ZnCo_2O_4$ shell layers significantly shifts the sharp band-edge absorption of ZnO NRs towards the longer wavelength region. The light-harvesting activity of the ZnO/ZCO nano-heterostructures has also been improved considerably, which is beneficial for improved PEC activity of the photoelectrodes. The improvement of light-harvesting efficiency due to the deposition of $ZnCo_2O_4$ shell layer over ZnO NRs plays a major role in enhancing the overall water splitting efficiency of the nano-heterostructure photoanodes. A shift in absorption wavelength threshold and absorbance in the visible light region has been found to increase with the thickness of the $ZnCo_2O_4$ shell layer. The ZnO/ZCO 3 photoanode exhibits a maximum shift in absorption edge with the maximum absorbance of visible light resulting in improved PEC activity. The direct evidence of the photocarrier recombination profile of the semiconductor photoanodes has been found by recording the PL emission spectra of the photoelectrodes (Fig. 5.6c).

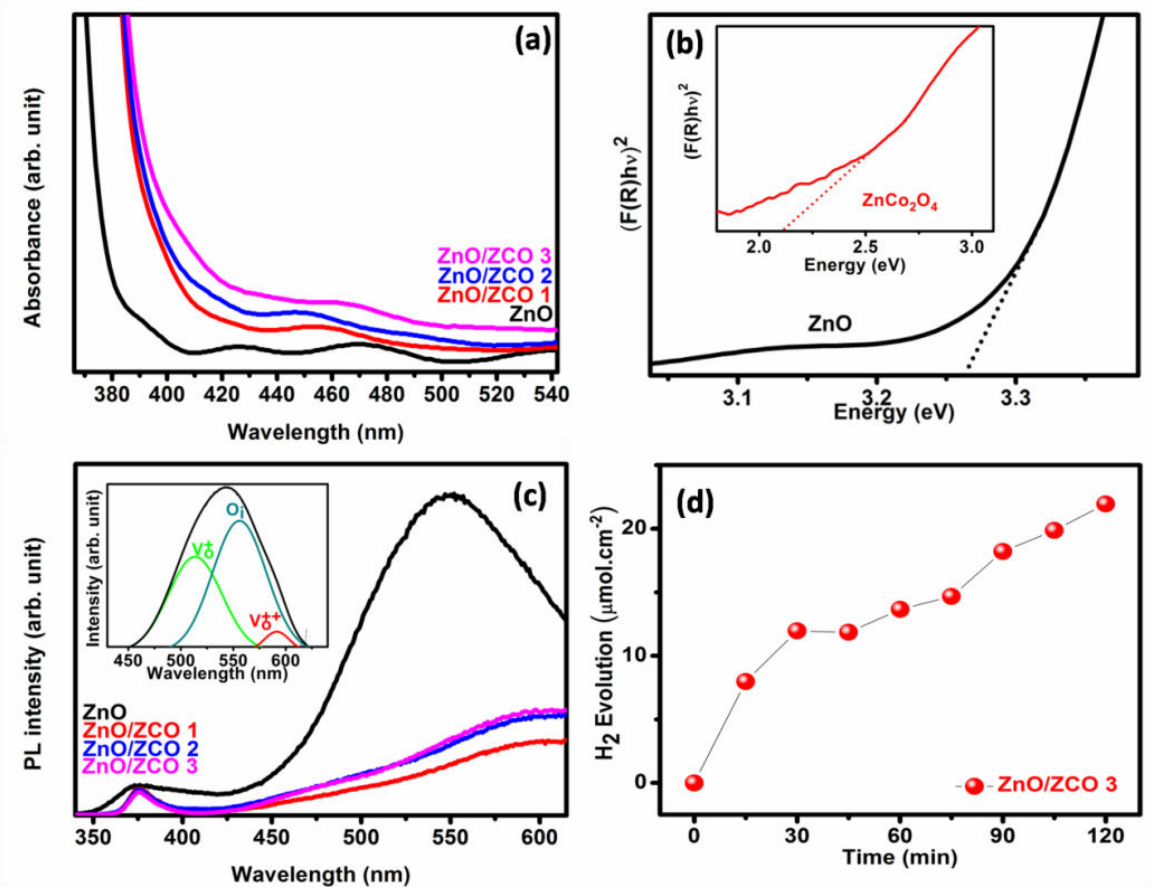

Figure 5.6: (a) UV-Vis absorption spectra of the as-prepared photoelectrodes. (b) Kubelka-Munk plot for ZnO NRs photoanode (Inset: Kubelka-Munk plot for $ZnCo_2O_4$). (c) The steady-state PL emission spectra of the photoanodes, recorded under an excitation wavelength of 320 nm (Inset: deconvoluted defect emission spectra of ZnO). (d) Photocatalytic hydrogen production study of the ZnO/ZCO 3 photoanode.

The PL emission spectrum of bare ZnO NRs consists of two emission bands, one in the UV region (at 376 nm) and the other in the visible region (400-615 nm). The peak at 376 nm appears due to radiative recombination of electron-hole pairs related to band edge transition [53]. The broadband emission in the visible wavelength region arises from the electron-hole recombination taking place at defect states. There are six well-known defect states in ZnO, including oxygen vacancies (V_o), oxygen interstitials (O_i), oxygen antisites (Zn_o), zinc vacancies (V_{zn}), zinc interstitials (Z_{ni}), and zinc antisites (O_{Zn}) [54]. However, the green emission band (~516 nm) of deconvoluted broad visible PL emission band of ZnO NRs (inset Fig. 5.6c) is expected to be originated because of recombination of electrons at singly ionized oxygen vacancies (V_o^+) [55–57]. On the other hand, the yellow emission band (552 nm) in the deconvoluted PL emission band

can be correlated to the radiative recombination between electrons in the conduction band with the holes trapped in the oxygen interstitials (O_i) [57,58]. The emission band located at ~590 nm can be attributed to the doubly ionized oxygen vacancy (V_o^{++}) [54]. Interestingly, the intense defect emission band of ZnO has been remarkably quenched after the formation of nano-heterojunction between ZnO and $ZnCo_2O_4$. Hence, it is expected that due to the interfacial band arrangement between the semiconductors, the photogenerated carriers can easily get transferred to one another. Thus the formation of nano-heterojunction boosts the photocarrier transfer across the hetero-interface, significantly reducing the photocarrier recombination probability. As a result, the intensity of the PL emission peaks quenched remarkably for nano-heterostructure photoanodes. Thus the reduced recombination of photocarriers in nano-heterostructure photoanodes results in enhanced photocurrent density leading to excellent improvement of PEC activity.

Figure 5.6d shows the amounts of hydrogen gas produced at the counter electrode (Pt) at different time intervals using the ZnO/ZCO 3 sample under illumination, which was found to be 22.5 μmol.cm^{-2} after 120 min of operation. The amount of collected hydrogen gas was increased almost linearly during the study. This result indicates the stable PEC water splitting performance of the optimized ZnO/ZCO 3 photoanode.

Figure 5.7a presents the Mott–Schottky (M-S) plots of all the as-synthesized photoelectrodes obtained using the following formula [59].

$$\frac{1}{C^2} = \frac{2}{e\epsilon\epsilon_0 A^2 N_d}\left(V - V_{fb} - \frac{kT}{e}\right) \quad (5.2)$$

Where e is the electronic charge, V_{fb} is the flat band potential, KT/e is the temperature correction term, and ε and ε_0 are the permittivity of semiconductor and free space, respectively.

The positive slope of the M-S curves of all the photoelectrodes (Fig.5.7a) confirms the *n*-type nature of the samples. The flat band potential (V_{fb}) of pristine ZnO NRs was found to be –0.2 V vs. NHE (Fig.5.7a). The pristine $ZnCo_2O_4$ was found to be a *p*-type semiconductor with a negative slope of M-S plot and the flat band potential of +1.09 V vs. NHE (inset of Fig. 5.7a). In comparison to pristine ZnO NRs, a positive shift in flat band potential has been observed for the ZnO/ZCO nano-heterostructure photoanodes, which also indicates the formation of *p*-*n* heterojunction between *p*-$ZnCo_2O_4$ and *n*-ZnO [60,61]. However, the conduction/valance band of an *n*-type/*p*-type semiconductor is ~0.2 V, more negative/positive than their flat band potential [61,62]. Therefore, the

bottom of the conduction band of *n*-ZnO NRs and the top of the valance band of *p*-$ZnCo_2O_4$ are nearly around –0.4 and +1.29 V vs. NHE, respectively.

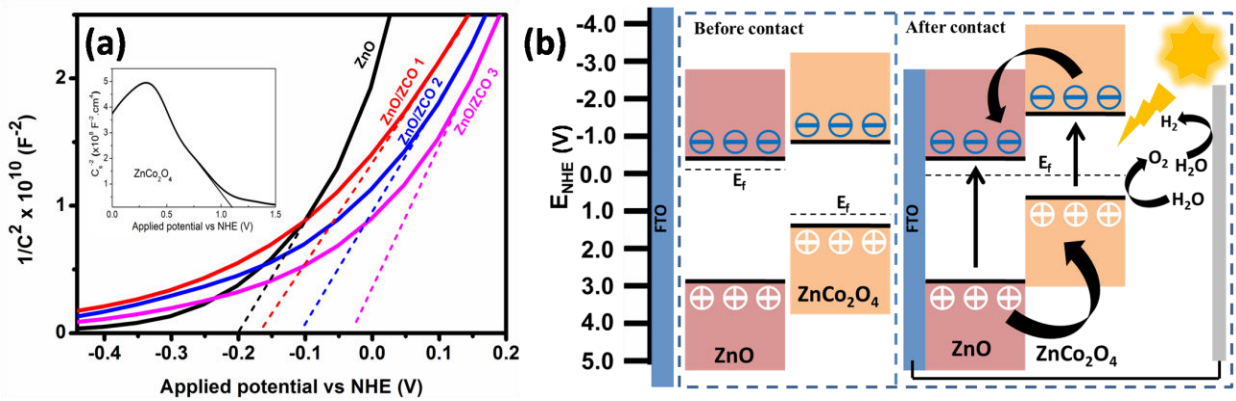

Figure 5.7: (a) Mott-Schottky (M-S) plots of the different as-prepared photoelectrodes (inset: M-S plot of $ZnCo_2O_4$). (b) Band energy diagram of *n*-ZnO and *p*-$ZnCo_2O_4$, before and after the formation of *n-p* heterojunction, with the probable photocarrier generation and transfer mechanism.

Based on the calculated values of band-gap energy of ZnO and $ZnCo_2O_4$, the valance band maxima of ZnO and the conduction band minima of $ZnCo_2O_4$ are positioned at ~2.86 and ~0.8 V vs. NHE, respectively [60]. The energy band diagram of *n*-ZnO and *p*-$ZnCo_2O_4$ before heterojunction formation is approximately shown in Fig.5.7b. Both the conduction and valance band of $ZnCo_2O_4$ is positioned at a higher energy level than that of the ZnO. Hence, after the formation of *n-p* junction, when the Fermi energy levels, the valance and conduction band of the two semiconductors will arrange them in a typical type-II fashion as shown in Fig.5.7b [60]. In the nano-heterojunction photoanode, the photoexcited electrons from the conduction band (Co $_{3d\text{-}eg}$ and Co $_{3d\text{-}t2g}$ levels) of *p*-$ZnCo_2O_4$ can quickly transfer to the conduction band of *n*-ZnO due to the type-II like band arrangement [63]. Similarly, the photogenerated holes from *n*-ZnO can rapidly migrate to *p*-$ZnCo_2O_4$ and finally transfer to the electrolyte to initiate the oxygen evolution reaction (OER). Thus the type-II like *p-n* heterojunction formation boosts effective photocarrier separation required to achieve excellent PEC activity. The *p*-$ZnCo_2O_4$ also exhibits certain kinds of advantages in the OER process. Under OER conditions, loss of Zn^{2+} ions from the tetrahedral site of spinel $ZnCo_2O_4$ creates cationic vacancies, which increases the accessibility of octahedral Co^{3+} sites and also initiates hydroxylation of Co ions near the surface region [64]. The catalytically active Co-rich environment at $ZnCo_2O_4$ surface is responsible for its excellent OER activity [36], which will further boost the OER kinetics of the nano-heterostructure photoanode.

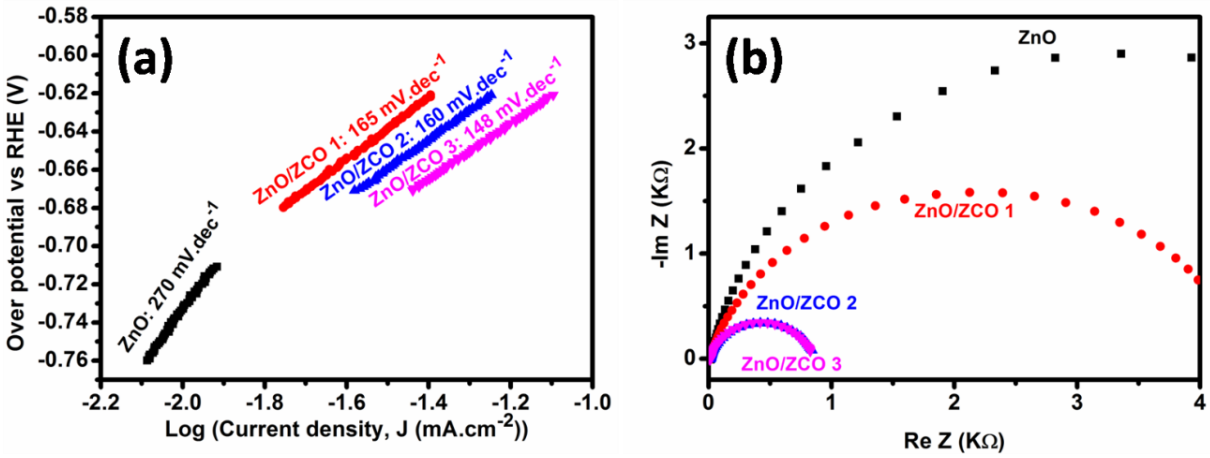

Figure 5.8: (a) Tafel plots (b) EIS curves of the as-prepared photoanodes.

The role of $ZnCo_2O_4$ OER catalysts on PEC reaction kinetics and its underlying effect in enhanced PEC activity of ZnO/ZCO photoanodes has been further studied by Tafel plots (Fig. 5.8a) [65]. Since the Tafel slopes are very often influenced by electron and mass transport, they can be used to understand the OER mechanism of respective photoanodes [65,66]. Tafel slope of ZnO NRs is 270 mV.dec^{-1}, whereas significantly lower Tafel slopes were obtained for ZnO/ZCO 1, 2, and 3 photoanodes with a typical value of 165, 160, and 148 mV.dec^{-1}, respectively. Larger Tafel slop is associated with a sluggish electron transport mechanism [67]. Therefore, a substantial decrease in the value of the Tafel slope for ZnO/ZCO indicates that the incorporation of ZCO boosts up the charge transport process because of enhanced surface OER. This study reveals that $ZnCo_2O_4$ is also acting as a suitable OER catalyst as well as forming a favourable *n-p* heterojunction with ZnO NRs to enhance the overall PEC activity of the nano-heterostructure photoanode.

The electrode/electrolyte interfacial charge transfer and recombination mechanism were further investigated by EIS, conducted at 0V vs. Ag/AgCl under illumination. Figure 5.8b shows the Nyquist plots of the photoanodes, which consist of semicircles with different diameters. Each semicircle for different photoanodes can be related to the appropriate equivalent circuit models. Figure 5.9 shows the equivalent circuit models for the ZnO/ZCO nano-heterojunction and ZnO NRs photoanodes, respectively, with a series resistance (R_s), interfacial resistance ($R_{ZnO/ZCO}$) at ZnO/ZCO heterojunction, trap resistance (R_{trap}), and the charge transfer resistance (R_{ct}) at electrode/electrolyte interface along with the interfacial capacitance ($C_{ZnO/ZCO}$) at ZnO/ZCO heterojunction, capacitance representing constant phase element (CPE_{bulk}) appears due to the charge trapping at the bulk or nano-heterojunction, and the capacitance related to charge

transfer process (C_{ss}) at the electrode/electrolyte interface. The calculated values of the different circuit parameters for the photoanodes are summarized in Table 5.1.

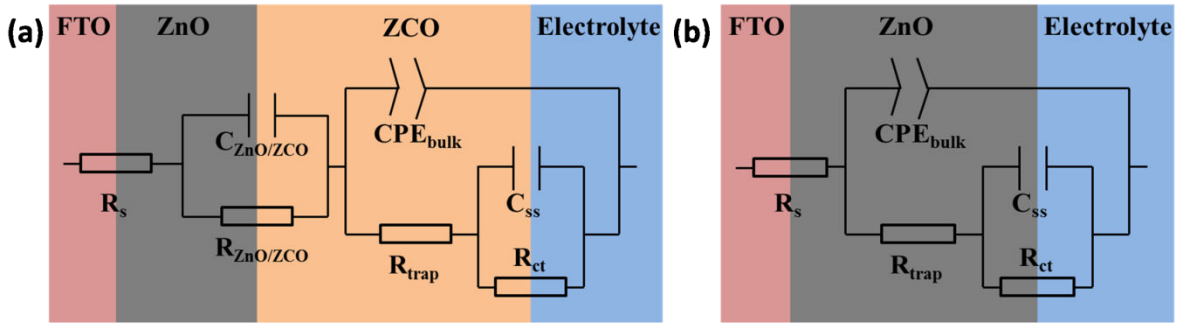

Figure 5.9: The equivalent circuit model for (a) ZnO/ZCO and (b) ZnO NRs photoanode.

It is found that the value of R_{trap} for the photoanodes has reduced because of ZCO anchoring. The lowest value of R_{trap} for ZnO/ZCO 3 again confirms enhanced separation of photocarriers for the photoanode [68].

Table 5.1: Summary of the values of the circuit parameters calculated from the equivalent circuit model for EIS measurements.

Photoanodes	R_s **(Ω)**	R_{trap} **(Ω)**	CPE_{bulk} **(F cm^{-2})**	R_{ct}**(Ω)**	C_{ss} **(F cm^{-2})**	$R_{ZnO/ZCO}$ **(Ω)**	$C_{ZnO/ZCO}$ **(F cm^{-2})**
ZnO	15.74	11.60	2.36×10^{-5}	7966.40	1.00×10^{-6}	--	--
ZnO/ZCO 1	13.41	6.99	3.24×10^{-5}	3467.40	5.56×10^{-6}	131.02	5.93×10^{-6}
ZnO/ZCO 2	12.33	6.13	2.89×10^{-5}	732.70	1.45×10^{-5}	60.95	2.51×10^{-5}
ZnO/ZCO 3	12.24	5.52	3.31×10^{-5}	722.85	1.53×10^{-5}	40.84	2.03×10^{-5}

The negligible variation of the values of CPE_{bulk} indicates that the resultant carrier density of all the photoanodes are almost the same, which is also evident from the similar slope of the M-S plots of the photoanodes [68]. However, the remarkable low R_{ct} and enhanced C_{ss} values for the ZCO anchored photoanodes show that the incorporation of ZCO significantly boosts rapid charge transfer kinetics at the electrode/electrolyte interface resulting in enhanced PEC water splitting activity. The lowest R_{trap} and R_{ct} and the highest value of C_{ss} for ZnO/ZCO 3 photoanode justify its

maximum photocurrent density and ABPE, leading to excellent PEC water oxidation activity.

5.4 Conclusions

The three-dimensional network of a type-II like *n*-ZnO/*p*-$ZnCo_2O_4$ core/shell nano-heterojunction photoanode was successfully fabricated through easy and cost-effective chemical routes. The effective light-harvesting ability of the resultant nano-heterojunction photoanodes was improved due to the incorporation of a narrow band-gap of *p*-$ZnCo_2O_4$. The favorable band alignment between the *n*-ZnO/*p*-$ZnCo_2O_4$ nano-heterojunction boosts the rapid separation of photogenerated electron-hole pairs, enhancing the photocarrier lifetime over the individual semiconductors. Moreover, the remarkable increase in charge transfer mechanism for the *n*-ZnO/*p*-$ZnCo_2O_4$ nano-heterojunction photoanode coupled with the enhanced surface catalytic reaction because of the *p*-$ZnCo_2O_4$ OER catalyst results in a significant increase in photocurrent density and ABPE (351% and 164%, at 1.23V vs. RHE), respectively, over the pristine ZnO NRs. The *n*-ZnO/*p*-$ZnCo_2O_4$ nano-heterojunction photoanode exhibits excellent photochemical stability during water splitting compared with the ZnO NRs. The *p*-$ZnCo_2O_4$ overlayer causes a significant reduction of surface defect states suppressing the photocarrier recombination, leading to a cathodic shift of the onset potential boosting the PEC water oxidation at a low applied voltage. Therefore, the synergistic coupling of *n*-ZnO and *p*-$ZnCo_2O_4$ for a nano-heterojunction photoelectrode serves as an ideal photoanode for solar-driven PEC water oxidation.

Bibliography

[1] D. Maity, K. Karmakar, D. Pal, S. Saha, G.G. Khan, K. Mandal, One-Dimensional p-ZnCo2O4/n-ZnO Nanoheterojunction Photoanode Enabling Photoelectrochemical Water Splitting, ACS Applied Energy Materials. 4 (2021) 11599–11608.

[2] A. Kudo, Y. Miseki, Heterogeneous photocatalyst materials for water splitting, Chemical Society Reviews. 38 (2009) 253–278.

[3] A. Fujishima, K. Honda, Electrochemical photolysis of water at a semiconductor electrode, Nature. 238 (1972) 37–38.

[4] J. Jian, Y. Xu, X. Yang, W. Liu, M. Fu, H. Yu, F. Xu, F. Feng, L. Jia, D. Friedrich, Embedding laser generated nanocrystals in BiVO 4 photoanode for efficient photoelectrochemical water splitting, Nature Communications. 10 (2019) 1–9.

[5] D.K. Lee, K.-S. Choi, Enhancing long-term photostability of BiVO 4 photoanodes for solar water splitting by tuning electrolyte composition, Nature Energy. 3 (2018) 53–60.

[6] J.Y. Kim, G. Magesh, D.H. Youn, J.-W. Jang, J. Kubota, K. Domen, J.S. Lee, Single-crystalline, wormlike hematite photoanodes for efficient solar water splitting, Scientific Reports. 3 (2013) 1–8.

[7] J. Leduc, Y. Goenuellue, P. Ghamgosar, S. You, J. Mouzon, H. Choi, A. Vomiero, M. Grosch, S. Mathur, Electronically-coupled phase boundaries in α-Fe2O3/Fe3O4 nanocomposite photoanodes for enhanced water oxidation, ACS Applied Nano Materials. 2 (2019) 334–342.

[8] J. Zhang, I. Salles, S. Pering, P.J. Cameron, D. Mattia, S. Eslava, Nanostructured WO 3 photoanodes for efficient water splitting via anodisation in citric acid, RSC Advances. 7 (2017) 35221–35227.

[9] Y. Li, Z. Liu, Z. Guo, M. Ruan, X. Li, Y. Liu, Efficient WO3 photoanode modified by Pt layer and plasmonic Ag for enhanced charge separation and transfer to promote

photoelectrochemical performances, ACS Sustainable Chemistry & Engineering. 7 (2019) 12582–12590.

[10] C.Y. Chot, M.N. Chong, A.K. Soh, K.W. Tan, J.D. Ocon, C. Saint, Facile synthesis and characterisation of functional MoO3 photoanode with self-photorechargeability, Journal of Alloys and Compounds. 838 (2020) 155624.

[11] D. Maity, K. Karmakar, K. Mandal, NN type core-shell heterojunction engineering with MoO3 over ZnO nanorod cores for enhanced solar energy harvesting application in a photoelectrochemical cell, Journal of Alloys and Compounds. 791 (2019) 739–746.

[12] S. Bai, J. Han, K. Zhang, J. Sun, J. Guo, R. Luo, D. Li, A. Chen, Triadic Layered Double Hydroxide Modified Semiconductor Heterojunction for PEC Water Splitting, ACS Sustainable Chemistry & Engineering. 8 (2020) 4076–4084.

[13] K. Jeong, P.R. Deshmukh, J. Park, Y. Sohn, W.G. Shin, ZnO-TiO2 core–shell nanowires: a sustainable photoanode for enhanced photoelectrochemical water splitting, ACS Sustainable Chemistry & Engineering. 6 (2018) 6518–6526.

[14] M. Wang, F. Ren, J. Zhou, G. Cai, L. Cai, Y. Hu, D. Wang, Y. Liu, L. Guo, S. Shen, N doping to ZnO nanorods for photoelectrochemical water splitting under visible light: engineered impurity distribution and terraced band structure, Scientific Reports. 5 (2015) 1–13.

[15] A. Galán-González, A.K. Sivan, J. Hernández-Ferrer, L. Bowen, L. Di Mario, F. Martelli, A.M. Benito, W.K. Maser, M.U. Chaudhry, A. Gallant, Cobalt-Doped ZnO Nanorods Coated with Nanoscale Metal–Organic Framework Shells for Water-Splitting Photoanodes, ACS Applied Nano Materials. 3 (2020) 7781–7788.

[16] A.A. Aboud, M. Shaban, N. Revaprasadu, Effect of Cu, Ni and Pb doping on the photo-electrochemical activity of ZnO thin films, RSC Advances. 9 (2019) 7729–7736.

[17] Y. Liu, X. Yan, Z. Kang, Y. Li, Y. Shen, Y. Sun, L. Wang, Y. Zhang, Synergistic effect of surface plasmonic particles and surface passivation layer on ZnO nanorods array for improved photoelectrochemical water splitting, Scientific Reports. 6 (2016) 1–7.

[18] T. Wang, R. Lv, P. Zhang, C. Li, J. Gong, Au nanoparticle sensitized ZnO nanopencil arrays for photoelectrochemical water splitting, Nanoscale. 7 (2015) 77–81.

[19] K. Kim, J.H. Moon, Three-dimensional bicontinuous BiVO4/ZnO photoanodes for high solar water-splitting performance at low bias potential, ACS Applied Materials & Interfaces. 10 (2018) 34238–34244.

[20] J. Jian, R. Kumar, J. Sun, Cu2O/ZnO p–n Junction Decorated with NiO x as a Protective Layer and Cocatalyst for Enhanced Photoelectrochemical Water Splitting, ACS Applied Energy Materials. 3 (2020) 10408–10414.

[21] C. Liu, F. Meng, L. Zhang, D. Zhang, S. Wei, K. Qi, J. Fan, H. Zhang, X. Cui, CuO/ZnO heterojunction nanoarrays for enhanced photoelectrochemical water oxidation, Applied Surface Science. 469 (2019) 276–282.

[22] J.-S. Yang, J.-J. Wu, Low-potential driven fully-depleted BiVO4/ZnO heterojunction nanodendrite array photoanodes for photoelectrochemical water splitting, Nano Energy. 32 (2017) 232–240.

[23] D. Kim, K. Yong, Boron doping induced charge transfer switching of a C3N4/ZnO photocatalyst from Z-scheme to type II to enhance photocatalytic hydrogen production, Applied Catalysis B: Environmental. 282 (2021) 119538.

[24] F.F. Abdi, L. Han, A.H. Smets, M. Zeman, B. Dam, R. Van De Krol, Efficient solar water splitting by enhanced charge separation in a bismuth vanadate-silicon tandem photoelectrode, Nature Communications. 4 (2013) 1–7.

[25] L. Pei, H. Wang, X. Wang, Z. Xu, S. Yan, Z. Zou, Nanostructured TaON/Ta 3 N 5 as a highly efficient type-II heterojunction photoanode for photoelectrochemical water splitting, Dalton Transactions. 47 (2018) 8949–8955.

[26] S.J. Moniz, J. Zhu, J. Tang, 1D Co-Pi modified BiVO4/ZnO junction cascade for efficient photoelectrochemical water cleavage, Advanced Energy Materials. 4 (2014) 1301590.

[27] Y.-K. Hsu, Y.-C. Chen, Y.-G. Lin, Novel ZnO/Fe2O3 core–shell nanowires for photoelectrochemical water splitting, ACS Applied Materials & Interfaces. 7 (2015) 14157–14162.

[28] S.Y. Chae, C.S. Lee, H. Jung, O.-S. Joo, B.K. Min, J.H. Kim, Y.J. Hwang, Insight into charge separation in WO3/BiVO4 heterojunction for solar water splitting, ACS Applied Materials & Interfaces. 9 (2017) 19780–19790.

[29] K. Kim, S.K. Nam, J.H. Park, J.H. Moon, Growth of BiVO 4 nanoparticles on a WO 3 porous scaffold: Improved water-splitting by high band-edge light harvesting, Journal of Materials Chemistry A. 7 (2019) 4480–4485.

[30] E.S. Kim, N. Nishimura, G. Magesh, J.Y. Kim, J.-W. Jang, H. Jun, J. Kubota, K. Domen, J.S. Lee, Fabrication of CaFe2O4/TaON heterojunction photoanode for

photoelectrochemical water oxidation, Journal of the American Chemical Society. 135 (2013) 5375–5383.

[31] H. Yang, J. Yan, Z. Lu, X. Cheng, Y. Tang, Photocatalytic activity evaluation of tetragonal CuFe2O4 nanoparticles for the H2 evolution under visible light irradiation, Journal of Alloys and Compounds. 476 (2009) 715–719.

[32] S. Wu, Y. Xu, X. Li, R. Tong, L. Chen, Y. Han, J. Wu, X. Zhang, Controlled synthesis of porous hierarchical ZnFe2O4 micro-/nanostructures with multifunctional photocatalytic performance, Inorganic Chemistry. 57 (2018) 15481–15488.

[33] Z. Wu, Y. Zhu, X. Ji, NiCo 2 O 4-based materials for electrochemical supercapacitors, Journal of Materials Chemistry A. 2 (2014) 14759–14772.

[34] D. Maity, K. Karmakar, D. Mandal, D. Pal, G.G. Khan, K. Mandal, Earth abundant transition metal ferrite nanoparticles anchored ZnO nanorods as efficient and stable photoanodes for solar water splitting, Nanotechnology. 31 (2020) 475403.

[35] H. Gao, F. Xiao, C.B. Ching, H. Duan, High-performance asymmetric supercapacitor based on graphene hydrogel and nanostructured MnO2, ACS Applied Materials & Interfaces. 4 (2012) 2801–2810.

[36] T.W. Kim, M.A. Woo, M. Regis, K.-S. Choi, Electrochemical synthesis of spinel type ZnCo2O4 electrodes for use as oxygen evolution reaction catalysts, The Journal of Physical Chemistry Letters. 5 (2014) 2370–2374.

[37] J. Li, J. Wang, D. Wexler, D. Shi, J. Liang, H. Liu, S. Xiong, Y. Qian, Simple synthesis of yolk-shelled ZnCo 2 O 4 microspheres towards enhancing the electrochemical performance of lithium-ion batteries in conjunction with a sodium carboxymethyl cellulose binder, Journal of Materials Chemistry A. 1 (2013) 15292–15299.

[38] H. Wu, Z. Lou, H. Yang, G. Shen, A flexible spiral-type supercapacitor based on ZnCo 2 O 4 nanorod electrodes, Nanoscale. 7 (2015) 1921–1926.

[39] S. Wang, Z. Ding, X. Wang, A stable ZnCo 2 O 4 cocatalyst for photocatalytic CO 2 reduction, Chemical Communications. 51 (2015) 1517–1519.

[40] B. Qu, L. Hu, Q. Li, Y. Wang, L. Chen, T. Wang, High-performance lithium-ion battery anode by direct growth of hierarchical ZnCo2O4 nanostructures on current collectors, ACS Applied Materials & Interfaces. 6 (2014) 731–736.

[41] Y. Li, Y. Chu, Y. Li, C. Ma, L. Li, A novel electrochemiluminescence biosensor: Inorganic-organic nanocomposite and ZnCo2O4 as the efficient emitter and accelerator, Sensors and Actuators B: Chemical. 303 (2020) 127222.

[42] A. Sarkar, K. Karmakar, G.G. Khan, Designing Co-Pi Modified One-Dimensional n–p TiO2/ZnCo2O4 Nanoheterostructure Photoanode with Reduced Electron–Hole Pair Recombination and Excellent Photoconversion Efficiency (> 3%), The Journal of Physical Chemistry C. 121 (2017) 25705–25717.

[43] J. Zhang, D. Zhang, Y. Yang, J. Ma, S. Cui, Y. Li, B. Yuan, Facile synthesis of ZnCo 2 O 4 mesoporous structures with enhanced electrocatalytic oxygen evolution reaction properties, RSC Advances. 6 (2016) 92699–92704.

[44] K. Karmakar, D. Maity, D. Pal, K. Mandal, G.G. Khan, Photo-Induced Exciton Dynamics and Broadband Light Harvesting in ZnO Nanorod-Templated Multilayered Two-Dimensional MoS2/MoO3 Photoanodes for Solar Fuel Generation, ACS Applied Nano Materials. 3 (2020) 1223–1231.

[45] L. Zhu, H. Li, Z. Liu, P. Xia, Y. Xie, D. Xiong, Synthesis of the 0D/3D CuO/ZnO heterojunction with enhanced photocatalytic activity, The Journal of Physical Chemistry C. 122 (2018) 9531–9539.

[46] S. Hao, B. Zhang, S. Ball, M. Copley, Z. Xu, M. Srinivasan, K. Zhou, S. Mhaisalkar, Y. Huang, Synthesis of multimodal porous ZnCo2O4 and its electrochemical properties as an anode material for lithium ion batteries, Journal of Power Sources. 294 (2015) 112–119.

[47] Y. Zhu, C. Cao, J. Zhang, X. Xu, Two-dimensional ultrathin ZnCo 2 O 4 nanosheets: general formation and lithium storage application, Journal of Materials Chemistry A. 3 (2015) 9556–9564.

[48] H. Chen, Q. Zhang, X. Han, J. Cai, M. Liu, Y. Yang, K. Zhang, 3D hierarchically porous zinc–nickel–cobalt oxide nanosheets grown on Ni foam as binder-free electrodes for electrochemical energy storage, Journal of Materials Chemistry A. 3 (2015) 24022–24032.

[49] X. Xiong, G. Waller, D. Ding, D. Chen, B. Rainwater, B. Zhao, Z. Wang, M. Liu, Controlled synthesis of NiCo2S4 nanostructured arrays on carbon fiber paper for high-performance pseudocapacitors, Nano Energy. 16 (2015) 71–80.

[50] K.-H. Ye, H. Li, D. Huang, S. Xiao, W. Qiu, M. Li, Y. Hu, W. Mai, H. Ji, S. Yang, Enhancing photoelectrochemical water splitting by combining work function tuning and heterojunction engineering, Nature Communications. 10 (2019) 1–9.

[51] L. Zhang, E. Reisner, J.J. Baumberg, Al-doped ZnO inverse opal networks as efficient electron collectors in BiVO 4 photoanodes for solar water oxidation, Energy & Environmental Science. 7 (2014) 1402–1408.

[52] N.J. Bell, Y.H. Ng, A. Du, H. Coster, S.C. Smith, R. Amal, Understanding the enhancement in photoelectrochemical properties of photocatalytically prepared TiO2-reduced graphene oxide composite, The Journal of Physical Chemistry C. 115 (2011) 6004–6009.

[53] M.L. Singla, M. Kumar, Optical characterization of ZnO nanoparticles capped with various surfactants, Journal of Luminescence. 129 (2009) 434–438.

[54] O.M. Ntwaeaborwa, S.J. Mofokeng, V. Kumar, R.E. Kroon, Structural, optical and photoluminescence properties of Eu3+ doped ZnO nanoparticles, Spectrochimica Acta Part A: Molecular and Biomolecular Spectroscopy. 182 (2017) 42–49.

[55] Ü. Özgür, Y.I. Alivov, C. Liu, A. Teke, Ma. Reshchikov, S. Doğan, V. Avrutin, S.-J. Cho, and H. Morkoç, A comprehensive review of ZnO materials and devices, Journal of Applied Physics. 98 (2005) 11.

[56] A. Teke, Ü. Özgür, S. Doğan, X. Gu, H. Morkoç, B. Nemeth, J. Nause, H.O. Everitt, Excitonic fine structure and recombination dynamics in single-crystalline ZnO, Physical Review B. 70 (2004) 195207.

[57] H. Zeng, G. Duan, Y. Li, S. Yang, X. Xu, W. Cai, Blue Luminescence of ZnO nanoparticles based on non-equilibrium processes: defect origins and emission controls, Advanced Functional Materials. 20 (2010) 561–572.

[58] S.A. Studenikin, N. Golego, M. Cocivera, Fabrication of green and orange photoluminescent, undoped ZnO films using spray pyrolysis, Journal of Applied Physics. 84 (1998) 2287–2294.

[59] K. Gelderman, L. Lee, S.W. Donne, Flat-band potential of a semiconductor: using the Mott–Schottky equation, Journal of Chemical Education. 84 (2007) 685.

[60] X. Chang, T. Wang, P. Zhang, J. Zhang, A. Li, J. Gong, Enhanced surface reaction kinetics and charge separation of p–n heterojunction Co3O4/BiVO4 photoanodes, Journal of the American Chemical Society. 137 (2015) 8356–8359.

[61] S. Wang, T. He, J.-H. Yun, Y. Hu, M. Xiao, A. Du, L. Wang, New Iron-Cobalt Oxide Catalysts Promoting BiVO4 Films for Photoelectrochemical Water Splitting, Advanced Functional Materials. 28 (2018) 1802685.

[62] Y. Matsumoto, Energy positions of oxide semiconductors and photocatalysis with iron complex oxides, Journal of Solid State Chemistry. 126 (1996) 227–234.

[63] B. Cui, H. Lin, X.-C. Zhao, J.-B. Li, W.-D. Li, Visible light induced photocatalytic activity of ZnCo2O4 nanoparticles, Acta Physico-Chimica Sinica. 27 (2011) 2411–2415.

[64] P.W. Menezes, A. Indra, A. Bergmann, P. Chernev, C. Walter, H. Dau, P. Strasser, M. Driess, Uncovering the prominent role of metal ions in octahedral versus tetrahedral sites of cobalt–zinc oxide catalysts for efficient oxidation of water, Journal of Materials Chemistry A. 4 (2016) 10014–10022.

[65] F. Song, X. Hu, Ultrathin cobalt–manganese layered double hydroxide is an efficient oxygen evolution catalyst, Journal of the American Chemical Society. 136 (2014) 16481–16484.

[66] H. Dau, C. Limberg, T. Reier, M. Risch, S. Roggan, P. Strasser, The mechanism of water oxidation: from electrolysis via homogeneous to biological catalysis, ChemCatChem. 2 (2010) 724–761.

[67] H. Vrubel, T. Moehl, M. Grätzel, X. Hu, Revealing and accelerating slow electron transport in amorphous molybdenum sulphide particles for hydrogen evolution reaction, Chemical Communications. 49 (2013) 8985–8987.

[68] M. Wang, A. Krasnok, S. Lepeshov, G. Hu, T. Jiang, J. Fang, B.A. Korgel, A. Alù, Y. Zheng, Suppressing material loss in the visible and near-infrared range for functional nanophotonics using bandgap engineering, Nature Communications. 11 (2020) 1–9.

Chapter 6

Dual Co-Catalyst Activated Fe_2O_3 Photoanodes for Solar Water Oxidation

Hematite (α-Fe_2O_3) photoanode suffers from significant photocarrier recombination and sluggish water oxidation kinetics for photoelectrochemical water splitting. This chapter demonstrates the construction of dual co-catalysts modified Fe_2O_3 nanorods photoanode by strategically incorporating CoPi and $Co(OH)_x$ to address these limitations. The Fe_2O_3/CoPi/$Co(OH)_x$ nanorods photoanode exhibits the lowest ever turn-on potential of 0.4 V_{RHE} (vs. reversible hydrogen electrode) and a photocurrent density of 0.55 mA cm^{-2} at 1.23 V_{RHE}, 358% higher than that of pristine Fe_2O_3 nanorods.

6.1 Preamble

Solar energy is a renewable energy resource, which provides secure, and sustainable energy harvesting capability by tackling global energy demand and the issue of climate change [1]. Photoelectrochemical (PEC) water splitting is a sustainable and eco-friendly pathway for the effective conversion and production of solar energy and fuels [2]. In PEC cell semiconductor photoelectrodes directly convert solar energy into H_2 and O_2 through water splitting [3]. Hematite (*a*-Fe_2O_3), as an n-type oxide semiconductor, has shown remarkable promise as the photoanode in PEC water splitting because of its merits like narrow bandgap (2–2.2eV) that allows absorbing 15% of the solar spectrum, a very positive valance band position ideal for water oxidation, stability against photochemical corrosion, natural abundance [1,4–8]. Despite these, the solar to hydrogen efficiency (STH) for hematite is far below its predicted theoretical value (~15%) [4]. Mainly, the poor electron mobility (10^{-2} to 10^{-1} $cm^2s^{-1}V^{-1}$), the short lifetime of charge carrier, a short hole diffusion length (L_D~ 1.5-5nm), and low absorption coefficient of hematite results in sluggish oxygen evolution reaction (OER) kinetics strongly dominated by photoinduced electron-hole recombination at the semiconductor/electrolyte junction and within the bulk [4,9–11]. As a result, hematite photoanode exhibits limited photocurrent density and large turn-on voltage for PEC water oxidation.

Studies have suggested that the water oxidation kinetics at the surface of hematite photoanode can be enhanced by improving the hole transfer efficiency [12–14]. Hence, effective surface state passivation of hematite photoanode can enhance hole transfer efficiency and surface photo-hole density by suppressing the photocarrier recombination leading to optimized water oxidation kinetics [1,12]. The incorporation of OER co-catalysts overlayers like $NiFeO_x$, Ni−Fe $(OH)_x$, and CoPi suppresses the surface state mediated recombination of photocarriers and accelerates the water oxidation reaction in hematite photoanode. The incorporation of earth-abundant CoPi co-catalyst on the hematite surface enhances the band bending at the semiconductor/electrolyte interface and reduces the surface carrier recombination shifting the turn-on potential negatively [15–17]. The CoPi overlayer also suppresses the trap state meditated charge transfer in hematite, which reduces the surface carrier recombination and the turn-on potential too [10]. Similarly, $Co(OH)_x$ is also a recognized hole-extraction OER co-catalyst, which is capable of boosting the interfacial charge transfer and quenching the excess energy barrier required for O-O bond formation [18–20]. However, the effect of $Co(OH)_x$ modification on the PEC property of hematite nanostructures is not properly studied.

Against this backdrop, this study demonstrates the synthesis of Fe_2O_3 NRs photoanode modified by dual CoPi and $Co(OH)_x$ OER co-catalysts for PEC water oxidation. The dual co-catalyst coupled Fe_2O_3/CoPi/$Co(OH)_x$ NRs photoanode exhibits enhanced light-harvesting efficiency with reduced surface state-related recombination in Fe_2O_3 NRs over the individual co-catalysts. The resultant carrier density and surface photovoltage of the photoanode increases, and the depletion width decreases due to dual co-catalyst anchoring. This results in enhanced photocurrent because of band bending, bosting the hole collection efficiency, and ultralow turn-on potential for PEC water oxidation in the nearly neutral pH conditions.

6.2 Experimental Methods

6.2.1 α-Fe_2O_3 Nanorods (NRs) Synthesis

The α-Fe_2O_3 NRs were grown on the conducting surface of FTO by one-step solvothermal method. A 30 ml clear homogeneous solution of Fe precursor was prepared by dissolving 0.15M $FeCl_3.6H_2O$ (Sigma Aldrich) and 1M $NaNO_3$ in DI water. Finally, the solution was transferred to a 50 ml sealed Teflon lined stainless steel autoclave with a pre-cleaned FTO substrate lined against the wall with conducting surface facing down. The autoclave was heated to 100°C for 3 hours. After cooling down to room temperature, the FeOOH nanorods grown on the FTO substrate were collected and thoroughly washed with DI water and ethanol several times. Finally, the α-Fe_2O_3 NRs were obtained by annealing the as-prepared FeOOH nanorods (NRs) at 550 °C for 2 hours.

6.2.2 Fe_2O_3/CoPi NRs Synthesis

The deposition of CoPi co-catalyst layer on Fe_2O_3 NRs was conducted by photoelectrodeposition (PED) method by a three-electrode electrochemical workstation using the as-prepared Fe_2O_3 NRs as a working electrode, an Ag/AgCl electrode as a reference electrode, and a platinum wire as a counter electrode. A 0.5 mM $Co(NO_3)_2$ solution in 0.1M potassium phosphate buffer (pH 7) was used as an electrolyte for PED. Before the deposition, each as-prepared Fe_2O_3 NRs sample was dipped into the aqueous electrolyte for 30 min, and then the PED has conducted at 0.9V vs. Ag/AgCl for 200 sec under 10 $mW.cm^{-2}$ white light illumination. The Fe_2O_3/CoPi sample prepared for 200 sec of PED is found to be the optimized sample. However, after the deposition, the samples were rinsed with DI water and ethanol and dried under a vacuum.

6.2.3 Fe_2O_3/CoPi/$Co(OH)_x$ NRs Synthesis

The $Co(OH)_x$ co-catalyst overlayer was grown on the surface of CoPi coated Fe_2O_3 NRs by the successive ionic layer adsorption and reaction (SILAR) method. The as-prepared Fe_2O_3/CoPi NRs sample was successively dipped into the 50 mM aqueous solution of $Co(CH_3COO)_2$, DI water, 100 mM aqueous solution of NaOH, and DI water for 60 sec each, to complete one cycle of $Co(OH)_x$ deposition. The Fe_2O_3/CoPi/$Co(OH)_x$ NRs sample prepared by repeating the SILAR process for five times provides the optimum performance.

6.2.4 Material Characterizations

The microstructure of the fabricated photoanodes was thoroughly investigated with a field emission scanning electron microscope (FESEM, FEI Quanta-200 Mark-2) and transmission electron microscopy (TEM, JEOL JEM 2100). The elemental distribution of constituent elements in the respective photoanodes was understood with energy-dispersive X-ray spectroscopy (EDAX, Oxford Instruments) mapping images. The ionic states of the constituents elements of resultant photoanodes were identified with X-ray photoelectron spectroscopy (XPS, Omicron Multiprobe Electron Spectroscopy System XM 500, X-ray source: monochromatic Al K_α line and vacuum level $2.5X10^{-10}$ mbar). The UV-Vis. spectra of the samples were studied using a JASCO V-670 Spectrophotometer.

6.2.5 Photoelectrochemical Studies

Photoelectrochemical studies of the as-prepared materials were carried with a software-controlled three-electrode electrochemical workstation (CHI660E, CH Instruments). Different photoanodes with a $1cm^2$ active area were used as working electrodes, a platinum wire as a counter electrode, and an Ag/AgCl electrode as the reference electrode. A 0.5M Na_2SO_4 aqueous solution (pH 6.4) was used as electrolyte and a AM 1.5 simulated solar light (intensity 100 $mW.cm^2$, LCS-100, Newport, Model 94011A) was used as light source. All the potential applied to the working electrode against Ag/AgCl electrode and converted to the RHE scale using the equation [21]

$$E_{RHE} = E_{Ag/AgCl} + 0.059 \times pH + E^0_{Ag/AgCl} \quad (6.1)$$

where, $E^o_{Ag/AgCl}$ = 0.1976 at 25°C and $E_{Ag/AgCl}$ is the experimentally recorded potential against Ag/AgCl reference electrode.

6.3 Results and Discussion

6.3.1 Morphological, Structural, and Chemical Analysis

The structure and morphology of the as-prepared Fe_2O_3 and Fe_2O_3/CoPi/$Co(OH)_x$ nanostructures examined with the field emission scanning electron microscope (FESEM) show vertically oriented dense arrays of one-dimensional nanorods (NRs) of diameter ~ 60 nm (Fig. 6.1a and b). The transmission electron microscope (TEM) micrograph (Fig. 6.1c) of the Fe_2O_3/CoPi/$Co(OH)_x$ further confirms the NRs like structure, where the deposition of a uniform ultra-thin co-catalysts overlayers on the surface of Fe_2O_3 NRs is evident (Fig. 6.1d). Fig. 6.1d reveals the growth of an extremely thin amorphous CoPi co-catalyst overlayer of thickness ~ 3 nm followed by another thin crystalline $Co(OH)_x$ co-catalyst overlayer (thickness ~ 5 nm) on the surface of Fe_2O_3 NRs. The high-resolution TEM (HRTEM) image (Fig. 6.1e) of Fe_2O_3/CoPi/$Co(OH)_x$ NRs demonstrates that the lattice spacing of 0.368 and 0.244 nm corresponds to the distance between [012] and [101] planes of Fe_2O_3 NRs and $Co(OH)_x$ overlayer. The SAED pattern (Fig. 6.1f) further confirms the [101] crystallographic orientation of $Co(OH)_x$ and [122], [226], [113] and [116] orientations of polycrystalline Fe_2O_3. The chemical state of the constituent elements of the as-prepared photoanodes was identified with X-ray photoelectron spectroscopy (XPS). The high-resolution XPS spectrum of Fe 2p (Fig. 6.1g) consists of doublets $2p_{3/2}$ and $2p_{1/2}$ situated at binding energies 711 and 724.8 eV, and the satellite peak at 719.1 eV corresponds to the +3 oxidation state of Fe [22,22–24]. Generally, satellite peaks appear due to the co-existence of X-ray source with slightly higher energy. Figure 6.1h shows the deconvoluted high-resolution XPS spectrum of Co 2p, where Co $2p_{1/2}$ and $2p_{3/2}$ peaks centered at 796.88 and 782.40eV, respectively, originate due to Co^{2+} state [25]. Similarly, the dublets at 795.40 and 780.17 eV corresponds to the Co $2p_{1/2,}$ and $2p_{3/2}$ can be attributed to the Co^{3+} states [25]. Moreover, the satellite peaks in Fig. 1h, centered at 795.2 and 804.25 eV, also appears because of the coexistence of Co^{2+} and $Co^{3+.}$ [12,26,27] Figure 6.1i shows the XPS spectrum of P 2p centered around 133.28 eV, indicating the presence of phosphate group in the as-prepared photoanode [28]. The deconvoluted XPS spectrum of O 1s (Fig. 6.1j) consists of three main peaks. The peaks at the binding energies of 528.70, 531, and 532.60 eV are assigned to the lattice oxygen, oxygen associated with phosphate and hydroxide groups or oxygen vacancies, respectively [25,27].

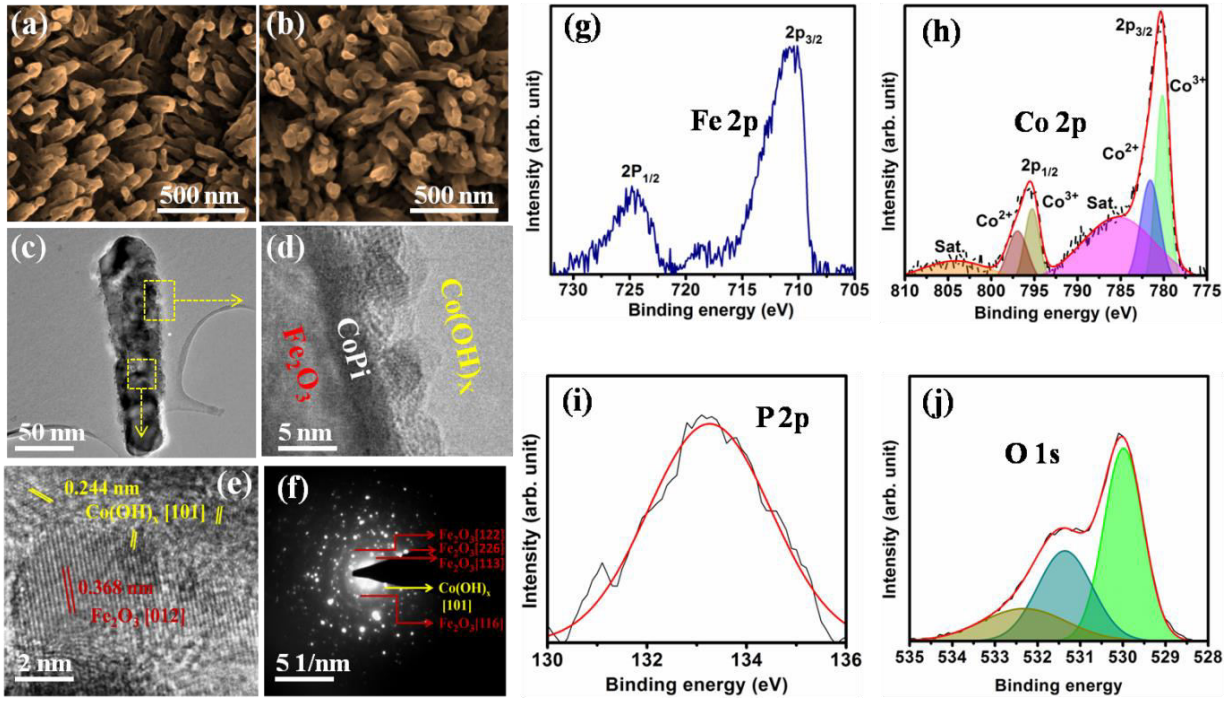

Figure 6.1: FESEM image of (a) Fe_2O_3 and (b) Fe_2O_3/CoPi/$Co(OH)_x$ NRs. (c) and (d) TEM micrographs, (e) HRTEM imageand (f) SAED pattern of the Fe_2O_3/CoPi/$Co(OH)_x$ NRs. High resolution XPS spectra of (g) Fe 2p, (h) Co 2p, (i) P 2p and (j) O 1s.

6.3.2 PEC and Optical Characterizations

The PEC performance of the pristine and the co-catalysts modified photoanodes was studied by recording the current vs. potential profile (Fig. 6.2a). Pristine Fe_2O_3 NRs exhibit a low photocurrent density of 0.12 mA.cm^{-2} at 1.23 V vs. RHE and a large turn-on potential of 1V_{RHE}. The optimized structure of the dual co-catalysts modified Fe_2O_3/CoPi/$Co(OH)_x$ NRs delivers an improved maximum photocurrent density of 0.55 mA.cm^{-2} at 1.23 V vs. RHE with a remarkably ultralow turn-on potential of 0.40 V_{RHE}

(Fig. 6.2b), which is the lowest value of turn-on potential reported for Fe_2O_3 photoanode till date (Table 6.1). The dual co-catalysts modified photoanode also exhibits impressive photocurrent density over the single co-catalyst anchored Fe_2O_3/$Co(OH)_x$ (0.23 mA.cm^{-2} at 1.23 V vs. RHE) and Fe_2O_3/CoPi (0.36 mA.cm^{-2} at 1.23 V vs. RHE) photoanodes. The water-splitting turn-on potential for the Fe_2O_3/$Co(OH)_x$ and Fe_2O_3/CoPi photoanodes also shifted cathodically to 0.47 and 0.51 V vs. RHE, respectively (Fig. 6.2b). The low turn-on potential and large photocurrent density of Fe_2O_3/CoPi/$Co(OH)_x$ NRs photoanode in nearly neutral pH conditions indicate the merit of synergistic coupling of

dual co-catalysts for OER. The enhanced photocurrent density of Fe_2O_3/CoPi/$Co(OH)_x$ NRs at the low applied potential region over the other photoanodes demonstrates that the dual co-catalyst loading significantly suppresses the surface state mediated recombination of holes in the photoanode. The current vs. potential profiles of the photoanodes under chopped illumination conditions (Fig. 6.2c) demonstrate that the Fe_2O_3/CoPi/$Co(OH)_x$ NRs photoanode exhibits enhanced photoresponse. Interestingly, the transient photocurrent decay for the dual co-catalyst modified Fe_2O_3/CoPi/$Co(OH)_x$ NRs photoanode has reduced over the other photoanodes.

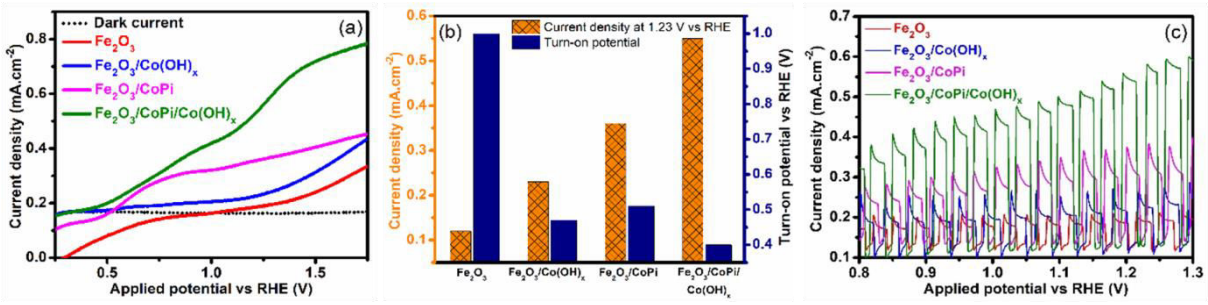

Figure 6.2: (a) The PECcurrent vs. potential plots, (b) variation of photocurrent density and turn-on potential, and (c) current vs. potential curves under chopped light.

This result indicates that the coupling of dual co-catalysts (CoPi and $Co(OH)_x$) reducees the surface state-related recombination, boosting rapid hole separation for OER [29]. Overall, the PEC studies suggest that incorporation of ultrathin CoPi layer on Fe_2O_3 NRs helps in rapid migration of photogenerated holes resulting in an enhanced lifetime for photocarrirs.

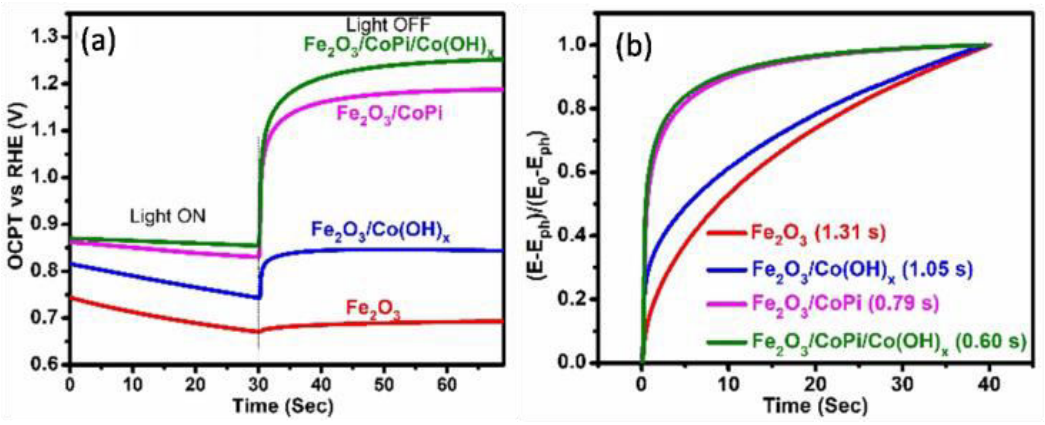

Figure 6.3: (a) OCPT vs. time plots and (b) normalized OCPT decay profiles under illumination and in the dark.

The presence of $Co(OH)_x$ co-catalyst over the CoPi further harvests the photo-holes from CoPi, confirming effective charge separation for water oxidation. Moreover, the hole scavenger $Co(OH)_x$ co-catalyst also provides active sites for water splitting boosting the OER kinetics and photocurrent.

Table 6.1: Summary of PEC performance of OER co-catalysts modified hematite photoanodes.

Photoanode [Ref]	Electrolyte	Turn-on voltage (V_{RHE})	Photocurrent density ($mA.cm^{-2}$) at 1.23 V_{RHE}
Fe_2O_3/CoPi/Co(OH)xNRs [This work]	0.5M Na_2SO_4	0.4	0.55
Fe_2O_3/CoPi thin film[1]	0.1M KPi	0.9	0.36
Fe_2O_3/CoPifilm[10]	0.1M KPi	1	0.25
HydrogentratedFe_2O_3/TiO_2/CoPi[30]	1 M KOH	0.55	6
Fe_2O_3/$NiFeO_x$[31]	1M NaOH	0.45	1.2
Fe_2O_3/$CoFeO_x$mesoporous[32]	1M NaOH	0.7	1.2
Fe_2O_3/$Co(OH)_2$/Co_3O_4 film[33]	0.1 M KOH	0.95	0.8
Ti:Fe_2O_3/Co_3O_4/CoPi NRs[34]	1 M KOH	0.64	2.7
Fe_2O_3/citrate/$NiFe(OH)_x$ NRs[12]	1 M KOH	0.5	0.55
Fe_2O_3/Co3O4 Nanoworm [35]	1 M KOH	0.62	3.48

The surface photovoltage generated at the photoanodes can be estimated from the difference in the open circuit potential (OCPT) under the dark to illumination conditions of the OCPT vs. time plots (Fig. 6.3a). The insignificant photovoltage generated at the surface of pristine Fe_2O_3 NRs (0.02 V vs. RHE) has enhanced because of co-catalysts anchoring. The surface photovoltage for Fe_2O_3/$Co(OH)_x$ and Fe_2O_3/CoPi photoanodes have been measured as 0.10 and 0.35 V_{RHE}, respectively. The dual co-

catalysts modified optimized structure of $Fe_2O_3/CoPi/Co(OH)_x$ NRs photoanode exhibits a top photovoltage of $0.40V_{RHE}$. The large photovoltage generated in $Fe_2O_3/CoPi/Co(OH)_x$ NRs photoanode signifies that the dual co-catalyst modification reduces the surface trap states resulting in the enhanced transfer of photogenerated holes for water oxidation.[21,36] The normalized OCPT vs. time plots (Fig. 6.3b), showing the photovoltage decay profile of the photoanodes, demonstrate that the co-catalyst modified photoanodes exhibits faster photovoltage decay compare to pristine Fe_2O_3 photoanode. The dual co-catalyst modified Fe_2O_3 photoanode was found to have the fastest photovoltage decay among all the photoanodes. The decay life time of individual photoanodes was calculated by fitting the normalized OCPT vs. time curves with a bi-exponential decay function with two time constants τ_1 and τ_2 [12].

$$f(t) = A_0 + A_1 e^{-\frac{t}{\tau_1}} + A_2 e^{-\frac{t}{\tau_2}} \tag{6.2}$$

and

$$\tau_m = \frac{\tau_1 \tau_2}{\tau_1 + \tau_2} \tag{6.3}$$

Where τ_1 and τ_2 are the time component associated with band-to-band and band-to-surface state recombination process. τ_m is the harmonic mean. The total half-life time is calculated as $\ln(2\tau_m)$ [12]. The photovoltage decay half life time for the Fe_2O_3, $Fe_2O_3/Co(OH)_x$, $Fe_2O_3/CoPi$, and $Fe_2O_3/CoPi/Co(OH)_x$ photoanodes are calculated as 1.31, 1.05, 0.79, and 0.60 s, respectively.The significantly reduced half life time for the $Fe_2O_3/CoPi/Co(OH)_x$ NRs photoanode indicates that the incorporation of dual co-catalysts has remarkably suppressed the surface states and quenched the loss of photo-holes due to the recombination at the surface states, improving hole transport for OER [12,34].

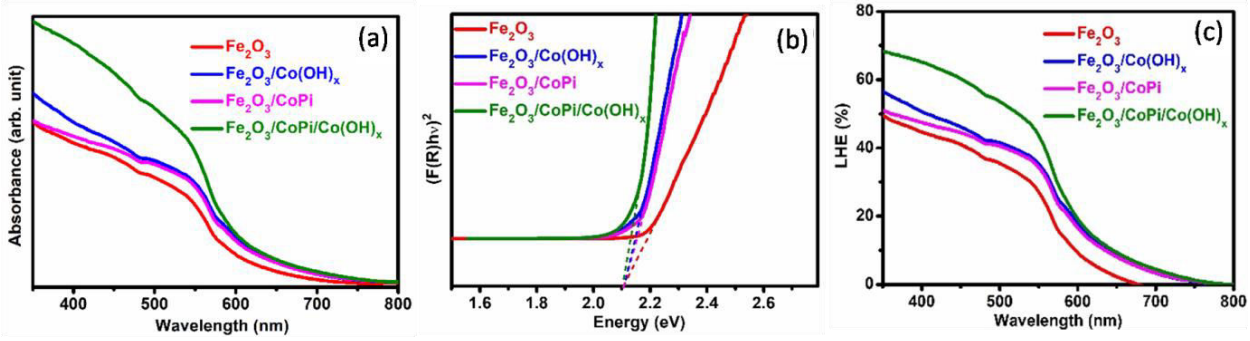

Figure 6.4: (a) The UV-vis absorption spectrum of the as-prepared photoanodes. (b) The Kubelka–Munk plots for the as-prepared photoanodes obtained from the UV-Vis data and (c) The light-harvesting efficiency (LHE%) of the different photoanodes.

The UV-vis absorption spectrum (Fig. 6.4a) of the photoanodes indicates that the band edge-related light absorption for the pristine Fe_2O_3 NRs has improved because of dual co-catalyst modification. The band-gap energy of all the photoanodes is calculated as 2.12 eV (Fig. 6.4b). The light-harvesting efficiency (LHE %) of the photoanodes is calculated as [29]

$$\text{LHE}\ (\%) = 1 - 10^{-A(\lambda)} \tag{6.4}$$

where $A(\lambda)$ is the absorbance at different wavelengths obtained from the UV-vis spectrum. The light-harvesting efficiency (LHE, %) of the photoanodes is shown in Fig. 6.4c. It is evident that the single co-catalyst modification only brings a nominal change in the LHE of the Fe_2O_3 NRs. However, the LHE is found to improve within 350–550 nm range because of dual co-catalyst coupling.

The charge trapping and transfer process at the photoanode/electrolyte interface was further investigated by EIS under illumination. The Nyquist plots of each photoanodes (Fig. 6.5a) were consisting of a semicircle with two arcs, fitted to an equivalent circuit model (Inset of Fig. 6.5a). The values of the charge trapping and transfer parameters calculated by using the equivalent circuit show that the values of R_{trap} have reduced for the co-catalysts modified photoanodes. The lowest value of R_{trap} for Fe_2O_3/CoPi/$Co(OH)_x$ NRs indicates the significant reduction of recombination of photoinduced electron-hole pair in this photoanode. The large enhancement in C_{bulk} value for the co-catalyst anchored photoanodes signifies the enhanced carrier densityof the photoanodes because of co-catalysts incorporation [37]. The significantly reduced R_{ct} and enhanced C_{ss} values for the co-catalysts modified photoanodes confirm the enhanced photocarrier transportation at photoanode/electrolyte interface resulting in water oxidation occurs via surface states [38]. The lowest value of R_{ct} and R_{trap} for the Fe_2O_3/CoPi/$Co(OH)_x$ NRs photoanode indicates that dual co-catalysts modification provides a conducting path to the photo-holes and improves the intrinsic conductivity of the photoanode, helping to achieve the highest photocurrent and low turn-on potential for PEC water oxidation [10].

The Mott-Schottky plots were recorded in the dark at a frequency of 10 kHz. The flat band potential (E_{fb}) was estimated from the Mott–Schottky plots, using the equation [39]

$$\frac{1}{C_s^2} = \frac{2}{e\varepsilon\varepsilon_0 A^2 N_d}\left(E - E_{fb} - \frac{k_B T}{e}\right) \tag{6.5}$$

where, C_s is the space charge capacitance, e is the elementary charge (1.6×10^{-19} C), ε is the dielectric constant of the semiconductor photoanode, ε_0 the free space permittivity, A is the geometrical area of the electrode, N_d is the carrier density, E is the applied potential, k_B the Boltzmann's constant, and T is the temperature in the absolute scale.

The flat band potentials (V_{fb}) of the photoanodes estimated from the Mott-Schottky (M-S) plots (Fig. 6.5d) demonstrate that the value in V_{fb} (~0.18 V vs. RHE) is nearly identical for all the photoanodes. This result indicates that the band unpinning does not have any contribution towards the water oxidation reaction under dark conditions [1]. The charge carrier density calculated from the slope of the M-S plot in the space charge region for the pristine Fe_2O_3 NRs (3.4×10^{18}) is found to increase because of co-catalyst modification.

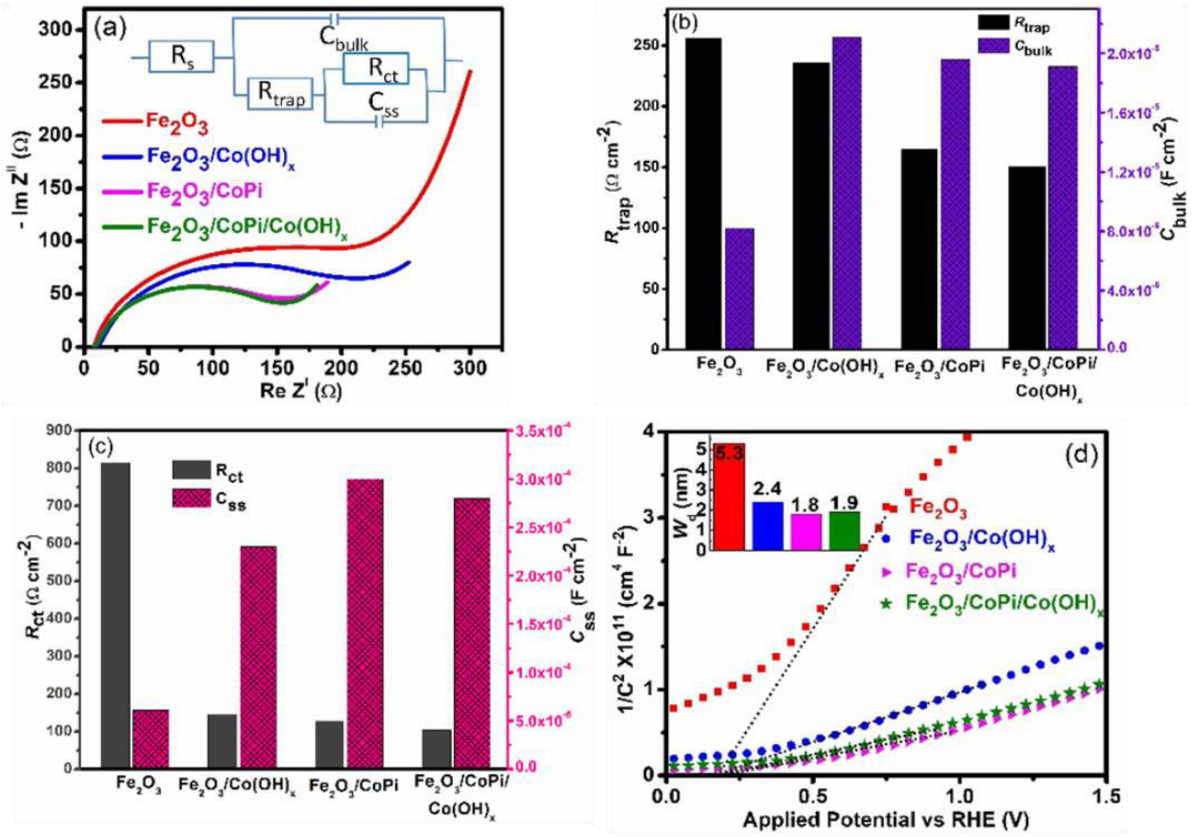

Figure 6.5: **(**a) EIS Nyquist plotsand the equivalent circuit diagram (inset), (b) variation of R_{trap} and $C_{bulk,}$ values (c) variation of R_{ct} and C_{ss} values, and (d) Mott–Schottky plots and variation of depletion width (W_d inset) for the different photoanodes.

The charge carrier density (N_d) was calculated using the following equation [40]

$$N_d = (2/e\varepsilon\varepsilon_0)[d(1/C^2)/dV]^{-1} \quad (6.6)$$

where e is the electron charge, ε is the dielectric constant of hematite, ε_0 is the permittivity of vacuum, and $d(1/C^2)/dV$ is the slop of the obtained Mott-Schottky curve. The charge carrier density for the $Fe_2O_3/Co(OH)_x$, $Fe_2O_3/CoPi$, and $Fe_2O_3/CoPi/Co(OH)_x$ NRs photoanodes are estimated as 1.6×10^{19}, 2.9×10^{19}, and

2.4×10^{19}, respectively. The co-catalyst modification can not significantly enhance the carrier density of the photoanodes, which again supports the enhanced charge transfer process to maximize the PEC performance in co-catalyst modified photoanodes [37]. The depletion width (W_d) was calculated from the equation [41]

$$W_d = ((2\varepsilon\varepsilon_0 V_{bi})/(eN_d))^{1/2} \quad (6.7)$$

Where ε is the dielectric constant of hematite, which was considered as 80, V_{bi} is the built-in potential, which was estimated by subtracting the flat-band potential from the applied potential. The depletion width (W_d) of the Fe_2O_3, Fe_2O_3/$Co(OH)_x$, Fe_2O_3/CoPi, and Fe_2O_3/CoPi/$Co(OH)_x$ NRs photoanodes are estimated as 5.3, 2.4, 1.8, and 1.9 nm, respectively, under the applied bias of 1.23 V vs. RHE (inset of Fig. 3d). A significant decrease of W_d for the co-catalyst modified photoanodes indicates favorable band bending for accelerated transfer of photoholes from the depletion region to the surface, suppressing the charge recombination [42]. However, here the Fe_2O_3/CoPi photoanode exhibits the highest carrier density and the shortest W_d value, which is consistent with the C_{bulk} value estimated in the EIS studies.

6.4 Conclusions

In summary, this work demonstrates the synthesis of CoPi and $Co(OH)_x$ dual co-catalysts modified hematite NRs photoanode with ultralow turn-on voltage (0.4 V vs. RHE) and high photocurrent density for water oxidation. The Fe_2O_3/CoPi/$Co(OH)_x$ shows enhanced light-harvesting efficiency over the other photoanodes. The PEC characteristics unveil that the dual co-catalyst overlayer also increases surface photovoltage generation through reduction of the surface states responsible for photocarrier recombination and boosts the photohole transfer for OER. The dual co-catalysts modification also enhances carrier density and reduces the depletion width, leading to large photocurrent and enhanced band bending for rapid hole collection. Overall the dual co-catalysts overlayer improves the oxygen evolution reaction kinetics and electrical conductivity for hematite NRs, resulting in improved PEC water oxidation. Therefore, the idea of modifying hematite NRs with dual OER co-catalysts overlayer can be adopted to enhance the PEC activity of other oxide semiconductors ($BiVO_4$, $BiFeO_3$, TiO_2, etc.).

Bibliography

[1] B. Klahr, S. Gimenez, F. Fabregat-Santiago, J. Bisquert, T.W. Hamann, Photoelectrochemical and impedance spectroscopic investigation of water oxidation with "Co–Pi"-coated hematite electrodes, Journal of the American Chemical Society. 134 (2012) 16693–16700.

[2] G.M. Carroll, D.K. Zhong, D.R. Gamelin, Mechanistic insights into solar water oxidation by cobalt-phosphate-modified α-Fe 2 O 3 photoanodes, Energy & Environmental Science. 8 (2015) 577–584.

[3] T. Hisatomi, J. Kubota, K. Domen, Recent advances in semiconductors for photocatalytic and photoelectrochemical water splitting, Chemical Society Reviews. 43 (2014) 7520–7535.

[4] K.-Y. Yoon, J. Park, M. Jung, S.-G. Ji, H. Lee, J.H. Seo, M.-J. Kwak, S.I. Seok, J.H. Lee, J.-H. Jang, NiFeOx decorated Ge-hematite/perovskite for an efficient water splitting system, Nature Communications. 12 (2021) 1–12.

[5] Q. Yang, J. Du, J. Li, Y. Wu, Y. Zhou, Y. Yang, D. Yang, H. He, Thermodynamic and kinetic influence of oxygen vacancies on the solar water oxidation reaction of α-Fe2O3 photoanodes, ACS Applied Materials & Interfaces. 12 (2020) 11625–11634.

[6] Y. Makimizu, J. Yoo, M. Poornajar, N.T. Nguyen, H.-J. Ahn, I. Hwang, S. Kment, P. Schmuki, Effects of low oxygen annealing on the photoelectrochemical water splitting properties of α-Fe 2 O 3, Journal of Materials Chemistry A. 8 (2020) 1315–1325.

[7] N.A. Arzaee, M.F.M. Noh, N.S.H.M. Ita, N.A. Mohamed, S.N.F.M. Nasir, I.N.N. Mumthas, A.F. Ismail, M.A.M. Teridi, Nanostructure-assisted charge transfer in α-Fe 2 O 3/gC 3 N 4 heterojunctions for efficient and highly stable photoelectrochemical water splitting, Dalton Transactions. 49 (2020) 11317–11328.

[8] J. Cai, H. Chen, C. Liu, S. Yin, H. Li, L. Xu, H. Liu, Q. Xie, Engineered Sn-and Mg-doped hematite photoanodes for efficient photoelectrochemical water oxidation, Dalton Transactions. 49 (2020) 11282–11289.

[9] R.F.G. Gardner, F. Sweett, D.W. Tanner, The electrical properties of alpha ferric oxide—I.: The impure oxide, Journal of Physics and Chemistry of Solids. 24 (1963) 1175–1181.

[10] G.M. Carroll, D.R. Gamelin, Kinetic analysis of photoelectrochemical water oxidation by mesostructured Co-Pi/α-Fe 2 O 3 photoanodes, Journal of Materials Chemistry A. 4 (2016) 2986–2994.

[11] F. Le Formal, N. Tetreault, M. Cornuz, T. Moehl, M. Grätzel, K. Sivula, Passivating surface states on water splitting hematite photoanodes with alumina overlayers, Chemical Science. 2 (2011) 737–743.

[12] M. Li, T. Liu, Y. Yang, W. Qiu, C. Liang, Y. Tong, Y. Li, Zipping up NiFe (OH) x-encapsulated hematite to achieve an ultralow turn-on potential for water oxidation, ACS Energy Letters. 4 (2019) 1983–1990.

[13] Z. Zhang, H. Nagashima, T. Tachikawa, Ultra-narrow depletion layers in a hematite mesocrystal-based photoanode for boosting multihole water oxidation, Angewandte Chemie. 132 (2020) 9132–9139.

[14] C.A. Mesa, L. Francas, K.R. Yang, P. Garrido-Barros, E. Pastor, Y. Ma, A. Kafizas, T.E. Rosser, M.T. Mayer, E. Reisner, Multihole water oxidation catalysis on haematite photoanodes revealed by operando spectroelectrochemistry and DFT, Nature Chemistry. 12 (2020) 82–89.

[15] M. Barroso, A.J. Cowan, S.R. Pendlebury, M. Grätzel, D.R. Klug, J.R. Durrant, The role of cobalt phosphate in enhancing the photocatalytic activity of α-Fe2O3 toward water oxidation, Journal of the American Chemical Society. 133 (2011) 14868–14871.

[16] M. Barroso, S.R. Pendlebury, A.J. Cowan, J.R. Durrant, Charge carrier trapping, recombination and transfer in hematite (α-Fe 2 O 3) water splitting photoanodes, Chemical Science. 4 (2013) 2724–2734.

[17] D.R. Gamelin, Catalyst or spectator?, Nature Chemistry. 4 (2012) 965–967.

[18] X. Li, M. Jia, Y. Lu, N. Li, Y.-Z. Zheng, X. Tao, M. Huang, Co (OH) 2/BiVO4 photoanode in tandem with a carbon-based perovskite solar cell for solar-driven overall water splitting, Electrochimica Acta. 330 (2020) 135183.

[19] R. Chen, C. Zhen, Y. Yang, X. Sun, J.T. Irvine, L. Wang, G. Liu, H.-M. Cheng, Boosting photoelectrochemical water splitting performance of Ta3N5 nanorod array photoanodes by forming a dual co-catalyst shell, Nano Energy. 59 (2019) 683–688.

[20] Z. Li, Y. Wu, G. Lu, Highly efficient hydrogen evolution over Co (OH) 2 nanoparticles modified g-C3N4 co-sensitized by Eosin Y and Rose Bengal under visible light irradiation, Applied Catalysis B: Environmental. 188 (2016) 56–64.

[21] D. Maity, K. Karmakar, D. Mandal, D. Pal, G.G. Khan, K. Mandal, Earth abundant transition metal ferrite nanoparticles anchored ZnO nanorods as efficient and stable photoanodes for solar water splitting, Nanotechnology. 31 (2020) 475403.

[22] G. Wang, Y. Ling, D.A. Wheeler, K.E. George, K. Horsley, C. Heske, J.Z. Zhang, Y. Li, Facile synthesis of highly photoactive α-Fe2O3-based films for water oxidation, Nano Letters. 11 (2011) 3503–3509.

[23] R. Zhang, Y. Fang, T. Chen, F. Qu, Z. Liu, G. Du, A.M. Asiri, T. Gao, X. Sun, Enhanced photoelectrochemical water oxidation performance of Fe2O3 nanorods array by S doping, ACS Sustainable Chemistry & Engineering. 5 (2017) 7502–7506.

[24] T. Fujii, F.M.F. De Groot, G.A. Sawatzky, F.C. Voogt, T. Hibma, K. Okada, In situ XPS analysis of various iron oxide films grown by NO 2-assisted molecular-beam epitaxy, Physical Review B. 59 (1999) 3195.

[25] D. Pal, A. Sarkar, N.G. Ghosh, D.M. Sanke, D. Maity, K. Karmakar, D. Sarkar, S.S. Zade, G.G. Khan, Integration of LaCo (OH) x Photo-Electrocatalyst and Plasmonic Gold Nanoparticles with Sb-Doped TiO2 Nanorods for Photoelectrochemical Water Oxidation, ACS Applied Nano Materials. (2021).

[26] G. Dong, H. Hu, L. Wang, Y. Zhang, Y. Bi, Remarkable enhancement on photoelectrochemical water splitting derived from well-crystallized Bi2WO6 and Co (OH) x with tunable oxidation state, Journal of Catalysis. 366 (2018) 258–265.

[27] B. He, Y. Wang, X. Liu, Y. Li, X. Hu, J. Huang, Y. Yu, Z. Shu, Z. Li, Y. Zhao, Spatial engineering of a Co (OH) x encapsulated p-Cu 2 S/n-BiVO 4 photoanode: simultaneously promoting charge separation and surface reaction kinetics in solar water splitting, Journal of Materials Chemistry A. 7 (2019) 6747–6752.

[28] Y. Zhang, D. Wang, X. Zhang, Y. Chen, L. Kong, P. Chen, Y. Wang, C. Wang, L. Wang, Y. Liu, Enhanced photoelectrochemical performance of nanoporous BiVO4 photoanode by combining surface deposited cobalt-phosphate with hydrogenation treatment, Electrochimica Acta. 195 (2016) 51–58.

[29] H. Zhang, D. Li, W.J. Byun, X. Wang, T.J. Shin, H.Y. Jeong, H. Han, C. Li, J.S. Lee, Gradient tantalum-doped hematite homojunction photoanode improves both photocurrents and turn-on voltage for solar water splitting, Nature Communications. 11 (2020) 1–11.

[30] T.H. Jeon, G. Moon, H. Park, W. Choi, Ultra-efficient and durable photoelectrochemical water oxidation using elaborately designed hematite nanorod arrays, Nano Energy. 39 (2017) 211–218.

[31] J.-W. Jang, C. Du, Y. Ye, Y. Lin, X. Yao, J. Thorne, E. Liu, G. McMahon, J. Zhu, A. Javey, Enabling unassisted solar water splitting by iron oxide and silicon, Nature Communications. 6 (2015) 1–5.

[32] L. Wang, N.T. Nguyen, P. Schmuki, A facile surface passivation of hematite photoanodes with iron titanate cocatalyst for enhanced water splitting, ChemSusChem. 9 (2016) 2048–2053.

[33] S.C. Riha, B.M. Klahr, E.C. Tyo, S. Seifert, S. Vajda, M.J. Pellin, T.W. Hamann, A.B. Martinson, Atomic layer deposition of a submonolayer catalyst for the enhanced photoelectrochemical performance of water oxidation with hematite, Acs Nano. 7 (2013) 2396–2405.

[34] S.-S. Yi, B.-R. Wulan, J.-M. Yan, Q. Jiang, Highly efficient photoelectrochemical water splitting: surface modification of cobalt-phosphate-loaded Co3O4/Fe2O3 p–n heterojunction nanorod arrays, Advanced Functional Materials. 29 (2019) 1801902.

[35] C. Li, Z. Chen, W. Yuan, Q.-H. Xu, C.M. Li, In situ growth of α-Fe 2 O 3@ Co 3 O 4 core–shell wormlike nanoarrays for a highly efficient photoelectrochemical water oxidation reaction, Nanoscale. 11 (2019) 1111–1122.

[36] Z. Li, Q. Zhang, X. Chen, F. Yang, D. Wang, L. Liu, J. Ye, Cl− modification for effective promotion of photoelectrochemical water oxidation over BiVO 4, Chemical Communications. 56 (2020) 13153–13156.

[37] M. Wang, A. Krasnok, S. Lepeshov, G. Hu, T. Jiang, J. Fang, B.A. Korgel, A. Alù, Y. Zheng, Suppressing material loss in the visible and near-infrared range for functional nanophotonics using bandgap engineering, Nature Communications. 11 (2020) 1–9.

[38] P. Tang, J. Arbiol, Bottom-up Engineering of Hematite Nanowire Heterostructures for Photoelectrochemical Water Splitting, in: ECS Meeting Abstracts, IOP Publishing, 2019: p. 1613.

[39] L. Yao, Y. Liu, H.-H. Cho, M. Xia, A. Sekar, B.P. Darwich, R.A. Wells, J.-H. Yum, D. Ren, M. Grätzel, A hybrid bulk-heterojunction photoanode for direct solar-to-chemical conversion, Energy & Environmental Science. 14 (2021) 3141–3151.

[40] M. Ye, J. Gong, Y. Lai, C. Lin, Z. Lin, High-efficiency photoelectrocatalytic hydrogen generation enabled by palladium quantum dots-sensitized TiO2 nanotube arrays, Journal of the American Chemical Society. 134 (2012) 15720–15723.

[41] X. Yang, A. Wolcott, G. Wang, A. Sobo, R.C. Fitzmorris, F. Qian, J.Z. Zhang, Y. Li, Nitrogen-doped ZnO nanowire arrays for photoelectrochemical water splitting, Nano Letters. 9 (2009) 2331–2336.

[42] B. Zhang, X. Huang, Y. Zhang, G. Lu, L. Chou, Y. Bi, Unveiling the activity and stability origin of BiVO4 photoanodes with FeNi oxyhydroxides for oxygen evolution, Angewandte Chemie International Edition. 59 (2020) 18990–18995.

Chapter 7 Conclusion and Future Scope of The Work

This chapter presents an overall conclusion of all the works included in this thesis and their scope in the scientific field in the future.

7.1 Conclusion

Energy is the primary demand of an industrially revolutionalized society to maintain its minimum standard of living. The development of a carbon-free energy economy is necessary for the sustainable development of society. The future energy infrastructure needs to be based on environmentally adequate alternative energy resources by replacing the conventional fuel-based energy supply. In this regard, renewable energy resources, primarily solar energy, provide a secure and sustainable scope of energy harvesting with the promise to tackle the global energy demand and the issue of climate change.

This thesis has been focused on the fabrication and development of different earth-abundant metal oxide semiconductor-based photoanodes for PEC water oxidation application. Primarily, we have fabricated one-dimensional nanostructure (nano rods) of ZnO and Fe_2O_3 on FTO coated glass substrates, serving as the pristine photoanodes of PEC cells. Various nanoscale surface engineering strategies, including the formation of the nano-heterojunction type photoanodes, have been adopted to overcome the limitations of a single photoanode material for PEC cell application. All the nanostructures have been fabricated through easy, scalable, and low-cost methods.

At first, we have fabricated an n-n type heterostructure between ZnO NRs and MoO_3 by employing a low-cost, easy and scalable spin coating technique. The thickness of the MoO_3 layer has been optimized in terms of spin coating event repetition by maximizing the photoconversion efficiency. Introducing the MoO_3 layer over ZnO NRs remarkably improves the visible-light-driven PEC water splitting activity. For the optimized ZnO/MoO_3 photoanode, an 8.3 and 4.76 fold increase has been observed in photocurrent density and ABPE, respectively, under visible light illumination. This study demonstrates that the n-ZnO/n-MoO_3 type heterojunction might be a potential strategy to mitigate the limitations involved in solar energy conversion in PEC cells.

In another work, the three-dimensional (3D) ZnO/$CoFe_2O_4$ and ZnO/$NiFe_2O_4$ type-II (n-n and n-p) heterojunction photoanodes have been successfully fabricated by assembling chemically synthesized $CoFe_2O_4$ and $NiFe_2O_4$ spinel ferrite nano-particles on the one dimensional pristine ZnO NRs by spin coating. The UV-visible light absorption ability of the respective heterojunction photoelectrodes was enhanced due to the narrow band-gap of $CoFe_2O_4$ and $NiFe_2O_4$ NPs. Significant enhancement in photocurrent density has been observed with ZnO/$CoFe_2O_4$ and ZnO/$NiFe_2O_4$ heterojunction photoanodes with a typical value of 1.13 and 1.23 $mA.cm^{-2}$, respectively, compared to 0.60 $mA.cm^{-2}$ current density of pristine ZnO NRs photoanode at 1.23V vs. RHE. The favorable type–II band alignment at *n-n* heterointerface boosts the charge

separation and transportation and suppresses the electron-hole pair recombination, resulting in excellent photocurrent density. Therefore the design of these nano-heterostructure provides an effective strategy to develop economic, earth-abundant materials-based electrodes with enhanced PEC performance.

Afterward, a three-dimensional network of a type-II like n-ZnO/p-$ZnCo_2O_4$ core/shell nano-heterojunction photoanode has been fabricated via coupling p-$ZnCo_2O_4$ through electrodeposition route. The effective light-harvesting ability and favorable band alignment boost the charge generation and rapid separation of electron-hole pairs in heterojunction photoanode. The remarkably improved charge transfer mechanism for the *n*-ZnO/*p*-$ZnCo_2O_4$ nano-heterojunction photoanode coupled with the enhanced surface catalytic reaction because of the *p*-$ZnCo_2O_4$ OER catalyst results in a 351% and 164% enhancement in photocurrent density and ABPE, respectively, over the pristine ZnO NRs. Therefore, the synergistic coupling of *n*-ZnO and *p*-$ZnCo_2O_4$ for a nano-heterojunction photoelectrode serves as an ideal photoanode for solar-driven PEC water oxidation.

In the final work, we have synthesized CoPi, and $Co(OH)_x$ dual co-catalysts modified Fe_2O_3 NRs photoanode by coupling cost-effective and straight forward photoelectrodeposition and SAILR method. The dual co-catalyst modification increases the surface photovoltage generation through reduction of the surface states responsible for photocarrier recombination in Fe_2O_3 and boosts the photo hole transfer for OER. The dual co-catalysts modification also enhances carrier density and reduces the depletion width, leading to a large photocurrent. Compared to pristine Fe_2O_3, a 358% enhancement in photocurrent density at 1.23V vs. RHE with an ultralow turn-on potential (0.4V vs. RHE, lowest ever known) has been observed Fe_2O_3/CoPi/$Co(OH)_x$ photoanode. Overall the dual co-catalysts overlayer improves the oxygen evolution reaction kinetics and electrical conductivity for hematite NRs, resulting in improved PEC water oxidation.

7.2 Future Scope

The research works presented in this dissertation set the platform for further research and development of various earth-abundant materials as photoanode in solar energy to chemical energy conversion in PEC cells through water splitting. The low-cost and easily scalable photoanode synthesis routes that have been presented in this thesis are especially attractive for PEC water splitting cell fabrication. The involvement of earth-abundant metal oxide semiconductor-based photoanodes provides a massive scope of further development due to their durability, reaction kinetics, and large-scale

production possibility. Over the past few decades, ZnO-based nanostructure photoanodes have shown tremendous potential to be used in PEC cells. They have favorable characteristics like carrier density, electron and hole mobility, band structure, natural abundance, and large-scale productivity. Enormous research and technological development is required to meet the current energy demand with metal oxide-based water splitting systems. The physics behind the different photoelectrochemical phenomena of the photoanodes has been explored in this thesis which will build up a better understanding and motivate other researchers in this particular direction of research. In particular, we have found the dual functional $ZnCo_2O_4$, which acts as a light-harvesting material and an OER catalyst, effectively suppresses the limitations of ZnO and significantly enhances photocurrent density; thereby, an increase in photoconversion efficiency has been observed with $ZnO/ZnCo_2O_4$ heterojunction photoanode. Therefore nano-heteroarchitecture designing with proper band-gap engineering could be an effective solution to enhance PEC activity of the earth-abundant metal oxide-based semiconductor photoanodes. On the other hand, we have shown that the dual co-catalyst (CoPi and $Co(OH)_x$) modification on Fe_2O_3 enhances the photocurrent density and shifts the water oxidation turn-on potential to a remarkably low value. This strategy could be applied to other metal oxide semiconductors to get excellent water splitting activity at low bias potential. It is evident that proper surface engineering is an effective approach to boost the PEC performance of the electrodes. Choice of suitable co-catalyst also enhances the surface reaction kinetics in photoelectrodes. However, our research work is confined to the laboratory-scale production of H_2 through solar water splitting. More research and developments are required for the large-scale production of H_2 by solar water splitting.